Climate variability over the tropical Indian Ocean since the Last Glacial Maximum and its impact on primary productivity : insights from model-data comparisons

Xinquan Zhou

Thèse de doctorat

NNT : 2021UPASJ014

université PARIS-SACLAY

Climate variability over the tropical Indian Ocean since the Last Glacial Maximum and its impact on primary productivity: insights from model-data comparisons

Variabilité climatique de l'Océan Indien Tropical depuis le Dernier Maximum Glaciaire et son impact sur la productivité primaire : apport des comparaisons modèles-données

Thèse de doctorat de l'université Paris-Saclay

École doctorale n° 579, Sciences mécaniques et énergétiques, matériaux et géosciences (SMEMAG)
Spécialité de doctorat: Météorologie, océanographie, physique de l'environnement
Unité de recherche : Université Paris-Saclay, CNRS, GEOPS, 91405, Orsay, France
Référent : Faculté des sciences d'Orsay

Thèse présentée et soutenue à Paris-Saclay, le 08/10/2021, par

Xinquan ZHOU

Composition du Jury

Pascale BRACONNOT Directrice de recherche (HDR), LSCE, Université Paris-Saclay	Présidente
Laurent BOPP Directeur de recherche (HDR), LMD, École Normale Supérieure	Rapporteur & Examinateur
Thibault DE GARIDEL-THORON Chargé de recherche (HDR), CEREGE, Aix-Marseille Université	Rapporteur & Examinateur
Johan ETOURNEAU Maître de conférences, Université de Bordeaux	Examinateur
Masa KAGEYAMA Directrice de recherche (HDR), LSCE, Université Paris-Saclay	Examinatrice
Chuanlian LIU Professeur, Tongji University	Examinateur

Direction de la thèse

Stéphanie DUCHAMP-ALPHONSE Maîtresse de conférences (HDR), Université Paris-Saclay	Directrice de thèse

Acknowledgements

For the moment, I would like to sincerely express my thanks to those who helped me a lot in this four-year PhD study. Without their kind helps, I can't complete this thesis.

I would first thank my supervisor, Dr. Stéphanie Duchamp-Alphonse. I met Stéphanie four years ago in Shanghai, and she gave me an opportunity to study in France. During these four years, she made great efforts in guiding me, provided helpful suggestions in science, and inspired me when I faced difficulties. I enjoyed our discussions and gained a lot of knowledge from her. For this thesis, she spent plenty of time on the correction. I am grateful for this. I also thank Pr. Christophe Colin for providing me suggestions, and he taught me a lot in paleoceanography. I thank Dr. Masa Kageyama and Dr. Franck Bassinot at LSCE for their constructive suggestions for my study. Masa provided me useful modelling data and taught me data processing. I learnt a lot from her classes about climate change. Franck gave me convenience in core sampling and selflessly shared his ideas during discussions. I also thank Dr. Luc Beaufort and Dr. Clara Bolton at CEREGE for sharing their ideas enlightening me. I thank Pr. Giuseppe Siani at GEOPS for teaching how to pick foraminifera. I thank all the members of the “Paléoclimats et Dynamique Sédimentarire” research team at GEOPS. My thanks also go to Pr. Chuanlian Liu at Tongji University, my master's degree supervisor, for encoring me all the time.

I thank Pr. Xavier Quidelleur and Mme. Thi Kim Ngan Ho for their kind helps in the routine procedures of the doctor school. Many thanks to Margaux Brandon, Alexis Derycke, Solène Poutout, and Ruifang Ma, colleagues working with me in the same office for two or three years. I really miss the time of our communications in science and daily lives. I really want to thank Margaux and Alexis, from whom I got to know France. I thank Yutian Ke, Ting Kong, Consuelo Martínez Fontaine and Xiaolei Pang, who I talked to, sharing my happiness and unhappiness. I thank the GEOPS football team for bringing me joy. I also thank Hongrui Zhang for sharing his ideas in science.

I appreciate the China Scholarship Council and the Université Paris-Saclay for providing me a scholarship lasting four years that supported my study and life in France.

At last, I would like to thank my parents, for their selfless love.

Contents

Résumé en français

Sous l'influence du réchauffement climatique entraîné par l'émission croissante de gaz à effet de serre d'origine anthropique, le climat de la Terre connait des changements importants. Pour mieux prévoir les changements futurs, il est important de connaître leur variabilité dans le passé et d'en comprendre les mécanismes. Aujourd'hui, des milliards de personnes vivent sur les pourtours de l'Océan Indien tropical, où l'évolution future de la dynamique du climat qui présente de fortes saisonnalités, reste mal connue. L'océan Indien tropical est sous l'influence de i) la mousson indienne caractérisée par des vents du sud-ouest en été et du nord-est en hiver, et ii) la circulation zonale de Walker représentée par des vents d'ouest équatoriaux qui impactent à leur tour, la distribution de la productivité primaire marine (PP) actuelle et passée. Très peu de reconstructions de PP dans le passé (paléo-PP) existent dans cette zone, et c'est particulièrement le cas lorsqu'on s'intéresse aux 25 000 dernières années qui enregistrent pourtant des changements importants des conditions climatiques limites liées à l'insolation, au volume de glace, au niveau marin et/ou aux concentrations en gaz à effet de serre. Cette période enregistre par ailleurs, d'importants changements dans la circulation méridienne de retournement Atlantique (AMOC) qui module le transport latitudinal de chaleur, en particulier pendant le Stade Heinrich 1 (HS1 ; 17.5-15 ka) et le Bølling-Allerød (BA ; 14.7-13 ka) et pendant le Dryas récent (YD ; 12.9-11.5 ka), respectivement caractérisés par des conditions froides et chaudes dans l'hémisphère Nord.

L'objectif de ce travail est de reconstruire les changements orbitaux à millénaires de la PP de l'océan Indien tropical depuis le dernier maximum glaciaire (DMG) via l'étude des assemblages de coccolithes de quatre carottes sédimentaires récoltées dans le Golfe du Bengale (GdB)/mer d'Andaman. (MD77-176, MD77-191, et BAR94-24) et la mer d'Arabie (MAr) (MD00-2354), et comprendre leurs relations avec la dynamique de la mousson indienne et de la circulation de Walker en utilisant les sorties des modèles IPSL-CM5A-LR (IPSL), AWI-ESM-1-1-LR (AWI), et CCSM3. Les résultats de la modélisation permettent d'interpréter à grande échelle, les données de paléo-PP obtenues qui sont comparées aux données paléoclimatiques de la littérature.

Cette thèse comprend six chapitres.

Le chapitre 1 repose sur la présentation des contextes atmosphérique, océanique et biologique de l'océan Indien tropical en se focalisant particulièrement sur la distribution de la PP dans les zones étudiées. Un « état de l'art » des travaux publiés dans la littérature permet de mettre en évidence les

questions restant en suspend quant à la dynamique de la circulation de la mousson indienne et de l'Indian Ocean Walker depuis le DGM et ainsi, de formuler les principaux objectifs de cette étude.

Le chapitre 2 décrit le matériel et les méthodes utilisés pour répondre aux objectifs énoncés, et donne des informations spécifiques sur les modèles d'âge des carottes de sédiments, les estimations de paléo-PP, et la modélisation climatique. Les changements de PP dans le passés sont reconstruits à l'aide d'une fonction de transfert basée sur la relation existante entre les pourcentages de l'espèce de coccolithes *Florisphaera profunda* (Fp %) dans les sédiments de surface et les teneurs en chlorophyll des eaux océaniques de surface. Par ailleurs, Fp habite la zone photique inférieure. Son abondance relative est donc directement liée aux changements de profondeur de la nutricline et l'étude des spécimens fossiles préservés dans les carottes sédimentaires permet aussi de reconstruire la dynamique de la nutricline dans le passé. Quatre simulations exécutées avec les modèles de l'IPSL ont été étudiées sous les conditions préindustrielles (CTRL), de l'Holocène moyen (HM), du DMG et du DMGf. Dans la simulation DMGf, un flux d'eau douce de 0,2 Sv est simulé dans l'océan Atlantique Nord pour forcer l'arrêt de l'AMOC par rapport à la simulation du DGM et ainsi se rapprocher des conditions du HS1. Trois simulations exécutées avec AWI ont été étudiées dans des conditions de CTRL, HM et DMG. La simulation transitoire, TraCE-21, a été exécutée avec CCSM3, dont les sorties couvrent les 22 derniers ka.

Le chapitre 3 présente les données de paléo-PP du site MD77-176, afin d'étudier la dynamique de la mousson d'été indienne (MEI) et son impact sur la PP du Nord-Est du GdB au cours des 26 derniers ka. Aujourd'hui, les changements de PP sont associés à des changements de la stratification des eaux océaniques de surface, liés aux conditions de salinité (SSS), elles-mêmes influencées par les apports en eau douce du système fluviatile Irrawaddy-Salween qui sont tributaires des changements d'intensité de la MEI. Au cours du DMG, les évènements de forte PP correspondent à des périodes ou des conditions de faible salinité prévalent (et vice versa). Ces relations suggèrent l'influence des apports fluviatiles et probablement ceux en nutriments depuis les embouchures des fleuves Irrawaddy-Salween alors devenues plus proximales, en raison d'un niveau marin plus bas. Dans un tel contexte, une plus forte (faible) MEI entraînerait un ruissellement plus élevé (réduit) sur les continents, des apports en nutriments fluvatiles plus forts (faibles) et une PP plus élevée (faible). Au cours de la dernière déglaciation et de l'Holocène, la relation entre la PP et la salinité des eaux de surface s'inverse et les intervalles de forte PP correspondent à des périodes ou les eaux de surface sont plus salées (et vice et versa). Ceci est particulièrement évident pendant les périodes HS1 et YD, lorsque la MEI est plus faible, et inversement pendant le B-A, lorsque la MEI est plus forte. Ces hypthèses sont confirmées

par les résultats des simulations DMGf et HM du modèle de l'IPSL et celles du modèle TraCE21 qui montrent que lorsque l'AMOC s'affaiblit (HS1, YD), la PP du site MD77-176 devient plus élevée en raison d'une augmentation de la SSS et d'une stratification plus faible dans le Nord Ouest du GdB. A l'inverse, lorsque l'AMOC se renforce (B-A) ou que des conditions de forte insolation estivale dans l'Hémisphère Nord (Holocène précoce à moyen, 8−6 ka) prévalent, la PP du Nord Ouest du GdB devient plus faible à cause d'une salinité plus faible, et d'une stratification renforcée.

Le chapitre 4 traite des variations de PP de la carotte MD00-2354 afin d'étudier la dynamique de la mousson indienne dans le Nord-Ouest de la Mer d'Arabie au cours des 23 derniers ka. Aujourd'hui, les changements de PP y sont contrôlés à la fois par l'upwelling côtier associé aux vents du sud-ouest en été, à la fois par le mélange des eaux océaniques de surface, induit par les vent du nord-est et le refroidissement de surface enregistrés en hiver. A l'échelle des 23 derniers ka, il semble que la PP était d'environ 90 % plus élevée au DMG qu'à l'Holocène. Ces résulats suggèrent la forte influence des conditions de mousson d'hiver sur la PP dans la région d'étude. En effet, lorsque la mousson d'hiver s'intensifie sous les conditions glaciaires caractérisées par des calottes de glace plus étendues et des concentrations en gaz à effet de serre plus faibles, un mélange plus fort des eaux de surface pendant l'hiver, associé à une diminution des températures pourraient augmenter la PP. Des tendances opposées seraient retrouvées au cours du B-A. et à l'HM, lorsque prévalent les conditions de déglaciation caractérisées par des calottes glaciaires réduites et des concentrations plus élevées en gaz à effet de serre. De telles hypothèses sont confirmées par les résultats de la simulation DMG exécutée avec IPSL. Toutefois, dans un tel contexte, on ne peut exclure que la fertilisation des eaux océaniques de surface par des apports éoliens (riches en nutriments) accrus, ait également contribué à l'augmentation de la PP.

Le chapitre 5 combine les résultats des chapitres 3 et 4 et se concentre sur la dynamique de la stratification des eaux océaniques de surface depuis le DMG, via l'utilisation des pourcentages de Fp des carottes MD77-176 et MD00-2354, et les simulations du modèle TraCE 21, en supposant que la stratification des eaux de surface dans le nord-est du GdB et le nord-ouest de la mer d'Arabie était respectivement contrôlée par la mousson d'été (chapitre 3) et la mousson d'hiver (chapitre 4). Les résultats les plus frappants montrent que lors de la dernière déglaciation, la mousson d'été était en opposition de phase avec la mousson d'hiver et toutes deux étaient rythmées par des changements d'intensité de l'AMOC. Pendant les périodes HS1 et YD, l'affaiblissement du transport de chaleur en Océan Atlantique Nord, lié à un affaiblissement de l'AMOC, accompagné par un refroidissement du continent eurasiatique, aurait été associé à une MEI plus faible et une MHI plus forte. Inversement, pendant la

période du B-A, lorsque l'AMOC s'intensifie, le renforcement du transport de chaleur en Océan Atlantique Nord, accompagné par une réchauffement du continent eurasiatique, se serait accompagné d'une MEI plus forte et d'une MHI plus faible.

Le chapitre 6 présente la PP reconstruite au niveau des carottes BAR94-24 et MD77-191, prélevées respectivement au large de la pointe nord-ouest de Sumatra et au large de la pointe sud de l'Inde, afin d'étudier la dynamique des vents zonaux et, par conséquent, les changements de la circulation de Walker depuis le DMG. Les données de PP de la carotte MD77-191 ne couvrant que les derniers 16 ka, elles ont été comparées et par des données de PP indirectes, et obtenues via le pourcentage de *Globigerina bulloides* d'une carotte sédimentaire voisine. Aujourd'hui, les deux carottes se situent au cœur d'upwelling côtiers générés par les vents d'ouest équatoriaux en été (MD77-191) et les vents d'est équatoriaux d'hiver (BAR94-24) et la PP est directement liées à la dynamique de la circulation de Walker. En assumant que cette relation se vérifie dans le passé, il semblerait que pendant le DMG, de plus fortes PP enregistrées au large de Sumatra et au large de l'Inde, suggèrent des vents d'est plus forts en hiver et des vents d'ouest plus forts en été. De telles assomptions sont confirmées par les sorties de modèles qui simulent des anomalies à la fois dans les vents équatoriaux d'Est en été, et dans les vent équatoriaux d'ouest en hiver. Dans tous les cas, les simulations des conditions moyennes annuelles révèlent des vents équatoriaux d'Est plus forts dans l'Océan Indien de l'océan Indien, et indiquent ainsi une circulation de Walker plus faible. Pendant l'HM, des PP plus faibles sont enregistrés au large de Sumatra et au large de l'Inde. Ces résultats corroborent les simulations numériques qui décrivent des vents d'est plus faibles au large de Sumatra pendant l'hiver, et des vents d'ouest plus faibles au Sud de l'Inde en été. Dans tous les cas, il semblerait que les vents d'Est dominent à l'échelle de l'année, et par conséquent, que l'océan Indien soit également associé à une circulation de Walker plus faible pendant cette période de temps. Par conséquent, la circulation de Walker dans l'océan Indien était plus faible qu'elle ne l'est actuellement pendant le DMG et le début de l'Holocène moyen, mais les deux états auraient une saisonnalité différente dans les changements de vents équatoriaux. Une circulation de Walker plus faible pendant le DMG était probablement liée à l'exposition des plateaux continentaux sous des conditions de Bas Niveau Marin tandis que celle enregistrée à l'HM était probablement associée à une insolation plus forte de l'Hémisphère Nord.

Globalement, ce travail confirme que le paléo-PP dans l'océan Indien tropical peut bien refléter les variations paléoclimatiques. Les variations de PP sont liées à des changements de teneur en nutriments dans la zone photique qui peuvent être influencés par des processus variés. Ces derniers

comprennent les gradients de salinité et de température de la partie supérieure de l'eau de mer qui contrôlent la stratification, les vents côtiers qui peuvent entraîner la remontée des eaux et les apports éoliens qui peuvent apporter des nutriments des continents. Dans tous les cas, ce travail permet de mieux comprendre la dynamique de la mousson indienne et son lien avec l'AMOC et la circulation de Walker avec des applications probables pour les projections climatiques futures.

Abstract in English

Under the influence of global warming driven by the increasing emission of anthropogenic greenhouse gases, the earth's climate will have significant changes. To better predict climate change in the future, it is important to know climate variability in the past and understand its mechanisms Today, billions of people live on the lands surrounding the tropical Indian Ocean, where climate evolution, characterized by strong seasonality, remains unknown. The tropical Indian Ocean is under the influence of both, the Indian monsoon characterized by southwesterly winds during summer and northeasterly winds during winter, and the zonal Walker circulation characterized by annual mean equatorial westerly winds. These mechanisms impact marine primary productivity (PP) today and in the past. However, very few paleo-PP reconstructions exist in that area so far, and this is particularly the case when dealing with the last 25 000 years (25 ka) despite their major contribution in understanding low-latitude climate patterns under changing boundary conditions such as insolation, ice volume, sea-level, and greenhouse gases concentrations. It also witnesses significant changes in the Atlantic Meridional Overturning Circulation (AMOC) that modulates latitudinal heat transport, particularly during the Heinrich Stadial 1 (HS1; 17.5−15 ka) and the Bølling–Allerød (B-A; 14.7−13 ka), as well as during the Younger Dryas (YD; 12.9−11.5 ka), characterized by cold and warm conditions in the northern hemisphere, respectively.

The aim of this work is to reconstruct orbital- to millennial-scales PP patterns of the tropical Indian Ocean since the Last Glacial Maximum (LGM) based on coccolith assemblage analyses of four sediment cores retrieved in the Bay of Bengal (BoB)/Andaman Sea (MD77-176, MD77-191, and BAR94-24) and the Arabian Sea (AS) (MD00-2354), and understand their relationships with the Indian Monsoon and Walker circulations using outputs from IPSL-CM5A-LR (IPSL), AWI-ESM-1-1-LR (AWI), and CCSM3 models. The modelling results help better interpret the paleo-PP records and published paleoclimate records on a broad overview.

This thesis includes six chapters.

Chapter 1 is related to the atmospheric, oceanic, and biologic contexts of the tropical Indian Ocean with a special focus on PP distribution in the studied areas. A “state of the art” of published studies helps to highlight the unsolved questions concerning the dynamics of the Indian Monsoon and Indian Ocean Walker circulation since the LGM and thus, to formulate the aims of this study.

Chapter 2 describes the material and methods used to fullfill the objectives, and give specific

information on sediment core age models, paleo-PP estimates, as well as climate modelling. Reconstructed paleo-PP are obtained using a transfer function based on *Florisphaera profunda* percentages (Fp %). Fp is a coccolithophore dwelling in the lower photic zone. Its relative abundance is sensitive to changes of nutricline depth and thus, to PP. Four simulations run with IPSL have been studied under conditions of pre-industrial (CTRL), mid-Holocene (MH), LGM, and LGM freshwater hosing (LGMf). In the LGMf simulation, a freshwater flux of 0.2 Sv was prescribed over the North Atlantic Ocean to force the AMOC shutdown in respect to the normal LGM simulation. Three simulations run with AWI have been studied under conditions of CTRL, MH, and LGM conditions. The transient simulation, TraCE-21, was run with CCSM3, whose outputs cover the last 22 ka.

Chapter 3 focuses on paleo-PP dynamics of site MD77-176, in order to study the dynamic of the Indian Summer Monsoon (ISM) in the northeastern BoB over the last 26 ka. Today, changes in PP are associated to changes in sea surface salinity (SSS)-related stratification that is driven by freshwater input from the Irrawaddy-Salween river systems and hence, by changes in the ISM. During the LGM, millennial-scale fluctuations of PP are found, and it appears that higher PP intervals correspond to fresher upper seawater (and vice versa). These relationships suggest the influence of nutrient inputs from closer river mouths associated with a lower sea level situation. In such a context, stronger (weaker) ISM might resulted in higher (reduced) run-off, stronger (lower) inputs of nutrients to the core site and thus higher (lower) PP. During the last deglaciation and the Holocene, the PP-salinity relationship is reversed compared to the LGM, and higher PP intervals correspond to saltier upper seawater (and vice versa). This is particularly obvious during HS1 and YD, when ISM is weaker, and inversely during B-A when ISM is stronger. Such patterns are confirmed by the results of LGMf and MH simulations run with IPSL as well as TraCE-21run with CCSM3. They both show that under AMOC shutdown (HS1, YD), PP became higher due to weaker freshwater input and salinity stratification while under stronger AMOC (B-A) and early-middle Holocene (EMH; 8−6 ka) characterized by a maximum in Northern Hemisphere summer insolation, PP became lower due to stronger freshwater input and salinity stratification.

Chapter 4 deals with paleo-PP variations from core MD00-2354 in order to study the dynamic of the Indian Monsoon in the northwestern AS over the last 23 ka. Today, PP changes at the study site are controlled by both, the coastal upwelling driven by southwesterly winds during summer, and the sea-surface mixing induced by northeasterly winds and surface cooling during winter. Over the last 23 ka, it appears that PP was about 90 % higher during the LGM than the Holocene. Relatively high PP is also found during HS1 and YD when AMOC shutdown, while relatively low PP is recorded during B-

A when AMOC reinforces. These patterns suggest the strong influence of winter monsoon conditions as well as high latitude climate conditions on PP. When Indian Winter Monsoon (IWM) intensified under glacial conditions characterized by larger ice sheets and lower greenhouse gases concentrations, stronger surface cooling and stronger mixing during winter increase PP in the northwestern part of the Arabian Sea. Opposite trends (and thus low PP) are found during the B-A. and the Holocene when deglacial conditions characterized by reduced ice sheets and higher greenhouse gases concentrations, prevailed. Such assumptions are supported by the results of LGM simulation run with IPSL. In such a context however, one cannot exclude that sea surface fertilization by increased nutrient (iron) rich aeolian inputs also contributed in rising PP during the LGM.

Chapter 5 combines results of chapters 3 and 4 and focuses on the upper seawater stratification dynamic since the LGM based on Fp% from cores MD77-176 and MD00-2354, and TraCE-21 simulations, assuming that stratification in the northeastern BoB and northwestern ArS were generally controlled by ISM (chapter 3) and IWM (chapter 4), respectively. The results show that during the last deglaciation, the ISM and IWM were anti-phased and both paced by millennial-scale fluctuations of the AMOC strength. During HS1 and YD, when AMOC shutdown, as the northward heat transport over the Atlantic Ocean weakened, Eurasia cooled, and the ISM weakened, while the IWM was stronger. Conversely, during B-A, when AMOC strenghtened, the northward heat transport over the Atlantic Ocean reinforced, Eurasia was warmer, and the ISM was stronger, while the IWM was weaker.

Chapter 6 presents reconstructed paleo-PP from cores BAR94-24 and MD77-191, retrieved off the northwestern tip of Sumatra and off the southern tip of India respectively, in order to infer zonal wind dynamics and hence, Indian Ocean Walker circulation changes since the LGM. Since core MD77-191 has no data in the LGM, PP off India is inferred from a record of *Globigerina bulloides* percentage from a nearby core. Empirical data are compared to simulations from the AWI model. Today, both cores are located within coastal upwelling cells that are driven by equatorial summer westerly winds and winter easterly winds, respectively. During the LGM, higher PP are recorded off Sumatra and off India, suggesting stronger winter easterlies and stronger summer westerlies, respectively. Such patterns are supported by the model outputs that simulate anomalous equatorial easterlies over the eastern Indian Ocean during winter, and anomalous westerlies over southern India, during summer. Overall, the model simulates annual mean equatorial easterlies over the equatorial Indian Ocean, with relatively less influent equatorial westerlies, thus indicating a weaker Walker circulation. During the EMH, lower PP are recorded both, off Sumatra and India. These results corroborate numerical simulations that depict weaker easterlies over the northwestern Sumatra during winter, and anomalous equatorial

easterlies over southern India and the eastern Indian Ocean during summer. The weaker winter easterlies are associated to anomalous cross-equator winds driven by anomalous meridional SLP gradient between Eurasia and the anomalous equatorial easterlies are associated to an anomalous zonal gradient of sea level pressure over the Indian Ocean. The model also reveals that the anomalous winds during summer dominate the annual state. As a result, annual mean equatorial easterlies are found in the eastern Indian Ocean, indicating an overall weaker Walker circulation. Consequently, the Indian Ocean Walker circulation was weaker than present during both, the LGM and EMH, but the two states show different seasonal patterns in equatorial winds. Weaker Walker circulation is probably driven by the exposure of continental shelves of the Maritime Continent during the LGM and to higher insolation during the EMH.

Overall, this work confirms that paleo-PP in the tropical Indian Ocean can well reflect the paleoclimate variations. PP variations are tied to the changes in nutrients contents in the photic zone. Several processes linked to climates can drive the changes. It includes the salinity and temperature gradients of the upper seawater that control the stratification, alongshore winds that can drive upwelling, and aeolian input that can bring continental nutrients. In all cases, this work helps better understanding the patterns and timing of the Indian monsoon and its link to the AMOC and the Walker circulation with probable applications for model projections under the recent global warming.

General Introduction

The atmosphere and hydrosphere of the Earth are two crucial reservoirs supporting lives and ecosystems. Within the atmosphere, the latitudinal distribution of heat results in pressure gradients that drive a large-scale meridional circulation. Because of the earth rotation and the Coriolis effect, the atmospheric movements are divided into several cells which constitute the so-called "atmospheric general circulation" (Fig. 1).

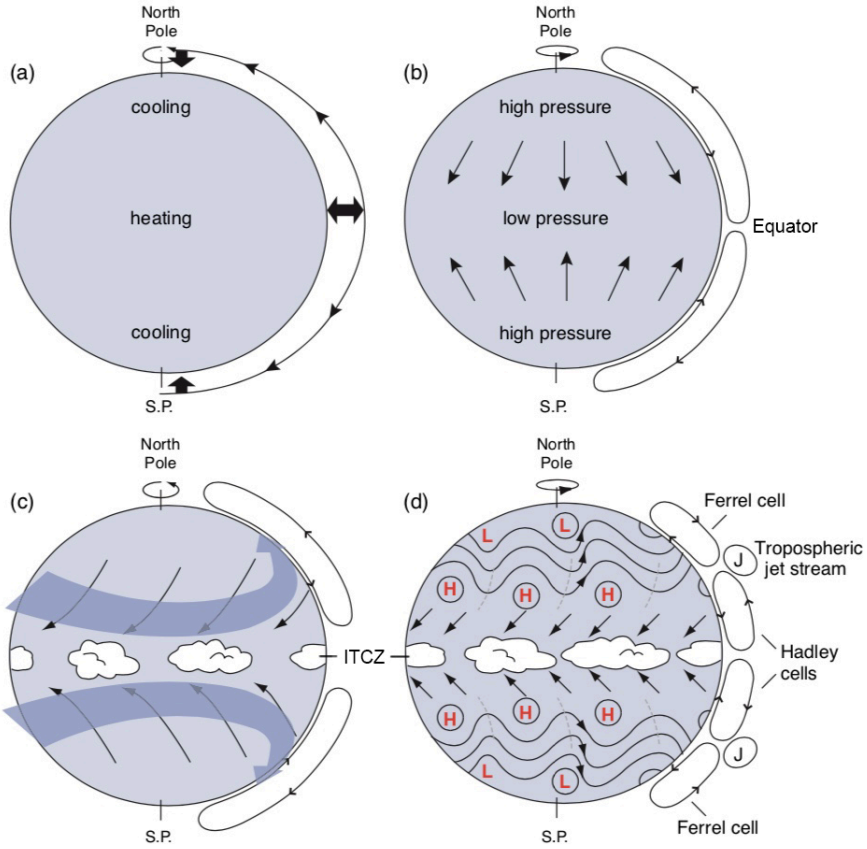

Fig. 1. Schematic representation of the general atmospheric circulation of the Earth with equinox conditions in the absence of land-sea contrasts. The cloud patterns mark the ICTZ. (Modified after Wallace and Hobbs, 2006).

Among these cells, the Hadley ones, located on either side of the equator, shape the Intertropical Convergence Zone (ITCZ) that represents the latitudinal belt with the strongest heating, ascending movements, and heaviest rainfall (Waliser et al., 1993; Fig. 1). The meridional thermal gradient is modulated by the seasonal insolation leading to the seasonal shifts of the ITCZ and the occurrence of monsoon climate systems. During summer, when the Northern Hemisphere more straightly receives the insolation, the ITCZ moves northward. It is accompanied by southeasterly winds over the northern tropical oceans, and high precipitation rates over the surrounded lands. During winter, when Southern Hemisphere more straightly receives the insolation, the ITCZ moves southward, southeasterly winds

over the northern tropical oceans turn to northeasterly, and the boreal precipitation rates get lower. Due to local land-sea configurations and interactions that drive specific feedbacks within the ocean-atmosphere, the amplitudes of both, the ITCZ shift and the monsoon systems, have zonal discrepancies. The largest amplitude of the ITCZ shift is found in the tropical Indian Ocean and South Asia due to the significant effect of thermal contrast between Eurasia and the tropical Indian Ocean (Fig. 2). It is associated with the most prominent of the world's monsoon systems that is the Indian monsoon, characterized by strong seasonal contrasts in the wind and precipitation patterns (Shankar et al., 2002; Gadgil, 2003). During summer, the southwesterly winds with moisture blow from the cooler Indian Ocean to the warmer South Asia resulting in heavy rainfall. During winter, the northeasterly winds blow from the lands carrying cold and dry air to the warmer Indian Ocean, and the South Asian rainfall becomes weaker.

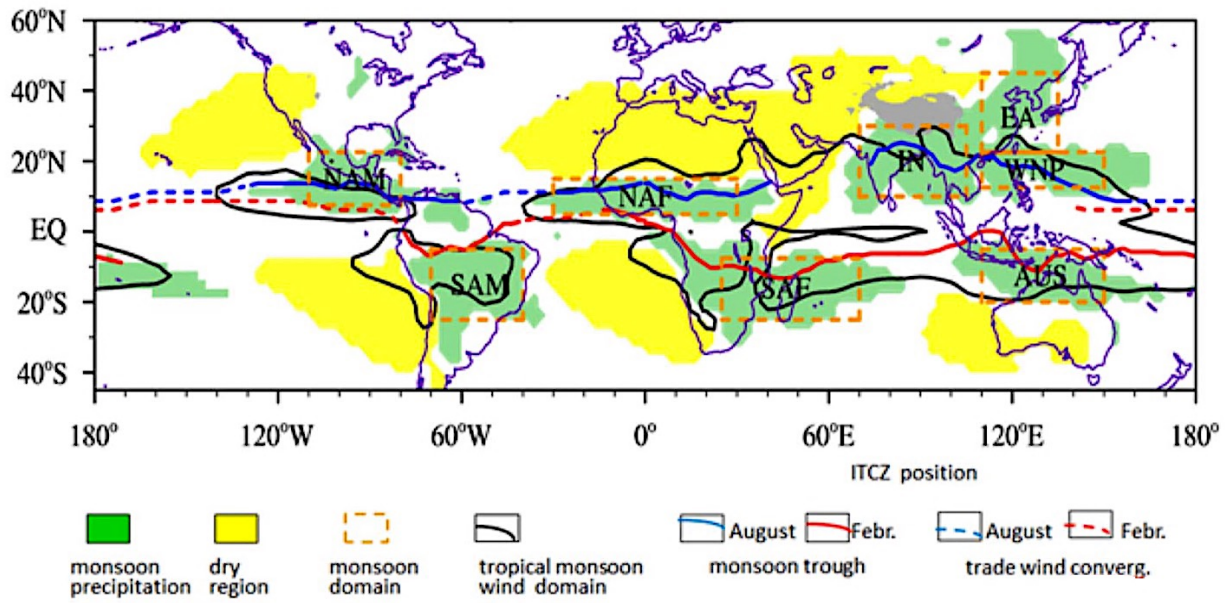

Fig. 2. The seasonal shift of the ITCZ and regional monsoon precipitation domains (in green) where local summer-minus-winter precipitation exceeds 300 mm, and the local summer precipitation exceeds 55% of the annual total. The dry regions, where local summer precipitation is < 150 mm are shown in yellow. The blue (red) lines indicate the ITCZ position for August (February). Solid lines are used to denote monsoon troughs while dashed lines mark trade wind convergences. The tropical monsoon wind domains are outlined by the black lines, which are delineated by the annual reversal of the 850 hPa zonal winds. EA = East Asia, IN = India, WNP = western North Pacific, AUS = Australia, NAF = North Africa, SAF = South Africa, NAM = North America, SAM = South America (from Wang et al., 2017).

Today, the Indian summer monsoon contributes about 80% of the rainfall over the Indian Peninsular, the southern foot of the Himalaya, and the northern Bay of Bengal (Wang and Ding, 2008). It supports Asian agricultural production and sustains the lives of billions of people. Therefore, anomalous rainfall associated either with droughts or floods has great impacts on the Earth population

as crops are damaged in both cases (Mall et al., 2006). Throughout the year, the Indian monsoon is linked to the Atlantic Meridional Overturning Circulation (AMOC), the zonally integrated component of surface to deep current in the Atlantic Ocean that transports heat from low- to high-latitude regions in the Atlantic, and thus modulates the meridional heat distribution of the Earth with specific impact on the thermal/pressure over the Eurasian continent (Liu et al., 2009). At interannual scale, anomalous states of the Indian monsoon are strongly coupled with, and modulated by, internal feedbacks within the ocean-atmosphere system, such as the El Niño-Southern Oscillation (ENSO) and the Indian Ocean Dipole (IOD) (Kumar et al., 1999; Ashok et al., 2001). These modes are tied to the sea surface temperature anomalies in the tropical Pacific and Indian Oceans. They also control the variability of the Walker circulation i.e., the zonal cells driven by the Indo-Pacific Warm Pool, the warmest oceanic region on the Earth (Bjerknes, 1969; DiNezio, 2010).

The Indian monsoon and Walker circulations impact bio-physical-chemical processes in the upper seawater as well, including primary productivity (PP), which is important in marine ecology, fisheries, and on a wider perspective, the global carbon cycle (Cermeño et al., 2008; Conti and Scardi, 2010). PP is the producing rate of organic carbon by ocean phytoplankton. During photosynthesis, single-celled plants convert light energy into chemical one and transform the water into oxygen and carbon dioxide (inorganic carbon) into organic carbon. Despite light availability, PP is modulated by the concentrations of available macro- and micro-nutrients in the euphotic zone that come either from the atmosphere or from below, and in all cases that are distributed according to the position of the nutri/thermocline (Fig. 3). When the nutricline get shallower (deeper), nutrients contents in the upper euphotic zone with strong light intensity become higher (lower), and thus, PP increases (decreases) (Fig. 3). This relationship is particularly obvious in the tropical Indian Ocean and within the Arabian Sea, one of the most productive marine areas of the world, characterized by an important upwelling system off Somalia and Oman during summer and a significant surface cooling-driven mixing off Pakistan during winter, that bring nutrient to the euphotic zone. It is also well expressed in the northern Bay of Bengal and the Andaman Sea that, contrary to the Arabian Sea, receive a huge amount of freshwater during summer and are therefore characterized by low sea-surface salinity conditions, a "barrier layer effect" (Prasanna Kumar et al., 2002; Madhupratap et al., 2003), and relatively low PP.

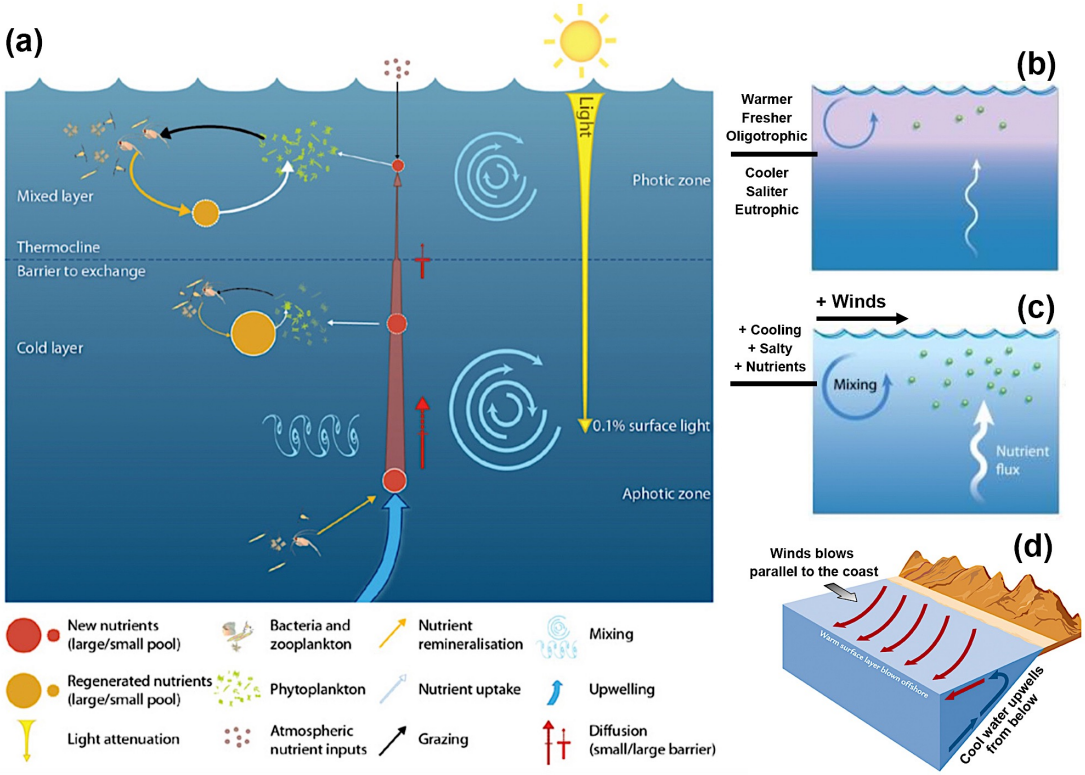

Fig. 3. (a) Key features of the upper layer of the ocean that determine primary production distribution in the tropical oceans. The photic zone, where photosynthesis occurs, typically extends to the depth that receives 0.1% of the surface light intensity in tropical areas. Below this, is the aphotic zone, where there is insufficient light for photosynthesis. The warmer mixed surface layer is separated from the deeper cold layer at the thermocline, where water temperature decreases abruptly. The thermocline is a barrier to mixing and the transfer of nutrients from the cold, deep water to the surface mixed layer. The cold layer is supplied with nutrients brought up from the aphotic zone by mixing, diffusion, and vertical advection (upwelling), depending on the location (from Le Borgne et al., 2011). (b, c) Schematic representations of the processes that can increase the nutrient availability and PP in the tropical oceans. These processes are strengthened surface winds and surface cooling and getting salty (from Doney, 2006). (d) Schematic representations of coastal upwelling driven by alongshore winds and the Ekman transport (from Ruddiman, 2013).

Since the industrial revolution, atmospheric and oceanic reservoirs are severely impacted by anthropogenic activities, and this is particularly the case within the climate system over the tropical Indian Ocean. It appears that because of greenhouse gas emissions due to human activities (mainly carbon dioxide), global temperature has increased by about 1 ℃ relative to the preindustrial period (IPCC, in press). Under such conditions, the dry areas on the earth appear to get drier, while the wet areas seem to get wetter (Seager et al., 2010; Trenberth et al., 2014). As for the Indian monsoon, the atmospheric circulations related to dynamic moisture flux do not strengthen, but the atmospheric specific humidity increase over the ITCZ that is expected to be strengthened in the future (Seager et al., 2010). This changed pattern triggers the increase of global monsoon area and precipitation rate (e.g. Hsu et al., 2011, 2012; D'Agostino et al., 2019), and results in substantial increases in mean peak

discharges of the South Asian rivers that can increase the occurrence of flooding (Mirza et al., 2002). Remarkably, PP in the tropical Indian Ocean is sensitive to the changing climate under global warming. The tropical Indian Ocean gets warmer and fresher, and as a result, the stratification becomes stronger leading to lower PP (Roxy et al., 2016). Actually, the response of the ocean-atmosphere feedback to global warming is still questioned. This is especially the case when dealing with the complex area that is the tropical Indian Ocean as it is under the influence of the Indian monsoon and Walker circulations that may be modulated by the AMOC, the ENSO, and the IOD, and as discrepancies still exist between the observation and modelling data (e.g. Bayr et al., 2014; Chen et al., 2017; Cai et al., 2021).

One of the major factors that precludes our complete understanding of climate variability today and in the future, is the short instrumental climatic records. If one wants to tackle the complexity of Earth climate mechanisms, climate variability in the past (i.e., at geological time scale) is a window into our future since it provides information facilitating the understanding of Earth system response to various external/internal forcing which can, under some circumstances, be analogies to the future. In other words, "**the Past holds the key to the Future"** and studying the past, makes it possible to study the mechanisms of climate changes in response to changing boundary conditions.

Monsoon and Walker circulation dynamics in the past have been the focus of recent decades' studies involving multi-timescale and multi-forcing factors (Fig. 4).

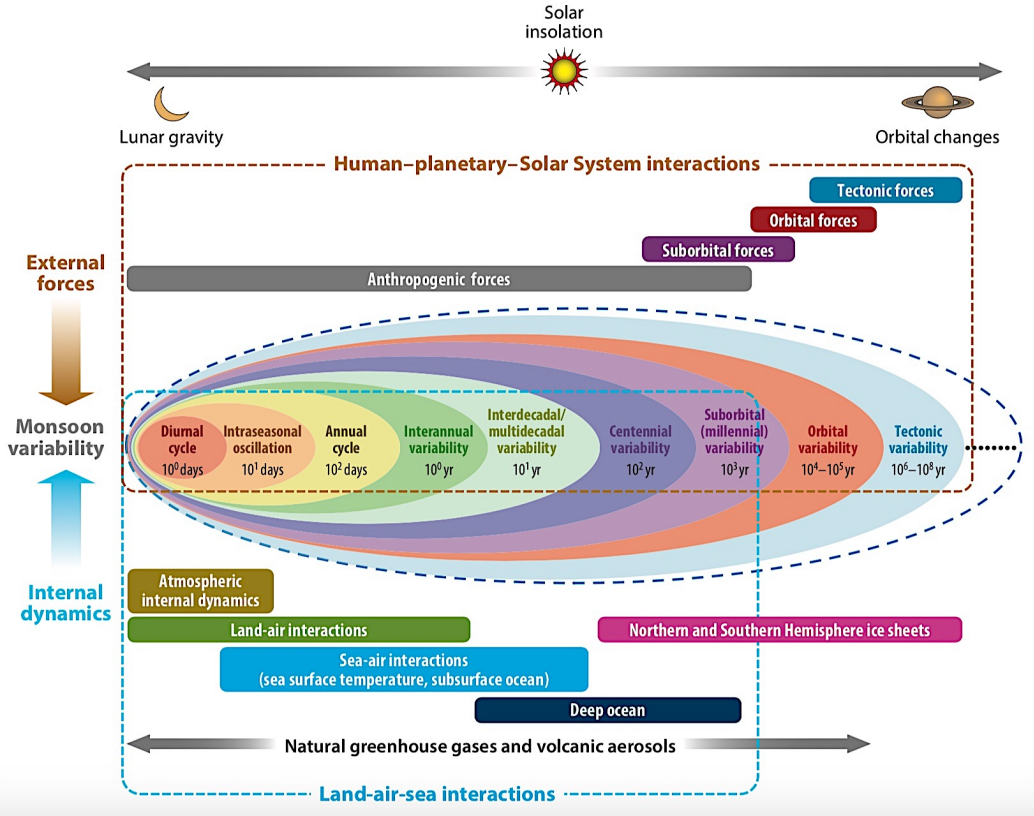

Fig. 4. Paleoclimate variability on multi-timescale and the forcing factors (From An et al., 2015).

Variations on the tectonic scale are not concerned in this study as it focuses on the period since the Last Glacial Maximum (LGM, 23 − 19 ka). Within this time interval, climate variability is comparable to past and present human civilizations, while several changing boundary conditions may be linked to those in the foreseeable future. Particularly, the LGM offers an excellent case study to investigate the ocean-atmosphere system response to conditions including relatively low atmospheric pCO_2 (about -100 ppm), low temperature (about -6 ℃ global averaged), large high-latitude ice sheets leading to low global sea-level (about -120 m), compared to preindustrial times (Peltier, 2004; Joos and Spahni, 2008; Kageyama et al., 2018; Tierney et al., 2020). During the deglaciation (19–11.5 ka), the glacial features gradually fade, while millennial scale oscillations are found in the AMOC, particularly during the Heinrich Stadial 1 (17.5–14.8 ka) and Younger Dryas (12.9–11.8 ka) cold periods, the Bølling–Allerød warm period (14.8–12.9 ka), characterized by significant changes in the input of melted freshwaters from the high-latitude North Atlantic regions (McManus et al., 2004; Clement and Peterson, 2008). The Holocene (11.5 ka–present), is associated with significant changes in the precession that modulates the seasonal and meridional distributions of the incoming insolation (Laskar et al., 2004).

There is no doubt that all the aforementioned forcing factors significantly impacted the climate over the tropical Indian Ocean (e.g., Schultz et al., 1998; Kudrass et al., 2001; Rashid et al., 2007; Dutt et al., 2015; Marzin and Braconnot, 2009; DiNezio and Tierney, 2013). However, uncertainties and questions remain unsolved, and this is particularly the case when dealing with the Indian monsoon and Walker circulation dynamics and their relationships with PP. First, there is still a lack of high-resolution quantitative PP reconstructions since the LGM. As mentioned above, PP is at the very interface between the atmosphere and the ocean and its variations in the past are therefore sensitive to temperature, freshwater input (rainfall), and wind dynamics that all can modulate the upper seawater stratification and the nutrient availability in the euphotic zone (Fig. 3). Consequently, paleo-PP has wide applicability in indicating paleoclimate, especially for the tropical Indian Ocean where different processes induce the hydrological discrepancy between the northeastern and northwestern parts. Second, it is necessary to use paleoclimate model-data comparisons considering changing boundary conditions since the LGM. Although the Indian monsoon and the Walker circulations have been the focus of numerous studies using general coupled models, very few deal with PP patterns and their relationships with atmospheric changes in the past (Bassinot et al., 2011; Le Mézo et al., 2017). Empirical data usually reflect local to regional signals, while model outputs can provide atmospheric and oceanic processes over a wide and usually global area. Therefore, it is important to combine these two crucial technical routes to explore the ocean-atmosphere system in the past and to obtain more

accurate paleoclimate interpretations.

Here, I've studied the variations of coccolith assemblages and report high-resolution paleo-PP records since the LGM from four well-dated sediment cores retrieved in the tropical Indian Ocean, based on the empirical equations that exist between the relative abundance of the lower euphotic zone dweller, *Florisphaera profunda* and annual PP (Molfino and McIntyre, 1990a; Beaufort et al., 1997, Hernández-Almeida et al., 2019). Cores MD77-176 and MD00-2354 collected in the northeastern Bay of Bengal and the northwestern Arabian Sea respectively, are closed to Eurasia, and are probably under the influence of land-sea interactions and thus, the Indian monsoon. Cores MD77-191 and BAR94-24, retrieved in the coastal upwelling systems off the southern tip of Indian and the northwestern tip of Sumatra are probably under the influence of equatorial winds and thus, the Walker circulation.

I've also used the outputs of three general coupled or earth system models. The IPSL-CM5A-LR model in the framework of the Paleoclimate Modelling Intercomparison Project (PMIP) phase 3 with a biogeochemical component, and the AWI-ESM-1-1-LR model in the framework of PMIP phase 4, both provide simulated results under LGM (21 ka) and Mid-Holocene (6 ka) conditions. The TraCE-21 transient simulation run with CCSM3 covers the last 22 kyr. The comparison between proxy records and modelling results is an important part of this study. It is particularly helpful to see if the conceptual atmospheric and oceanic interpretations of the paleo-PP records match the simulations. The conceptual interpretations come from the relationship between PP, seawater structures, and atmospheric circulations revealed by instrumental observations. I've identified the biophysical processes controlling PP changes in different regions by using observation data or reviewing previous studies.

This thesis is divided into six chapters. Chapters 1 and 2 are devoted to the context and the material and methods I've used in this work. Chapters 3 to 6 are presented as "published", or "about to be published" papers. I am aware that this hybrid structure implies repetitions. However, it provides crucial and complementary information that makes what I feel is a much-improved doctoral thesis. In detail, in **Chapter 1,** I provide a synthesis of the atmospheric, oceanic, and biological contexts of the tropical Indian Ocean, and their variations in the past as revealed by previous studies. It helps me detailing the main questions that exist so far. **Chapter 2** contains the descriptions of the materials and methods I've used in this study. In **Chapter 3**, I present the PP reconstruction obtained at site MD77-176 and combine the result with the outputs of IPSL-CM5A and TraCE-21. I highlight that paleo-PP in the Bay of Bengal reflects the variations of seawater stratification controlled by sea surface salinity and summer monsoon rainfall. In **Chapter 4** I've used the same strategy as in chapter 3, but this chapter focuses on the result of core MD00-2354 located in the northwestern Arabian Sea. Paleo-PP in the Arabian Sea appears mainly influenced by processes linked to the winter monsoon and aeolian input.

In **Chapter 5**, I try and provide a broader overview of the evolution of seawater stratification in the northern Indian Ocean and its relationship with the Indian winter and summer monsoons by comparing the coccolith records (Fp%) shown in chapters 3 and 4 with TraCE-21 outputs. I highlight that the anti-phase between summer and winter monsoons in response to the AMOC forcing. In **Chapter 6,** I show PP reconstructions at sites MD77-191 and BAR94-24, as well as outputs of AWI-ESM-1-1-LR. The records reveal evolutions of equatorial winds and Indian Ocean Walker circulation since the LGM. Both, the empirical and modelling data highlight weakened Walker circulation during the LGM and the Early-Mid Holocene.

Chapter 1

Atmospheric, oceanic, and biological contexts of the tropical Indian Ocean

In this chapter, I present modern climatological and oceanographical settings of the tropical Indian Ocean and its surrounding lands, with specific highlights on the bio-chemo- and physical processes in the northern and equatorial Indian Ocean, including interannual anomalies of the climate and oceanic systems. I also make a brief review of previous studies focusing on climate and oceanic changes in South Asia and the northern Indian Ocean since the Last Glacial Maximum, with a special focus on the primary productivity signal.

1.1. Geographical setting

The tropical Indian Ocean, between 30°N and 30°S, is surrounded by lands/islands that are, in a clockwise direction: East Africa, Arabian Peninsula, Iranian Plateau, South Asia, and Southeast Asia (belonging to the Eurasian Continent), Sumatra, Java, and Australia (Fig. 1.1). The northwestern and northeastern parts of the Indian Ocean are represented by the Arabian Sea (AS), and the Bay of Bengal (BoB) /Andaman Sea (ADS), respectively (Fig. 1.1). The AS and the BoB are separated by the Indian Peninsula, while the BoB and the ADS are separated by the Andaman Islands. The northeastern AS is connected to the Gulf of Oman and the Persian Gulf through the Strait of Hormuz; its western part is connected to the Gulf of Aden and the Red Sea through the Mandab Strait. Deserts prevail over the Arabian Peninsula and Iranian Plateau. These areas are therefore important dust sources to the Arabian Sea (Ackerman and Cox, 1989; Husar et al., 1997).

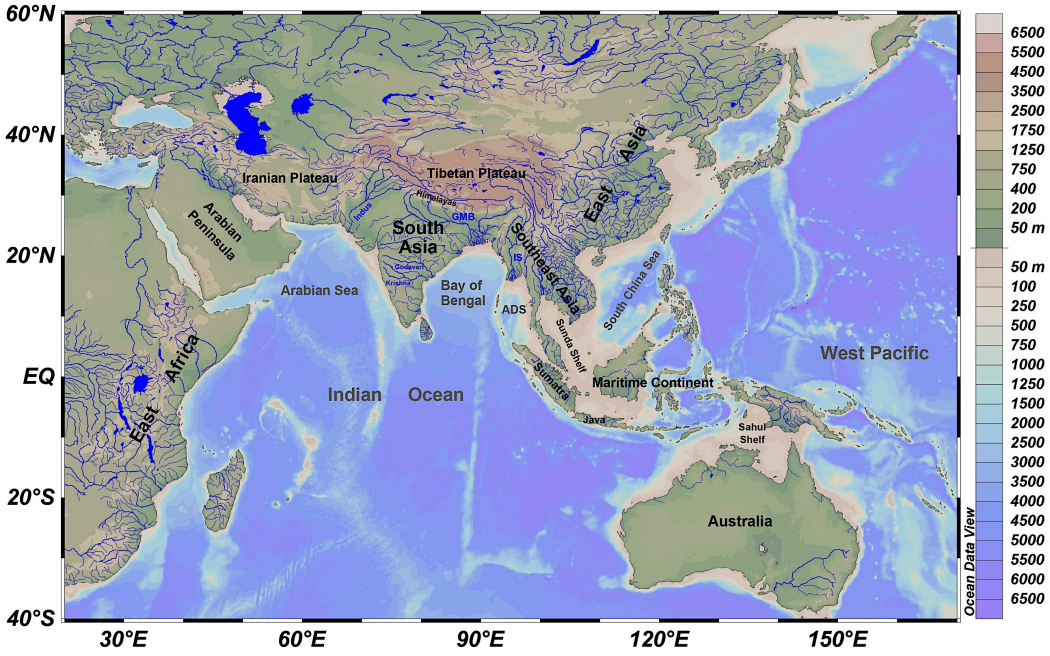

Fig. 1.1. Geographic setting and bathymetry/Topography of the Indian Ocean and surrounding lands. ADS = Andaman Sea; GMB = Ganges-Brahmaputra-Meghna river system; IS = Irrawaddy-Salween river system.

Several large rivers originating from the Tibetan Plateau and the Himalayas i.e., the region with the highest topographic prominences in the world, drain the South Asian subcontinent and feed the northern Indian Ocean. These rivers made part of large river systems such as the Ganges-Brahmaputra-Meghna, the Irrawaddy-Salween, and the Indus ones, that provide a large amount of freshwater to the BoB (~1300 km^3 y^{-1}), the ADS (~1000 km^3 y^{-1}), and the AS (~243 km^3 y^{-1}), respectively. These river systems carry huge amounts of sediments as well. They create important fans, the Bengal fan being the largest submarine fan in the world (Curray et al., 2002). Moreover, several smaller rivers, such as

the Godavari and Krishna rivers originating from the mountains on the west coast of India, flow into the western Bay of Bengal as well.

1.2. Atmospheric context

1.2.1. Indian monsoon

The tropical Indian Ocean is under the influence of the Indian monsoon, also named the South Asian monsoon, which can be defined according to the land-sea thermal contrast that exists in the area (Webster and Fasullo, 2015; Fig. 1.2). It can be interpreted as dynamic sea-breezes resulting from the differential heating.

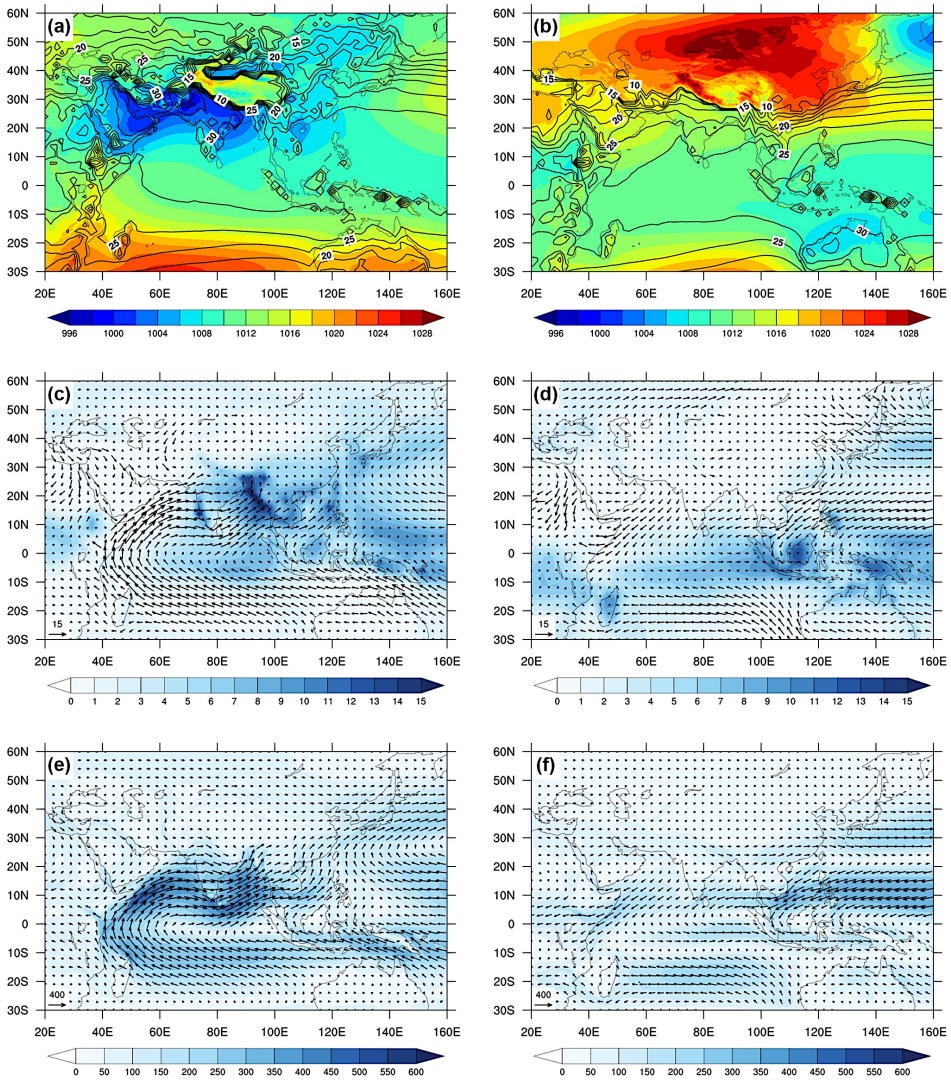

Fig. 1.2. Climatology of (a, c, d) summer (May−September) and (b, d, f) winter (November−March) mean. Data are from the ERA5 reanalysis (https://www.ecmwf.int/en/forecasts/datasets/reanalysis-datasets/era5) of the period 1979-2919. (a, b) Sea level pressure (shaded, hPa) and air surface temperature (contours, °C). (c) and (d) Precipitation rate (shaded, mm day^{-1}) and 925 hPa wind speed (vectors, m s^{-1}). (e) and (f) Vertically integrated moisture flux (kg m^{-1} s^{-1}).

During summer, Eurasia becomes warmer than the Indian Ocean, and a low-pressure cell is generated over the Arabian Peninsula and South Asia, while the pressures over the Indian Ocean and Australia are higher (Fig. 1.2a). This feature is associated with low tropospheric winds that blow from the southern Indian Ocean and Australia to South Asia. These winds split into two branches in the northern Indian Ocean, one over the AS and one over the BoB. They carry a large amount of moisture and result in heavy rainfall over South Asia (Figs. 1.2c, e). The summer monsoon rainfall peaks in August contributing to about 70−80 % of the annual rainfall in most of India (Dixit and Tandon, 2016). Remarkably, the southeasterly winds that occur off Java are tied to the Australian (austral) winter monsoon.

During winter, Eurasia is cooler than the Indian Ocean. A high-pressure cell is found over Siberia and Mongolia, while the pressure over the Indian Ocean is lower (Fig. 1.2b). Low tropospheric winds blow from the lands to the Indian Ocean, carrying continental cold and dry air that results in relatively weak rainfall over South Asia (Figs. 1.2d, f). Once they crossed over the Indian Ocean, they transport moisture to southeastern India and Africa, resulting in relatively strong local rainfall (Figs. 1.2d, f; Srinivasan and Ramamurthy, 1973; Chevalier et al., 2017).

1.2.2. Walker circulation

The tropical Indian Ocean is also under the influence of the Walker circulation (Bjerknes et al., 1969; Lau and Yang et al., 2015). Indeed, it belongs to the western part of the Indo-Pacific Warm Pool (IPWP) that is characterized by the warmest surface seawater in the world with mean seawater temperatures as high as 28°C (Fig. 1.3).

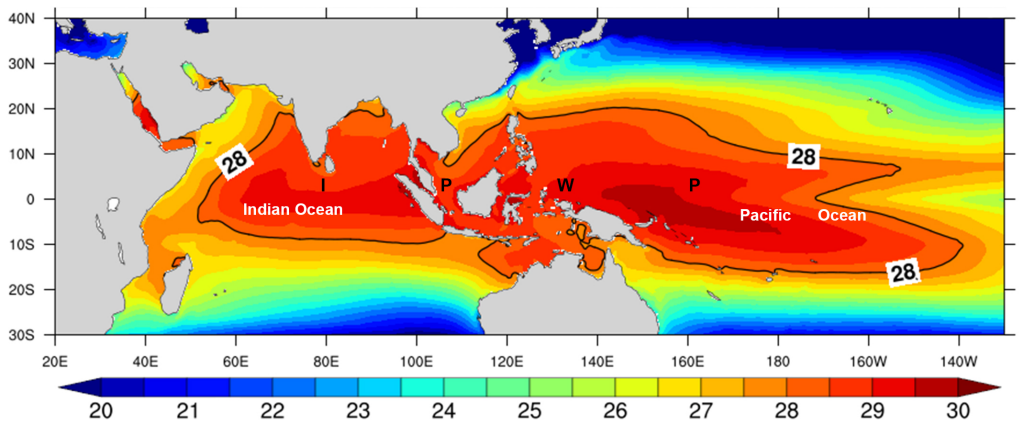

Fig. 1.3. Annual mean climatology of SST (°C). The region of the Indo-Pacific Warm Pool (IPWP) is defined by the 28 °C isotherm line. Data is from NOAA OI SST V2 (https://psl.noaa.gov/data/gridded/data.noaa.oisst.v2.highres.html).

The IPWP drives strong convections and upward air movements over the Maritime Continent (Fasullo et al., 1999; Neale et al., 2003). One branch of this ascending air moves eastward aloft over the Pacific Ocean, descends over the eastern Pacific, and moves back westward at low levels. Another branch moves westward aloft over the Indian Ocean, descends in the western Indian Ocean, and moves back eastward through low-level winds (Fig. 1.4). In short, for the tropical Indian Ocean, a strong convergence zone occurs over the eastern Indian Ocean and the Maritime Continent, while a divergence zone is found over the western Indian Ocean (Figs. 1.4b, c).

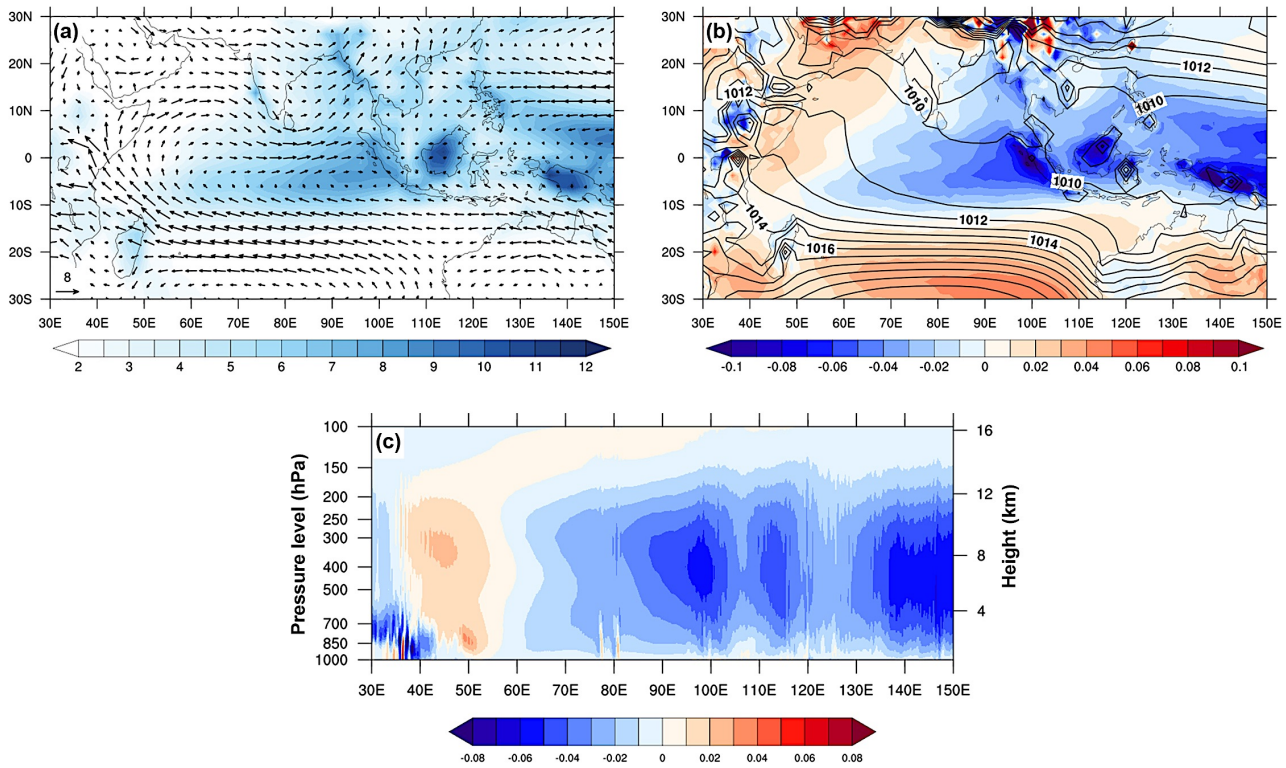

Fig. 1.4. The pattern of Indian Ocean Walker circulation is shown by annual mean climatology. (a) Precipitation rate (shaded, mm day^{-1}) and 850 hP wind speed (vectors, m s^{-1}). (b) Vertical velocity at 500 hPa level (shaded, Pa s^{-1}) and sea level pressure (contours, hPa). (c) Vertical velocity (Pa s^{-1}) over the equatorial Indian Ocean (10°S−10°N averaged).

This pattern creates the zonal atmospheric cell over the tropical Indian Ocean i.e., the Indian Ocean Walker circulation *s.s.*, different from the meridional Hadley cells that are controlled by the meridional differential heating. In all cases, the Walker circulation controls the annual mean states of rainfall over the equatorial Indian Ocean, usually characterized by wet conditions to the east and dry ones to the west (Neale et al., 2003; Dayem et al., 2007; Limbu et al., 2019; King et al., 2021; Fig. 1.4a). However, to the difference of the Pacific branch, the Indian Ocean Walker circulation has strong seasonal and interannual variations coupled to the Indian monsoon. Indeed, the equatorial westerly winds usually

peak from spring to autumn and are weaker in winter.

1.3. Oceanic context

1.3.1 Surface circulation

The monsoonal winds impact the surface of the tropical Indian Ocean and therefore, seasonal reversal currents are observed (Schott and McCreary, 2001; Shankar et al., 2002). During summer, southwesterly winds drive a general clockwise circulation that is well represented in the AS by seawater flowing northeastward in its western part (Fig. 1.5), creating the East African Coast Current (EACC), and by seawater flowing southward along the western coast of India, that is the West Indian Coast Current (WICC). This latter one makes part of the Southwest Monsoon Current (SMC) that connects the southeastern AS to the southwestern BoB. In the BoB, a strong northward flow called the East Indian Coast Current (EICC) is found along the eastern coast of India. During winter, northeasterly winds are accompanied by a general anti-clockwise circulation. The directions of the EICC and WICC are reversed. They both are connected by the Northeast Monsoon Current (NMC) flowing from the southwestern BoB into the southeastern AS (Fig. 1.5).

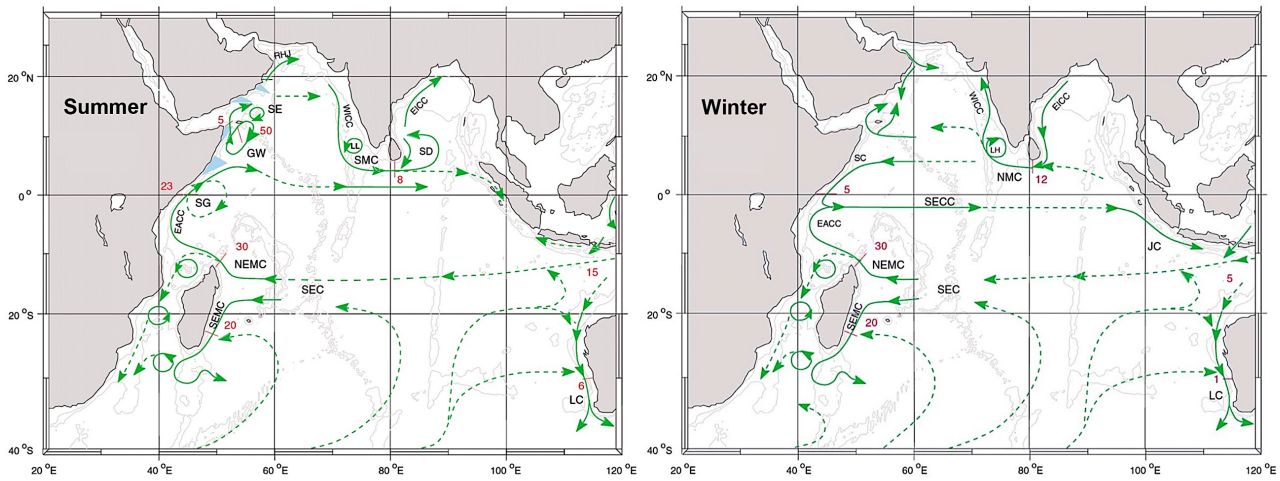

Fig. 1.5. A schematic representation of identified current branches during the summer and winter (Schott and McCreary, 2001), including some choke point transport numbers (Sv). SEC = South Equatorial Current; SECC = South Equatorial Countercurrent; NEMC, SEMC = Northeast and Southeast Madagascar Current; EACC = East African Coast Current; SC = Somali Current, SG = Southern Gyre; GW = Great Whirl and associated upwelling wedges; SE = Socotra Eddy; RHJ = Ras al Hadd Jet and upwelling wedges off Oman; WICC = West Indian Coast Current; LH, LL = Laccadive High and Low; EICC = East Indian Coast Current, SMC, NMC = Southwest and Northeast Monsoon Current; JC = South Java Current; LC = Leeuwin Current.

Over the entire year, the surface currents around 20°S are represented by a westward zonal flow, the South Equatorial Current (SEC), that is forced by the annual southeast trade winds. This flow turns into a northward direction on the western coast of the Indian Ocean and forms an eastward flow near

the equator, called the Wyrtki Jet or the South Equatorial Countercurrent (SECC) (Fig. 1.5). The Wyrtki Jet is tied to the Indian Ocean Walker circulation and is thus relatively strong from spring to autumn and relatively weak during winter (Wyriki et al., 1973).

1.3.2 SST, SSS, and density distributions

The sea surface temperature (SST) in the northern Indian Ocean has significant seasonal variations (Figs. 1.6a–c; Shenoi et al., 2009). It ranges between 24 °C and 29 °C during summer and between 24 °C and 27 °C during winter, with annual means of 26–28 °C. The SST difference between the BoB and the AS is the largest during summer, thanks to the IPWP and the strong surface cooling that occurs in the western part of the AS due to the occurrence of coastal upwelling off Somalia and Oman (see section 1.3.3.2 for details). During winter, surface cooling occurs in both, but the one observed in the AS is stronger and has a larger southward extension than the one recorded in the BoB.

The spatial discrepancy is also significant in the sea surface salinity (SSS) conditions (Figs. 1.6d–f; Rao and Sivakumar, 2003; Subrahmanyam et al., 2011). SSS in the BoB is lower than 34–35 psu (Figs. 1.6d, e) while SSS in the AS is higher than 35–36 psu during both monsoonal seasons (Figs. 1.6d, e). Throughout the year, it results in an overall ~ 2 psu east-west SSS gradient in the northern Indian Ocean (Fig. 1.6f). Such gradient is smaller (0.5–1 psu) over the equatorial Indian Ocean. Remarkably, the lowest SSS (< 30 psu) is found nearby the river mouths in the BoB and the ADS during summer, reflecting the peaks of river discharges (Fig. 1.6d).

The features of SST and SSS shape those of sea surface density (sigma-t, σ_{0m}, kg m^{-3}) and significant differences are indeed highlighted between the BoB and the AS, and between the eastern and western equatorial Indian Ocean (Figs. 1.6g–i). During summer, σ_{0m} in the BoB ranges between 17 and 21 kg m^{-3}, while in the AS, it is of ~ 23 kg m^{-3} (Fig. 1.6g). Over the equatorial Indian Ocean, the eastern part is ~ 1 kg m^{-3} lower than the western part (Fig. 1.6g). During winter, σ_{0m} in BoB is between 20 and 21 kg m^{-3}, while in the AS, it varies between 23 and 24 kg m^{-3} (Fig. 1.6h). The discrepancy between the equatorial eastern and western parts is smaller than during summer (Fig. 1.6h). Throughout the year, such patterns result in an east-west σ_{0m} gradient of ~ 3 kg m^{-3} in the northern Indian Ocean (Fig. 1.6i) and 1–2 kg m^{-3} in the equatorial Indian Ocean (Fig. 1.6i). The density difference between 150 m and the surface ($\Delta\sigma_{150-0m}$, kg m^{-3}) can help to quantify the upper seawater stratification (Figs. 1.6j–l). Its spatial pattern in the tropical Indian Ocean usually reflects the σ_{0m} distribution during the two monsoonal seasons (Figs. 1.6i, k). Throughout the year, strong stratification ($\Delta\sigma_{150-0m}$ > 5 kg m^{-3}) is found in the BoB and the equatorial eastern Indian Ocean, while the density difference in the AS is relatively low (~2 kg m^{-3}) (Fig. 1.6l).

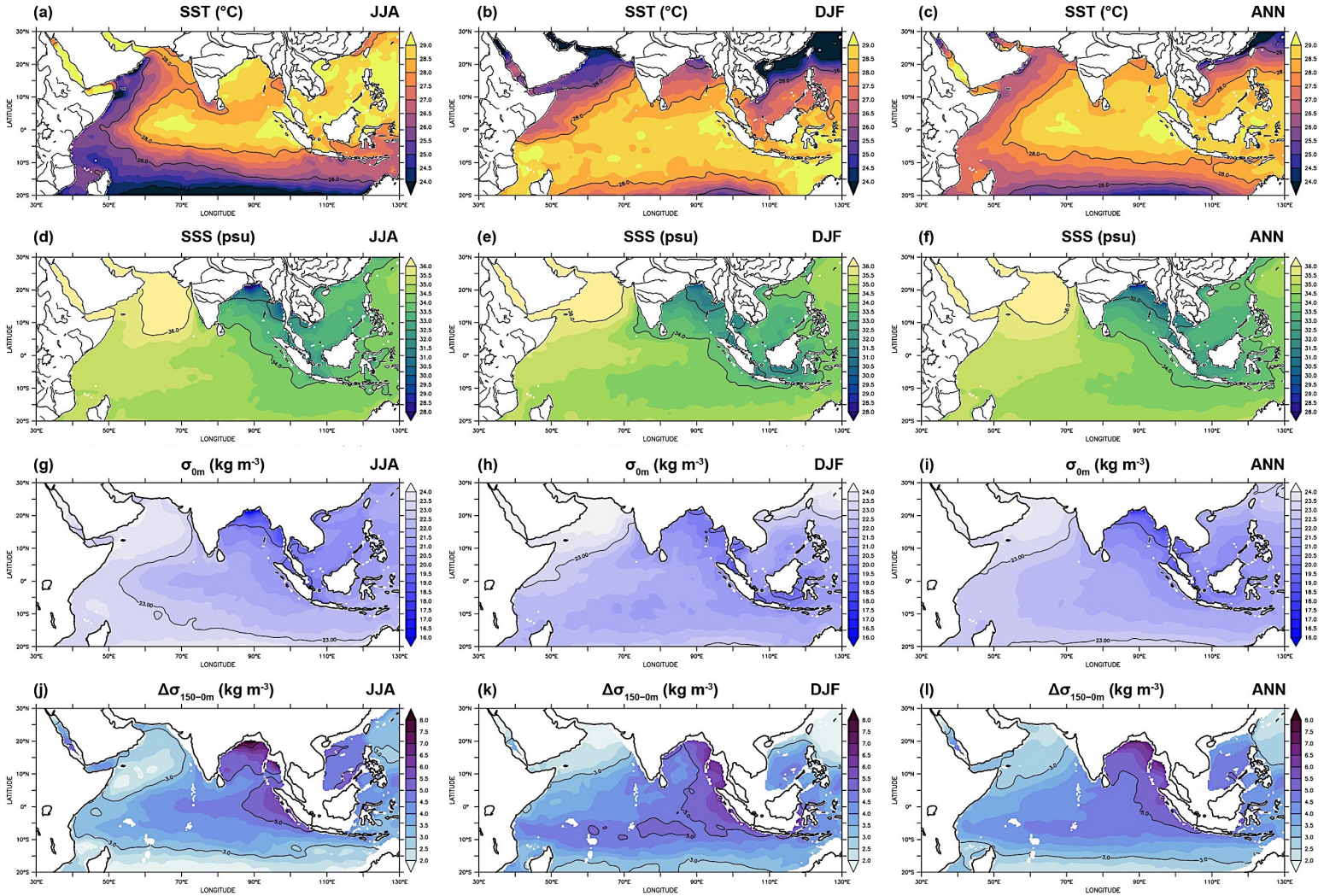

Fig. 1.6. Climatology of (a−c) sea surface temperature (SST, °C), (d−f) sea surface salinity (SSS, psu), (g−i) sea surface density (sigma-t, σ_{0m}, kg m^{-3}), and (j−l) upper seawater stratification quantified by the density difference ($\Delta\sigma_{150-0m}$, kg m^{-3}) between 150 m and the surface. The left column is the summer mean (June−July−August, JJA). The middle column is the winter mean (December−January−February, DJF). The right column is the annual mean. Data are the World Ocean Atlas 2018.

In summary, the eastern part of the Indian Ocean, including the BoB has higher SST, lower SSS, and stronger upper seawater stratification than its western part that includes the AS. Such features are controlled by the IPWP, the Indian monsoon, and the Walker circulations.

1.3.3. Primary productivity patterns

Primary productivity (PP) of the tropical Indian Ocean fluctuates between ~ 50 and 450 gC m^{-2} yr^{-1} in open-sea settings (Fig. 1.7) and reaches up to 1000 gC m^{-2} yr^{-1} in coastal areas (Behrenfeld and Falkowski, 1997), as documented in the northernmost BoB and ADS off the Ganges-Brahmaputra-Meghna and the Irrawaddy-Salween river systems (Fig. 1.7).

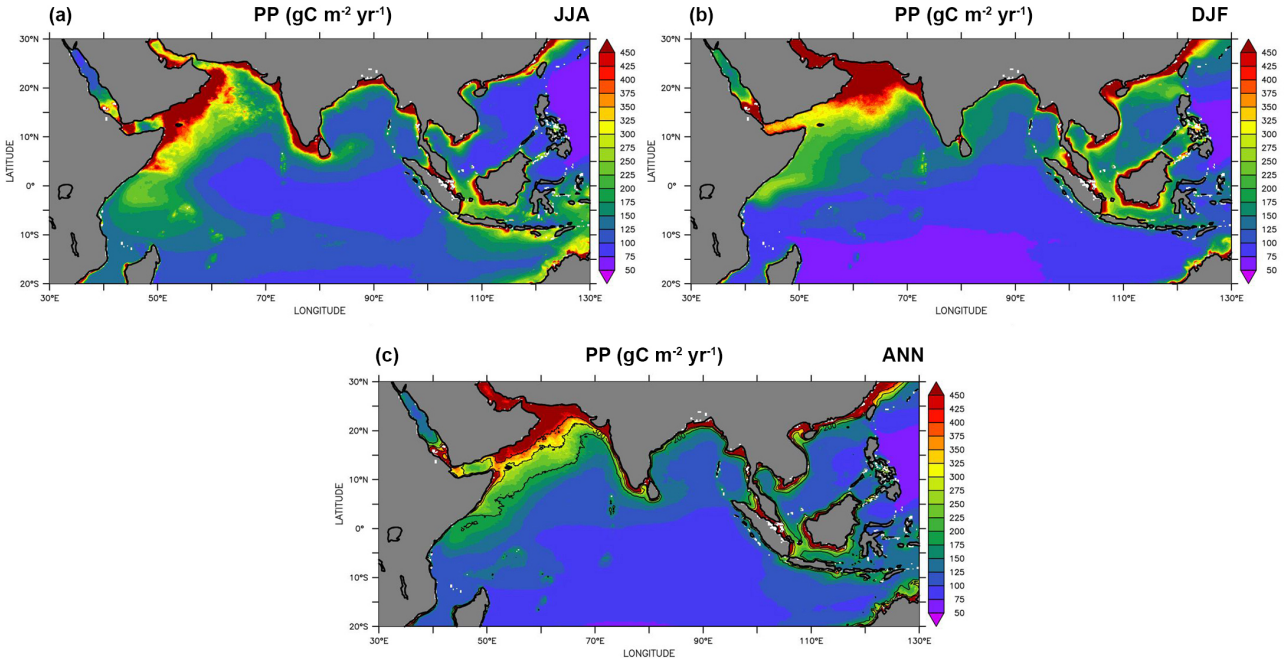

Fig. 1.7. (a) Summer, (b) winter, and (c) annual mean integrated primary productivity (gC m^{-2} yr^{-1}). Data is from the Ocean Production website (http://sites.science.oregonstate.edu/ocean.productivity).

The most striking pattern documented at this scale is the overall wide cells of very high PP within the AS during both winter and summer seasons compared to the BoB/ADS and the equatorial eastern tropical ocean. PP is particularly high in the western AS in the coastal upwelling system off Oman and Somalia (see section 1.3.3.2 for details). High PP is also observed off the Southern tip of India and to a lesser degree off Java and Sumatra, where seasonal upwelling systems are created as well.

1.3.3.1 In the Bay of Bengal and the Andaman Sea

The low PP in the BoB and the ADS mainly results from the "barrier layer effect" that is caused by the freshwater input from river systems leading to the low SSS (Prasanna Kumar et al., 2002;

Vinayachandran et al., 2002a; Fig. 1.6). This is reflected in the vertical profiles of seawater temperature, salinity, and density in the BoB (Fig. 1.8; Vinayachandran et al., 2002a). Freshwater plumes result from both rivers and rainfalls, and lead to decreased SSS, while SST remains stable. The lower SSS makes the density gradient to be larger in the upper water column and limits the mixing of seawater. Compared to the AS, the upper seawater in the BoB is very stable (Fig. 1.9), and the monsoonal winds are generally unable to overcome the barrier layer. As a result, the upward movements of the eutrophic subsurface seawater are generally inhibited, and the nutrients contents in the euphotic zone are thus usually low, resulting in low PP (Prasanna Kumar et al., 2002; Madhupratap et al., 2003).

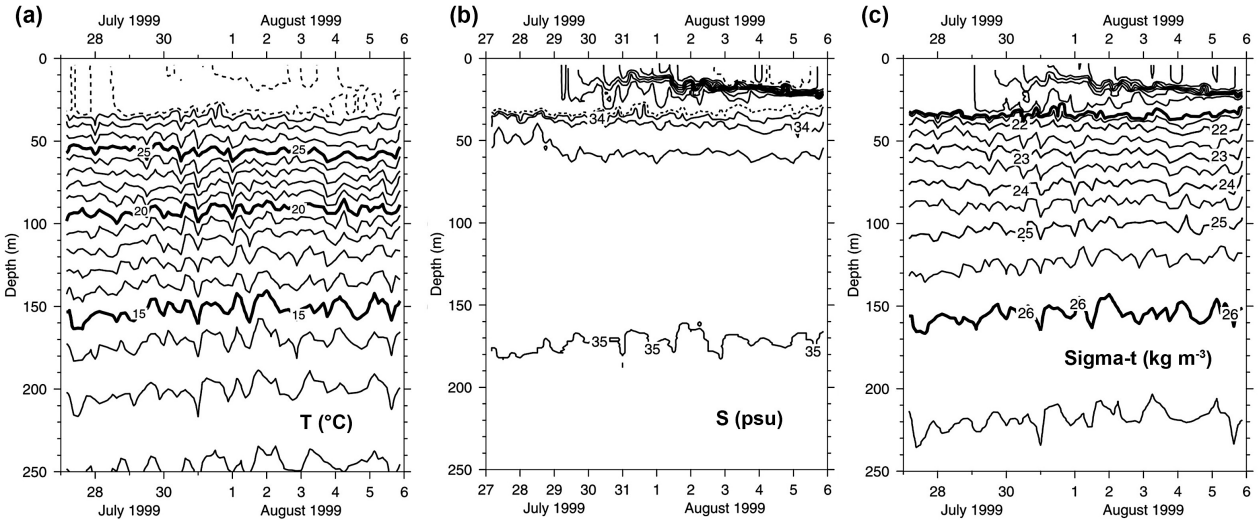

Fig. 1.8. An observation of the barrier layer formation. Time depth sections of (a) temperature, (b) salinity, and (c) density (sigma-t) at a CTD site (17.5°N, 89°E) (Vinayachandran et al., 2002a). The barrier layer induced by surface freshening starts at the end of July 1999.

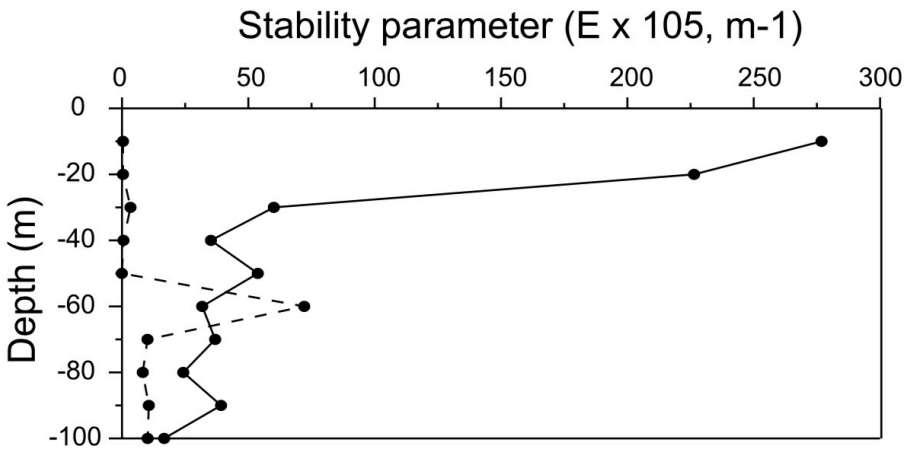

Fig. 1.9. Profiles of upper ocean static stability parameter in the northern Arabian Sea (19°N, 64°E) and Bay of Bengal (19°N, 88°E) (Prasanna Kumar et al., 2002).

Despite the strong "barrier layer effect", seasonal and regional blooms occur when the barrier layer can be broken by some dynamic processes. These regions are the northwestern and southwestern BoB in summer, and the western BoB and the southern ADS off Sumatra in winter. The alongshore westerly winds during summer drive a very strong upwelling cell off the southern tip of Indian resulting in high PP (Figs. 1.10a, b; Rao et al., 2006; Thushara and Vinayachandran, 2020). This high PP cell can invade into the southern BoB under the influences of eastward surface currents and the positive wind stress curls (Vinayachandran et al., 2004). Summer southwesterly winds can also drive coastal upwelling off northeastern India but this bloom is relatively weak and disappears further east, once it reaches the south-westward extension of the low SSS river plume (Thushara and Vinayachandran, 2016). Winter winds have positive wind stress curls over the southwestern BoB and northwestern Sumatra that together with the coastal Ekman transport drive high PP (Figs. 1.10a, b; Vinayachandran et al., 2005; Tan et al., 2006).

1.3.3.2 In the Arabian Sea

Contrary to the BoB and the ADS, the upper seawater column of the AS is relatively instable, showing lower static stability (a variable quantifying the seawater vertical density gradient of seawater), by an order of magnitude (Prasanna Kumar et al., 2002; Fig. 1.9). This is the main factor resulting in the major PP differences that exist between the two parts of the northern Indian Ocean.

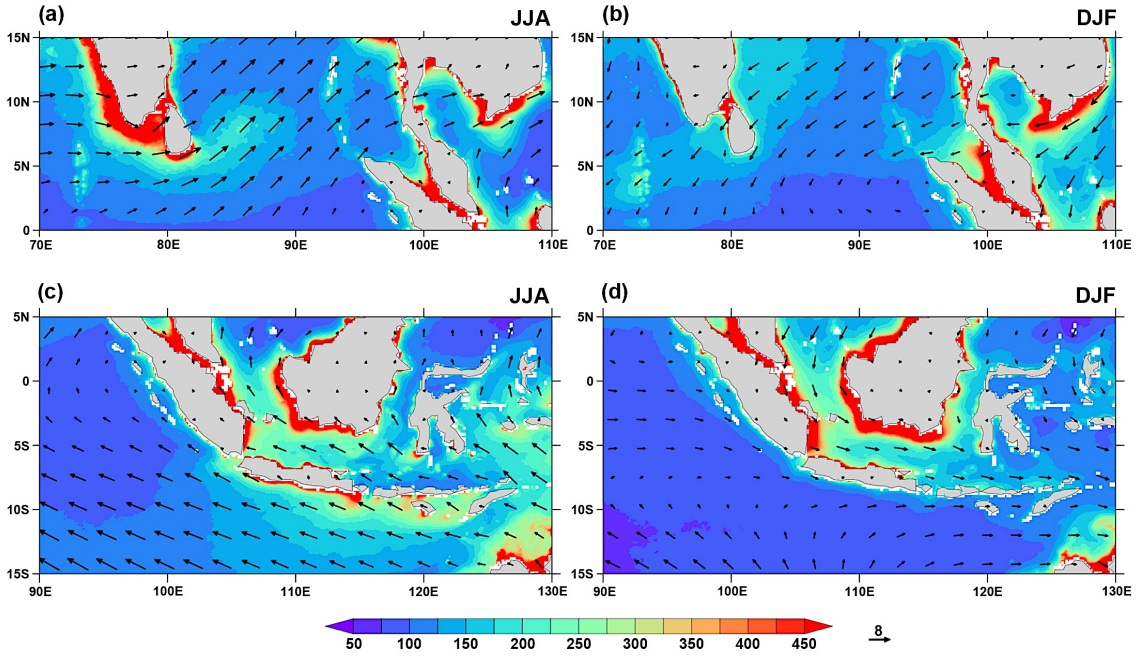

Fig. 1.10. Summer (JJA) and winter (DJF) primary productivity (gC m^{-2} yr^{-1}) and surface winds (vectors; m s^{-1}). Data is from the Ocean Production website (http://sites.science.oregonstate.edu/ocean.productivity), and the ERA5 reanalysis (https://www.ecmwf.int/en/forecasts/datasets/reanalysis-datasets/era5)

Several physical processes make the AS be one of the most productive oceanic regions in the world (Madhupratap et al., 1996; McCreary et al., 1996). During summer, southwesterly winds contain a relatively straight jet that is called the Findlater Jet. To the left of this jet, wind stress curls are positive, while to the right, they are negative (Fig. 1.11a). The alongshore winds together with the positive curls drive coastal upwelling and together with the Ekman pumping they form a large-sale seawater area characterized by low SST, shallow mixed-layer, and high PP (McCreary et al., 1996; Lee et al., 2000; McCreary et al., 2009). The upward movement of the seawater has been observed in the upper 200 m (Lee et al., 2000). The nutrients from the eutrophic subsurface seawater are dynamically driven to move upward feeding the upper euphotic zone and sustain the high PP. The offshore currents and eastward advection promote the extension of this high PP seawater to the central AS (Prasanna Kumar et al., 2001a).

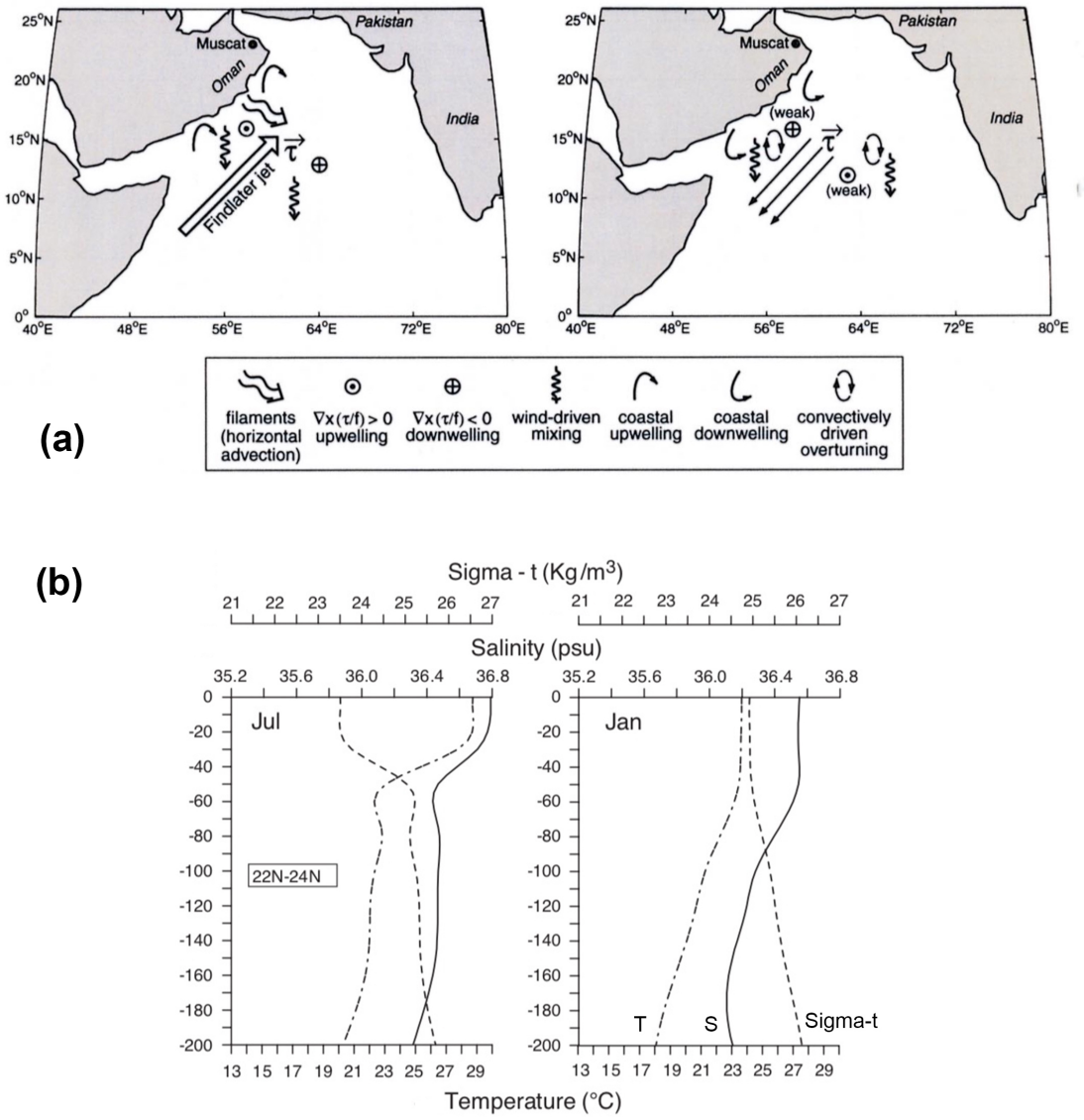

Fig. 1.11. (a) Schematic representations of the various physical processes that may act during the summer (left) and winter (right) monsoons (Lee et al., 2000). The large hollow arrow marks the Findlater Jet in the summer monsoon schematic (right). The three smaller vectors represent weaker, less concentrated winds during the winter monsoon (left). Coastal upwelling occurs during the summer monsoon in the western Arabian Sea, and this seawater is advected eastward. Convection mixing occurs during the winter monsoon in the northern and central Arabian Sea. (b) Vertical profiles of monthly mean climatology of temperature, salinity, and density (sigma-t) in the northern Arabian Sea (22−24°N, 62−66°N) (Prasanna Kumar et al., 2005).

During winter, the coastal upwelling in the western AS disappears, as the northeasterly winds are not accompanied by significant positive wind stress curls (Fig. 1.11a). Instead, winter winds that carry cold and dry air drive strong surface evaporation and cooling in the northern AS (Prasanna Kumar et al., 2001a, 2005). They result in a deeper mixed-layer and smaller density gradient in the upper seawater (Fig. 1.11b). Sometimes, the subsurface density is even lower than the surface and convective mixing happens. This process can also bring nutrients from the subsurface to the surface and result in high PP in the northern Arabian Sea.

1.3.3.4 Off Sumatra and Java coasts

PP off Java is high in boreal summer. It reflects the coastal upwelling system driven by southeasterly alongshore winds (and associated with the Australian winter monsoon). The western Sumatra coast is closed to the equator, and thus the Coriolis effect is weak resulting in a weaker upwelling. Moreover, the Wyrtki Jet linked to the Indian Ocean Walker circulation generates downwelling Kelvin waves propagating to the eastern equatorial Indian Ocean which can deepen the thermocline and nutricline (e.g. Vinayachandran et al., 2002b). As a result, PP off the Sumatra is lower than in the equatorial western Indian Ocean and off Java (Figs. 1.7, 1.10c, d).

1.4. Atmospheric and oceanic modulations

The tropical Indian Ocean is under the influence of a complex ocean-atmosphere system that is involved in many teleconnections at both regional and global scales.

On a regional point of view, the Indian monsoon is directly connected to the East Asian and Australian monsoons (Wang et al., 2003). The summer southwesterly winds over the northern Indian Ocean extent to the South China Sea and transport moisture to Southeast and East Asia. This moisture flux contributes to the East Asian monsoon even if this system is also strongly influenced by the heat contrast between China mainland and the western Pacific Ocean. The winds that flow over the Indian Ocean across the equator, connect the Indian and Australian monsoons. It results in their reversed seasonality of rainfall patterns. During boreal summer, the winds blowing from northern Australia and the tropical southeastern Indian Ocean join the southeasterly trade winds that are associated to the Indian summer monsoon. During boreal winter, the winds that blow from Eurasia, bring moisture to northern Australia and are linked to the austral monsoon rainfall. Anomalous states of the heating over the East Asia/Pacific and Australia/southeastern Indian Ocean can thus modulate the Indian monsoon and the tropical Indian Ocean hydrology. On interdecadal and interannual scales, the Indian monsoon is coupled with tropical ocean-atmosphere modes, such as the El Niño-Southern Oscillation (ENSO) or the Indian Ocean Dipole (IOD) (Fig. 1.12). The ENSO reflects the anomalous state over the Pacific Ocean and can be quantified by the SST anomaly in the central tropical Pacific (Trenberth and Hoar, 1997). When a positive ENSO event occurs during the summer monsoon season, a warmer tropical Pacific drives a large-scale atmospheric convergence and divergence over the Maritime Continent and South Asia respectively, and thus, South Asian rainfall becomes weaker than normal (Ju and Slingo, 1995; Ashok et al., 2001; Godgil et al., 2004). When a negative ENSO event happens associated with a colder tropical Pacific, the anomalous atmospheric circulation is opposite to that during a positive

ENSO, and an anomalous convergence favours the above normal South Asian rainfall (Mujumdar et al., 2012; Aneesh and Sijikumar, 2018). The IOD is quantified by the difference of SST anomalies between the western (10°S−10°N, 50°E−70°E) and southeastern (10°S−0°, 90°E−110°E) Indian Ocean (Saji et al., 1999). When a positive IOD event occurs during summer and autumn, the surface cooling in the tropical southeastern Indian Ocean drives a divergence zone together with cross-equator southeasterly wind anomalies, that can transport a higher amount of moisture to South Asia leading to a stronger than normal rainfall in that region (Ashok et al., 2001; Ashok et al., 2004; Krishnaswamy et al., 2015). When a negative IOD event occurs, the anomalous circulation is opposite, and South Asian rainfall becomes weaker than normal (Ashok et al., 2001). The interaction between ENSO and IOD is important in driving the Indian summer monsoon anomalies considering both rainfall amount and intra-seasonal cycle (Wu and Kirtman, 2004; Ajayamohan et al., 2008; Ratna et al., 2020). They have opposite effects since the positive IOD can reduce the drier tendency caused by the positive ENSO (Ashok et al., 2001; Ashok et al., 2004; Hrudya et al., 2021; Ratna et al., 2020). Both the ENSO and IOD also control equatorial processes that are tied to the Walker circulation (e.g., Lau and Nath, 2000; Krishnamurthy and Goswami, 2000; Tozuka et al., 2016; Limbu and Guirong, 2019). The IOD is important here, in the sense that it directly controls the equatorial processes over the Indian Ocean. The SST anomaly in the southeastern Indian Ocean can drive anomalous equatorial winds and modulate the rainfalls over the Indonesian and East Africa (e.g., Abram et al., 2003; Ummenhofer et al., 2009; Cai et al., 2009; Brown et al., 2009; Lim and Hendon, 2015). The anomalous equatorial winds can further influence the equatorial ocean currents and the thermocline/nutricline depths in the entire equatorial Indian Ocean (e.g. Murtugudde et al., 1999, 2000; Vinayachandran et al., 2002b; Iskandar et al., 2009; Wiggert et al., 2009; Currie et al., 2013; Shi and Wang, 2021). A positive IOD can drive a shallower (deeper) thermocline/nutricline depth and thus higher (lower) PP in the equatorial eastern (western) Indian Ocean, while a negative IOD leads to opposite conditions (Vinayachandran et al., 2002b; Thushara and Vinayachandran, 2020; Shi and Wang, 2021).

On a wider point of view, the Indian monsoon belongs to the Global Monsoon System (Wang and Ding, 2008), which is described by the worldwide seasonal displacement of the Inter Tropical Convergence Zone (ITCZ) related to the meridional energy balance (Schneider et al., 2014) (Figs. 1 and 2 in General Introduction). Today, the mean ITCZ is generally located north of the equator because the Atlantic Ocean circulation transports energy/heat northward, which renders the Northern Hemisphere warmer than the Southern Hemisphere (Philander et al., 1996). However, if/when this northward energy flux or the Northern Hemisphere insolation is weaker, the ITCZ moves southward. The southward movement is associated with weaker summer monsoon rainfalls and stronger winter

monsoons over the Northern Hemisphere (Schneider et al., 2014). Therefore, anomalous states of the Atlantic Ocean circulation can modulate the Indian monsoon, and the tropical Indian Ocean hydrology as well. Remarkably, the Atlantic Meridional Overturning Circulation (AMOC), which includes the northward flow of warm salty water in the upper Atlantic and the southward flow of the relatively cold and fresh North Atlantic Deep Water in the deep Atlantic, is a major source for the substantial northward Atlantic heat transport across the equator (Ganachaud and Wunsch, 2000; Talley, 2003; Trenberth and Solomon, 1994; Trenberth and Caron, 2001; Trenberth and Fasullo, 2008). The modulation of AMOC is reflected in the multidecadal variability of the tropical Indian Ocean climate (Fig. 1.12). Multidecadal variability of the AMOC drives the Atlantic Multidecadal Variability (AMV) that is defined by SST anomalies in the northern Atlantic Ocean (Kerr, 2000; Rayner et al., 2003; Zhang et al., 2019). Numerous studies have found that during a positive AMV phase associated to a stronger AMOC, the northward heat transport over the Atlantic is stronger leading to warming over Eurasia. Under this change, the ITCZ shifts northward and the Indian summer monsoon becomes stronger, while the winter monsoon gets weaker (e.g. Goswami et al., 2006; Lu et al., 2006; Zhang and Delworth, 2006; Wang et al., 2009; Luo et al., 2011).

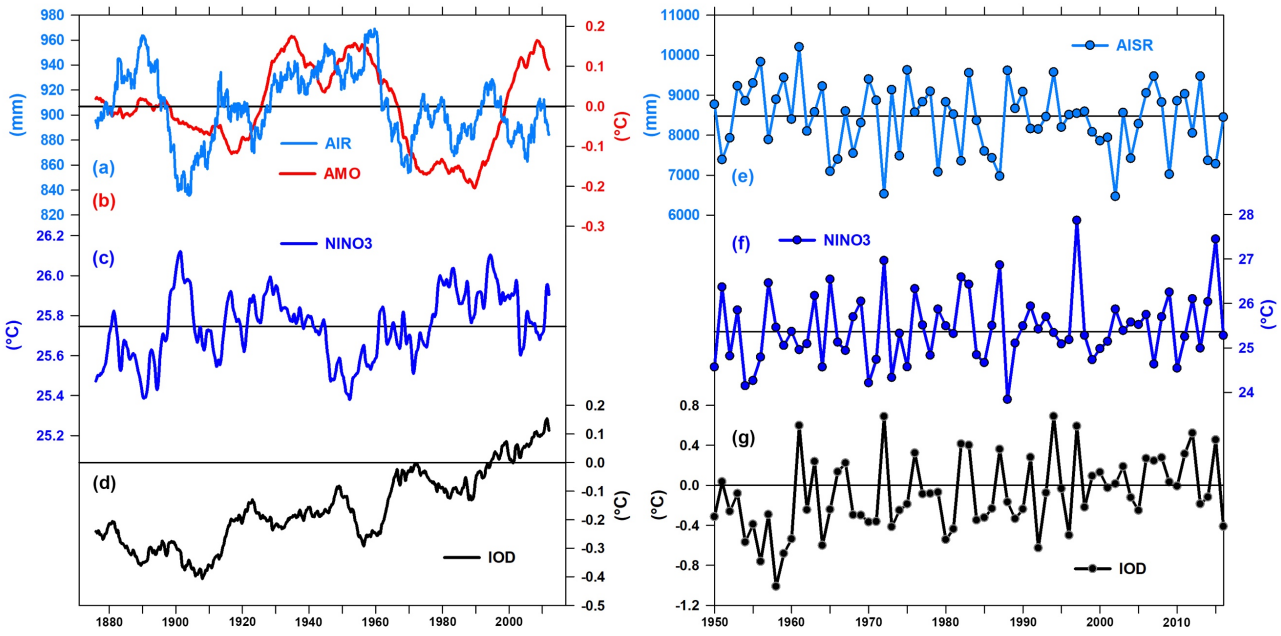

Fig. 1.12. (a) All Indian rainfall (10-year smoothing). (b) Atlantic Multidecadal Oscillation quantified by the 10-year smoothing SST anomaly in the northern Atlantic (0°−65°N, 80°W−0°E). (c) 10-year smoothing ENSO index defined by NINO3 SST (5°S−5°N, 150°W−90°W). (d) 10-year smoothing IOD index defined by SST anomalies between the western (10°S−10°N, 50°E−70°E) and the southeastern (10°S−0°, 90°E−110°E) Indian Ocean. (e) All Indian summer rainfall. (f) ENSO index. (g) IOD index. Data are from https://climatedataguide.ucar.edu/climate-data/atlantic-multi-decadal-oscillation-amo; https://psl.noaa.gov/gcos_wgsp/Timeseries/Nino3/; https://tropmet.res.in/.

All these studies and findings reveal the complexity of the climate variability over the studied area. However, the period with observations is limited, and it hampers the accurate future climate simulations as we lack a complete understanding of the mechanisms controlling the variability at different time scales. The teleconnections and ocean-atmosphere interactions also exist in the past, and studying the past will help us obtain a more complete knowledge of the climate variability over the tropical Indian Ocean.

1.5. Past changes since the Last Glacial Maximum

The Indian (summer and winter) monsoon together with the Walker circulation witness significant variations since the Last Glacial Maximum (LGM). Previous studies are usually based on proxies and simulations that mainly focus on parameters such as wind intensity, precipitation, SST, and SSS. Marine PP reconstructions are usually based on sedimentary TOC records. Due to the importance of such data in this work, and because they are not always included within a regional paleoclimate scenario, I have chosen to devote a single section to PP at the end of this section.

1.5.1. Indian monsoon patterns

1.5.1.1 During summer

- **Empirical data**

Studies focusing on the dynamic of Indian summer monsoon in the past, are usually based on the reconstructions of i) rainfall patterns over South Asia (e.g., Contreras-Rosales et al., 2014; Dutt et al., 2015), ii) southwesterly wind intensity over the AS (e.g. Ivanochko et al., 2005; Bassinot et al., 2011) and iii) SSS conditions in the BoB and the ADS (e.g. Kudrass et al., 2001; Rashid et al., 2007) (Fig. 1.13). Additionally, several studies based on lacustrine sediments help to infer climate patterns and more particularly monsoon rainfall over the continents. High-resolution records exist for the southern Tibetan Plateau and southwestern China (e.g., Kasper et al., 2015; Zhang et al., 2020), a few reach the LGM in northern and northwestern India (e.g. Sinha et al., 2006). Most of the records from South Asia only span the Holocene interval (Misra et al., 2019; Dixit, 2020). The proxies that are commonly used are (clay) mineral assemblages, stable isotopes signals, pollen assemblages, and sedimentary organic contents (e.g. Menzel et al., 2014; Prasad et al., 2014; Dixit et al., 2014a; Sarkar et al., 2015; Rajmanickam et al., 2016; Sandeep et al., 2017; Kumar et al., 2019). Results and interpretations of the main studies are highlighted in Fig. 1.13 (see Tables A1−A3 in Appendix), based on the differences between the LGM and the Late Holocene (LH), and between the Early-Mid Holocene (EMH) and LH.

Depending on the proxies, the lacustrine sediment records indicate that the summer monsoon was weaker during the LGM, HS1, and YD as arid conditions prevailed, and was stronger during the B-A and EMH as wetter conditions prevailed (Wasson et al., 1984; Sharma et al., 2004; Sinha et al., 2006) (Fig. 1.13). Reviews on the Holocene records have been given by Misra et al. (2019) and Dixit (2020). Most of these records reveal a peak in the summer monsoon and wettest climate during the EMH corresponding to the so-called Holocene Climate Optimum, and a trend to drier conditions from the EMH to the Late Holocene. Some records reveal centennial scale events that document drier conditions at 8.2 ka and 4.2 ka (Dixit et al., 2014a, 2014b). The lacustrine records from India are supported by those from southwestern China and the southern Tibetan Plateau (e.g., Nishimura et al., 2014; Günther et al., 2015; Kasper et al., 2015; Zhu et al., 2015; Peng et al., 2019; Sun et al., 2019; Zhang et al., 2020; Fig. 1.13), and confirm summer monsoon variations since the LGM revealed by records from South Asia.

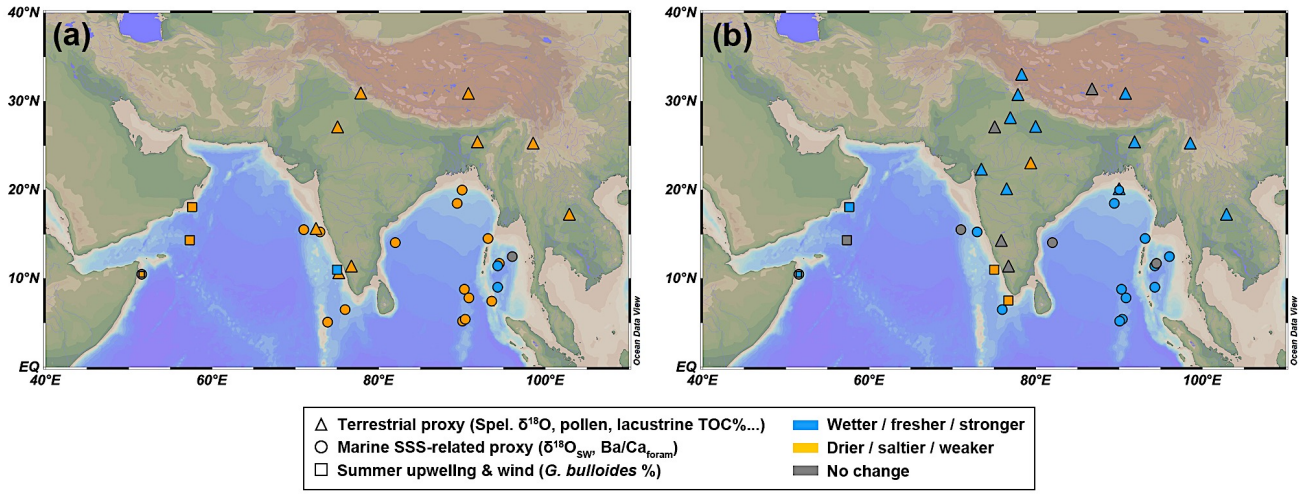

Fig. 1.13. Network of summer monsoon proxies capturing climate changes (a) between LGM and Late Holocene, and (b) between the Early-Mid Holocene and Late Holocene. The means of LGM, Early-Mid Holocene, and Late Holocene were respectively calculated by the available values that are within the periods 23−18 ka, 8−5 ka, and 4−0 ka. The triangles mark the records of terrestrial proxies of moisture/rainfall, e.g. speleothem $\delta^{18}O$, pollen assemblages, and lacustrine TOC%, $\delta^{13}C_{carb}$, $\delta^{13}C_{org}$ signal. The dots mark the SSS records. The rectangles indicate the records of summer upwelling that indicate the alongshore winds that are reconstructed by the *G. bulloide*s %. The core/site names, coordinates, proxies, and references of these paleoclimate records are shown in Tables A1−A3, in the Appendix.

In detail, speleothem records from South Asia, which are mainly based on $\delta^{18}O$ signals, have been the focus of the paleoclimate community as they can provide paleoclimate signals from decadal to centennial scales (Kaushal et al., 2018). It exists two useful referee speleothem $\delta^{18}O$ records that help to reconstruct the summer Indian monsoon dynamic so far: in the Mawmluh Cave (northeastern India)

(Berkelhammer et al., 2013; Dutt et al., 2015; Lechleitner et al., 2017; Huguet et al., 2018), and in the Bitto Cave (northwestern India) (Kathayat et al., 2016). Despite some hiatus, both signals together indicate that the Indian summer monsoon was weaker during the LGM, HS1, and YD and stronger during B-A and EMH. Moreover, these records show that the insolation might directly force the summer monsoon, while ice volume might account for the glacial-interglacial cycles.

Marine sediments have been widely studied to reconstruct the Indian summer monsoon as it provides continuous paleo-records. The evolution of SSS in the BoB and the ADS, based on the seawater oxygen isotope signal from planktonic foraminifera calibrated by SST and ice volume effects, has been widely used to unravel precipitation changes (Duplessy, 1982; Kudrass et al., 2001; Rashid et al., 2007; Govil and Naidu et al., 2011; Marzin et al., 2013; Gebregiorgis et al., 2016; Sijinkumar et al., 2016; Nisson-Kerr et al., 2019; Liu et al., 2021). These studies show that SSS in the BoB was higher than present during the LGM, HS1, and YD, and lower than present during the EMH, which is in agreement with the terrestrial records (Fig. 1.13). As for the ADS, SSS during the LGM is comparable to the present, implying a local relative freshness (Rashid et al., 2007; Sijinkumar et al., 2016). Additionally, trace element ratios such as Ba/Ca and Mn/Ca obtained on surface-dwelling foraminifera have been related to river runoff (Gebregiorgis et al., 2016; Nisson-Kerr et al., 2019), while the δD and $\delta^{13}C$ signals obtained on sedimentary plant waxes have been used to represent vegetation types and moisture conditions (Contreras-Rosales et al., 2014). These proxies all show similar results as those associated to SSS conditions. The evolution of upwelling intensity in the western AS, usually based on the abundance of planktonic foraminifer *Globigerina bulloides*, has been considered to represent the variations of summer southwesterly winds (Clemens et al., 1991; Curry et al., 1992; Schulz et al., 2002). The results since the LGM are in agreement with the reconstructions from South Asia and the BoB related to rainfall showing weaker southwesterly winds during the LGM, HS1, and YD, and stronger during the B-A and EMH (Naidu and Malmgren, 1996; Gupta et al., 2003, 2013, 2015; Bassinot et al., 2011).

In conclusion, as shown in Fig. 1.13, it appears that nearly all the terrestrial and marine records reveal drier conditions associated with weaker summer winds over the Arabian Sea during LGM, and a wetter condition during the EMH.

- **Modelling studies**

Modelling studies on the Asian monsoon started in the 1980s using uncoupled general circulation models (Kutzbach et al., 1981; Kuzbach and Street-Perrott, 1985). These studies find that the monsoon circulation can be strengthened under the Early-Holocene orbital parameters as the smaller precession

increases solar radiation in summer and warms the land more relative to the ocean. Since the 1990s, the Paleoclimate Modelling Intercomparison Project (PMIP) started conducting simulations run with atmosphere general circulation models designed by different institutes and aimed at studying two periods: the LGM (21 ka) and the Mid-Holocene (MH, 6 ka) (Joussaume et al., 1999).

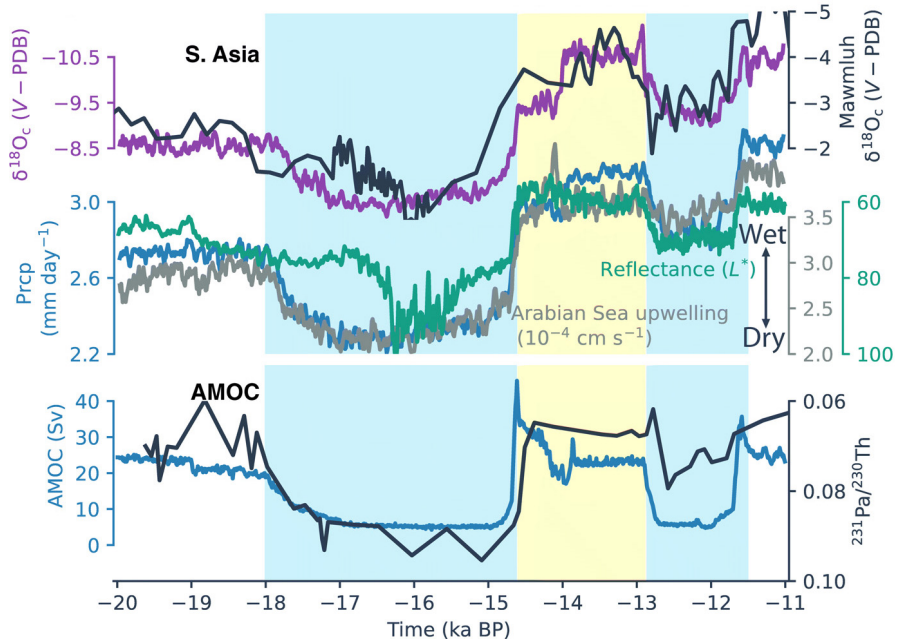

Fig. 1.14. Hydroclimate-δ18O evolution in the iTRACE simulation and observation related to the Indian summer monsoon: records of speleothem $\delta^{18}O$ record from Mawmluh Cave, total reflectance in the Arabian Sea, and AMOC proxy ($^{231}Pa/^{230}Th$); modelling annual δ18O of precipitation, annual precipitation, Arabian Sea upwelling (southwesterly) intensity, and AMOC strength. (From He et al., 2021)

After the PMIP phase 1, ocean-atmosphere coupled models started to be used such as for the following PMIP phases (Braconnot et al., 2007a, 2012). The coupled ocean–atmosphere general circulation models make the studies on the feedbacks between the ocean and the Indian summer monsoon possible (e.g., Braconnot et al., 2000; Zhao et al., 2005; Marzin et al., 2009). The incorporation of the dynamic ocean induces a one to two-months delay of the warming over the ocean compared to the land and drive the convection over the ocean in the late summer that is favorable for the retreat of monsoon rainfall over the land (Zhao et al., 2005; Marzin et al., 2009). The MH simulations in the framework of PMIP phases 2 and 3 all show stronger summer and annual rainfall over South Asia, and northward movement of the ITCZ relative to the pre-industrial period (Zhao et al., 2005; Braconnot et al., 2007b; Zhao and Harrison, 2012; Boos and Korty, 2016; D'Agostino et al., 2019). The stronger summer precipitation is mainly due to the strengthened dynamic monsoon circulations and moisture flux (D'Agostino et al., 2019). Orbital parameters during the LGM are similar to the pre-industrial, but the greenhouse gases concentrations are much lower and ice sheets

are much larger. Most of the LGM simulations in the framework of different PMIP phases indicate weaker summer and annual precipitation over South Asia, and southward movement of the ITCZ (Braconnot et al., 2007b; Jiang et al., 2015; Yan et al., 2016). The global monsoon precipitation and domain are both reduced under LGM conditions (Jiang et al., 2015; Yan et al., 2016). Single forcing experiments show that the effects of greenhouse gas and ice sheet on the Indian summer monsoon rainfall are similar, which can both reduce the land-sea thermal contrast (Shi et al., 2019).

Paleoclimate records reveal the abrupt changes of the Indian summer monsoon during the last glaciation and deglaciation corresponding to the North Hemisphere ice core records (e.g. Schulz et al., 1998; Marzin et al., 2013). The teleconnection between these abrupt changes and the fluctuations of AMOC strength has been studied by using general coupled models. In the simulations, freshwater flux is applied in the North Atlantic to force the AMOC to collapse and shutdown, which are the so-called fresh water hosing experiments (e.g. Kageyama et al., 2013). Kageyama et al. (2013) used multi-model to run the fresh water hosing experiments under LGM conditions and find that the North Atlantic is colder under the weakened AMOC in most of the simulations, and a drier climate prevails over South Asia in at least half of the simulations. Latterly, Marzin et al. (2013) did several fresh water hosing experiments under LGM conditions using the IPSL-CM4 model and proposed that a dipole of SST anomalies in the tropical Atlantic under a weakened AMOC state is key to weaken the Indian summer monsoon. Recently, based on a transient simulation under the near-realistic forcing, He et al. (2021) find that the southwesterly monsoon winds and Indian summer monsoon rainfall are enhanced during the B-A with stronger AMOC compared to the HS1 and YD, and this changed pattern is responsible for the depletion in speleothem $\delta^{18}O$ (Fig. 1.14).

1.5.1.2 During winter

The studies focusing on the evolution of the winter Indian monsoon are much less than those on the summer monsoon so far, partially because of the lack of proxies restricted to the signal of winter wind intensity. A summary of the representative records with winter monsoon interpretations are shown in Fig. 1.15 (see Table A4 in Appendix), highlighting the differences between LGM and Late Holocene, and between Early-Mid Holocene and Late Holocene.

One strategy is to focus on the low-salinity tongue from the BoB invading the eastern AS, a process controlled by the surface current driven by winter northeasterly winds (Sarkar et al., 1990; Mahesh and Banakar, 2014). Stronger northeasterly winds can drive further westward inflow and induce lower SSS in the eastern Arabian Sea. This situation was proposed to occur during the LGM under stronger winter monsoon. However, the SSS itself is controlled by the summer rainfall as well.

A few works aim at differentiating between the summer and winter monsoon signals in the AS, based on sedimentary planktonic foraminifera species that show summer vs winter blooms (Schulz et al., 2002; Ishikawa and Oda, 2007; Singh et al., 2016). For example, while *G. bulloides* is a widely used indicator of the upwelling driven by summer southwesterly winds, *Globigerina falconensis* and *Neogloboquadrina dutertrei*, were suggested as typical species of the winter monsoon. Ishikawa and Oda (2007) showed that the variations of relative abundance of winter monsoon species in the western AS are reversed to the *G. bulloides* in glacial-interglacial cycles, implying that the winter monsoon was strengthened during the LGM while the summer monsoon was weakened. However, these results are very few and only qualitative. Additionally, since strong surface cooling and convective mixing occur in the northern AS during winter (section 1.3.3.2), the SST records have been used to unravel winter monsoon intensity in the past (e.g. Böll et al., 2014; Böll et al., 2015). Over the last 25 kyrs, Dahl and Oppo (2006) revealed that the SST in the AS is much lower than present (of ~1−4 °C) in the northern part during the LGM and the Early-Holocene implying the strengthened winter monsoon during these periods.

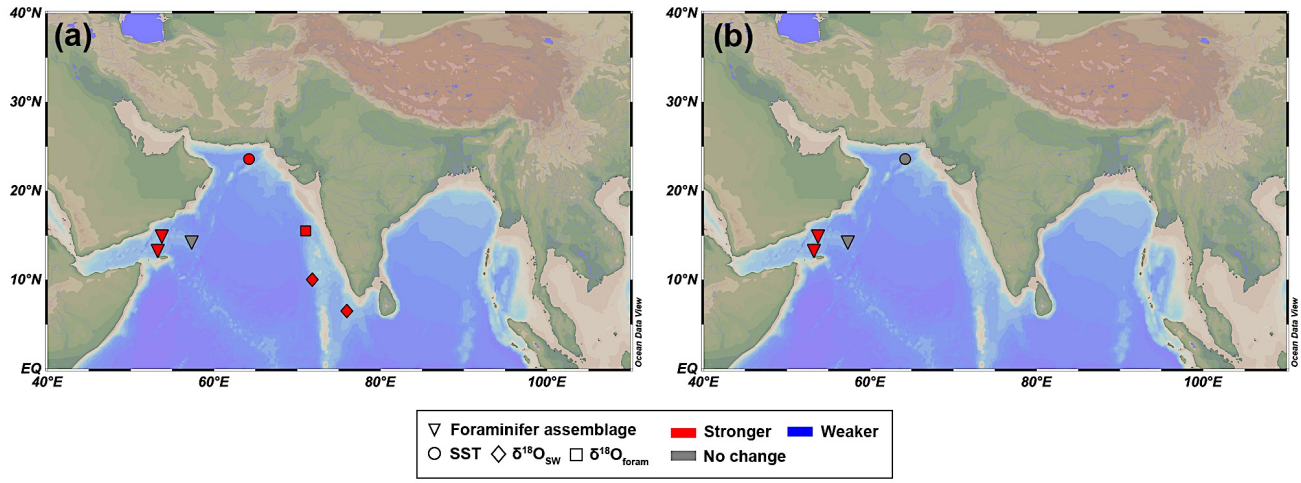

Fig. 1.15. Network of winter monsoon proxies capturing climate changes (a) between LGM and Late Holocene, and (b) between the Early-Mid Holocene and Late Holocene. The means of LGM, Early-Mid Holocene, and Late Holocene were respectively calculated by the available values that are within the periods 23−18 ka, 8−5 ka, and 4−0 ka. The triangles mark the proxy using foraminifer assemblage. The dots indicate the SST record with winter monsoon interpretation. The diamonds and rectangles show the winter monsoon interpretation related to the SSS anomaly. Red (blue) markers indicate the interpretation of stronger (weaker) winter monsoon in the original papers. The core/site names, coordinates, proxies, and references of these paleoclimate records are shown in Tables A4 in the Appendix.

In conclusion, it appears that the very few data dealing with the Indian winter monsoon so far, come from the AS (Fig. 1.15). They all indicate a stronger winter monsoon during the LGM while conditions during the Early-Mid Holocene are not obvious.

1.5.2. Indian Ocean Walker circulation

A few studies focused on the evolution of Walker circulation over the Indian Ocean associated with the rainfall patterns over the Maritime Continent and eastern Africa, and the changes of upper seawater structure in the equatorial Indian Ocean. The results of reconstructed rainfall indicate drier conditions over the Maritime Continent and wetter ones over equatorial eastern Africa during the LGM, thus implying a weaker Walker circulation (DiNezio and Tierney, 2013; DiNezio et al., 2018; Fig. 1.16a, see Table A5 in Appendix). This anomalous state is supported by several modelling data showing anomalous divergence and convergence cells over the Maritime Continent and the western Indian Ocean respectively, which are associated with anomalous surface southeasterlies and equatorial easterlies over the Indian Ocean (DiNezio and Tierney, 2013; DiNezio et al., 2018; Fig. 1.17). This anomalous circulation is probably induced by the exposure of Sahul Shelf and Sunda Shelf under LGM conditions, which can drive a Bjerknes feedback in the southeastern Indian Ocean and strengthen the anomalous westward zonal winds (Bjerknes, 1969; DiNezio et al., 2016). On the other hand, a stronger Walker circulation during the LGM is proposed by Mohtadi et al. (2017), based on the reconstructed deeper thermocline depth in the southeastern Indian Ocean. This stronger Walker circulation is also supported by some other modelling data (Mohtadi et al., 2017) (Fig. 1.17).

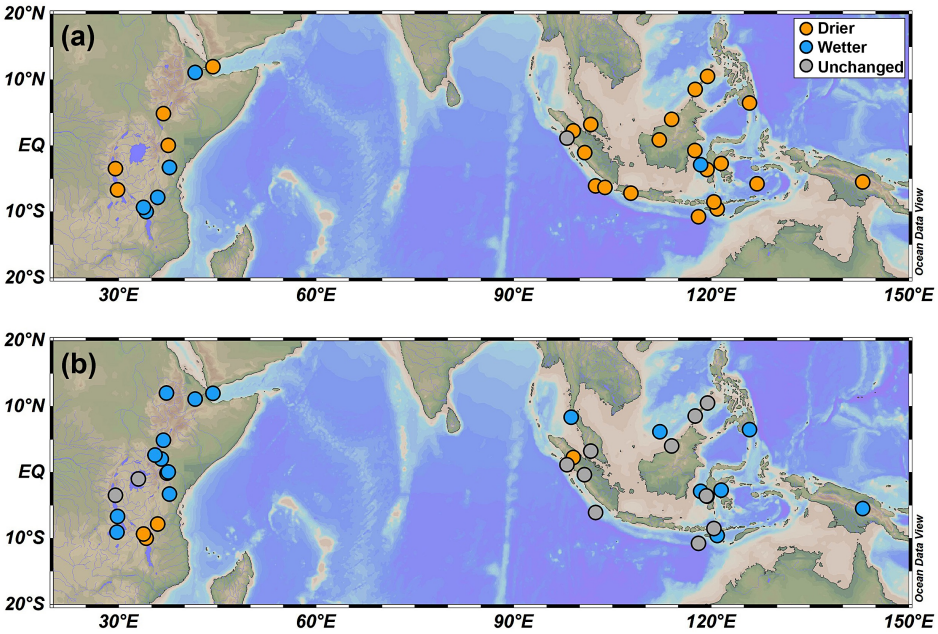

Fig. 1.16. Network of terrestrial hydroclimate/rainfall records in the between 15°S and 15°N from the Maritime Continent and eastern Africa (a) Climate changes between LGM and Late Holocene, and (b) between the Early-Mid Holocene and Late Holocene. The means of LGM, Early-Mid Holocene, and Late Holocene were respectively calculated by the available values that are within the periods 23−18 ka, 8−5 ka, and 4−0 ka. The core/site names, coordinates, proxies, and references of these paleoclimate records are shown in Tables A5 in the Appendix.

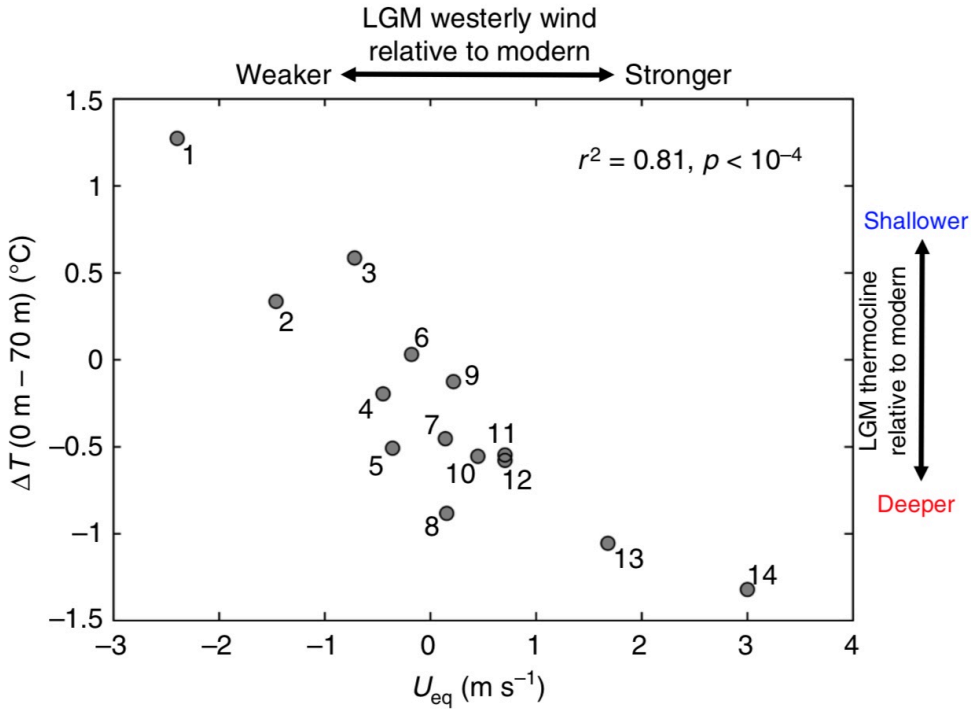

Fig. 1.17. Results of PMIP3 and PMIP3 models showing the difference between the LGM and pre-industrial. LGM thermocline depth anomaly in the eastern Indian Ocean vs. equatorial Indian Ocean zonal wind anomaly. ΔT is used as a measure for thermocline depth and defined as the annual mean temperature difference between surface and 70 m averaged over the eastern Indian Ocean region 4° N–6°S, 94° E–104°E. U_{eq} is defined as the annual mean zonal low-level (925 hPa) wind averaged over 5°N–5°S, 50°E–100°E. HadCM3 model (No. 1) simulates a weaker Walker circulation during the LGM, while CCSM3 (No. 13) and FGOALS-g1.0 (No. 14) models simulate a stronger Walker circulation. (From Mohtadi et al., 2017).

The discussions on the response of Walker circulation to the precession parameter over the Holocene are less developed despite the occurrence of rainfall records over the Maritime Continent and eastern Africa during that period (Fig. 1.16b, Table A5). The wetter climate during the EMH over Africa is proposed as a strengthening of the North Africa monsoon (Chevalier et al., 2017). The moisture over the Maritime Continent is nearly unchanged (Fig. 1.16b). These results indicate a different pattern of rainfall during the EMH compared to that during the LGM, which implies a different response of Indian Ocean Walker circulation. Moreover, weakened summer westerly winds over the equatorial Indian Ocean during this period have been found by both proxies and models (e.g., Bassinot et al., 2011), which suggest a weakened Walker circulation. Recently, paleoclimate simulations reveal that during the Holocene, the Indian Ocean Walker circulation was reacted to the precession-related changes in seasonality and that stronger seasonality could drive more frequent positive IOD events in the southeastern Indian Ocean, and thus weaker Walker circulation (Iwakiri and Watanabe, 2019).

1.5.3. Paleo-PP data

Paleo-records related to PP are mainly reported in the AS since very few exist in the BoB so far (Fig. 1.18). They are based on sedimentary total organic carbon contents (percentages or mass accumulation rates), excess barium (Ba/Al) signals, and biogenic opal fluxes (e.g., Reichart et al., 1997; Schulz et al., 1998; Budziak et al., 2000; Pattan et al., 2003; Ivanochko et al., 2005; Banakar et al., 2005; Singh et al., 2006; Ishfaq et al., 2013; Phillips et al., 2014; Li et al., 2019). Only two records are based on the relative abundance of the coccolith *Florisphaera profunda* (Fp%) in the northern and western AS (Rogalla and Andruleit, 2005). In all cases, very few provide high time resolution patterns since the LGM.

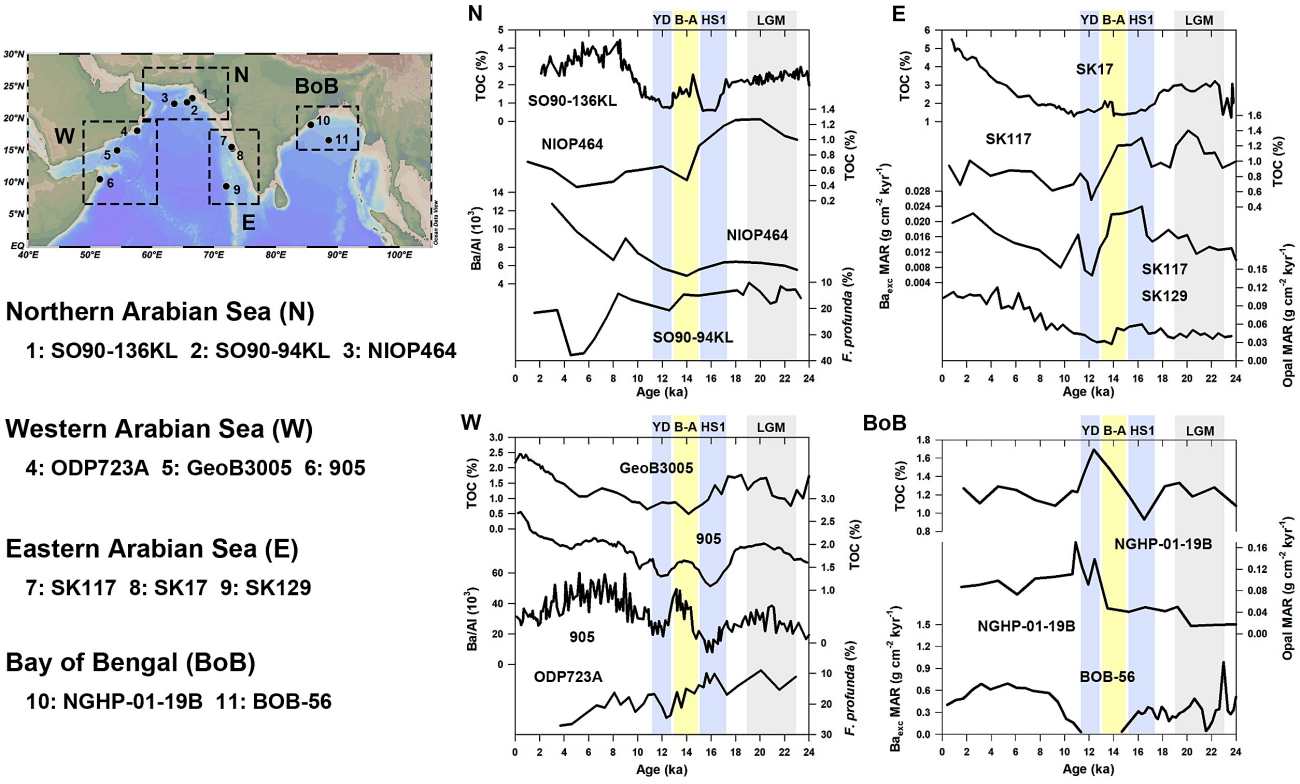

Fig. 1.18. Representative PP records covering the last 24 kyr in the northern (N), western (W), and eastern Arabian Sea (E), and the Bay of Bengal (BoB). Common PP proxies are the total organic carbon content, excess Ba (Ba/Al ratio or Ba MAR), biogenic opal MAR, and relative abundance of *F. profunda*. Data are from Reichart et al. (1997), Schulz et al. (1998), Budziak et al. (2000), Pattan et al. (2003), Ivanochko et al. (2005), Rogalla and Andruleit (2005), Banakar et al. (2005), Singh et al. (2006), Ishfaq et al. (2013), Phillips et al. (2014), and Li et al. (2019).

In detail, high-resolution TOC contents have been measured on marine sediment cores from the northeastern AS, closed to the Indus river mouth (Schulz et al., 1998; Deplazes et al., 2014). The records show lower TOC% during the LGM, the HS1, and the YD, and higher TOC% during the B-A and the EMH (Fig. 1.18). The higher values are interpreted either as stronger advection of upwelling

in the west, or stronger Indus river discharge that are both related to the strengthening of the Indian summer monsoon (Schulz et al., 1998; Deplazes et al., 2014). However, another TOC% record from the northern AS shows a very different trend with a decrease from the LGM to Holocene. TOC% discrepancies are also found in the eastern AS between two cores that are very closed to each other (Fig. 1.18).

Excess Ba is also used as a PP-related proxy, as it is proposed to be possibly associated with phytoplanktonic organic carbon (Dymond et al., 1992; Dehairs et al., 2000). However, in both, the AS and the BoB, excess Ba signals do not match TOC% from nearby sites (Fig. 1.18). That is only in the western AS, that a high-resolution excess Ba record (core 905) shows similar variations compared to TOC% from the northern AS. The data showing higher PP during B-A and EMB, and lower PP during LGM, HS1, and YD, suggest the summer monsoon interpretation of excess Ba.

In the tropical Indian Ocean, the biogenic opal is related to diatom productivity. Therefore, rather than the total PP, the flux of opal is linked to the siliceous primary productivity. This proxy is widely used in high-latitude oceanic regions where the nutrients concentrations and especially those of phosphorus are high enough to support diatoms (e.g., Charles et al., 1991; Pondaven et al., 2000; Bradtmiller et al., 2009). Interestingly, it appears that a few records of opal fluxes mirror some TOC% in the eastern AS and the BoB (Pattan et al., 2003; Balaji et al., 2018; Fig. 1.18).

Fp% has been proved to be related to PP based on a transfer function method where relatively low Fp% reflects relatively high PP and vice versa (Beaufort et al., 1997; see chapter 2 for details). Since the two Fp% signals obtained in the northern and western AS are relatively low during the LGM, PP is most probably high during this time interval compared to the Holocene, which questions numerous TOC and excess Ba signals obtained in the area, so far. Unfortunately, Fp% records are very few in the tropical Indian Ocean and only depict low time-resolution trends. Besides, they have not been used to reconstruct quantitative PP.

Even if multi-proxy studies are crucial to reconstruct paleoenvironmental conditions and hence paleo-PP, the aforementioned results highlight some limitations associated with low-resolution sedimentary organic carbon and excess Ba signals when referring to PP in the tropical Indian Ocean. The content of organic carbon in marine sediments can be influenced by several factors in addition to PP. Indeed, TOC% may not only reflect phytoplankton productivity but can also be associated with terrestrial carbon input, especially nearby river mouths. It can also be impacted by the efficiency of the exported productivity and hence, remineralisation processes in the seawater column and at the sea floor which are tied to the seawater oxygen content, the texture of sediments, and the dilution by detrital materials (Paropkari et al., 1992; van der Weijden et al., 1999; Cowie et al., 2005). Excess Ba may

also be influenced by several other factors than PP, such as the amount of terrigenous Ba inputs, and redox conditions in the sediments (Babu et al., 2002; Nair et al., 2005).

In all cases, it appears that our knowledge of PP distribution in the tropical Indian Ocean since the LGM is limited, which restricts our clear understanding of the regional air-sea dynamics, and more especially, the relationship between the climate setting and the upper seawater structure. This limitation is associated to both, the lack of direct quantitative reconstruction of PP based on the powerful tool that is the transfer function that links Fp% to PP (Beaufort et al., 1997); and the lack of studies considering both, PP reconstructions and simulations in the area (Bassinot et al., 2011; Le Mézo et al., 2017).

1.6. Summary

The main key points of this chapter are:

i- Today, the hydrology and PP in the tropical Indian Ocean are highly coupled to the atmospheric circulations i.e., the Indian monsoon and the Walker circulations. The mechanisms controlling PP in the BoB/ADS and the AS Indian Ocean are very different.

ii- The climate variability of the tropical Indian Ocean is complex and several factors, including teleconnections within the ocean-atmosphere system, have important effects, particularly on multidecadal to interannual scales.

iii- Studying the climate and ocean variability since the LGM helps us better understanding the mechanisms and feedbacks within the ocean-atmosphere system under changing boundary conditions. However, the evolution of the Indian summer monsoon is better studied than the winter monsoon and Walker circulation.

iv- Paleo-PP variations can represent processes at the interface between ocean and atmosphere, but (low-resolution) data that exist so far, show some discrepancies which highlight the need for quantitative PP reconstructions since the LGM.

v- In all cases, proxy reconstructions and paleoclimate simulations appear to be two important ways to fulfill the aforementioned objectives.

Following these, it appears necessary to improve the study on the climate variability in the tropical Indian Ocean since the LGM based on new high-resolution PP records, published terrestrial and marine data compilations, and model-proxy comparisons. PP records (and particularly those related to Fp %) are important as they provide crucial information at the very interface between the ocean and the atmosphere. They also have the potential to reconstruct the variability of both, Indian summer and

winter monsoons, together with the Indian Ocean Walker circulation. Convincing paleo-PP records combined with published hydroclimate data can improve our knowledge of the variability of climate systems and their interactions on a regional scale, considering both the atmosphere and ocean realms and their interactions. The model-data comparison can further give a deeper and broader understanding of these regional signals in the context of changing boundary conditions on a global scale.

Chapter 2

Materials and Methods

This chapter focuses on the materials and methods. First, I present the four sediment cores I've selected to fulfill my objectives. Second, I describe methods to prepare and analyze coccolith smear slides as well as the principle of the transfer function used to estimate PP based on the percentages of Florisphaera profunda retrieved in each core. Third, I describe the outputs I've used from the CCSM3, IPSL-CM5A-LR, and AWI-ESM-1-1-LR climate models.

2.1. Sediment cores, age models, and sampling strategy

Four marine sediment cores retrieved in the tropical Indian Ocean have been chosen for PP reconstructions to fulfill our scientific objectives (Fig. 2.1). These are:

i- core MD77-176 from the northeastern BoB where the "barrier layer" effect is significant due to the strong rainfall and freshwater input of the Irrawaddy-Salween river system, and where PP patterns might be associated with the summer monsoon intensity.

ii- Core MD00-2354 from the northwestern Arabian Sea where PP may be influenced by both, the summer and winter monsoons.

iii- Cores BAR94-24 and MD77-191, closed to the equator, within coastal upwelling systems, and under the influences of equatorial zonal winds. PP signals from these two cores might be suitable to unravel the Walker circulation dynamic.

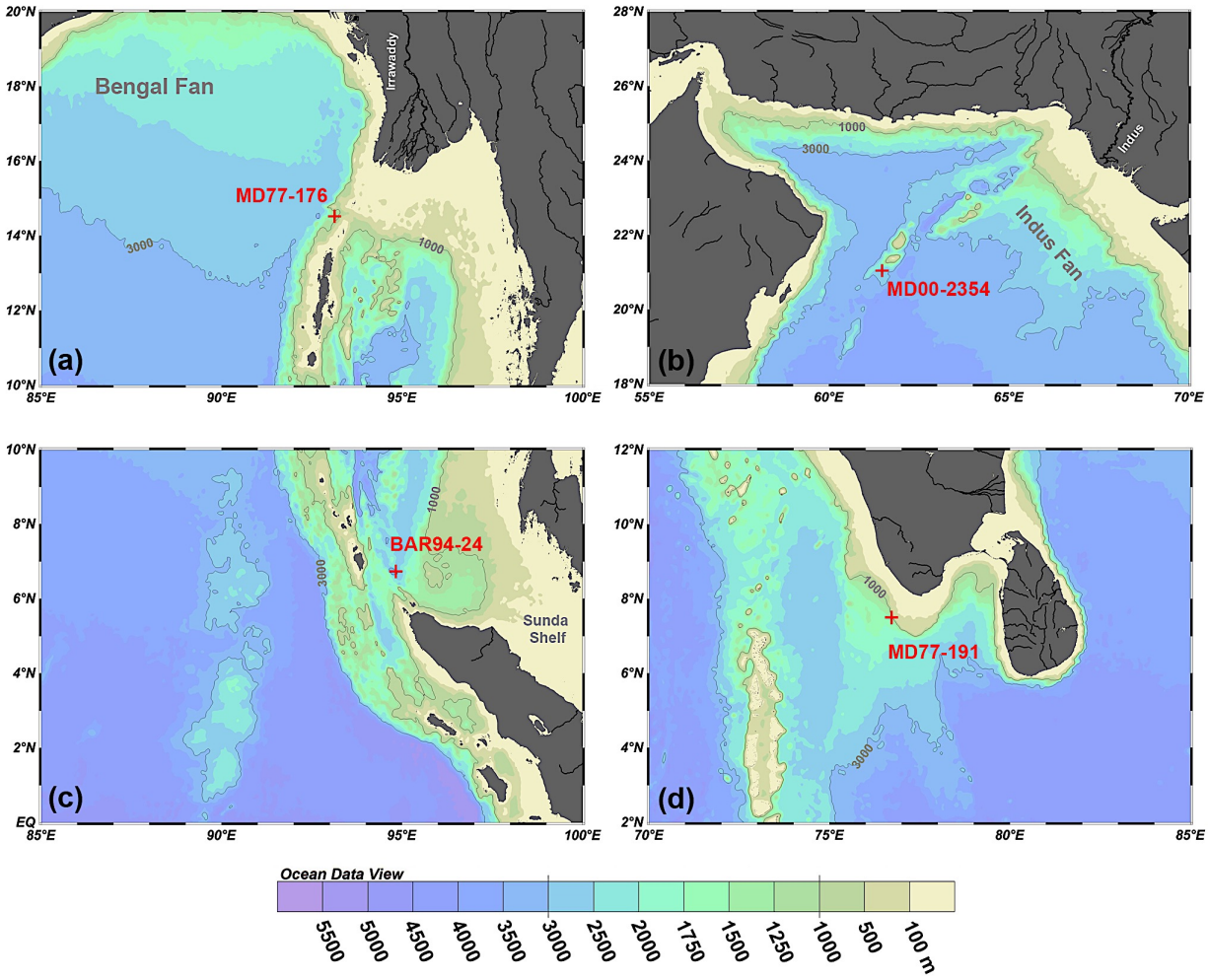

Fig. 2.1. Ocean bathymetric maps and locations of the studied cores (a) MD77-176, (b) MD00-2354, (c) BAR94-24, and (d) MD77-191.

2.1.1. Northeastern Bay of Bengal: core MD77-176

Core MD77-176 (14.52°N, 93.13°E; Fig. 2.1a) was retrieved in the NE BoB, at the junction with the ADS, during the OSIRIS 3 cruise of the R.V. *Marion Dufresne* in 1977. The site lies ~ 200 km southwest of the modern Irrawaddy River mouth, in-between the Myanmar shelf and the Andaman Islands. It was retrieved on the continental slope at a water depth of 1375 m, i.e., above the modern lysocline located between ~ 2000 and ~ 2800 m in the N BoB (Cullen and Prell, 1984). The lithology consists of olive grey terrigenous clay and silty clay layers with foraminifera- and nannofossil-bearing oozes. Its age model was previously established by Marzin et al. (2013) based on 31 accelerator mass spectrometry (AMS) ^{14}C ages combined with the MD77-176 high-resolution oxygen isotope record obtained on the planktonic foraminifera *Globigerinoides ruber*, which were correlated with the GISP2 Greenland ice core oxygen isotope curve. The correlated age model is consistent with the AMS ^{14}C age model, especially after 20 ka (Marzin et al., 2013). The sedimentation rates recorded at site MD77-176 (~25 cm kyr^{-1} and up to 40 cm kyr^{-1} for the Holocene) provide a good opportunity to study productivity patterns over the last 26 kyr with millennial to centennial resolutions (Fig. 2.2). A total of 212 samples were analyzed, with temporal resolutions between ~50 and 400 years.

2.1.2. Northwestern Arabian Sea: core MD00-2354

Core MD00-2354 (21.04°N, 61.475°E; Fig. 2.1b) was collected in the NW AS by *R.V. Marion Dufresne* in 2000. It is located ~210 km off the Oman Margin on the southwestern slope of the Murray Ridge, at 2740 water depth i.e., above the modern lysocline (~3300 m; Cullen and Prell, 1984). The lithology of this sediment core mainly consists of homogenous grey clay and foraminifera- and nannofossil-bearing oozes. Its age model has been established by Böll et al. (2015) based on the correlation of the $\delta^{18}O$ signal obtained on foraminifera *G. ruber* to the $\delta^{18}O_{G.\ ruber}$ record of 74KL sediment core retrieved in the western AS, and the $\delta^{18}O$ signal of GISP2 ice core (Fig. 2.2). The studied interval spans the last ~23 kyr, with sedimentation rate ranging between ~10 and 110 cm kyr^{-1}. A total of 300 samples were analyzed, with temporal resolutions between ~20 and 100 years.

2.1.3. Southeastern Andaman Sea: core BAR94-24

Core BAR94-24 (6.73°N, 94.83°E; Fig. 2.1c) was collected in the SE ADS aboard the N/O *Baruna Jaya*, during the BARAT cruises (1994). The site lies ~150 km off the northwestern tip of Sumatra, in-between the tip and the Andaman Islands. The water depth of the site is 2676 m. The lysocline is approximately 3800 m in the eastern equatorial Indian Ocean, and thus this core locates above the

lysocline (Cullen and Prell, 1984).

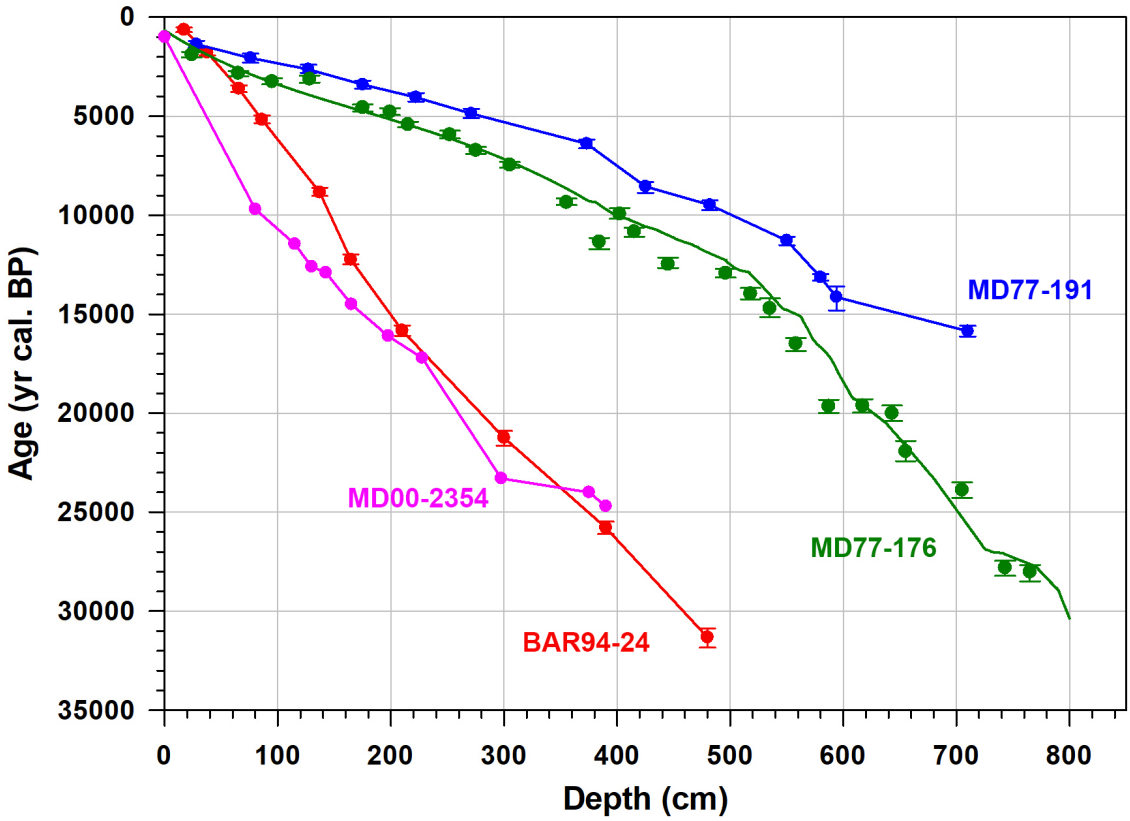

Fig. 2.2. Age models of the studied cores. The dots with error bars are the age points calculated from AMS ^{14}C ages (Mathien-Blard , 2008; Bassinot et al., 2011; Marin et al., 2013; Ma et al., 2020; this study). The green curve is the tuned age model of core MD77-176 (Marzin et al., 2013). The pink dots are the GISP2 δ18O events (Böll et al., 2015).

The age model of this core is based on 10 AMS ^{14}C ages obtained on planktonic foraminifera *G.ruber* and *Globigerinoides sacculifer*. Six data are from the PhD thesis of Mathien-Blard (2008), and four data have been obtained here, using the same method. The AMS ^{14}C ages are converted to calendar ages using the online software CALIB version 8.2, and the MARINE20 curve (global ocean age: 550 years) (Fig. 2.2). The studied interval covers the last 26 kyr with sedimentation rates varying between 8 and 23 cm kyr^{-1} (average of 16 cm kyr^{-1}). A total of 175 samples were analyzed, with temporal resolutions between ~ 50 and 250 years.

2.1.4. Southern tip of India: core MD77-191

Core MD77-191 (7.5°N, 76.72°E; Fig. 2.1d) was collected off the southern tip of India aboard the R.V. *Marion Dufresne* during the OSIRIS 3 (1977) cruise. The water depth of this core is 1254 m that is above the lysocline (see above). Its age model is based on 13 AMS ^{14}C ages from Bassinot et al. (2011) and Ma et al. (2020). The AMS ^{14}C ages are converted to calendar ages using the online

software CALIB version 8.2, and the MARINE20 curve (global ocean age: 550 years) (Fig. 2.2). Core MD77-191 spans the last 16 kyr with sedimentation rates ranging between 13 and 90 cm kyr^{-1} (average of 58 cm kyr^{-1}). A total of 406 samples were analyzed, with temporal resolutions between ~ 20 and 85 years.

2.2. Paleo-PP estimations based on coccoliths

2.2.1. Basic information

Coccoliths are calcareous scales secreted by coccolithophores. Coccolithophores are marine micro-algae (Billard and Inouye, 2004), and taxonomically belong to **Kingdom** Chromista, **Phylum** Haptophyta, and **Class** Coccolithophyceae (AlgaeBase: http://www.algaebase.org). Coccolithophores are one of the main open-ocean primary producers with a distinctive role in the plankton. They contribute to about 10 to 20 % of the total chlorophyll-a and primary production in the non-bloom open-ocean, and up to 40 % in the regions of coccolithophore blooms (Poulton et al., 2007; Poulton et al., 2013). This primary production is, therefore, an important part of the exported primary productivity that accounts for the soft tissue pump. Coccolithophores also play an important role in the carbonate export and participate in the carbonate counter pump (Rost and Riebesell, 2004; Duchamp-Alphonse et al., 2018). Indeed, the coccoliths they produced, contribute to a large fraction of the deep-sea calcareous sediment (Young and Ziveri, 2000; Ziveri et al., 2007; Broecker and Clark, 2009).

Coccolithophores are sensitive to the changes of conditions in the euphotic zone, including light intensity, nutrients contents, temperature, and salinity. Early studies have revealed the significantly biogeographic distributions of the coccolithophore assemblages characterized by the latitude zones (Winter et al., 1994). Although some species are ubiquitous and thrive within large ranges of environmental variables, most of the coccolithophores have environmental preferences (Young, 1994; Winter et al., 1994; Balch et al., 2004). Therefore, the distributions of coccoliths assemblages in marine surface sediments generally reflect the biogeography of coccolithophores (Roth et al., 1994; Baumann et al., 2004; Ziveri et al., 2004; Boeckel et al., 2006; Saavedra-Pallitero et al., 2010).

Coccoliths from sediment cores are documented as good materials for paleoenvironmental reconstructions. Variations of coccolith assemblages in the sedimentary sequences are usually related to past changes in climate and hydrological conditions and have been used in broad topics of paleoclimatology and paleoceanography including changes in nutrient availability, SST, and SSS (e.g., Flores et al., 1999; Kinkel et al., 2000; Baumann and Freitag, 2004; Saavedra-Pellitero et al., 2011). In the tropical oceans, coccoliths assemblages are efficient for the reconstructions of PP and nutricline depth that are related to wind dynamics (e.g. Molfino and McIntyre, 1990a, Beaufort et al., 1997; see

section 2.2.2). In the tropical Indian Ocean, the reports of coccolith assemblage are sparse in paleoclimate studies, and records with high-resolution since the LGM are rare (Beaufort et al., 1997; Rogalla and Andruleit, 2005; Andruleit et al., 2008; Tangunan et al., 2017).

2.2.2. Coccolith analysis

Slides for the coccolith analysis are prepared using the "settling" technique described in Duchamp-Alphonse et al. (2018) after Beaufort et al. (2014). About 0.004 g of dry sediment is diluted in 28 mL Luchon^{TM} water (pH 8, bicarbonate 78.1 mg L^{-1}, total dissolved solid 83 mg L^{-1}) within a flat beaker and settled on a 12 × 12 mm coverslip for 4 hours. After pumping the clear liquid out, the coverslip is then dried at 60 °C in an oven and mounted on a slide with NOA74 glue. This technique ensures a homogenous distribution of coccoliths on the coverslip.

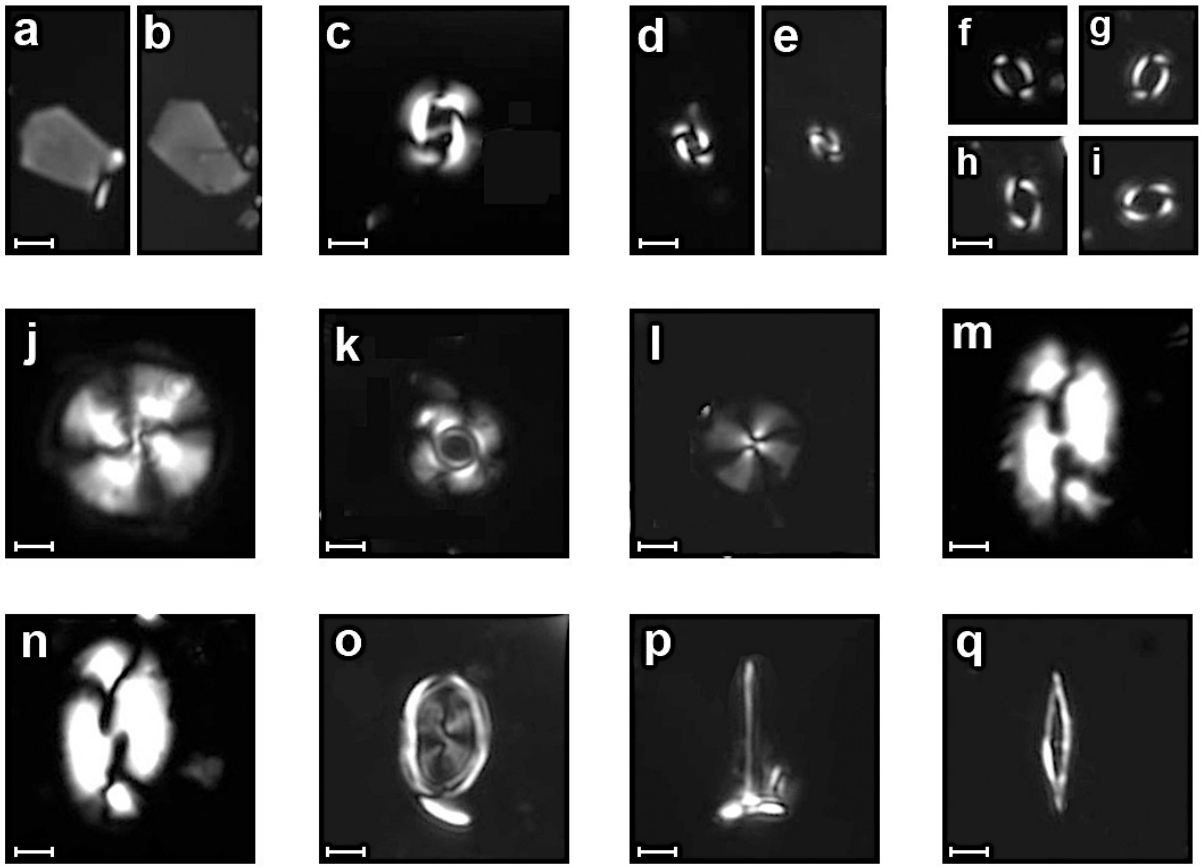

Fig. 2.3. Optical micrographs of the common coccoliths that were observed in this study. All micrographs are crossed polar images at × 1000 magnification and from different depths of the core MO00-2354 located in the northwestern Arabian Sea. The lengths of the white scales represent 2 µm. (a, b) *Florisphaera profunda* (4−5 cm, 201−202 cm). (c) *Gephyrocapsa oceanic* (201−202 cm). (d, e) small *Gephyrocapsa* spp. (134−135 cm). (f−i) *Emiliania huxleyi* (4−5 cm, 134−135 cm, 201−202 cm). (j) *Calcidiscus leptoporus* (4−5 cm). (k) *Umblicosphaera sibogae* (179−180 cm). (l) *Oolithotus fragilis* (153−154 cm). (m) *Helicosphaera carteri* (4−5 cm). (n) *Helicosphaera wallichii* (179−180 cm). (o) *Syracosphaera* spp. (p) *Rhabdosphaera* spp. (201−202 cm). (q) *Calciosolenia* spp. (179−180 cm).

Slides are analyzed with a polarized light microscope (Leica DM6000B) at × 1000 magnification at the Geoscience Paris-Saclay (GEOPS, Orsay, France). For each slide, at least 500 coccolith specimens were counted by human eyes under at least three random fields of view. The relative abundance of each species is calculated as X% = 100 · (species X number / total coccolith number). The "settling" technique allows the calculation of absolute abundance of each species, through the equation: AA = (N · S) / (f · n · W), where AA means the absolute abundance (n/g sediment), N is the total counted number of this species, S is the bottom area of the beaker (diameter: 70 mm), f is the area of the coverslip, n is the number of counted fields of view, W is the sediment weight diluted in the water. The coccolith taxonomy and identification is based on Young (1998) and the Nannotaxa3 website (https://www.mikrotax.org) The common species observed in this study are shown in Fig. 2.3.

The coccoliths of *F. profunda*, which constitute the artichoke-like coccosphere, are rectangle-like single calcite crystals, and are slightly tapered and terminate at the broader end by a pair of crystal faces (Fig. 2.3). Most of the coccoliths of upper euphotic zone dwellers from the tropics belong to the Noelaerhabdaceae Family, such as *Emiliania huxleyi*, and *Geophyrocapsa oceanica*, whose coccoliths are shield-like constituted by multi-calcite crystal (Fig. 2.3).

2.2.2. Use of coccoliths as nutricline depth and paleo-PP indicators

The most workable and efficient application of coccolith assemblages is in the nutricline depth and PP reconstructions. While most of the species of coccolithophore live in the upper euphotic zone and prefer high light intensity conditions, *Florisphaera profunda* lives in the lower euphotic zone at water depths of ~100−200 m where light intensity and temperature are reduced, but where the nutrients contents are higher than those in the upper euphotic zone (Okada and Honjo, 1973; Okada and McIntyre, 1979; Venrick, 1982; Reid, 1980; Fig. 2.4a). When the nutricline gets shallower, more nutrients are brought into the upper euphotic zone where the light intensity is high, and this can make the bloom of the upper dwelling coccolithophores possible, while the relative abundance of *F. profunda* (Fp%) decrease. Conversely, when the nutricline becomes deeper, the abundances of upper dwellers reduce, while the relative abundance of *F. profunda* increases (Figs. 2.4b, c).

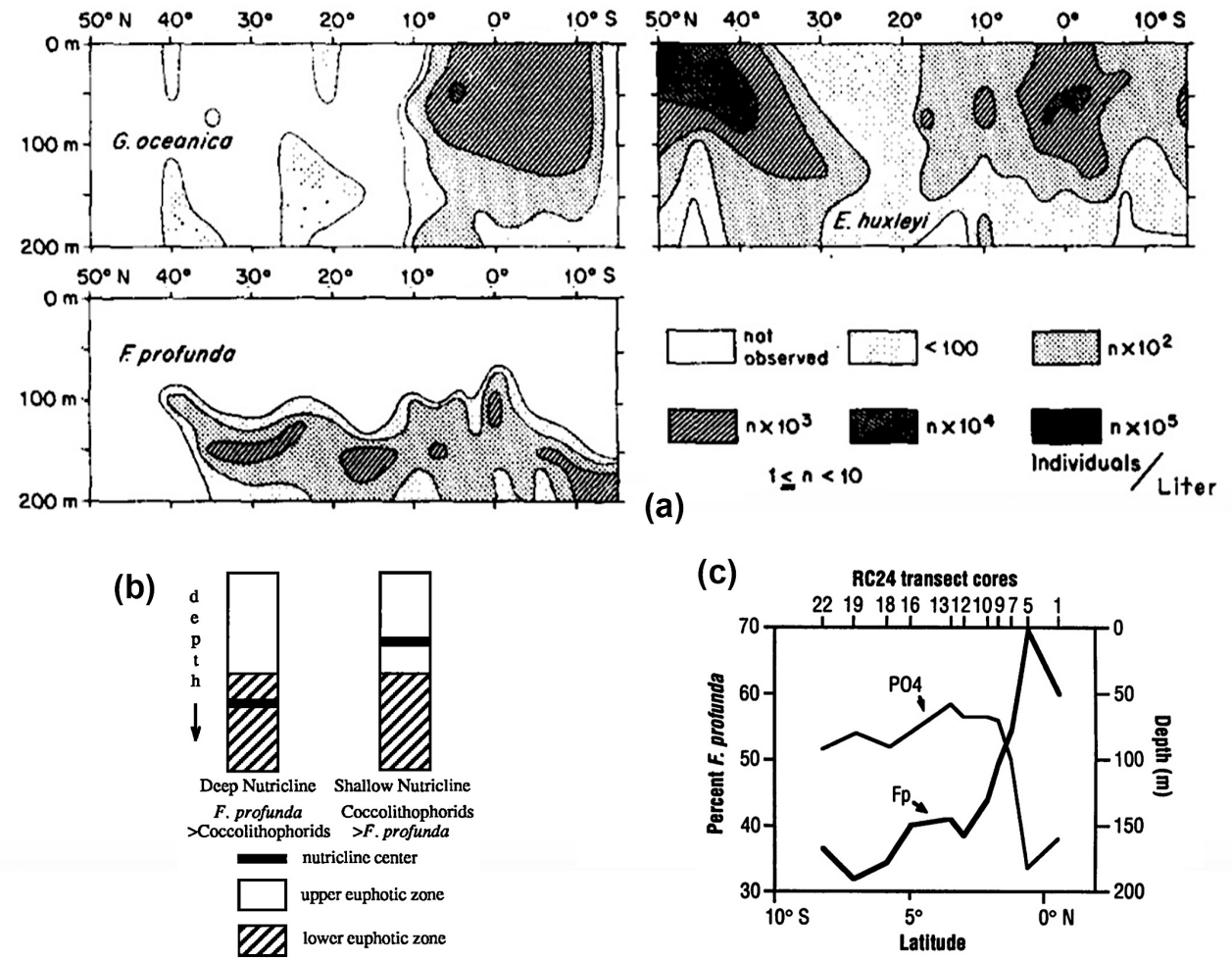

Fig. 2.4. (a) Species distribution in the upper 200 m water column along a traverse in the Pacific (155°W) during August to November 1969 (modified from Okada and Honjo, 1973). (b) Conceptual model of nutricline control of the abundance (in sediment samples) of *F. profunda*, which dwells the lower euphotic zone while all other coccolithophores inhabit the upper euphotic zone (from Molfino and McIntyre, 1990a). (c) Plots of *F. profunda* percentage in a transect of surface sediment samples (10°W−13.5°W), and the nutricline depth of the upper seawater, defined by the depth of the 1.0 µmol L^{-1} phosphate value (from Molfino and McIntyre, 1990a).

The relative abundance of fossil specimens of *F. profunda* was used for the first time by Molfino and McIntyre (1990a, 1990b) for reconstructing the variations of nutricline depth in the equatorial Atlantic at orbital and millennial scales. They have been helpful to reconstruct the evolution of the upwelling in the eastern equatorial Atlantic associated to the intensity of the equatorial easterly winds. Latterly, Beaufort et al. (1997) developed a transfer function method to quantify the primary productivity (PP) using sedimentary Fp% signal. They first established an Fp%-annual PP empirical relationship in the AS and the western Indian Ocean based on PP estimates from satellite observations and Fp% in surface sediments. This method has been used for PP reconstructions in the tropical seas to reflect the wind dynamics related to the climate evolutions (e.g. Beaufort et al., 1997, 2003, 2010; de Garidel-Thoron et al., 2001; Liu et al., 2008; Zhang et al., 2016). Recently, Hernández-Almeida et

al. (2019) further proved the robustness of Fp% as a quantitative proxy of annual PP by investigating surface sediments and sediment trap Fp% signals worldwide. They suggest that this method is workable for the tropical oceans (30°S−30°N) and provide several specific empirical equations of Fp% related -PP for each tropical region (Fig. 2.5).

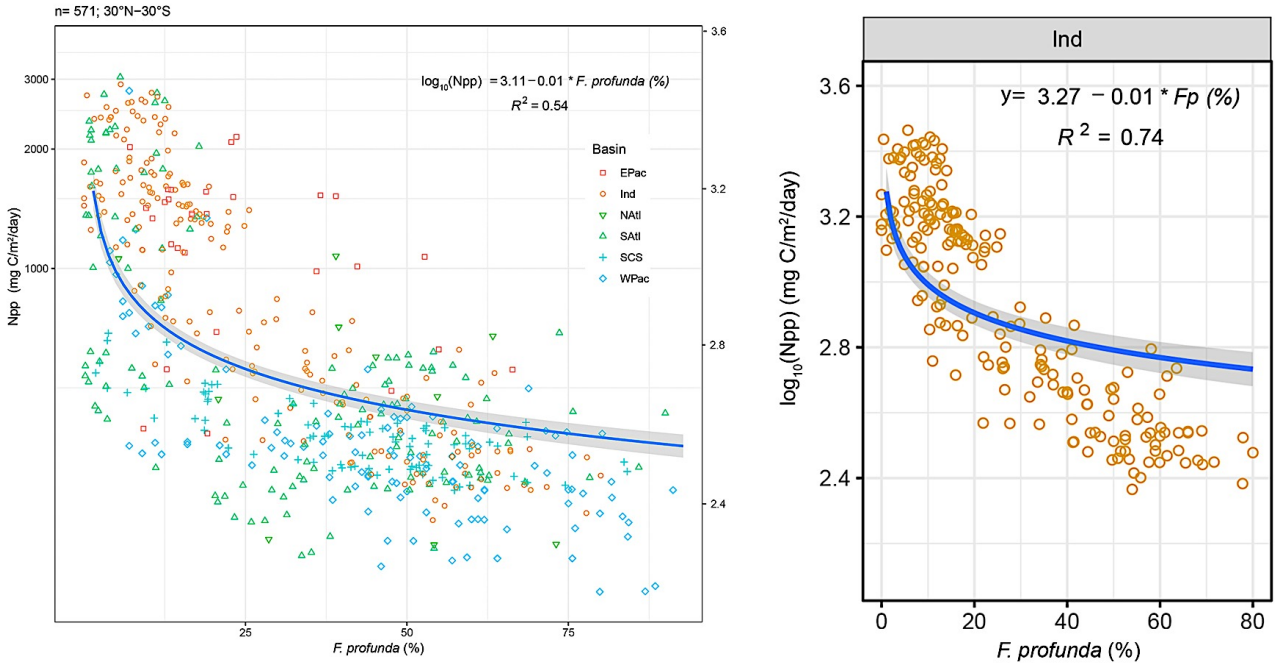

Fig. 2.5. (a) Correlation between global surface sediment *F. profunda* % and net primary productivity (Npp) for samples between 30°N and 30°S, after potential outlier removal (>2SD) (n = 571). Epac = East Pacific; Ind = Indian Ocean; NAtl = North Atlantic; SAtl = South Atlantic; SCS = South China Sea; WPac = West Pacific. (b) Correlation between surface sediment *F. profunda* % and Npp for samples between 30°N and 30°S in the Indian Ocean. Blue lines represent the logarithmic regression. (From Hernández- Almeida et al., 2019)

Here, I've used the equation published by Hernández- Almeida et al. (2019), which is suitable for the tropical Indian Ocean (Fig. 2.5b): PP = [10(3.27−0.01×Fp%)] × 365/1000. The unit of estimated PP is grams of carbon per meter squared per year (g C m^{-2} yr^{-1}). Fp% is the abundance of *F. profunda* relative to the total abundance of coccoliths.

2.3. Models and paleoclimate simulations

2.5.1. IPSL-CM5A-LR

IPSL-CM5A-LR (Institut Pierre-Simon Laplace Coupled Ocean-Atmosphere General Circulation Model) is an Earth System Model that contributes to the Coupled Model Intercomparison Project phase 5 (CMIP5; Taylor et al., 2012) and the Paleoclimate Modelling Intercomparison Project phase 3 (PMIP3; Braconnot et al., 2012). It belongs to the IPSL-CM5 platform that allows for a consistent suite

of models with various degrees of complexity and number of components, and different resolutions (Dufresne et al., 2013). IPSL-CM5A-LR is composed of the LMDZ5A atmospheric general circulation model (Hourdin et al., 2013) directly coupled to the ORCHIDEE land surface model (Krinner et al. 2005), and the NEMO v3.2 ocean model (Madec, 2011) (Fig. 2.6a). The ocean model includes the OPA9 ocean general circulation model, the LIM2 sea-ice model (Fichefet and Maqueda, 1997), and the PISCES biogeochemical model (Aumont and Bopp, 2006). The atmospheric model has a regular horizontal grid of 96 × 96 (lon × lat) points that consists of 26 vertical levels. The horizontal oceanic grid is irregular with 189 × 149 (lon × lat) points corresponding to a nominal resolution of 2° and consists of 25 vertical levels with intervals from 10 m for the first 150 m and up to 500 m for the bottom of the ocean.

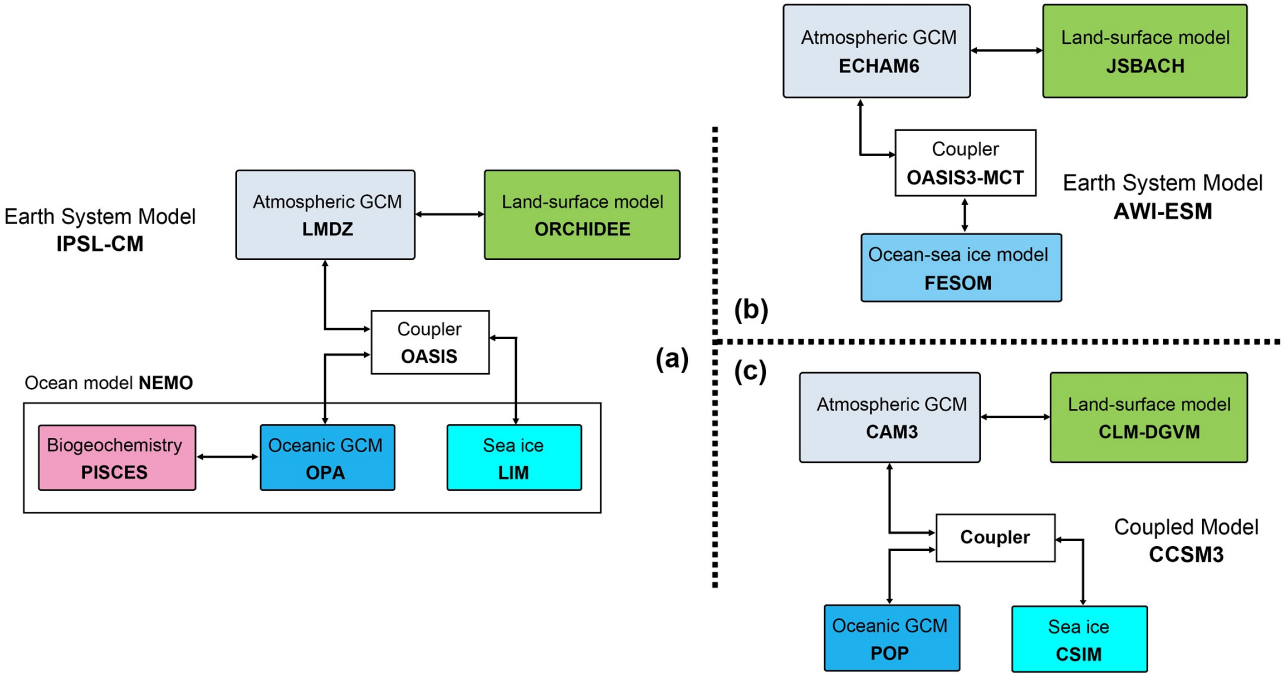

Fig. 2.6. Schematic overview of the components of (a) IPSL-CM5A-LR, (b) AWI-ESM-1-1-LR, and (c) CCSM3.

Three simulations exploited here are in the framework of CMIP5 and PMIP3: the pre-industrial controlling experiment (CTRL), the Mid-Holocene experiment (MH), and the Last Glacial Maximum experiment (LGM). The boundary conditions include the ice sheets volumes, sea level height, earth orbital parameters, and greenhouse gases concentrations. The ice sheet reconstruction and evolution are based on the Pmip3 (Abe-Ouchi et al., 2015). The set-ups of these three simulations can be seen in Table 2.1. The fourth simulation is a freshwater hosing experiment, in which a fresh water flux of 0.2 Sv is applied over the North Atlantic Ocean under the same boundary conditions of LGM. The fresh water flux can force the AMOC to slow down (Fig. 2.7a).

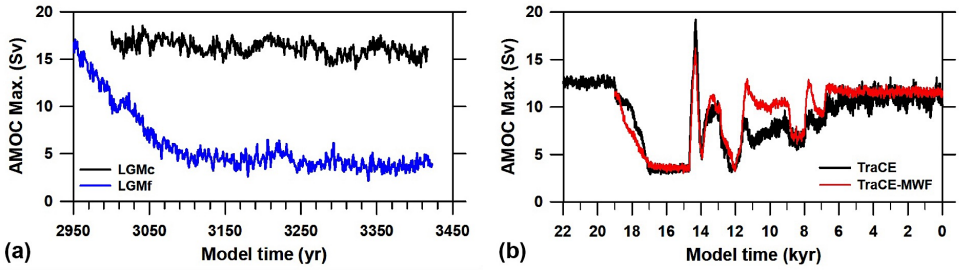

Fig. 2.7. Changes of the maximum in the AMOC stream function below 500 m (AMOC strength) in (a) the LGM and LGMf simulations run with IPSL-CM5A-LR, and (b) the TraCE-21 full and MWF simulations.

An advantage of IPSL-CM5A-LR is that it can simulate the oceanic biogeochemical variables by the PISCES model. This model includes two phytoplankton types, i.e., nannophytoplankton and diatoms, whose growth rates are directly limited by the external availability of nutrients. Five different nutrients are involved: nitrate, ammonium, phosphate, silicate, and iron. For the simulations used in this study, the nutrients supplied by rivers and aeolian dust to the oceans, are set to be the same. Therefore, any change of nutrient contents in the euphotic zone in these simulations is linked to the oceanic processes, such as the upwelling and seawater mixing. The PISCE model has been used for studying the global scale carbon cycles and PP (e.g., Aumont and Bopp, 2006; Gehlen et al., 2006; Mariotti et al., 2012). Le Mézo et al. (2017) have used the PISCES model coupled in IPSL-CM5A-LR to study the dynamics of summer PP in the AS and its linkage to the changes of summer monsoon pattern.

Table 2.1. Forcing and boundary conditions of the simulation run with IPSL-CM5A-LR (Le Mézo et al., 2017) and the simulations in the framework of PMIP4 (in the brackets; Eyring et al., 2016; Kageyama et al., 2017; Otto-Bliesner et al., 2017). Precession is defined as the longitude of the perihelion, relative to the moving vernal equinox, minus 180°. Pmip3 ice sheet stands for the PMIP3 ice sheet reconstruction (Abe-Ouchi et al., 2015). ICE-6G_C is the ice sheet stands for the PMIP4 ice sheet reconstruction (Peltier et al., 2015).

Simulation name	**CTRL**	**MH**	**LGM**
Time (ka)	0	6	21
Ice sheets	present	present	pmip3 (ICE-6G_C)
Sea level difference (m)	0	0	-120
Eccentricity	0.016715 (0.016764)	0.018682	0.018994
Obliquity (°)	22.392 (22.459)	24.105	22.949
Precession (ω−180°)	102.7 (100.33)	0.87	114.42
CO_2 (ppm)	284	280 (264.4)	185 (190.0)
N_2O (ppm)	275 (273)	270 (262)	200
CH_4 (ppm)	791 (808.2)	650 (597)	350 (375)

2.5.2. AWI-ESM-1-1-LR

AWI-ESM-1-1-LR (Alfred Wegener Institut Earth System Model; termed AWI-ESM), which contributes to the Coupled Model Intercomparison Project phase 6 (CMIP6; Eyring et al., 2016) and the Paleoclimate Modelling Intercomparison Project phase 4 (PMIP4; Kageyama et al., 2018) is an extension of the AWI-CM model (Sidorenko et al., 2015). It has three components: the ECHAM6 atmospheric general circulation model (Stevens et al., 2013), the JSBACH land surface model (Raddatz et al., 2007), and the FESOM sea ice-ocean model (Sidorenko et al., 2011) (Fig. 2.6b). The atmospheric model has a regular horizontal grid of 192 × 96 points that consists of 47 vertical levels. The FESOM model is based on the finite-element approach, designed to work on unstructured meshes, and discretized on a triangular grid. Therefore, it has various resolutions in different regions, from ~ 20 to 150 km (Fig. 2.8).

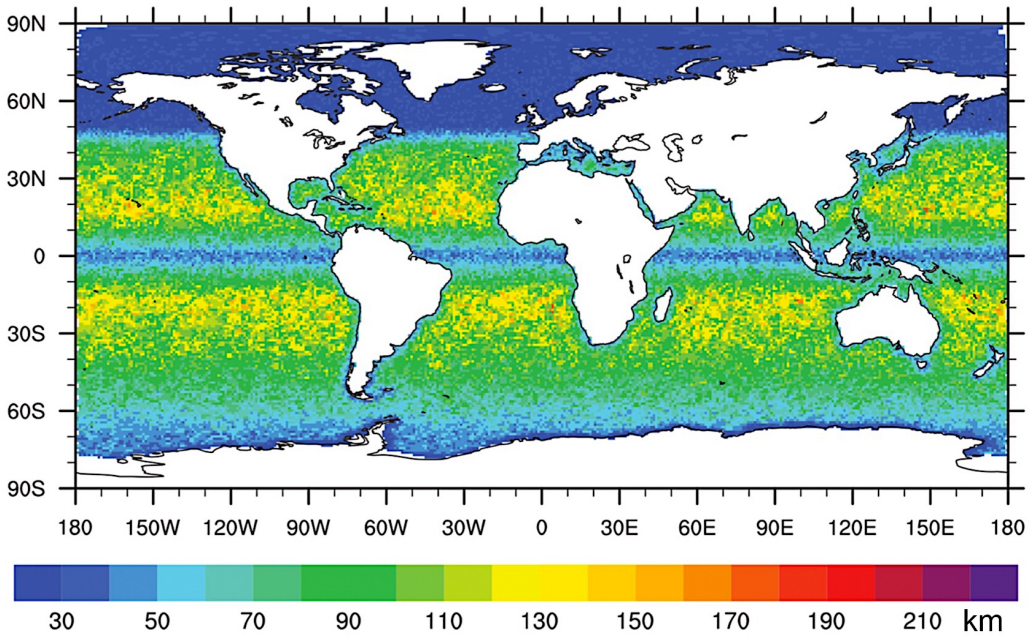

Fig. 2.8. FESOM mesh resolution applied in AWI-ESM simulations (From Shi et al., 2020).

Three simulations exploited here are in the framework of CMIP6 and PMIP4: the CTRL, MH, and LGM. The ice sheet reconstruction and evolution are based on the ICE-6G_C reconstruction (Peltier et al., 2015). The set-ups of these three simulations can be seen in Table 2.1. The oceanic unstructured meshes are a unique feature of AWI-ESM. The multi-resolution capability of FESOM model allows for regional focus in an otherwise global setup and can avoid the effect of geography (Sidorenko et al., 2011; Wang et al., 2014). The AWI-ESM has been used to the global climate changes on multi-timescale (Lohmann et al., 2020; Shi et al., 2020).

The simulations were conducted by the Alfred Wegener Institute Helmholtz Center for Polar and Marine Research (Bremerhaven, Germany), and the data were provided by Xiaoxu Shi and Gerrit Lohmann.

2.5.3. TraCE-21

TraCE-21 is a transient paleoclimate simulation run with the National Center for Atmospheric Research Community Climate System Model Version 3 (CCSM3, Collins et al., 2006a; Liu et al., 2009; Fig. 2.6c). CCSM3 is composed of the CAM3 atmospheric model (Collins et al., 2006b), the POP oceanic model (Smith and Gent, 2002), the CLM-DGVM land surface and vegetation model (Bonan et al., 2002; Dickinson et al., 2006), and the CSIM sea-ice model (Briegleb et al., 2004). The atmospheric model has a regular atmospheric horizontal grid of 96 × 48 (lon × lat) points that consists of 26 vertical levels. The horizontal oceanic grid is irregular with 100 × 116 (lon × lat) points with 25 vertical levels.

TraCE-21 was started at the end of an 1800-year LGM equilibrium simulation run with CCSM3 and then was forced by the realistic climatic forcing (Fig. 2.9), including orbital parameters, greenhouse gases concentrations, and ice sheets (ICE-5G reconstruction) (Peltier et al., 2004). Four single forcing sensitivity experiments are also integrated into the full TraCE-21 simulation: the orbital parameter experiment (ORB), greenhouse gases experiment (GHG), ice sheet experiment (ICE), and melt water flux experiment (MWF). The melt water flux is set to force the AMOC strength to fluctuates (Fig. 2.7b), and details of its scheme can be found in He (2011).

An advantage of TraCE-21 simulation is its transient outputs. It is very useful for studying the atmospheric and oceanic variations during the last deglaciation concerned with the forcing of the AMOC (Liu et al., 2009). It has been used to study the evolution of the East Asian monsoon considering both the wind intensity and precipitation rate (e.g. Liu et al., 2014; Wen et al., 2016), the climate over the Tibetan Plateau (Yan et al., 2020), and the African rainfall (Otto-Bliesner et al., 2014). One limitation of using TraCE-21 simulation is that its oceanic outputs are only available for the annual mean. Moreover, this simulation does not contain the oceanic biogeochemical outputs.

I use the decadal mean seasonal averaged datasets. Data are available on the website of Earth System Grid: https://earthsystemgrid.org/project/trace.html.

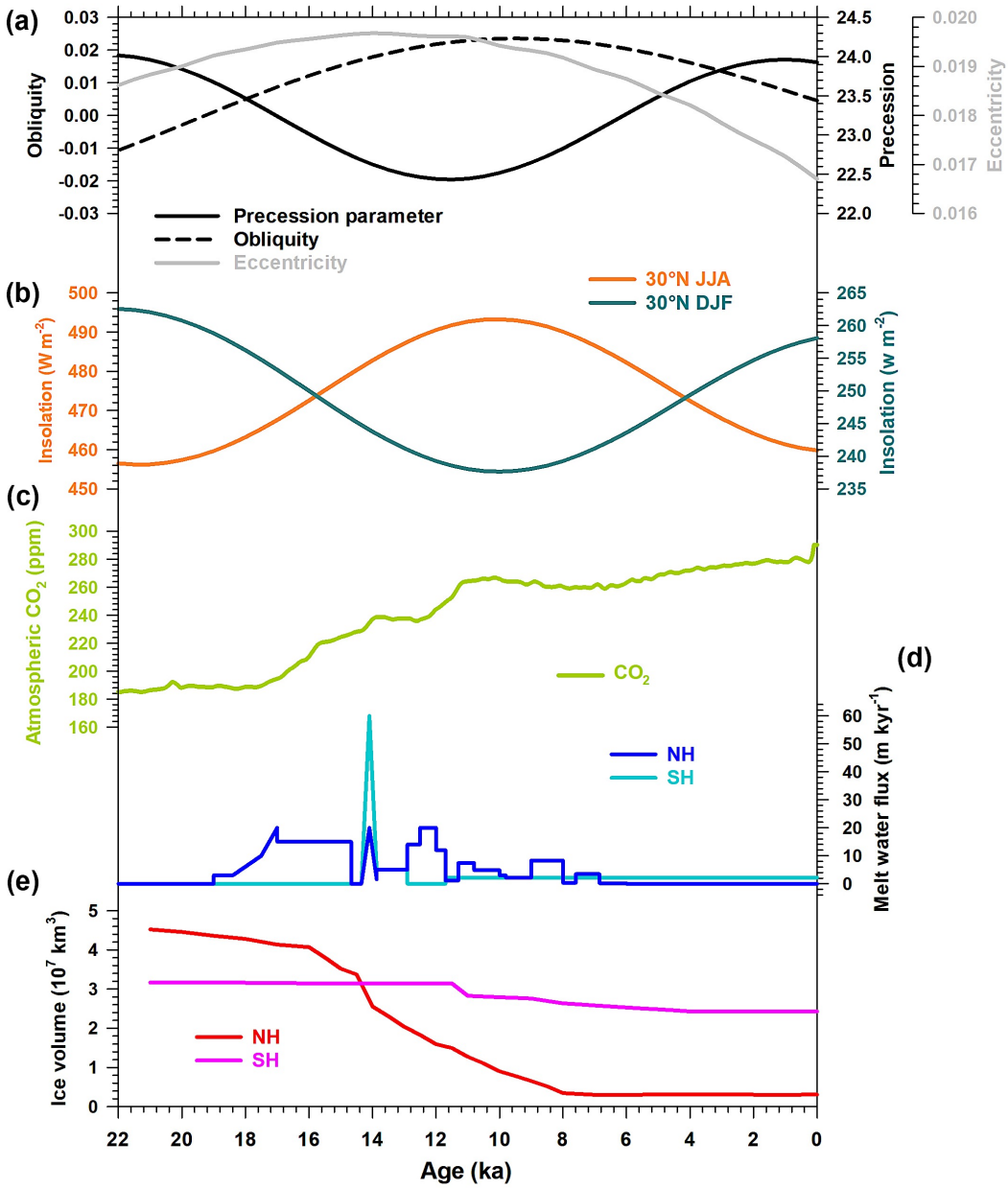

Fig. 2.9. Evolutions of external forcing used in TraCE-21 simulation. (a) Orbital parameters including the standard precession parameter, obliquity, and eccentricity. (b) Summer and winter insolation at 30°N (Laskar et al., 2004). (c) Atmospheric greenhouse gas concentration is represented by carbon dioxide (Joos and Spahni, 2008). (d) Meltwater fluxes in the Southern Hemisphere and Northern Hemisphere. (e) Ice volumes in the Southern Hemisphere and Northern Hemisphere (Peltier, 2004).

Chapter 3

Dynamics of primary productivity in the northeastern Bay of Bengal over the last 26 000 years

A very few paleo-PP records have been reported in the Bay of Bengal so far. Here I provide a new one, spanning the last 26 kyr, based on the Florisphaera profunda (%) signal of core MD77-176, retrieved at 14.5°N of latitude, at the junction between the Bay of Bengal and the Andaman Sea. Together with published PP and paleoenvironmental records that I combine to model outputs from IPSL-CM5A-LR and TraCE-21, I suggest this reconstructed-PP to be highly related to SSS and the "barrier layer" effect that characterize this basin especially between 19 and 1 ka, including the last deglaciation and the Holocene. This record represents the Indian summer monsoon rainfall modulated by AMOC strength and precession.

The coccolith data of core MD77-176 can be found by this link :

https://cp.copernicus.org/articles/16/1969/2020/cp-16-1969-2020-supplement.pdf

Clim. Past, 16, 1969–1986, 2020
https://doi.org/10.5194/cp-16-1969-2020

Climate of the Past
Open Access
EGU

Dynamics of primary productivity in the northeastern Bay of Bengal over the last 26 000 years

Xinquan Zhou[1], Stéphanie Duchamp-Alphonse[1], Masa Kageyama[2], Franck Bassinot[2], Luc Beaufort[3], and Christophe Colin[1]

[1]Université Paris-Saclay, Géosciences Paris Sud, UMR 8148, CNRS, Rue du Belvédère, 91405 Orsay, France
[2]Laboratoire des Sciences du Climat et de l'Environnement, UMR 8112, CEA/CNRS/UVSQ, Université Paris-Saclay, Centre CEA-Saclay, Orme des Merisiers, 91191 Gif-sur-Yvette, France
[3]Centre de Recherche et d'Enseignement de Géosciences de l'Environnement, UMR 7330, CNRS/IRD/Aix-Marseille Université, Av. Louis Philibert, BP80, 13545 Aix-en-Provence, France

Correspondence: Xinquan Zhou (xinquan.zhou@universite-paris-saclay.fr)

Received: 17 February 2020 – Discussion started: 6 March 2020
Revised: 23 September 2020 – Accepted: 15 October 2020 – Published: 28 October 2020

Abstract. At present, variations of primary productivity (PP) in the Bay of Bengal (BoB) are driven by salinity-related stratification, which is controlled by the Indian summer monsoon (ISM). The relationships between PP, precipitation, and more generally climate in the past are not clearly understood. Here, we present a new record of PP based on the examination of coccolithophore assemblages in a 26 000-year sedimentary series retrieved in the northeastern BoB (core MD77-176). We compare our PP records to published climate and monsoon records, as well as outputs from numerical experiments obtained with the Earth system model IPSL-CM5A-LR, including the marine biogeochemical component PISCES, and with the transient climate simulation TraCE-21. Our results show that PP was most probably controlled by nutrient contents and distribution within the upper water column, which were predominantly influenced by (i) regional river systems between 26 and 19 ka, i.e. when sea level was relatively low and climate was relatively dry, and (ii) salinity-related stratification over the last 19 kyr, i.e. when sea level rose and more humid conditions prevailed. During that period, salinity and stratification were directly related to monsoon precipitation dynamics, which were chiefly forced by both insolation and Atlantic meridional overturning circulation (AMOC) strength. During Heinrich Stadial 1 and the Younger Dryas, i.e. when the AMOC collapsed, weaker South Asian precipitation diminished stratification and enhanced PP. During Bølling–Allerød, i.e. when the AMOC recovered, stronger South Asian precipitation increased stratification and subdued PP. Similarly, the precipitation peak recorded around the middle–early Holocene is consistent with a stronger stratification that drives PP minima.

1 Introduction

The climatology and oceanography of South Asia and the north Indian Ocean are dominated by the Indian monsoon, which is characterized by strong seasonal contrasts in wind and precipitation patterns (Shankar et al., 2002; Gadgil, 2003). During the Northern Hemisphere summer season, the north Indian Ocean is strongly influenced by southwesterly winds blowing from the sea toward the Asian continent, thus carrying large amounts of moisture onto land. During the winter season, the winds blow over the continent toward the Indian Ocean from the northeast, thus causing relatively dry conditions on land, with precipitation moved over the ocean. Monsoon precipitation is directly associated with the position of the Intertropical Convergence Zone (ITCZ; Schneider et al., 2014), whose latitudinal displacement is paced by seasonal changes in insolation due to the obliquity of the Earth's axis and precession, and it results from variations in the land–sea thermal contrast caused by differences in heat capacity of the continent and the ocean (Meehl, 1994, 1997; Webster, 1998; Wang et al., 2003). It is also influenced by teleconnections with the El Niño–Southern Oscillation and the Indian Ocean Dipole, two climate modes of interannual

Published by Copernicus Publications on behalf of the European Geosciences Union.

variability that develop from air–sea interactions in the tropical Pacific and drive significant changes within the Indian Ocean (Ashok et al., 2004; Wang et al., 2008; Currie et al., 2013; Jourdain et al., 2013).

Remarkably, the eastern part of the north Indian Ocean, i.e. the Bay of Bengal (BoB) and the Andaman Sea, receives heavier annual precipitation than its western counterpart, i.e. the Arabian Sea (AS). This pattern, together with differences in local evaporation, results in hydrological and ecological differences between these two areas (e.g. Prasanna Kumar et al., 2002; Vinayachandran et al., 2002; Shenoi et al., 2002; Shi et al., 2002; Dey and Singh, 2003; Rao and Sivakumar, 2003; Prasad, 2004; Currie et al., 2013). A noteworthy characteristic of modern conditions prevailing in the north Indian Ocean is the low PP in the BoB and the Andaman Sea compared to the AS (Prasanna Kumar et al., 2002). Previous studies revealed that low annual PP in the BoB results from important freshwater input by rivers and direct rainfall on the sea, which cause a strong stratification of the upper seawater column and an impoverishment of nutrients in surface layers (Vinayachandran et al., 2002; Madhupratap et al., 2003; Gauns et al., 2005). In contrast, the AS has high PP, which is mainly associated with high nutrient content in the upper layer thanks to wind-driven mixing during winter and coastal upwelling during summer (Schott, 1983; Anderson and Prell, 1992; Madhupratap et al., 1996; Gardner et al., 1999; Prasanna Kumar et al., 2001; Wiggert et al., 2005). Both the BoB and AS are characterized by a relatively small sea surface temperature (SST) seasonal cycle. Thus, seasonal and interannual changes in PP result chiefly from variations in the nutricline depth (i.e. variations in nutrient availability in the photic zone) controlled by salinity-related stratification of the upper seawater column in relation to local evaporation–precipitation balance, river runoff, and/or dynamical processes such as wind-driven mixing and/or upwelling (e.g. Lévy et al., 2001; Vinayachandran et al., 2002; Chiba et al., 2004; Rao et al., 2011; van de Poll et al., 2013; Behara and Vinayachandran, 2016; Spiro Jaeger and Mahadevan, 2018).

Past changes in PP at both orbital and millennial scales in the western and northern AS have been widely studied, and authors have interpreted PP variations as chiefly reflecting changes in the intensity of Indian summer monsoon (ISM) southwesterly winds (e.g. Schulz et al., 1998; Ivanova et al., 2003; Ivanochko et al., 2005; Singh et al., 2011). Far less is known about past changes in PP in the BoB and their link to changes in monsoon precipitation, although reconstructions and climate model simulations have clearly pointed to important changes in ISM precipitation driven by both orbital forcing and fast changes at high latitude, such as those associated with the Atlantic meridional overturning circulation (AMOC) (e.g. Braconnot et al., 2007a, b; Kageyama et al., 2013; Marzin et al., 2013; Contreras-Rosales et al., 2014). The poorer attention devoted to past PP in the BoB is in part due to the absence of high-time-resolution PP records in the BoB and the Andaman Sea (Phillips et al., 2014; Da Silva et al., 2017; Li et al., 2019), which precludes our complete understanding of how monsoon climate changes impact tropical ocean ecology through different mechanisms and at different timescales. To fill this gap, reliable paleo-PP records are needed for that region.

Coccolithophores are marine-calcifying phytoplankton organisms that constitute one of the most important "functional groups" responsible for primary production and export of carbonate particles (i.e. the coccoliths they produce) to the sedimentary reservoir. The coccoliths preserved in marine sediment are good study material for paleoenvironmental reconstructions. Particularly, *Florisphaera profunda* is a lower-photic-zone dweller, and its relative abundance in marine coccolithophore assemblages obtained from sediments has been successfully used to reconstruct past changes in the nutricline depth and PP (Molfino and McIntyre, 1990a, b; Beaufort et al., 1997; Zhang et al., 2016; Hernández-Almeida et al., 2019).

In this study, we provide the first record of coccolith assemblage changes in the BoB. The relative abundance of *F. profunda* in the sediment core MD77-176 makes it possible to reconstruct at high temporal resolution paleo-PP over the last 26 kyr in the northeastern BoB. The studied period covers a complete precession cycle and the last deglaciation. This time interval is characterized by rapid climate changes remotely controlled by Northern Hemisphere high-latitude climate and disruptions of the AMOC (McManus et al., 2004; Clement and Peterson, 2008; Liu et al., 2009; Wolff et al., 2010; Clark et al., 2012), as observed during the cold periods of Heinrich Stadial 1 (17–14.8 ka) and the Younger Dryas (12.9–11.8 ka) when massive collapses of Northern Hemisphere ice shelves released prodigious volume of icebergs and fresh water in the North Atlantic Ocean (Heinrich, 1988). In addition, we used the outputs of paleoclimate experiments obtained with the Institut Pierre Simon Laplace Earth System Model version 5 (IPSL-CM5A-LR) (Dufresne et al., 2013), in which marine biogeochemistry is represented, and the transient climate simulations run with the Community Climate System Model version 3 (CCSM3) (He, 2008; Collins et al., 2006a) to analyse our reconstructed PP results in terms of the local evolution of upper seawater stratification and monsoon climate dynamics. Based on our reconstructed PP record and modelling results documented through integrated PP maps as well as oceanic parameter profiles and cross plots, we unravelled the dynamical relationship between PP in the northeastern BoB and the Indian monsoon at both orbital and millennial timescales.

2 Site description and oceanographic setting

Core MD77-176 (14°30′5″ N, 93°07′6″ E) was retrieved from the northeastern BoB, at the junction with the Andaman Sea, during the OSIRIS 3 cruise of the R.V. *Marion*

Dufresne in 1977 (Fig. 1a). The site lies ~ 200 km southwest of the modern Irrawaddy River mouth. It was retrieved on the continental slope at a water depth of 1375 m, i.e. above the modern lysocline located between ~ 2000 and ~ 2800 m in the northern BoB (Cullen and Prell, 1984; Belyaeva and Burmistrova, 1985). The lithology consists of olive grey terrigenous clay and silty clay layers with foraminifera- and nannofossil-bearing oozes.

At our core site, the lowest and highest SSTs recorded during winter (~ 26 °C) and summer (~ 28–29 °C), respectively, clearly reflect the relatively low-amplitude SST seasonal changes (~ 2–3 °C) observed in the area (Locarnini et al., 2010). The oceanic environment is under the influence of the Indian monsoon and shows strong seasonal variations in evaporation and precipitation that are expected under such conditions (Webster et al., 1998; Schott and McCreary, 2001; Shankar et al., 2002; Gadgil, 2003). During the summer, moisture-rich southwesterly surface winds blowing from the Indian Ocean result in heavy precipitation (Fig. 1b, d; Lau et al., 2000; Chen, 2003; Randel and Park, 2006). During winter, dry and cool northeasterly surface winds, weaker than the summer winds, blow from Himalayan highlands and result in drier conditions (Fig. 1c, e).

The summer precipitation rates over the BoB, the Andaman Sea, and the surrounding lands (up to 15 mm d^{-1}) are much higher than in the AS (1–3 mm d^{-1}; Fig. 1d, k). This heavy precipitation area covers the catchments of the Ganges–Brahmaputra–Meghna (GBM) and Irrawaddy–Salween (IS) river systems and thus generates massive freshwater discharge (up to 4050 km^3 yr^{-1}) to the ocean (Sengupta et al., 2006). This input of fresh water depletes sea surface salinity (SSS) at our core site (lower than 33 psu) in the same way as the entire northern BoB and Andaman Sea, which is occupied by a low-salinity tongue, with the largest extension in November, several months later than the peak of summer precipitation (Akhil et al., 2014; Fournier et al., 2017; Fig. 1f, g, l). Low SSS decreases sea surface density, thereby increasing the density gradient of the upper water column and thus leading to a strong stratification that impedes the transfer of nutrients from the nutrient-rich deep layer into the euphotic zone. Such a "barrier layer" effect results in generally low annual PP (around 100–140 g C m^{-2} yr^{-1}) in this area (Prasanna Kumar et al., 2002; Madhupratap et al., 2003; Fig. 1h, i), with maxima being reached during winter when increased surface wind intensity together with decreased precipitation enhance upper seawater column mixing. The low annual PP at the studied site indicates that this area is not significantly influenced by nutrient inputs from rivers, which is different from nearshore settings characterized by annual PP maxima (up to 340 g C m^{-2} yr^{-1}). By contrast, evaporation is high and precipitation is low over the AS. It generates higher SSS (higher than 35 psu) than in the BoB (Fig. 1f, g, l). Such SSS conditions and therefore the absence of strong stratification make it possible for the development of upwelling and convective mixing during summer and winter, respectively, and thus high PP through the year (up to 320–340 g C m^{-2} yr^{-1}; Fig. 1h) (Anderson and Prell, 1992; Prasanna Kumar et al., 2001, 2009; McCreary et al., 2009).

3 Materials and methods

3.1 Age model and sampling

The age model of core MD77-176 was previously established by Marzin et al. (2013) based on 31 accelerator mass spectrometry (AMS) ^{14}C ages combined with the MD77-176 high-resolution oxygen isotope record obtained on the planktonic foraminifera *Globigerinoides ruber*, which were correlated with the GISP2 Greenland ice core oxygen isotope curve. The correlated age model is consistent with the AMS ^{14}C age model, especially after 20 kyr (Marzin et al., 2013). The sedimentation rates recorded at site MD77-176 (~ 25 cm kyr^{-1} and up to 40 cm kyr^{-1} for the Holocene) provide a good opportunity to study productivity patterns over the last 26 kyr with millennial to centennial resolutions (Fig. S1 in the Supplement).

3.2 Coccolith analysis and PP reconstruction

For coccolith data, a total of 212 samples were analysed, with a temporal resolution of ~ 50 to 400 years. Slides were prepared using the "settling" technique described in Duchamp-Alphonse et al. (2018) after Beaufort et al. (2014). About 0.004 g of dry sediment was diluted in 28 mL Luchon™ water (pH 8, bicarbonate 78.1 mg L^{-1}, total dissolved solid 83 mg L^{-1}) within a flat beaker and settled on a 12 × 12 mm coverslip for 4 h. After pumping the clear liquid out, the coverslip was then dried at 60 °C in an oven and mounted on a slide with NOA74 glue. This technique ensures a homogenous distribution of coccoliths on the coverslip.

Slices were analysed with a polarized light microscope (Leica DM6000B) at × 1000 magnification. For each slice, at least 500 coccolith specimens were counted by human eyes under at least three random fields of view. The relative abundance of *F. profunda* (Fp%) was calculated as Fp% = 100 × (Fp number / total coccolith number). The 95 % confidence interval for Fp% was calculated following the method of Patterson and Fishbein (1984) and corresponds to a reproducibility smaller than ± 5 %.

Fp% indicates the relative depth of the nutricline, which is critical for PP (Molfino and McIntyre, 1990a, b). In contrast to most coccolith species that are found in the upper photic zone (< 100 m of water depth), *F. profunda* dwells in the lower photic zone at water depths of ~ 100–200 m (Okada and Honjo, 1973). Therefore, when the nutricline gets shallower, more nutrients are brought into the upper euphotic zone and primary production increases, while the relative abundance of *F. profunda* decreases. By contrast, when the nutricline becomes deeper and primary production de-

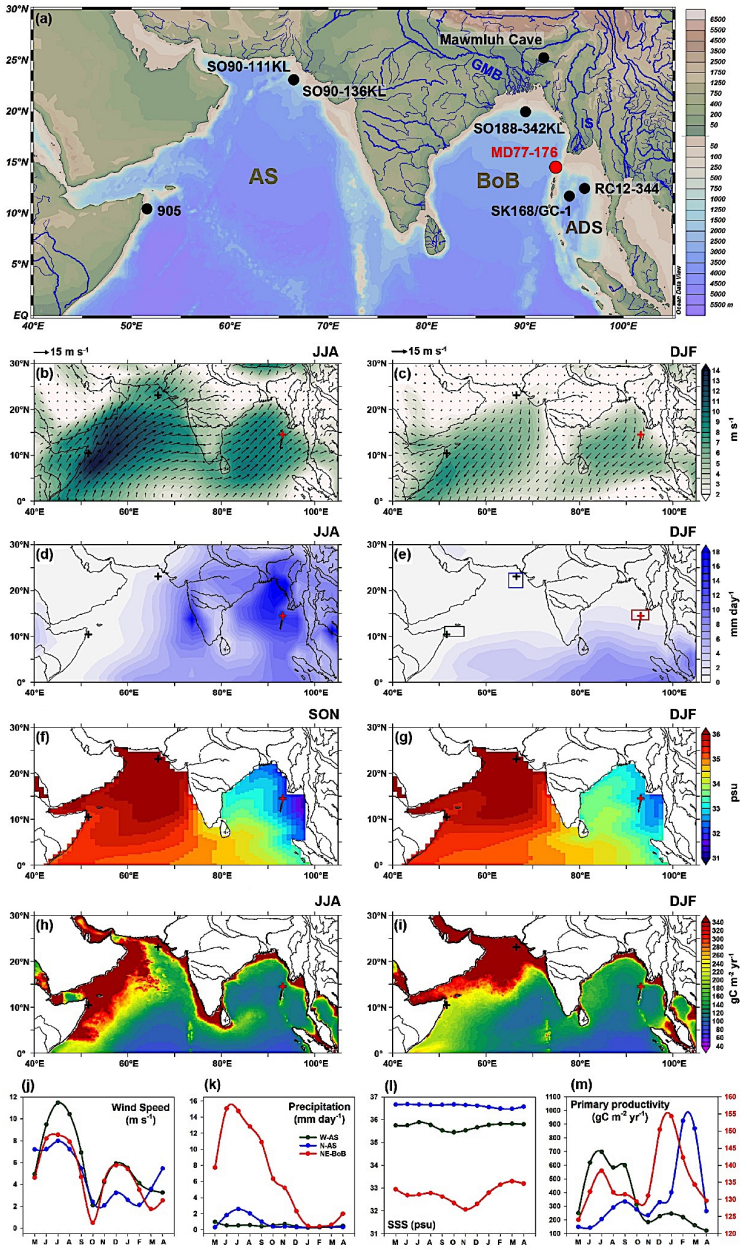

Figure 1. **(a)** Geographic setting and bathymetric map of the Indian monsoon climate zone including the Arabian Sea (AS), the Bay of Bengal (BoB), the Andaman Sea (ADS), the Ganges–Brahmaputra–Meghna river system (GMB), and the Irrawaddy–Salween river system (IS). The map was created with Ocean Data View software (© Reiner Schlitzer, Alfred Wegener Institute) with its built-in global high-resolution bathymetric data (GlobHR). The location of the sediment core MD77-176 is marked by the red circle. Black circles mark the locations of published records shown in Fig. 6. **(b, c)** Mean (from 1979 to 2018) surface wind speed and wind vectors for Northern Hemisphere (NH) summer (June–July–August, JJA) and winter (December–January–February, DJF), respectively. Data are from NCEP-DOE Reanalysis 2 (https://psl.noaa.gov/data/gridded/data.ncep.reanalysis2.html, last access: 25 October 2020). **(d, e)** Mean (from 1979 to 2018) precipitation rate for NH winter and summer, respectively. Data are from the CPC Merged Analysis of Precipitation (https://psl.noaa.gov/data/gridded/data.cmap.html, last access: 25 October 2020). **(f, g)** Mean (from 1979 to 2018) surface seawater salinity (SSS) for NH autumn (September–October–November, SON) and winter, respectively. Data are from the NCEP Global Ocean Data Assimilation System (https://psl.noaa.gov/data/gridded/data.godas.html, last access: 25 October 2020). **(h, i)** Mean (from 2003 to 2018) net primary productivity for NH summer and winter, respectively. PP data are based on MODIS chlorophyll *a* and calculated using the Vertical Generalized Production Model (VGPM; Behrenfeld and Falkowski, 1997) (http://science.oregonstate.edu/ocean.productivity, last access: 25 October 2020). **(j–m)** Regional climatology and oceanography in the western AS, northern AS, and northeastern BoB. The regions of data extraction are marked by coloured rectangles in panel **(e)**. Data sources are the same as above.

creases, the relative abundance of *F. profunda* increases. This relationship between Fp% and nutricline depth is the basis of PP reconstructions via Fp% in marine sediment. Beaufort et al. (1997) first established an Fp%–PP empirical relationship in the AS based on PP estimates from satellite observations and Fp% in surface sediments. In this study, we estimated PP for the last 26 kyr using a recently published Fp%–PP empirical equation suited for the tropical Indian Ocean (Hernández-Almeida et al., 2019): $\mathrm{PP} = [10^{(3.27-0.01\times \mathrm{Fp\%})}] \times 365/1000$. The unit of estimated PP is grams of carbon per metre squared per year ($\mathrm{g\,C\,m^{-2}\,yr^{-1}}$).

3.3 Paleoclimate simulations

3.3.1 Experiments run with IPSL-CM5A-LR

IPSL-CM5A-LR (termed IPSL-CM5A in the following) is an Earth system model (ESM) developed at the Institut Pierre Simon Laplace (Dufresne et al., 2013) for the Coupled Model Intercomparison Project phase 5 (CMIP5; Taylor et al., 2012) and the Paleoclimate Modelling Intercomparison Project phase 3 (PMIP3; Braconnot et al., 2012). It is composed of several model components representing the atmospheric general circulation and physics (LMDZ5A; Hourdin et al., 2013), the land surface (ORCHIDEE; Krinner et al., 2005), and the ocean (NEMO v3.2; Madec, 2008), which includes the ocean general circulation and physics (OPA9), sea ice (LIM-2; Fichefet and Maqueda, 1997), and marine biogeochemistry (PISCES; Aumont and Bopp, 2006). The LMDZ atmospheric grid is regular in the horizontal with 96×95 points in longitude $\times$ latitude (corresponding to a resolution of $\sim 3.75° \times 1.9°$) and 39 irregularly spaced vertical levels. The oceanic grid is curvilinear, with 182×149 points corresponding to a nominal resolution of 2° and 31 vertical levels. It is refined close to the Equator, where the resolution reaches $\sim 0.5°$.

Four experiments set under different boundary conditions were exploited in this study. Three of them were run for the PMIP3 exercise: the pre-industrial experiment (CTRL), the mid-Holocene experiment (MH), and the Last Glacial Maximum experiment (LGMc). Boundary conditions and details for these three experiments can be found in Le Mézo et al. (2017). The fourth experiment (LGMf) is a freshwater "hosing" simulation similar to the IPSL-CM4 freshwater hosing simulation (Kageyama et al., 2013), in which a freshwater flux of 0.2 Sv is applied under LGM (LGMc) conditions over the North Atlantic Ocean, the Nordic Seas, and the Arctic Ocean, which causes the AMOC to slow down (Fig. S2). Both LGMf and LGMc were run for nearly 500 model years. The monthly outputs averaged over the last 100 years of the four experiments were used to compare their mean states. In addition, we focused on monthly results averaged over successive periods of 10 years for the LGMc and LGMf experiments to analyse the transient effects of AMOC changes.

In the glacial experiments (LGMc and LGMf) the sea level is lower, resulting in more extensive continents, including in the study area. The core location is then closer to the coast. In these simulations, the river mouth locations, at which fresh water and nutrients from rivers are brought to the ocean, are moved together with the modified coastline. In particular, the GBM river mouth is brought to the south of its present location, while the IS river mouth is brought northeastward. These locations have been chosen as they reflect the closest LGM coastal points to the present river mouths and the most probably river paths during low sea level conditions. In our relatively simple set-up, for the MH, LGMc, and LGMf simulations we are using the same nutrient content of river inputs for the CTRL simulations, in which they are prescribed according to Ludwig et al. (1996). However, due to the sea level drop and associated continental extension under glacial conditions, in LGMc and LGMf, the nutrients from rivers are less diluted before reaching a fixed location.

Several parameters were extracted to describe climate conditions, including surface wind speed and precipitation minus evaporation rates ($P - E$), as well as ocean conditions: potential temperature (T_θ), salinity, nitrate content (NO_3^-), upper seawater stratification based on the potential density (σ_T) difference between 200 and 5 m (ΔPD; Behrenfeld et al., 2006), and primary productivity (PP). T_θ and salinity of the top layer of the oceanic model are used as SST and SSS.

3.3.2 TraCE-21 simulation

TraCE-21 (termed TraCE in the following) is a transient simulation of the global climate evolution over the last 22 kyr which was run with the CCSM3 model designed by the National Center of Atmosphere Research (He, 2008; Collins et al., 2006a; Liu et al., 2009). CCSM3 is a global, coupled ocean–atmosphere–sea ice–land surface climate model run without flux adjustment (Collins et al., 2006a). It includes four components representing the atmosphere (CAM3; Collins et al., 2006b), land surface (CLM3; Dickinson et al., 2006), sea ice (CSIM5; Briegleb et al., 2004), and ocean (POP; Smith and Gent, 2002). The forcing of the TraCE-21 simulation comprises changes in insolation due to the slow variations of astronomical parameters (ORB), atmospheric greenhouse gases (GHGs) as measured in ice cores, topography, land surface type, coastlines (ICE-5G; Peltier, 2004), and freshwater discharge from melting ice sheets, which force the AMOC strength to change (MWF; Fig. S3). In addition to the full TraCE-21 simulation, we used the four single-forcing sensitivity experiments (ORB, GHG, MWF, and ICE), with only one of the forcings mentioned above allowed to evolve through time, while the three others are kept fixed at their 19 ka value. Atmosphere decadal mean seasonally averaged and ocean decadal mean annually averaged datasets were downloaded from the website of the Earth System Grid: https://earthsystemgrid.org/project/trace.html (last access: 25 October 2020). They have been used to pro-

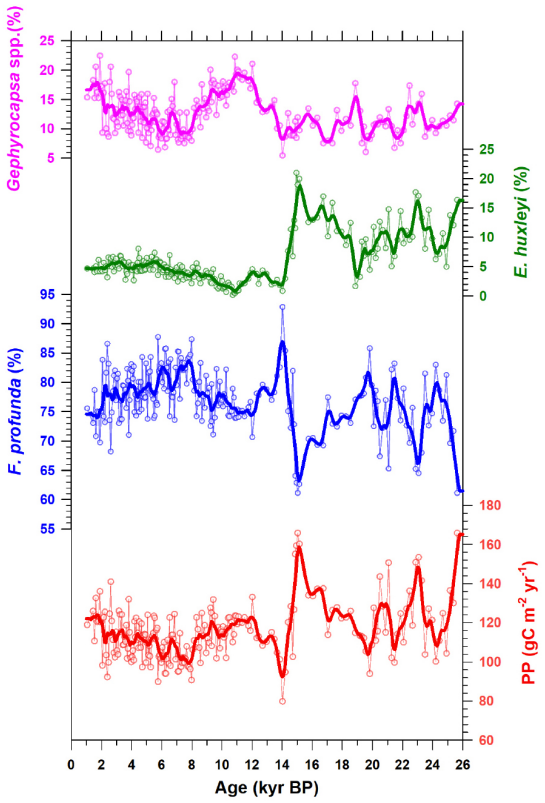

Figure 2. Relative abundance changes (%) of main coccolith species and reconstructed PP of core MD77-176: *Gephyrocapsa* spp. (pink), *Emiliania huxleyi* (green), *Florisphaera profunda* (blue), PP (red). The curves are smoothed results (five-point moving average of 0.1 kyr interpolation of original data).

vide the same atmospheric and oceanic parameters simulated by the IPSL model, but over the last 26 kyr and with the exception of marine biogeochemical variables which are not computed in the CCSM3.

4 Results

4.1 Coccolith abundances and reconstructed PP over the last 26 kyr

At the studied site, coccolith assemblages mainly consist of *Florisphaera profunda*, *Emiliania huxleyi*, and *Gephyrocapsa* spp. *F. profunda* largely dominates the assemblage (> 60 %) over the last 26 kyr, while *E. huxleyi* and *Gephyrocapsa* spp. never exceed 23 % (Fig. 2). Such relative contributions are coherent with coccolith distribution in sediment traps from the northern BoB (Stoll et al., 2007), which shows a high abundance of *F. profunda* due to a strong salinity-related stratification and low surface nutrient concentration (see Sect. 2).

The most striking shifts of coccolith abundances are observed between ∼ 20 and ∼ 11 ka, particularly around 15–14 ka when *F. profunda* drastically increases from 60 % to 93 %, while *E. huxleyi* decreases from 22 % to 1 % and *Gephyrocapsa* spp. slightly decreases from 12 % to 5 %. Such patterns subdivide the record into three main time intervals: (i) from ∼ 26 to 19 ka when *F. profunda* depicts relatively high-amplitude variations, ranging from 60 % to 85 % with minima at ∼ 25, 23, and 21 ka, while *E. huxleyi* and *Gephyrocapsa* spp. both average ∼ 10%; (ii) from 19 to 11 ka when *F. profunda*, *E. huxleyi*, and *Gephyrocapsa* spp. depict their highest variations (up to about 33 %, 21 %, and 15 % in amplitude, respectively); and (iii) from 11 to 1 ka when *F. profunda* shows a long-term increasing trend up to 8 kyr, a maxima of 85 % between 8 and 6 kyr, and a long-term decreasing trend up to 1 kyr, while *Gephyrocapsa* spp. abundances exceed those of *E. huxleyi* despite minima of ∼ 7 % between 8 and 6 ka.

Estimated PP varies between 80 and 170 g C m^{-2} yr^{-1} (Fig. 2). Remarkably, values obtained during the late Holocene (∼ 125 g C m^{-2} yr^{-1}) are comparable to those recorded in the study area today (annual PP mean of ∼ 135 g C m^{-2} yr^{-1}). Because estimated PP is inversely related to *F. profunda* percentages (see Sect. 3.2), PP reconstructed over the last 26 kyr mirrors *F. profunda* distribution. It is characterized by peaks higher than 140 g C m^{-2} yr^{-1} at ∼ 25, 23, and 21 ka. Changes with the largest amplitude are found over the deglaciation with a maximum (∼ 170 g C m^{-2} yr^{-1}) and a minimum (∼ 80 g C m^{-2} yr^{-1}) observed at ∼ 15 and 14 ka, respectively. Relatively low PP is recorded during the Holocene, with minima of 90 g C m^{-2} yr^{-1} obtained between 8 and 6 ka.

4.2 Simulated PP and physicochemical profiles

Simulated annual and seasonal (summer and winter) patterns of PP (g C m^{-2} yr^{-1}) are shown for the BoB and the Andaman Sea in Fig. 3, where the MH and LGMc simulations are compared to the CTRL and where the LGMf simulation is compared to the LGMc, highlighting the effects of the AMOC slowdown. According to the CTRL simulation, the coastal northern BoB and Andaman Sea as well as the southwestern BoB appear to be the most productive areas under pre-industrial conditions, which is in accordance with the Vertical Generalized Production Model (VGPM), representing in situ PP distribution based on satellite-derived chlorophyll concentration (Fig. 1h, i; Behrenfeld and Falkowski, 1997). In all cases, high PP (> 220 g C m^{-2} yr^{-1}) is related to high nutrient contents in the upper column, thanks to the influence of river discharge (northern coastal BoB and Andaman Sea) or the development of coastal upwelling (southwestern BoB; Vinayachandran et al., 2004). Hence, despite its coarse spatial resolution, the IPSL-CM5A model is able to represent the main area of high PP and the seasonal cycles. The differences in annual PP between MH and CTRL reveal

a dipole structure in the studied area, with slightly lower PP in the western part of the BoB and slightly higher PP in the eastern part including the Andaman Sea. A strong signal of lower PP is found in the southwestern BoB during summer and in the northern BoB during winter. Slightly higher PP is found in the eastern BoB and the Andaman Sea, mainly during summer. The overall increase in annual PP simulated within the centre part of the BoB during the LGM compared to pre-industrial (LGMc–CTRL) reflects the general PP increase simulated during the summer season. This area is an extension of the high PP found by the CTRL simulation within the southwestern BoB. One of the most striking patterns highlighted by this comparison is the important increase in annual PP in the northeastern part of the BoB at the junction with the Andaman Sea, which reflects significant increases in PP during both summer and winter seasons, while PP in the northern BoB and the whole Andaman Sea is lower. This pattern highlights the CTRL river mouth grid shift toward the northeastern BoB during the LGM (Sect. 3.3.1) and its most probable location closer to the MD77-176 site in that period. Between LMGf and LGMc, PP is lower in the entire BoB, except in the northeastern part of the BoB in winter, for which a higher annual PP is simulated.

Summer and winter vertical profiles are extracted from grids at the GBM and the IS river mouths for CTRL and MH (Fig. 4), as well as from grids at the northeastern BoB, near the location where core MD77-176 was retrieved, for CTRL, MH, LGMc, and LGMf (Fig. 5).

CTRL and MH river mouth profiles depict PP maxima within the surface layers (0–50 m), where reduced salinity and density conditions help maintain a nutricline around 50 m of water depth in both seasons (Fig. 4). In all cases, temperatures and SSS are lower during the MH compared to CTRL. The most striking difference is observed for the GBM river mouth system, where salinity is clearly lower within the surface layer (0–30 m) during MH compared to CTRL, especially during winter, while temperature change is limited. Such a pattern results in lower density in the surface layer and a stronger density gradient within the upper 200 m of the seawater (i.e. stronger salinity-related stratification) during winter in the MH. Under such conditions, nutrient content and thus PP are lower in the upper 30 m of water depth.

For the CTRL profiles of the northeastern BoB, PP maxima are found at ∼ 75 m of water depth, just above the nutricline, in both seasons (Fig. 5). Such a pattern reflects what is found in the open sea environment of the BoB at present (Madhupratap et al., 2003). MH PP profiles show no large difference compared to the CTRL ones. It is only during winter that salinity is significantly lower, between 0 and 50 m of water depth, and that the associated increase in the density gradient within the photic zone is related to slightly lower PP.

PP profiles of LGMc and LGMf are very different from those of CTRL and MH. They are associated with generally saltier and/or colder surface waters. Interestingly, high PP is found in the surface layers (0–50 m) where nutrient contents are higher than CTRL and MH conditions (Fig. 5). Such distributions show that nutrient content and PP are comparable to those found in the CTRL river mouth profiles, particularly during winter when LGMc and LGMf simulations of the salinity gradient show a shallower halocline that raises the density gradient of surface layers and is thus accompanied by a shallower pycnocline. It indicates that PP reacts to the shift from the open sea environment configuration during CTRL and MH simulations to the more coastal one during LGMc and LGMf simulations, as previously documented in Sect. 3.3.1. Interestingly, during the winter, PP and nutrient contents between 0 and 30 m water depths in LGMf are higher than those of LGMc. Such patterns are associated with higher salinity in surface waters and a reduced density gradient that might promote upper layer mixing. Overall, the LMGc, LMGf, and MH simulations do not show a strong difference in the vertical variation of temperature compared to the MH. Changes in PP and nutrient contents are rather associated with modifications in the density gradient thanks to salinity changes, which highlight the importance of salinity-related stratification vs. mixing in the PP distribution in the past.

5 Discussion: forcing factors behind PP variations over the last 26 kyr as revealed by a model–data comparison

5.1 The last glacial period

During the LGM (23–19 ka), i.e. when drier conditions prevailed in the area, our reconstructed PP estimates average $\sim 120\,\mathrm{g\,C\,m^{-2}\,yr^{-1}}$, which is nearly the same value as the one reconstructed for the late Holocene (2–1 ka) (Figs. 6i and 7f, g). An important discovery is the high-amplitude millennial-scale variations that PP depicts from 26 to 19 ka. Such variations mirror those of SSS (seawater δ^{18}O anomaly signal) obtained on the same core (Fig. 6h) and to some extent in the Andaman Sea (Fig. 6e, g), thus documenting high PP intervals at times of low SSS pulses and vice versa. In such a context, the most plausible explanation for higher PP coeval with low SSS involves higher nutrient inputs from rivers. Indeed, during the LGM and relatively low sea level, a more proximal IS river mouth system might promote freshwater and terrigenous nutrient transfer to our core site, thus decreasing (increasing) SSS and increasing (decreasing) nutrient content and PP, according to South Asia precipitation and riverine flux dynamics. Such millennial-scale variations are readily seen in the record of South Asian monsoonal precipitation, thus confirming our assumption. Indeed, despite long-term aridity during the LMG, as documented by the net precipitation results of the TraCE simulation together with δ^{18}O and δD alkane signals from cave speleothems and marine sediments, respectively (Fig. 6c, d), rapid SSS decreases at our core site are in phase with short-term increases in pre-

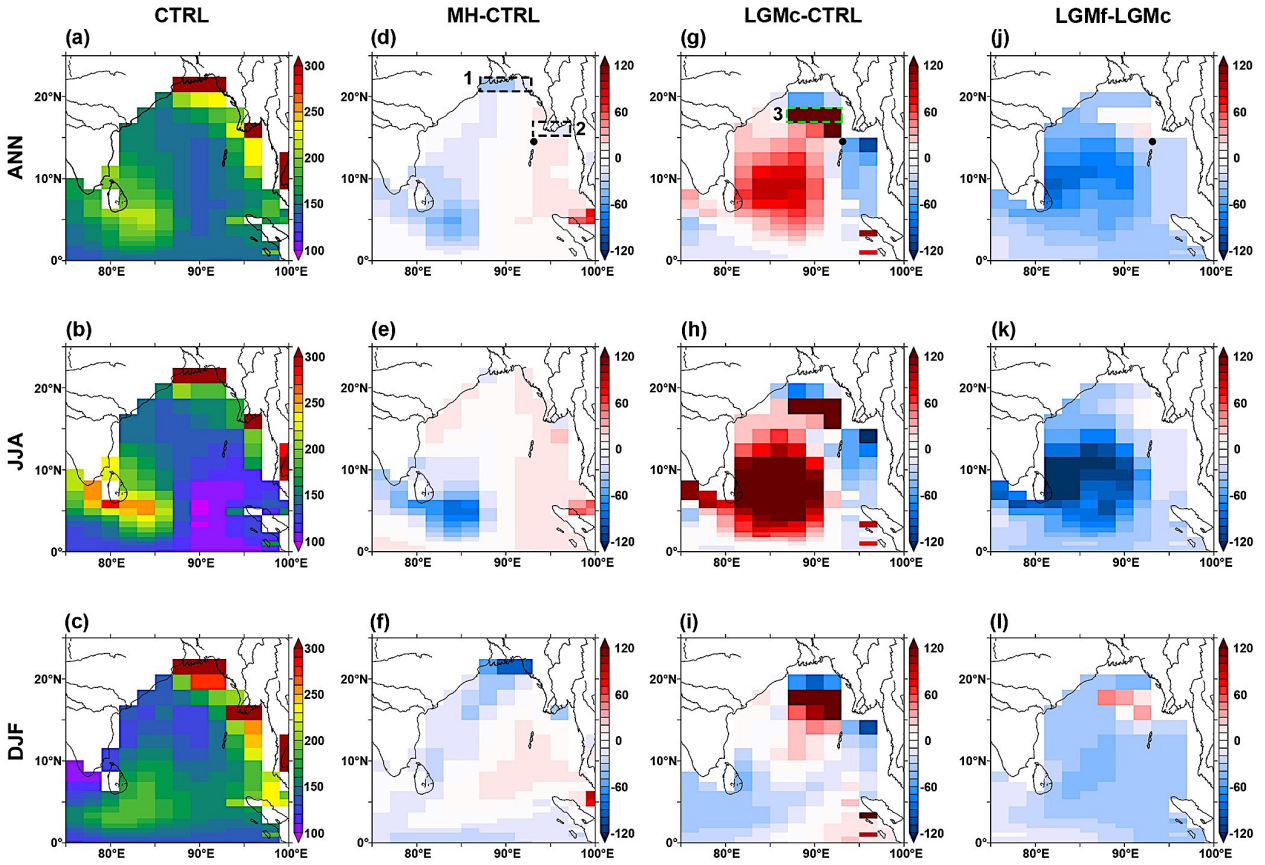

Figure 3. IPSL-CM5A-LR-simulated integrated PP of the full water column ($g\,C\,m^{-2}\,yr^{-1}$) for the pre-industrial (CTRL) **(a–c)**. PP differences between the mid-Holocene (MH) and CTRL **(d–f)**, the Last Glacial Maximum (LGMc) and CTRL **(g–i)**, and the Last Glacial Maximum under AMOC shutdown (LGMf) and LGMc **(j–l)**. Results are shown for annual mean (ANN), summer (June–July–August, JJA), and winter (December–January–February, DJF). Rectangles 1 and 2 in panel **(d)** mark the grids from which the vertical profiles in Fig. 4 are extracted. Rectangle 3 in panel **(e)** marks the grids from which the vertical profiles in Fig. 5 are extracted. The black dots mark the location of core MD77-176.

cipitation and vice versa (Fig. 6h). They are also found in IPSL-CM5A simulations with higher PP and higher nutrient contents within the upper 50 m of the photic zone during LGMf and LGMc compared to MH and CTRL, reflecting higher terrigenous nutrient inputs to the studied site as the IS river mouth system probably migrates northward, i.e closer to our core site (Sect. 4.2). Interestingly, the highest reconstructed PP ($\sim 160\,g\,C\,m^{-2}\,yr^{-1}$) remains lower than the simulated PP at river mouths ($> 220\,g\,C\,m^{-2}\,yr^{-1}$), thus suggesting that core MD77-176 is not within the coastal environment during the LGM but is rather influenced by the nutrient-enriched river system plume. The local specificities of the area have in part been highlighted by Sijinkumar et al. (2016), who reported lower SSS compared to the modern time in the northern Andaman Sea due to major changes in basin morphologies between the two periods, thanks to the sea level being significantly lower during the LGM compared to modern times. Therefore, in such contexts, one cannot exclude the possibility that both the low sea level conditions and the migration of the IS river mouth system might result in the specific SSS and PP records obtained at our core site. In all cases, it appears that between 26 and 19 ka, the IS river system renders MD77-176 PP sensitive to millennial-scale variations in South Asian monsoonal precipitation, as it modulates riverine flux and the extent of the nutrient-rich riverine plume in the area.

5.2 The last deglaciation

During the last deglaciation (19–11 ka), the most striking changes in reconstructed PP covary positively with SSS, especially after the 19–17 ka transient period when high PP intervals correspond to high SSS ones and vice versa (Fig. 6h, i). Both signals show three stages that correspond to abrupt temperature changes in the North Atlantic Ocean, i.e. the cold Heinrich Stadial 1 (HS1; 17–14.8 ka),

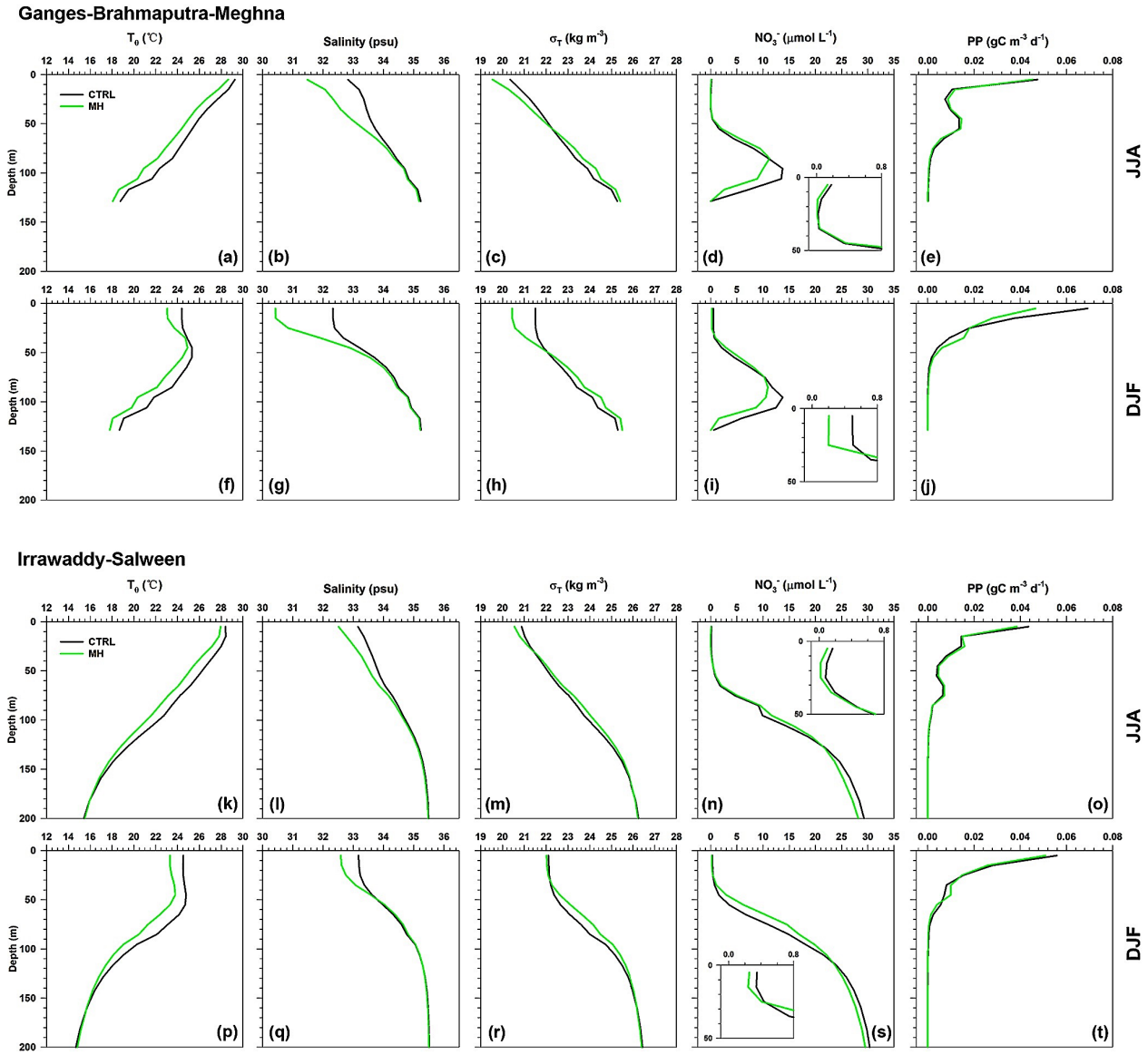

Figure 4. Simulated ocean profiles between 0 and 200 water depths in the MH and CTRL simulations run with IPSL-CM5A-LR. Data in panels **(a)**–**(j)** have been extracted from the grids located in the Ganges–Brahmaputra–Meghna river mouth (rectangle 1 in Fig. 3d). **(a–e)** Results for summer (June–July–August, JJA). **(f–j)** Results for winter (December–January–February, DJF). Data in panels **(k)**–**(t)** have been extracted from the grids located in the Irrawaddy–Salween river mouth (rectangle 2 in Fig. 3d). **(k–o)** Results for summer (JJA). **(p–t)** Results for winter (DJF). The parameters shown here are potential temperature (T_θ), salinity, potential density (sigma-t, σ_T), nitrate concentration of seawater representing seawater nutrient content (NO_3^-), and total primary productivity (PP). The nutricline, halocline, and pycnocline are the depths with the largest vertical gradients of nutrient content, potential density, and salinity under the upper seawater layers.

the warm Bølling–Allerød (B-A; 14.8–12.9 ka), and the cold Younger Dryas (YD; 12.9–11.8 ka), which are characterized by changes in AMOC strength (Fig. 6b, h, i; Elliot et al., 2002; McManus et al., 2004). The AMOC is a component in inter-hemispheric transport of heat (e.g. Liu et al., 2009; Buckley and Marshall, 2016) and its changes in intensity, which are related to the inter-hemisphere temperature gradient and have a strong influence on tropical Atlantic (Wang et al., 2004; Peterson et al., 2000; Peterson and Huaug, 2006; Swingedouw et al., 2009) and South Asia rainfall (Overpeck et al., 1996; Barber et al., 1999; Fleitmann et al., 2003; Gupta et al., 2003; Murton et al., 2010; Yu et al., 2010; Cai et al., 2012; Marzin et al., 2013). Cold periods in the North Atlantic are associated with a relatively weak AMOC, low

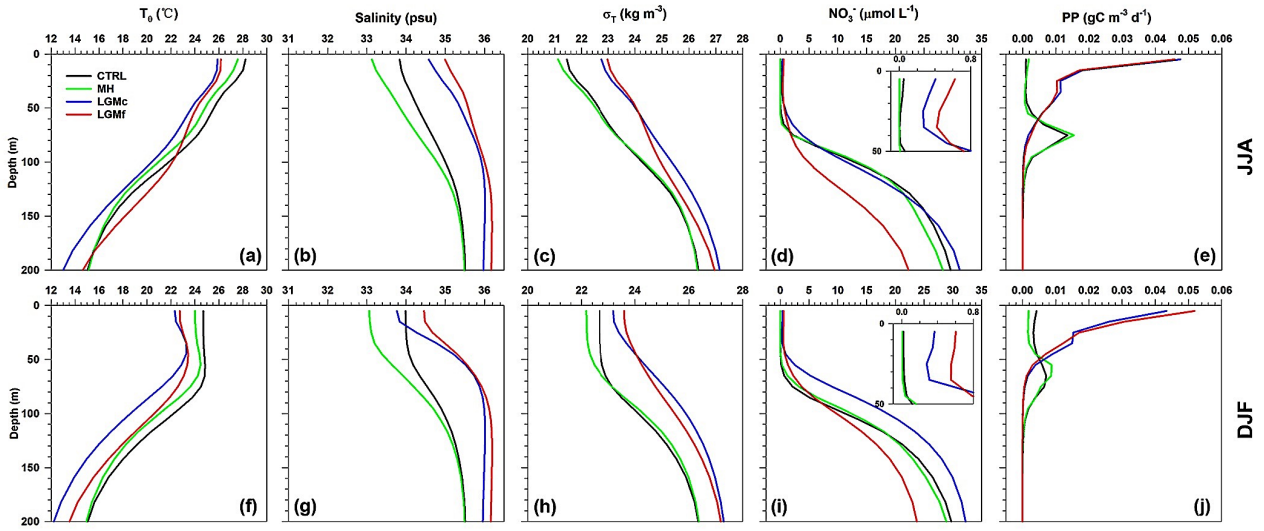

Figure 5. Simulated ocean profiles between 0 and 200 m of water depth in four experiments run with IPSL-CM5A-LR. **(a–e)** Results for summer (June–July–August, JJA). **(f–j)** Results for winter (December–January–February, DJF). Data have been extracted from the grids located in the northeastern part of the BoB closed to the MD77-176 core site (rectangle 3 in Fig. 3e). The parameters shown here are potential temperature (T_θ), salinity, potential density (sigma-t, σ_T), nitrate concentration of seawater representing seawater nutrient content (NO_3^-), and total primary productivity (PP). The nutricline, halocline, and pycnocline are the depths with the largest vertical gradients of nutrient content, potential density, and salinity under the upper seawater layers.

monsoon precipitation, and vice versa. The relationship between South Asian rainfall and the AMOC during the last deglaciation has been studied by Marzin et al. (2013) based on several water hosing experiments run with the IPSL-CM4 model. They found a strong positive correlation between the AMOC strength and South Asian summer precipitation rates and pointed out that temperature anomalies over the tropical Atlantic Ocean are key elements in modulating the teleconnection mechanisms between the AMOC and South Asian rainfall. It has been proposed that a southward shift of the ITCZ was triggered by low tropical Atlantic Ocean temperatures and weakened AMOC during HS1 and possibly the YD (Stocker and Johnsen, 2003; Gupta et al., 2003; Goswami et al., 2006; Li et al., 2008; Pausata et al., 2011; McGee et al., 2014; Schneider et al., 2014). Such variations of moisture are simulated here in the IPSL-CM5A housing simulation (LGMf), which shows weaker summer winds and drier climate over the AS and South Asia when the AMOC is weakened compared to the LGMc simulation (Fig. 7k, n). They are also observed in the TraCE simulation over the deglaciation, with millennial-scale variations of net precipitation being mainly forced by changes in AMOC strength and the colder periods (HS1 and YD) being associated with weaker precipitation (Figs. 6d, S4). More importantly, the reconstructed records and TraCE results together show that weaker net precipitation intervals correspond to higher SSS ones, which indicates that South Asian net precipitation controls the salinity budget in the BoB and Andaman Sea (Figs. 6d, h). Since SSS and PP variations at the MD77-176 site are highly correlated with the upper seawater density gradient (stratification) while SST remains relatively stable (Fig. 6f, h, i), it seems reasonable to propose that during the last deglaciation, PP variations are directly driven by precipitation dynamics through changes in upper water column stratification associated with SSS variations (the so-called "barrier layer" effect). An important finding is that millennial-scale variations of MD77-176 PP are anti-phased with those in the western and northern AS (Fig. 6j, k), which are indicators of local summer wind strength. We interpret these anti-phased PP patterns as reflecting the fact that weaker summer winds (i.e. reduced PP) over the AS, by bringing less moisture to South Asia, result in subdued freshwater inputs within the NE BoB that weaken stratification and increase PP. In contrast, stronger summer winds (i.e. higher PP) over the AS reinforce precipitation over South Asia, enhance freshwater inputs within the NE BoB, and ultimately decrease PP through enhanced stratification.

The relationships between the ITCZ, southwesterly winds over the AS, South Asian rainfall, SSS, and stratification over the northern BoB and Andaman Sea are confirmed by IPSL-CM5A. Compared to LGMc, LGMf clearly shows higher SSS and weaker stratification, especially in the northeastern BoB, under weakened AMOC conditions (Fig. 7k–o). The areas with higher PP in the northeastern BoB that correspond to the LGMc river mouth grids match those with the largest increase in SSS (Figs. 3j and 7m), indicating that salinity stratification controls PP, even under an unchanged amount of nutrient inputs from rivers (Sect. 3.3.1). The relationship

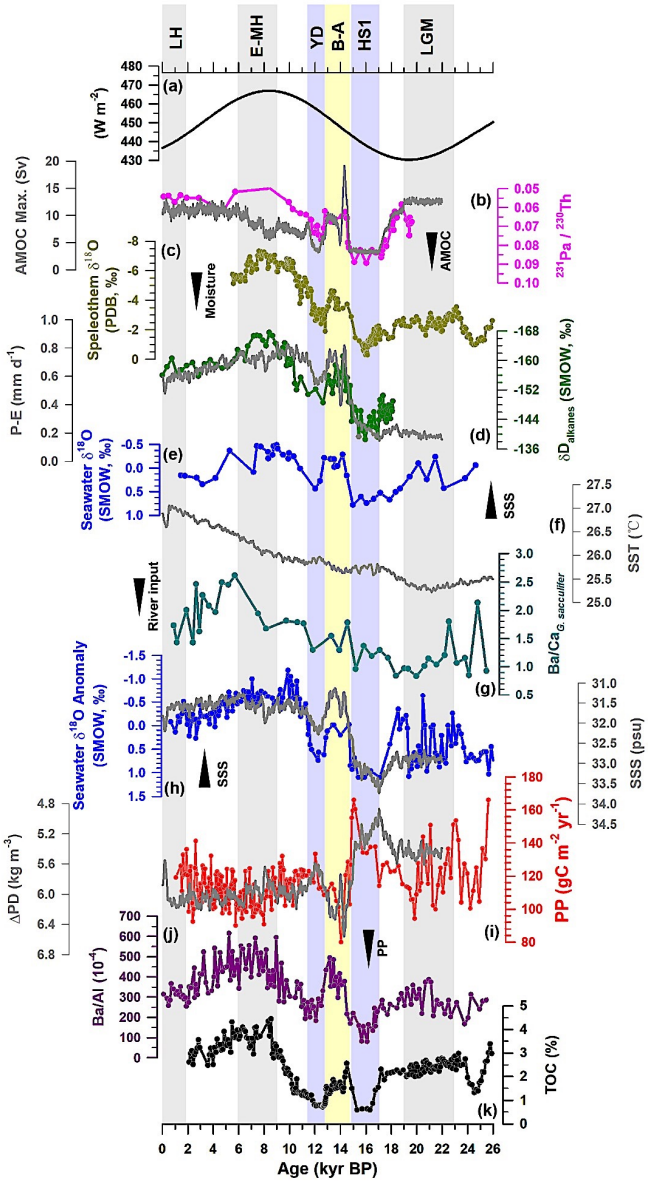

Figure 6. **(a)** 30° N August insolation (Laskar et al., 2004). **(b)** AMOC strength indicated by the $^{231}Pa/^{230}Th$ ratio of marine sediment from the western subtropical Atlantic Ocean (in pink, McManus et al., 2004). The changes in the maximum AMOC stream function below 500 m (AMOC strength) in TraCE-21 (in grey). **(c)** Mawmluh Cave speleothem $\delta^{18}O$ signal (Dutt et al., 2015). **(d)** Alkane δD signal in marine core SO188-342 (in green, Contreras-Rosales et al., 2014) and simulated annual mean precipitation minus evaporation of TraCE-21 (in grey). **(e)** Seawater $\delta^{18}O$ record of core RC12-344 (Rashid et al., 2007). **(f)** Simulated annual mean SST in the NE BoB. **(g)** Ba/Ca ratio derived from the mixed layer foraminifer species *Globigerinoides sacculifer* from core SK 168/GC-1 (Gebregiogis et al., 2016). **(h)** Seawater $\delta^{18}O$ anomaly record of core MD77-176 (Marzin et al., 2013). **(i)** Estimated PP record of core MD77-176 (this study, in red) and simulated annual mean potential density gradient between 200 and 5 m for TraCE-21 (in grey), which reflects the stratification of the upper seawater (Behrenfeld et al., 2006). **(j)** Ba/Al ratio of sediment core 905 (Ivanochko et al., 2005). **(k)** Total organic carbon weight percentage of core SO90-136KL (Schulz et al., 1998). TraCE curves are shown using 100-year averaged results. The results of single forcing experiments are shown in Fig. S4. Core locations of all these records above are marked in Fig. 1a. Grids of extracted TraCE data are shown in Fig. S5. High-resolution reconstructed and Trace21 data provide coherent climate patterns for the following: (i) 26–19 ka when higher PP is associated with lower SSS, lower moister conditions, and vice versa, highlighting the control that the river mouth system exerts on PP; (ii) 19–11 ka when higher PP, in phase with AMOC strength, is associated with higher SSS and reduced precipitation, highlighting the impact of high-latitude climate on South Asian precipitation, salinity-related stratification, and PP; and (iii) 11–1 ka when higher PP, in phase with August insolation, is associated with higher SSS and reduced precipitation, highlighting the impact of insolation on South Asian precipitation on salinity-related stratification and PP during the Holocene, more particularly during the Early Holocene Climatic Optimum (∼ 8–6 ka).

https://doi.org/10.5194/cp-16-1969-2020 Clim. Past, 16, 1969–1986, 2020

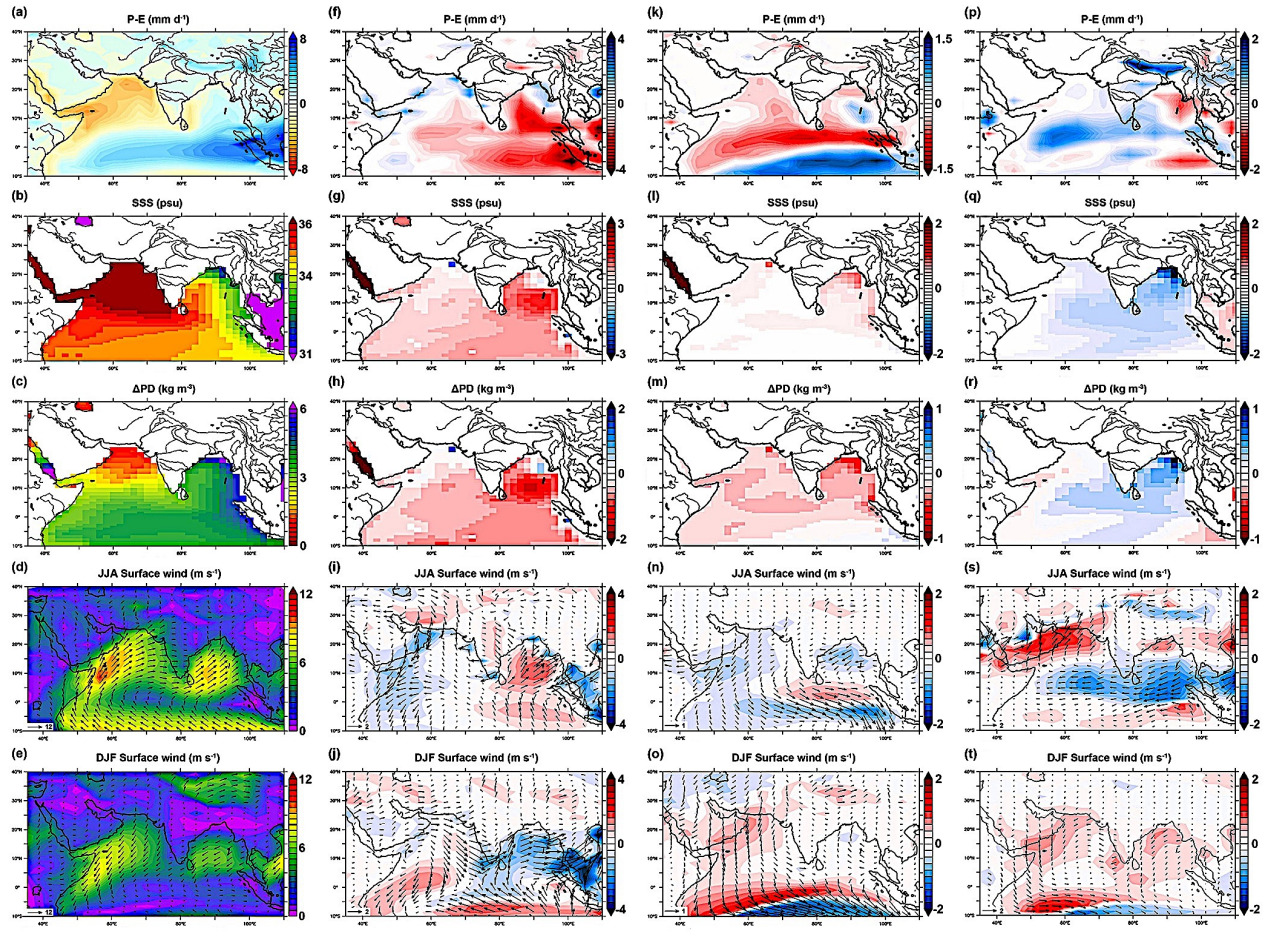

Figure 7. IPSL-CM5A-LR outputs. **(a–e)** Results of CTRL. **(f–j)** Differences between LGMc and CTRL. **(k–o)** Differences between LGMf and LGMc. **(p–t)** Differences between MH and CTRL. The parameters are annual mean precipitation minus evaporation ($P - E$, net precipitation), sea surface salinity (SSS), potential density gradient between 200 and 5 m (stratification of the upper seawater; Behrenfeld et al., 2006), and summer (June–July–August, JJA) and winter (December–January–February, DJF) surface wind speed and vectors. These figures give the results of simulated changes in climate and oceanic conditions over South Asia and the northern Indian Ocean. Stronger net precipitation is marked by blue, higher SSS is marked by red, stronger stratification is marked by blue, and stronger surface wind is marked by red.

that exists between the salinity stratification and PP of these grids is shown in Fig. 8. It clearly shows a positive correlation between PP and nitrate contents and between nitrate contents in the upper photic zone (0–50 water depth) and SSS. In such a context, PP is therefore inversely correlated with the stratification, with high PP being associated with high nutrients, high SSS, and a reduced vertical density gradient. Moreover, the annual simulated PP increase is mainly associated with PP increase during winter (Fig. 3l), which mirrors the winter peak of PP observed in modern times (Fig. 1m).

Although LGMf is not set under the complete conditions of HS1 or YD (higher atmospheric pCO_2 and sea level compared to the LGM), it helps decipher the control that salinity stratification exerts on PP in the northeastern BoB under weakened AMOC conditions and lower South Asian rainfall. Together with the robust relationships that exist between reconstructed PP, SSS, South Asia rainfall, and AS southwesterly winds, we can conclude that as the sea level rises during the last deglaciation, the location of MD77-176 is less influenced by nutrient inputs from the IS river mouth system than during the last glacial period and that the barrier layer effect dominates. Therefore, PP variability is highly controlled by the changes in salinity stratification that are linked to the changes in AMOC strength and monsoon precipitation.

5.3 The Holocene

During the Holocene (11–1 ka), long-term decreasing trends in reconstructed PP match long-term decreasing trends in SSS, increasing trends in South Asian precipitation, and in-

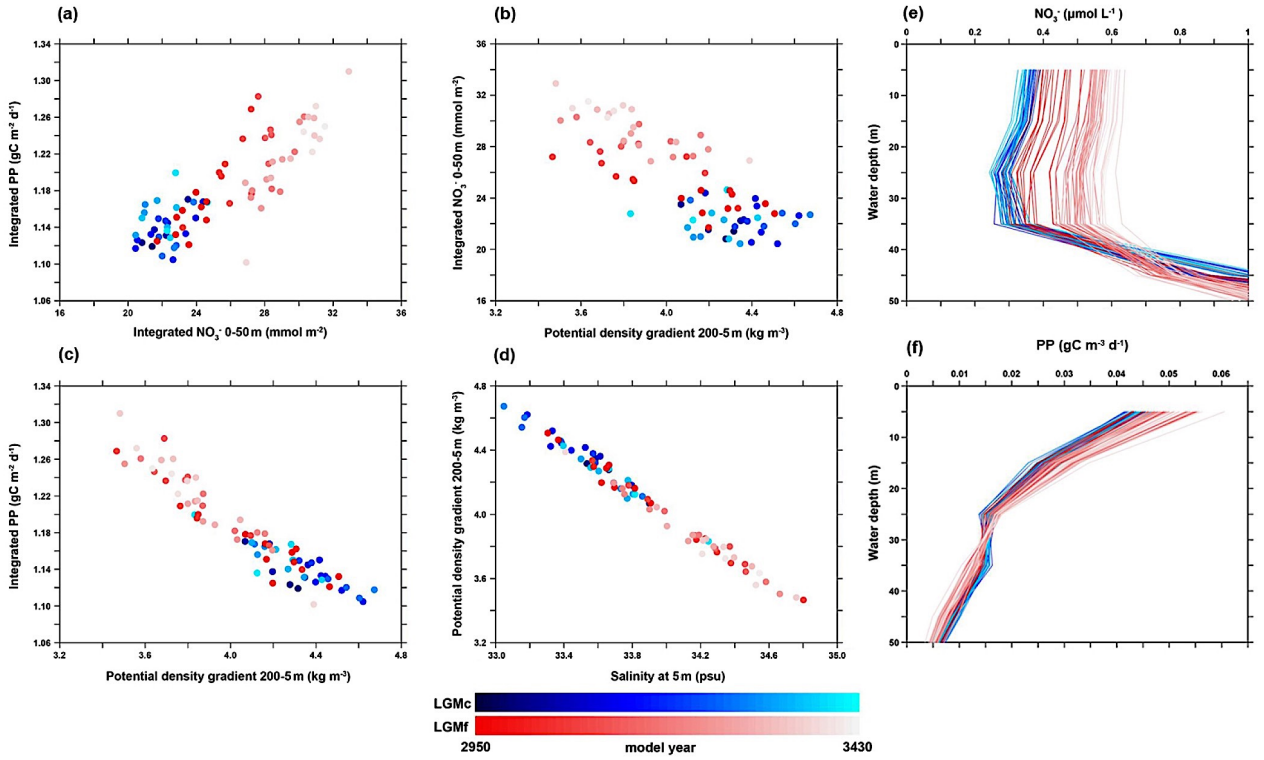

Figure 8. IPSL-CM5A-LR outputs. **(a–d)** Cross plots between different oceanic parameters in LGMc and LGMf. **(e, f)** Vertical profiles of nitrate content and PP in LGMc and LGMf. All the results are from winter (December–January–February) and every curve represents an average of 10 model years. Data have been extracted from the grids located in the northeastern part of the BoB close to the MD77-176 core site (rectangle 3 in Fig. 3e). They highlight the control that salinity stratification exerts on upper layer nutrient content and integrated PP: higher PP is found when higher SSS drives weaker stratification.

creasing trends in AS PP, while simulated SST shows a gradual increase of ∼ 1 °C across the area (Fig. 6). Therefore, the relationships between these parameters are similar to those we observed over the last deglaciation. The most obvious pattern is found during the early–middle Holocene (8–6 ka) when PP and SSS minima correspond to South Asian precipitation and AS PP maxima. This time interval, also called the Early Holocene Climatic Optimum (EHCO; e.g. Ciais et al., 1992; Contreras-Rosales et al., 2014), is characterized by higher Northern Hemisphere (NH) summer insolation compared to present, as highlighted by a maximum in the 30° N August mean insolation (Fig. 6a) and the peak of the insolation difference between 6 ka and the present day over low- and mid-latitude areas (Marzin and Braconnot, 2009). Under enhanced boreal summer insolation, the MH simulation reveals stronger southwesterly summer winds over the AS and enhanced net precipitation over South Asia (Fig. 7p, s), thanks to the northward shift of the ITCZ system (Bassinot et al., 2011; McGee et al., 2014; Schneider et al., 2014). Lower SSS and a higher density gradient (stronger stratification) are concomitantly documented over the entire BoB, but they are particularly obvious in the northern BoB (Fig. 7q, r), which is directly influenced by the freshwater budget and input from the GBM river system (Behara and Vinayachandran, 2016). All these elements suggest that during the Holocene PP changes in the northeastern BoB were most probably driven by salinity stratification associated with the changes in precipitation. This is confirmed by the comparison between the MH and CTRL profiles of the GMB river mouth system, which highlights lower nutrient contents and PP in the upper seawater associated with reduced SSS and an increased density gradient between 0 and 30 m water depths (Sect. 4.2, Fig. 4).

6 Conclusion

We document, for the first time, a 26 kyr PP record for the northeastern BoB using an empirical equation relating Fp% to PP. Comparisons of this PP signal with previous geochemical data and new model outputs helped us propose two coherent scenarios behind PP distribution during the 26–19 and 19–1 ka intervals. In all cases, PP is related to nutrient content and distribution at the sea surface. From 26 to 19 ka, when drier and lower sea level conditions prevailed,

millennial-scale PP changes are most probably related to nutrient discharge from the Irrawaddy–Salween river mouth system, which is paced by South Asian monsoon precipitation changes. Over the last 19 kyr, while sea level rise and more humid conditions prevailed, millennial-scale PP variations over the deglaciation and long-term trends over the Holocene are rather controlled by salinity-related stratification that monitors nutrient distribution within the photic zone and is therefore less influenced by nutrient inputs from the IS river mouth system. We demonstrate more generally that stratification dynamics during that period are driven by Indian monsoon precipitation changes, which generate changes in freshwater supply to the ocean. The analysis of climate model outputs provides additional evidence for the salinity stratification hypothesis and helps demonstrate that paleoceanographic changes are forced by AMOC dynamics during the last deglaciation and insolation during the Holocene.

Data availability. Coccolith data from core MD77-176 can be found in the Supplement.

Supplement. The supplement related to this article is available online at: https://doi.org/10.5194/cp-16-1969-2020-supplement.

Author contributions. XZ, SDA, MK, and CC developed the idea. CC and FB provided sediment samples. XZ did coccolith analysis and visualization of the climate modelling results. The datasets of climate model IPSL-CM5A-LR were provided by MK. FB and LB joined the discussion and gave additional ideas for the paper. All authors contributed to the paper writing.

Competing interests. The authors declare that they have no conflict of interest.

Acknowledgements. The authors are grateful to the two anonymous reviewers for their helpful comments and suggestions. Xinquan Zhou thanks the China Scholarship Council (CSC) for providing a scholarship and the Laboratoire des Sciences du Climat et de l'Environnement (LSCE) for admitting his study related to the climate model. He also thanks Hongrui Zhang for personal communication. The simulations presented in this work have been run on the TGCC (Très Grand Centre de Calcul du CEA) supercomputing equipment under the gen2212 project, provided by GENCI (Grand Equipement National de Calcul Intensif). The authors wish to thank all of the people who developed to IPSLCM5A model, which was used for this study, and who ran the model for the CMIP5 and PMIP3.

Review statement. This paper was edited by Qiuzhen Yin and reviewed by two anonymous referees.

References

Akhil, V. P., Durand, F., Lengaigne, M., Vialard, J., Keerthi, M. G., Gopalakrishna, V. V., Deltel, C., Papa, F., and de Boyer Montegut, C.: A modeling study of the processes of surface salinity seasonal cycle in the Bay of Bengal, J. Geophys. Res.-Oceans, 119, 3926–3947, 2014.

Anderson, D. M. and Prell, W. L.: The structure of the southwest monsoon winds over the Arabian Sea during the late Quaternary: observation, simulations, and marine geologic evidence, J. Geophys. Res., 97, 15481–15487, 1992.

Ashok, K., Guan, Z., Saji, N. H., and Yamagata, T.: Individual and combined inflences of ENSO and the Indian Ocean Dipole on the Indian Summer Monsoon, J. Climate, 17, 3141–3155, 2004.

Aumont, O. and Bopp, L.: Globalizing results from ocean in situ iron fertilization studies, Global Biogeochem. Cy., 20, GB2017, https://doi.org/10.1029/2005GB002591, 2006.

Barber, D. C., Dyke, A., Hillaire-Marcel, C., Jennings, A. E., Andrews, J. T., Kerwin, M. W., Bilodeau, G., McNeely, R., Southon, J., Morehead, M. D., and Gagnon, J.-M.: Forcing of the cold event of 8200 years ago by catastrophic drainage of Laurentide lakes, Nature, 400, 344–348, 1999.

Bassinot, F. C., Marzin, C., Braconnot, P., Marti, O., Mathien-Blard, E., Lombard, F., and Bopp, L.: Holocene evolution of summer winds and marine productivity in the tropical Indian Ocean in response to insolation forcing: data-model comparison, Clim. Past, 7, 815–829, https://doi.org/10.5194/cp-7-815-2011, 2011.

Beaufort, L., Lancelot, Y., Camberlin, P., Cayre, O., Vincent, E., Bassinot, F., and Labeyrie, L.: Insolation cycles as a major control of Equatorial Indian Ocean primary production, Science, 278, 1451–1454, 1997.

Beaufort, L., Barbarin, N., and Gally, Y.: Optical measurements to determine the thickness of calcite crystals and the mass of thin carbon particles such as coccoliths, Nat. Protoc., 9, 633–642, 2014.

Behara, A. and Vinayachandran, P. N.: An OGCM study of the impact of rain and river water forcing on the Bay of Bengal, J. Geophys. Res.-Oceans, 121, 2425–2446, 2016.

Behrenfeld, M. J. and Falkowski, P. G.: Photosynthetic rates derived from satellite-based chlorophyll concentration, Limnol. Oceanogr., 42, 1–20, 1997.

Behrenfeld, M. J., O'Malley, R. T., Siegel, D. A., McClain, C. R., Sarmiento, J. L., Feldman, G. C., Milligan, A. J., Falkowski, P. G., Letelier, R. M., and Boss, E. S.: Climate-driven trends in contemporary ocean productivity, Nature, 444, 752–755, 2006.

Belyaeva, N. V. and Burmistrova, I. I.: Critical carbonate levels in the Indian Ocean, J. Foramin. Res., 15, 337–341, 1985.

Braconnot, P., Otto-Bliesner, B., Harrison, S., Joussaume, S., Peterchmitt, J.-Y., Abe-Ouchi, A., Crucifix, M., Driesschaert, E., Fichefet, Th., Hewitt, C. D., Kageyama, M., Kitoh, A., Laîné, A., Loutre, M.-F., Marti, O., Merkel, U., Ramstein, G., Valdes, P., Weber, S. L., Yu, Y., and Zhao, Y.: Results of PMIP2 coupled simulations of the Mid-Holocene and Last Glacial Maximum – Part 1: experiments and large-scale features, Clim. Past, 3, 261–277, https://doi.org/10.5194/cp-3-261-2007, 2007a.

Braconnot, P., Otto-Bliesner, B., Harrison, S., Joussaume, S., Peterchmitt, J.-Y., Abe-Ouchi, A., Crucifix, M., Driesschaert, E., Fichefet, Th., Hewitt, C. D., Kageyama, M., Kitoh, A., Loutre, M.-F., Marti, O., Merkel, U., Ramstein, G., Valdes, P., We-

ber, L., Yu, Y., and Zhao, Y.: Results of PMIP2 coupled simulations of the Mid-Holocene and Last Glacial Maximum – Part 2: feedbacks with emphasis on the location of the ITCZ and mid- and high latitudes heat budget, Clim. Past, 3, 279–296, https://doi.org/10.5194/cp-3-279-2007, 2007b.

Braconnot, P., Harrison, S. P., Kageyama, M., Bartlein, P. J., Masson-Delmotte, V., Abe-Ouchi, A., Otto-Bliesner, B., and Zhao, Y.: Evaluation of climate models using palaeoclimatic data, Nat. Clim. Change, 2, 417–424, 2012.

Briegleb, B. P., Bitz, C. M., Hunke, E. C., Lipscomb, W. H., Holland, M., Schramm, J. L., and Moritz, R. E.: Scientific description of the sea ice component in the Community Climate System Model, Version 3, University Corporation for Atmospheric Research, Boulder, Colorado, USA, 2004.

Buckley, M. W. and Marshall, J.: Observations, inferences, and mechanisms of the Atlantic Meridional Overturning Circulation: A review, Rev. Geophys., 54, 5–63, 2016.

Cai, Y., Zhang, H., Cheng, H., An, Z., Edwards, R. L., Wang, X., Tan, L., Liang, F., Wang, J., and Kelly, M.: The Holocene Indian Monsoon variablility over the southern Tibetan Plateau and its teleconnections, Earth Planet. Sc. Lett., 335–336, 135–144, 2012.

Chen, T.-C.: Maintenance of summer monsoon circulations: a planetary-scale perspective, J. Climate, 16, 2022–2037, 2003.

Chiba, S., Ono, T., Tadokoro, K., Midorikawa, T., and Saino, T.: Increased stratification and decreased lower trophic level productivity in the Oyashio Region of the North Pacific: A 30-year retrospective study, J. Oceanogr., 60, 149–162, 2004.

Ciais, P., Petit., J. R., Jouzel, J., Lorius, C., Barkov, N. I., Lipenkov. V., and Nicolaiev, V.: Evidence for an early Holocene climatic optimum in the Antarctic deep ice-core record, Clim. Dynam., 6, 169–177, 1992.

Clark, P. U., Shakun, J. D., Baker, P. A., Bartlein, P. J., Brewer, S., Brook, E., Carlson, A. E., Cheng, H., Kaufman, D. S., Liu, Z., Marchitto, T. M., Mix, A. C., Morrill, C., Otto-Bliesner, B. L., Pahnke, K., Russell, J. M., Whitlock, C., Adkins, J. F., Blois, J. L., Clark, J., Colman, S. M., Curry, W. B., Flower, B. P., He, F., Johnson, T. C., Lynch-Stieglitz, J., Markgraf, V., McManus, J., Mitrovica, J. X., Moreno, P. I., and Williams, J. W.: Global climate evolution during the last deglaciation, P. Natl. Acad. Sci. USA, 109, E1134–E1142, 2012.

Clement, A. C. and Peterson, L. C.: Mechanisms of abrupt climate change of the last glacial period, Rev. Geophys., 46, RG4002, https://doi.org/10.1029/2006RG000204, 2008.

Collins, W. D., Bitz, C. M., Blackmon, M. L., Bonan, G. B., Bretheton, C. S., Carton, J. A., Chang, P., Doney, S. C., Hack, J. J., Henderson, T. B., Kiehl, J. T., Large, W. G., McKenna, D. S., Santer, B. D., and Smith, R. D.: The Community Climate System Model Version 3 (CCSM3), J. Climate, 19, 2122–2143, 2006a.

Collins, W. D., Rasch, P. J., Boville, B. A., Hack, J. J., McCaa, J. R., Williamson, D. L., Briegleb, B. P., Bitz, C. M., Lin, S.-J., and Zhang, M.: The formulation and atmospheric simulation of the Community Atmosphere Model Version 3 (CAM3), J. Climate, 19, 2144–2161, 2006b.

Contreras-Rosales, L. A., Jennerjahn, T., Tharammal, T., Meyer, V., Lückge, A., Paul, A., and Schefuß, E.: Evolution of the Indian Summer Monsoon and terrestrial vegetation in the Bay of Bengal region during the past 18 ka, Quaternary Sci. Rev., 102, 133–148, 2014.

Cullen, J. L. and Prell, W. L.: Planktonic foraminifera of the northern Indian Ocean: Distribution and preservation in surface sediments, Mar. Micropaleontol., 9, 1–52, 1984.

Currie, J. C., Lengaigne, M., Vialard, J., Kaplan, D. M., Aumont, O., Naqvi, S. W. A., and Maury, O.: Indian Ocean Dipole and El Niño/Southern Oscillation impacts on regional chlorophyll anomalies in the Indian Ocean, Biogeosciences, 10, 6677–6698, https://doi.org/10.5194/bg-10-6677-2013, 2013.

Da Silva, R., Mazumdar, A., Mapder, T., Peketi, A., Joshi, R. K., Shaji, A., Mahalashmi, P., Sawant, B., Naik, B. G., Carvalho, M. A., and Molletti, S. K.: Salinity stratification controlled productivity variation over 300 ky in the Bay of Bengal, Sci. Rep., 7, 14439, https://doi.org/10.1038/s41598-017-14781-3, 2017.

Dey, S. and Singh, R. P.: Comparison of chlorophyll distributions in the northeastern Arabian Sea and southern Bay of Bengal using IRS-P4 Ocean Color Monitor data, Remote Sens. Environ., 85, 424–428, 2003.

Dickinson, R. E., Oleson, K. W., Bonan, G., Hoffman, F., Thirnton, P., Vertenstein, M., Yang, Z.-L., and Zeng, X.: The Community Land Model and its climate statistics as a component of the Community Climate System Model, J. Climate, 19, 2302–2324, 2006.

Duchamp-Alphonse, S., Siani, G, Michel, E., Beaufort, L, Gally, Y., and Jaccard, S. L.: Enhanced ocean-atmosphere carbon partitioning via the carbonate counter pump during the last deglacial, Nat. Commun., 9, 2396, https://doi.org/10.1038/s41467-018-04625-7, 2018.

Dufresne, J.-L., Foujols, M.-A., Denvil, S., Caubel, A., Marti, O., Aumont, O., Balkanski, Y., Bekki, S., Bellenger, H., Benshila, R., Bony, S., Bopp, L., Braconnot, P., Brockmann, P., Cadule, P., Cheruy, F., Codron, F., Cozic, A., Cugnet, D., de Noblet, N., Duvel, J.-P., Ethé, C., Fairhead, L., Fichefet, T., Flavoni, S., Friedlingstein, P., Grandpeix, J.-Y., Guez, L., Guilyardi, E., Hauglustaine, D. A., Hourdin, F., Idelkadi, A., Ghattas, J., Joussaume, S., Kageyama, M., Krinner, G., Labetoulle, S., Lahellec, A., Lefebvre, M.-P., Lefevre, F., Levy, C., Li, Z. X., Lloyd, J., Lott, F., Madec, G., Mancip, M., Marchand, M., Masson, S., Meurdesoif, Y., Mignot, J., Musat, I., Parouty, S., Polcher, J., Rio, C., Schulz, M., Swingedouw, D., Szopa, S., Talandier, C., Terray, P., Viovy, N., and Vuichard, N.: Climate change projections using the IPSL-CM5 Earth System Model: from CMIP3 to CMIP5, Clim. Dynam., 40, 2123–2165, 2013.

Dutt, S., Gupta, A. K., Clemens, S. C., Cheng, H., Singh, R. K., Kathayat, G., and Edwards, R. L.: Abrupt changes in Indian summer monsoon strength during 33 800 to 5500 years B.P., Geophys. Res. Lett., 42, 5526–5532, 2015.

Elliot, M., Labeyrie, L., and Duplessy, J.-C.: Changes in North Atlantic deep-water formation associated with the Dansgaard-Oeschger temperature oscillations (60–10 ka), Quaternary Sci. Rev., 21, 1153–1165, 2002.

Fichefet, T. and Maqueda, M. A. M.: Sensitivity of a global sea ice model to the treatment of ice thermodynamics and dynamics, J. Geophys. Res.-Oceans, 102, 12609–12646, 1997.

Fleitmann, D., Burns, S. J., Mudelsee, M., Neff, U., Kramers, J., Mangini, A., and Matter, A.: Holocene forcing of the Indian Monsoon recored in a stalagmite from southern Oman, Science, 300, 1737–1739, 2003.

Fournier, S., Vialard, F., Lengaigne, M., Lee, T., Gierach, M. M., and Chaitanya, A. V. S.: Modulation of the Ganges-Brahmaputra River Plume by the Indian Ocean Dipole and Eddies inferred

from satellite observations, J. Geophys. Res.-Oceans, 122, 9591–9604, 2017.

Gadgil, S.: The Indian Monsoon and its variability, Annu. Rev. Earth Pl. Sc., 31, 429–467, 2003.

Gardner, W. D., Gundersen, J. S., Richardson, M. J., and Walsh, I. D.: The role of seasonal and diel changes in mixed-layer depth on carbon and chlorophyll distributions in the Arabian Sea, Deep-Sea Res. Pt. II, 46, 1833–1858, 1999.

Gauns, M., Madhupratap, M., Ramaiah, N., Jyothibabu, R., Fernandes, V., Paul, J. T., and Prasanna Kumar, S.: Comparative accounts of biological productivity characteristics and estimates of carbon fluxes in the Arabian Sea and the Bay of Bengal, Deep-Sea Res. Pt. II, 52, 2003–2017, 2005.

Gebregiorgis, D., Hathorne, E. C., Sijinkumar, A. V., Nagender Nath, B., Nürnberg, D., and Frank, M.: South Asian summer monsoon variability during the last ∼ 54 kyrs inferred from surface salinity and river runoff proxies, Quaternary Sci. Rev., 138, 6–15, 2016.

Goswami, B. N., Madhusoodanan, M. S., Neema, C. P., and Sengupta, D.: A physical mechanism for North Atlantic SST influence on the Indian summer monsoon, Geophys. Res. Lett., 33, L02706, https://doi.org/10.1029/2005GL024803, 2006.

Gupta, A. K., Andrews, D. M., and Overpeck, J. T.: Abrupt changes in the Asian southwest monsoon during the Holocene and their links to the North Atlantic Ocean, Nature, 421, 354–357, 2003.

He, F.: Simulating transient climate evolution of the last deglaciation with CCSM3, PhD dissertation, University of Wisconsin-Madison, Madison, Wisconsin, USA, 2008.

Heinrich, H.: Origin and consequences of cyclic ice rafting in the northeast Atlantic Ocean during the past 130 000 years, Quaternary Res., 29, 142–152, 1988.

Hernández-Almeida, I., Ausín, B., Saavedra-Pellitero, M., Baumann, K.-H., and Stoll, H. M.: Quantitative reconstruction of primary productivity in low latitudes during the last glacial maximum and the mid-to-late Holocene from a global *Florisphaera profunda* calibration dataset, Quaternary Sci. Rev., 205, 166–181, 2019.

Hourdin, F., Foujols, M.-A., Codron, F., Guemas, V., Dufresne, J.-L., Bony, S., Denvil, S., Guez, L., Lott, F., Ghattas, J., Braconnot, P., Marti, O., Meurdesoif, Y., and Bopp, L.: Impact of the LMDZ atmospheric grid configuration on the climate and sensitivity of the IPSL-CM5A coupled model, Clim. Dynam., 40, 2167–2192, https://doi.org/10.1007/s00382-012-1411-3, 2013.

Ivanochko, T. S., Ganeshram, R. S., Brummer, G. A., Ganssen, G., Jung, S. J. A., Moreton, S. G., and Kroon, D.: Variations in tropical convection as an amplifier of global climate change at the millennial scale, Earth Planet. Sc. Lett., 235, 302–314, 2005.

Ivanova, E., Schiebel, R., Singh, A. D., Schmiedl, G., Niebler, H.-S., and Hemleben, C.: Primary production in the Arabian Sea during the last 135 000 years, Palaeogeogr. Paleocl., 197, 61–82, 2003.

Jourdain, N. C., Gupta, A. S., Taschetto, A. S., Ummenhofer, C. C., Moise, A. F., and Ashok, K.: The Indo-Australian monsoon and its relationship to ENSO and IOD in reanalysis data and the CMIP3/CMIP5 simulations, Clim. Dynam., 41, 3073–3102, 2013.

Kageyama, M., Merkel, U., Otto-Bliesner, B., Prange, M., Abe-Ouchi, A., Lohmann, G., Ohgaito, R., Roche, D. M., Singarayer, J., Swingedouw, D., and X Zhang: Climatic impacts of fresh water hosing under Last Glacial Maximum conditions: a multi-model study, Clim. Past, 9, 935–953, https://doi.org/10.5194/cp-9-935-2013, 2013.

Krinner, G., Viovy, N., de Noblet-Ducoudré, N., Ogée, J., Polcher, J., Friedlingstein, P., Ciais, P., Sitch, S., and Prentice, I. C.: A dynamic global vegetation model for studies of the coupled atmosphere-biosphere system, Global Biogeochem. Cy., 19, GB1015, https://doi.org/10.1029/2003GB002199, 2005.

Laskar, J., Robutel, P., Joutel, F., Gastineau, M., Correia, A. C. M., and Levrard, B.: A long-term numerical solution for the insolation quantities of the Earth, Astronomy and Astrophysics, 428, 261–285, 2004.

Lau, K.-M., Kim, K.-M., and Yang, S.: Dynamicsal and boundary forcing characteristics of regional components of the Asian Summer Monsoon, J. Climate, 13, 2461–2482, 2000.

Le Mézo, P., Beaufort, L., Bopp, L., Braconnot, P., and Kageyama, M.: From monsoon to marine productivity in the Arabian Sea: insights from glacial and interglacial climates, Clim. Past, 13, 759–778, https://doi.org/10.5194/cp-13-759-2017, 2017.

Lévy, M., Klein, P., and Treguier, A.-M.: Impact of sub-mesoscale physics on production and subduction of phytoplankton in an oligotrophic regime, J. Mar. Res., 59, 535–565, 2001.

Li, S., Perlwitz, J., Quan, X., and Hoerling, M. P.: Modelling the influence of North Atlantic multidecadal warmth on the Indian summer rainfall, Geophys. Res. Lett., 35, L05804, https://doi.org/10.1029/2007GL032901, 2008.

Li, J., Liu, S., Shi, X., Zhang, H., Fang, X., Cao, P., Yang, G., Xue, X., Khokiattiwong, S., and Kornkanitnan, N.: Sedimentary responses to the sea level and Indian summer monsoon changes in the central Bay of Bengal since 40 ka, Mar. Geol., 415, 105947, https://doi.org/10.1016/j.margeo.2019.05.006, 2019.

Liu, Z., Otto-Bliesner, B. L., He, F., Brady, W. C., Tomas, R., Clark, P. U., Carlson, A. E., Lynch-Stieglitz, J., Curry, W., Brook, E., Erickson, D., Jacob, R., Kutzbach, J., and Cheng, J.: Transient Simulation of Last Deglaciaiton with a new mechanism for Bølling-Allerød Warming, Science, 325, 310–314, 2009.

Locarnini, R. A., Mishonov, A. V., Antonov, J. I., Boyer, T. P., Garcia, H. E., Baranova, O. K., Zweng, M. M., ans Johnson, D. R.: World ocean atlas 2009, in: Temperature, edited by: Levitus, S., NOAA Atlas NESDIS 68, 1. Government Printing Office, Washington, D.C., USA, p. 184, 2010.

Ludwig, W., Probst, J.-L., and Kempe, S.: Predicting the oceanic input of organic carbon by continental erosion, Global Biogeochem. Cy., 10, 23–41, 1996.

Madec, G.: NEMO ocean engine, Note du pôle de modélisation, Institut Pierre-Simon Laplace (IPSL), Paris, France, No. 27, ISSN 1288-1619, 2008.

Madhupratap, M., Prasanna Kumar, S., Bhattathiri, P. M. A., Dileep Kumar, M., Raghukumar, S., Nair, K. K. C., and Ramaiah, N.: Mechanism of the biological response to winter cooling in the northeastern Arabian Sea, Nature, 384, 549–552, 1996.

Madhupratap, M., Gauns, M., Ramaiah, N., Prasanna Kumar, S., Muraleedharan, P. M., Sousa, S. N., and Muraleedharan, U.: Biogeochemistry of the Bay of Bengal: physical, chemical and primary productivity characteristics of the central and western Bay of Bengal during summer monsoon 2001, Deep-Sea Res. Pt. II, 50, 881–896, 2003.

Marzin, C. and Braconnot, P.: Variations of Indian and African monsoons induced by insolation changes a 6 and 9.5 kyr BP, Clim. Dynam., 33, 215–231, 2009.

Marzin, C., Kallel, N., Kageyama, M., Duplessy, J.-C., and Braconnot, P.: Glacial fluctuations of the Indian monsoon and their relationship with North Atlantic climate: new data and modelling experiments, Clim. Past, 9, 2135–2151, https://doi.org/10.5194/cp-9-2135-2013, 2013.

McCreary, J. P., Murtugudde, R., Vialard, J., Vinayachandran, P. N., Wiggert, J. D., Hood, R. R., Shankar, D., and Shetye, S.: Biophysical processes in the Indian Ocean, Geoph. Monog. Series, 185, 9–32, https://doi.org/10.1029/2008GM000768, 2009.

McGee, D., Donohoe, A., Marshall, J., and Ferreira, D.: Changes in ITCZ location and cross-equatorial heat transport at the Last Glacial Maximum, Heinrich Stadial 1, and the mid-Holocene, Earth Planet. Sc. Lett., 390, 69–79, 2014.

McManus, J. F., Francois, R., Gherardi, J.-M., Keigwin, L. D., and Brown-Leger, S.: Collapse and rapid resumption of Atlantic meridional circulation linked to deglacial climate changes, Nature, 428, 834–837, 2004.

Meehl, G. A.: Couple land-ocean-atmosphere processes and South Asian Monsoon variability, Science, 266, 263–267, 1994.

Meehl, G. A.: The South Asian Monsoon and the Tropospheric Biennial Oscillation, J. Climate, 10, 1921–1943, 1997.

Molfino, B. and McIntyre, A.: Precessional forcing of nutricline dynamics in the Equatorial Atlantic, Science, 249, 766–769, 1990a.

Molfino, B. and McIntyre, A.: Nutricline variation in the Equatorial Atlantic coincident with the Younger Dryas, Paleoceanography, 5, 997–1008, 1990b.

Murton, J. B., Bateman, M. D., Dallimore, S. R., Teller, J. T., and Yang, Z.: Identification of Younger Dryas outburst flood path from Lake Agassiz to the Arctic Ocean, Nature, 464, 740–743, 2010.

Okada, H. and Honjo, S.: The distribution of oceanic coccolithophorids in the Pacific, Deep-Sea Res., 20, 355–364, 1973.

Overpeck, J., Anderson, D., Trumbore, S., and Prell, W.: The southwest Indian Monsoon over the last 18 000 year, Clim. Dynam., 12, 213–225, 1996.

Patterson, R. T. and Fishbein, E.: Re-examination of the statistical methods used to determine the number of point counts needed for micropaleontological quantitative research, J. Paleontol., 63, 245–248, 1984.

Pausata, F. S. R., Battusti, D. S., Nisancioglu, K. H., and Bitz, C. M.: Chinese stalagmite δ^{18}O controlled by changes in the Indian monsoon during a simulated Heinrich event, Nat. Geosci., 4, 474–480, 2011.

Peltier, W. R.: Global glacial isostasy and the surface of the ice-age earth: The ICE-5G (VM2) model and GRACE, Annu. Rev. Earth Pl. Sc., 32, 111–149, 2004.

Peterson, L. C. and Huang, G. H.: Variability in mean latitude of the Atlantic Intertropical Convergence Zone as recorded by riverine input of sediments to the Cariaco Basin (Venezuela), Palaeogeogr. Palaeocl., 234, 97–113, 2006.

Peterson, L. C., Haug, G. H., Hughen, K. A., and Röhl, U.: Rapid changes in the hydrologic cycle of the tropical Atlantic during the last Glacial, Science, 290, 1947–1951, 2000.

Phillips, S. C., Johnson, J. E., Giosan, L., and Rose, K.: Monsson-influenced variation in productivity and lithogenic sediment flux since 110 ka in the offshore Mahanadi Basin, northern Bay of Bengal, Mar. Petrol. Geol., 58, 502–525, 2014.

Prasad, T. G.: A comparison of mixed-layer dynamics between the Arabian Sea and Bay of Bengal: One-dimensional model results, J. Geophys. Res., 109, C03035,https://doi.org/10.1029/2003JC002000, 2004.

Prasanna Kumar, S., Madhupratap, M., Dileep Kumar, M., Muraleedharan, P. M., de Souza, S. N., Gauns, M., and Sarma, V. V. S. S.: High biological productivity in the central Arabian Sea during the summer monsoon driven by Ekman pumping and lateral advection, Curr. Sci. India, 81, 1633–1638, 2001.

Prasanna Kumar, S., Muraleedharan, P. M., Prasad, T. G., Gauns, M., Ramaiah, N., de Souza, S. N., Sardesai, S., and Madhupratap, M.: Why is the Bay of Bengal less productive during summer monsoon compared to the Arabian Sea? Geophys. Res. Lett., 29, 2235, https://doi.org/10.1029/2002GL016013, 2002.

Prasanna Kumar, S., Narvekar, J., Nuncio, M. Ganus, M., and Sardesai, S.: What drives the biological productivity of the Northern Indian Ocean?, Geoph. Monog. Series, 185, 33–56, https://doi.org/10.1029/2008GM000757, 2009.

Randel, W. J. and Park, M.: Deep convective influence on the Asian summer monsoon anticyclone and associated tracer variability observed with Atmospheric Infrared Sounder (AIRS), J. Geophys. Res.-Atmos., 111, D12314, https://doi.org/10.1029/2005JD006490, 2006.

Rao, S. A., Saha, S. K., Pokhrel, S., Sundar, D., Dhakate, A. R., Mahapatra, S., Ali, S., Chaudhari, H. S., Shreeram, P., Vasimalla, S., Srikanth, A. S., and Suresh, R. R. V.: Modulation of SST, SSS over northern Bay of Bengal on ISO time scale, J. Geophys. Res., 116, C09026, https://doi.org/10.1029/2010JC006804, 2011.

Rao, R. R. and Sivakumar, R.: Seasonal variability of sea surface salinity and salt budget of the mixed layer of the north Indian Ocean, J. Geophys. Res., 108, C13009, https://doi.org/10.1029/2001JC000907, 2003.

Rashid, H., Flowe, B. P. Poore, R. Z., and Quinn, T. M.: A $\sim$25 ka Indian Ocean monsoon variability record from the Andaman Sea, Quaternary Sci. Rev., 26, 2586–2597, 2007.

Schott, F.: Monsoon response of the Somali Current and associated upwelling, Prog. Oceanogr., 12, 357–381, 1983.

Schott, F. A. and McCreary, J. P.: The monsoon circulation of the Indian Ocean, Prog. Oceanogr., 51, 1–123, 2001.

Schneider, T., Bischoff, T., and Huang, G. H.: Migrations and dynamics of the intertropical convergence zone, Nature, 513, 45–53, 2014.

Schulz, H., von Rad, U., and Erlenkeuser, H.: Correlation between Arabian Sea and Greenland climate oscillations of the past 110 000 years, Nature, 393, 54–57, 1998.

Sengupta, D., Bharath Raj, G. N., and Shenoi, S. S. C.: Surface freshwater from Bay of Bengal runoff and Indonesian Throughflow in the tropical Indian Ocean, Geophys. Res. Lett., 33, L22609, https://doi.org/10.1029/2006GL027573, 2006.

Shankar, D., Vinayachandran, P. N., and Unnikrishnan, A. S.: The monsoon currents in the north Indian Ocean, Prog. Oceanogr., 52, 63–120, 2002.

Shenoi, S. S. C., Shankar, D., and Shetye, S. R.: Differences in heat budgets of the near-surface Arabian Sea and Bay of Bengal: Implications for the summer monsoon, J. Geophys. Res., 107, C63052, https://doi.org/10.1029/2000JC000679, 2002.

Shi, W., Morrison, J. M., and Bryden, H. L.: Water, heat and freshwater flux out of northern Indian Ocean in September–October 1995, Deep-Sea Res. Pt. II, 49, 1231–1252, 2002.

Sijinkumar, A. V., Clemens, S., Nath, B. N., Prell, W., Benshila, R., and Lengaigne, M.: $\delta^{18}O$ and salinity variability from the Last Glacial Maximum to Recent in the Bay of Bengal and Andaman Sea, Quaternary Sci. Rev., 135, 79–91, 2016.

Singh, A. D., Jung, S. J. A., Darling, K., Ganeshram, R., Ivanochko, T., and Kroon, D.: Productivity collapses in the Arabian Sea during glacial cold phases, Paleoceanography, 26, PA3210, https://doi.org/10.1029/2009PA001923, 2011.

Smith, R. D. and Gent, P. R.: Reference manual for the Parallel Ocean Program (POP), ocean component of the Community Climate System Model (CCSM2.0 and 3.0), Los Alamos National Laboratory, Los Alamos, New Mexico, USA, LAUR-02-2484, 2002.

Spiro Jaeger, G. and Mahadevan, A.: Submesoscale-selective compensation of fronts in a salinity-stratified ocean, Sci. Adv., 4, e1701504, https://doi.org/10.1126/sciadv.1701504, 2018.

Stocker, T. F. and Johnsen, S. J.: A minimum thermodynamics model for the bipolar seesaw, Paleoceanography, 18, 1087, https://doi.org/10.1029/2003PA000920, 2003.

Stoll H. M., Arevalos, A., Burke, A., Ziveri, P., Mortyn, G., Shimizu, N., and Unger, D.: Seasonal cycles in biogenic production and export in Northern Bay of Bengal sediments traps, Deep-Sea Res. Pt. II, 54, 558–580, 2007.

Swingedouw, D., Mignot, J., Braconnot, P., Mosquet, E., Kageyama, M., and Alkama, R.: Impact of freshwater release in the North Atlantic under different climate conditions in an OAGCM, J. Climate, 22, 6377–6403, 2009.

Taylor, K. E., Stouffer, R. J., and Meehl, G. A.: An overview of CMIP5 and the experiment design, B. Am. Meteorol. Soc., 93, 485–498, 2012.

van de Poll, W. H., Kulk, G., Timmermans, K. R., Brussaard, C. P. D., van der Woerd, H. J., Kehoe, M. J., Mojica, K. D. A., Visser, R. J. W., Rozema, P. D., and Buma, A. G. J.: Phytoplankton chlorophyll *a* biomass, composition, and productivity along a temperature and stratification gradient in the northeast Atlantic Ocean, Biogeosciences, 10, 4227–4240, https://doi.org/10.5194/bg-10-4227-2013, 2013.

Vinayachandran, P. N., Murty, V. S. N., and Ramesh Bahu, V.: Observations of barrier layer formation in the Bay of Bengal during summer monsoon, J. Geophys. Res., 107, 8018, https://doi.org/10.1029/2001JC000831, 2002.

Vinayachandran, P. N., Chauhan, P, Mohan, M., and Nayak, S.: Biological response of the sea around Sri Lanka to summer monsoon, Geophys. Res. Lett., 31, L01302, https://doi.org/10.1029/2003GL018533, 2004.

Wang, B., Clemens, S. C., and Liu, P.: Contrasting the Indian and East Asian monsoons: implications on geologic timescales, Mar. Geol., 201, 5–21, 2003.

Wang, B., Yang, J., Zhou, T., and Wang, B.: Interdecadal changes in the major modes of Asian-Australian Monsoon variability: strengthening relationship with ENSO since the late 1970s, J. Climate, 21, 1771–1789, 2008.

Wang, X., Auler, A. S., Edwards, R. L., Cheng, H., Cristalli, P. S., Smart, P. L., Richards, D. A., and Shen, C.-C.: Wet periods in northeastern Brazil over the past 210 kyr linked to distant climate anomalies, Nature, 432, 740–743, 2004.

Webster, P. J., Magaña, V. O., Palmer, T. N., Shukla, J. Tmas, R. A., Yanai, M., and Yasunari, T.: Monsoons: Processes, predictability, and the prospects for prediction, J. Geophys. Res., 103, 14451–14510, 1998.

Wiggert, J. D., Hood, R. R., Banse, K., and Kindle, J. C.: Monsoon-driven biogeochemical processes in the Arabian Sea, Prog. Oceanogr., 65, 176–213, 2005.

Wolff, E. W., Chappellaz, J., Blunier, T., Rasmussen, S. O., and Svensson, A.: Millennial-scale variability during the last glacial: The ice core record, Quaternary Sci. Rev., 29, 2828–2838, 2010.

Yu, S.-Y., Colman, S. M. Lowell, T. V., Milne, G. A., Fisher, T. G., Breckenridge, A., Boyd, M., and Teller, J. T.: Freshwater ourbrust from Lake Superior as a trigger for the cold event 9300 years ago, Science, 328, 1262–1266, 2010.

Zhang, H., Liu, C., Jin, X., Shi, J., Zhao, S., and Jian, Z.: Dynamics of primary productivity in the northern South China Sea over the past 24 000 years, Geochem. Geophy. Geosy., 17, 4878–4891, 2016.

Supplementary Figures

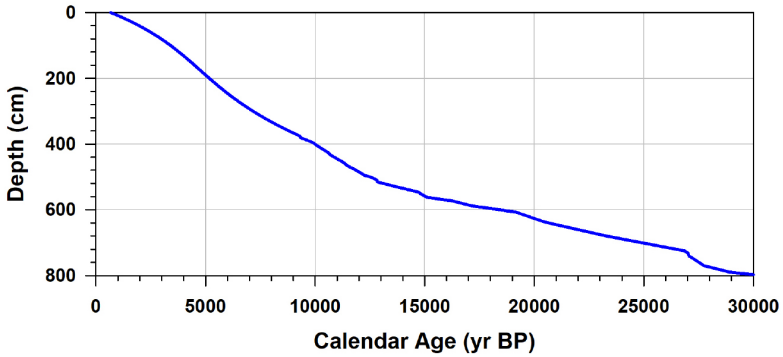

Fig. S1. Age model of core MD77-176. This age model was a tuned model constructed by Marzin et al., (2013).

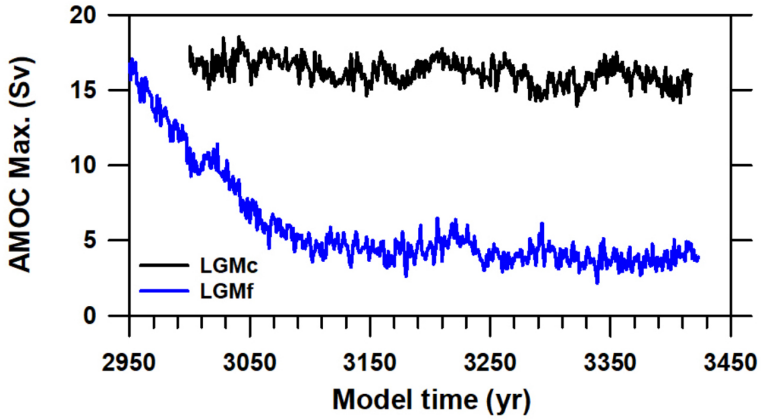

Fig. S2. Changes of the maximum in the AMOC stream function below 500 m (AMOC strength) in LGMc and LGMf experiments run with IPSL-CM5A-LR for nearly 500 model years, which are labeled from 2950 to 3450 in the numerical experiments.

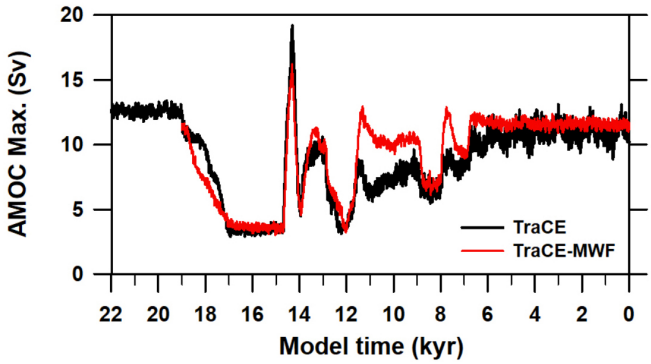

Fig. S3. Changes of the maximum in the AMOC stream function below 500 m (AMOC strength) in the full TraCE-21 simulation over the 22 kyr model time and melt water of ice sheets single forcing simulation (MWF) over the 19 kyr model time. Significant variations are found between 19 and 11 kyr (the deglaciation)

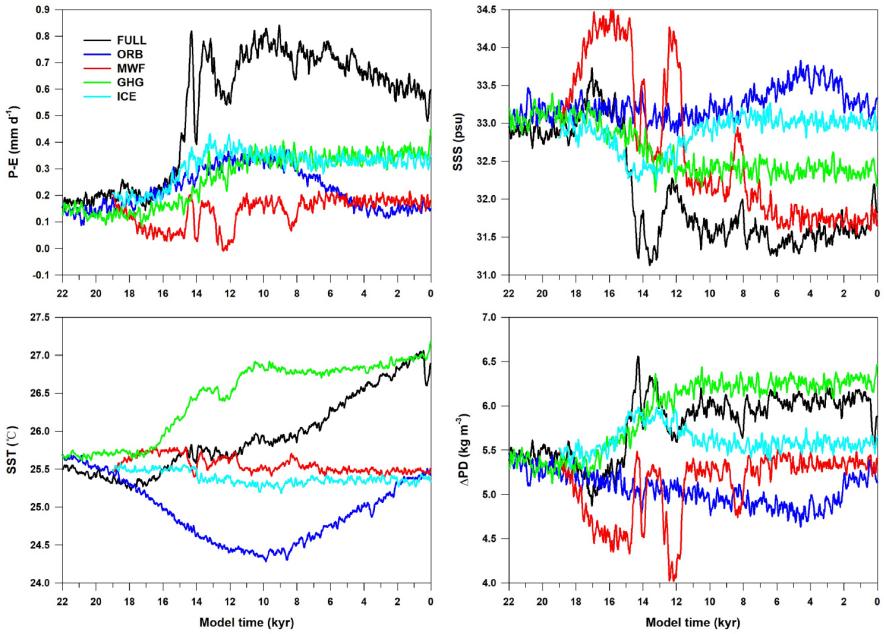

Fig. S4. Annual mean results of net precipitation (P-E), SSS, SST and potential density difference between 200 and 5 m (ΔPD) in full TraCE-21 simulation, and single forcing simulations (section 3.3.2): orbital insolation (ORB), green-house gas concentration (GHG), meltwater flux (MWF) and ice sheet (ICE). Over the last deglaciation time from 19 to 11 kyr, the results show that the millennial-scale variations of net precipitation, SSS and stratification are mainly contributed by MWF forcing which moderated AMOC strength. The changes in other single forcing experiment show no obvious millennial-scale variations during the last deglaciation. The changes of SST during the deglaciation is very limited.

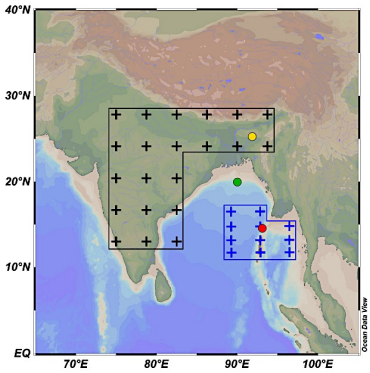

Fig. S5. Geographic map of South Asia, the Bay of Bengal and the Andaman Sea, the The map was created by the Ocean Data View software (©Reiner Schlitzer, Alfred Wegener Institute) with its built-in global high resolution bathymetric data (GlobHR). The grids of data extracting. Black cross are grids for TraCE-21 atmospheric outputs. Blue grids are for TraCE-21 oceanic outputs. The yellow, green and red dots mark the locations of Mawmluh Cave, core SO188-342 and core MD77-176 respectively.

Chapter 4

Variations of primary productivity in the northwestern Arabian Sea since the Last Glacial Maximum and their paleoclimate implications

Although paleo-PP has been studied in the Arabian Sea, it lacks high-resolution quantitative records. Here, I provide a PP record with a time resolution shorter than 1000 years, by using Florisphaera profunda % of core MD00-2354, retrieved at ~21°N of latitude, in the northwestern part of the basin. Together with published PP and paleoenvironmental records and model outputs from IPSL-CM5A-LR and TraCE-21, I suggest that this reconstructed-PP mainly reflects winter monsoon processes, and especially convective mixing and aeolian dust input.

Variations of primary productivity in the northwestern Arabian Sea since the Last Glacial Maximum and their paleoclimate implications

Xinquan Zhou[1], Stéphanie Duchamp-Alphonse[1], Masa Kageyama[2], Franck Bassinot[2], Florian Doressoundiram - Catherine Kissel[2]

[1]Université Paris-Saclay, Géosciences Paris Saclay, CNRS, Rue du Belvédère, 91405 Orsay, France
[2]Laboratoire des Sciences du Climat et de l'Environnement, CEA/CNRS/UVSQ, Université Paris-Saclay, Centre CEA-Saclay, Orme des Merisiers, 91191 Gif-sur-Yvette, France

In preparation

Abstract: The Arabian Sea is one of the most productive oceanic regions in the world due to the control of nutrient availability by summer and winter monsoons. The previous studies of the imprint of oceanic primary productivity (PP) in sediments from the Arabian Sea yielded diverse results depending on the used proxies with still unprecise paleoclimatic interpretations. Here, we provide a new high-resolution annual PP record since the Last Glacial Maximum (LGM) based on the variations of coccolith assemblage in a sediment core (MD00-2354) from the northwestern Arabian Sea. Our record shows a ~90 % higher PP during the LGM relative to the Holocene. In addition, significant millennial-scale variations are described during the last deglaciation with higher PP during the cold periods of Heinrich Stadial 1 (HS1) and Younger Dryas (YD) and lower PP during the warm Bølling-Allerød (B-A) period. Over the Holocene, PP is slightly lower during the Early-Mid Holocene (EMH) than the Late-Holocene. Based on the model-data comparison, we propose that when the summer monsoon was weakened during the LGM, HS1, and YD, higher PP were driven by the strengthened surface-cooling driven convective mixing associated to stronger winter monsoon processes, and by the increase of aeolian input. During HS1 and YD, high PP was also associated to a weaker AMOC, while the pattern was reverse during the B-A warm period characterized by lower PP. During the EMH, the summer monsoon was at maximum while PP was at a minimum. Our interpretation is that this pattern results from the restricted advection of summer upwelling cell under negative wind stress curls, limited winter convective mixing, and lower aeolian input.

Key words: Northwestern Arabian Sea, annual primary productivity, Last Glacial Maximum, last deglaciation, winter monsoon, aeolian input

1. Introduction

The Arabian Sea (AS) is one of the most productive oceanic regions in the world due to the important supply of nutrients to the euphotic zone either from surrounding continents through aeolian dust activity, or from below through wind-driven coastal upwelling or surface cooling-driven convective mixing (Lee et al., 2000; Prasanna Kumar and Narvekar, 2005; Jickells et al., 2005; Bali et al., 2019). Indeed, this semi-enclosed basin is surrounded by vast arid and supra-arid lands and collects a substantial amount of dust material, mainly from the Arabian Peninsula and Iran (Yu et al., 2013; Notaro et al., 2015; Rezazadeh et al., 2013; Ramaswamy et al., 2017; Mashat et al., 2018), that provides a combination of the essential nutrients nitrogen, phosphorus, and iron for primary producers (Jickells et al., 2005; Patra et al., 2007; Singh et al., 2008; Banerjee and Prasanna Kumar, 2014; Guieu et al., 2019; Bali et al., 2019). It is also under the influence of the Indian monsoon system, characterized by seasonal shifts of prevailing surface winds and precipitations that shape the AS upper circulations, and nutrient and PP distributions. During the summer monsoon i.e., from May to September, strong wet southwesterly winds, run diagonally across the AS and contribute to the development of clockwise upper ocean circulation (Schott and McCreary, 2001; Wang and Ding, 2008). Associated with intense alongshore winds and Ekman pumping, it creates a strong coastal upwelling off Somalia and Oman, that brings cold and nutrient-rich waters to the euphotic zone and hence, sustains a high PP cell that extends up to the central parts of the basin (Bartolacci and Luther, 1999; Lee et al., 2000; Prasanna Kumar et al., 2001a; Fig. 4.1). During the winter monsoon i.e., from November to March, dry and cold winds blow from the Asian continent to the southwest. They result in an anti-clockwise pattern associated with a convective mixing north of 15°N that leads to the development of a high productivity cell in the northern part of the AS as cold and nutrient-rich intermediate waters resurface (Schott and McCreary, 2001; Prasanna Kumar et al., 2001b; Prasanna Kumar and Narvekar, 2005; Fig. 4.1).

The imprint of PP in marine sediments from the AS has already been the focus of studies that aimed at understanding the Indian monsoon dynamic in the past on different time scales (e.g., Shimmield et al., 1990; Anderson and Prell, 1993; Ziegler et al., 2010a, 2010b; Agnihotri et al., 2002; Jung et al., 2002; Gupta et al., 2003, 2015; Bialik et al., 2020). The studies concluded about strengthened upwelling and summer southwesterly winds during the interglacial and interstadial periods (e.g., Bølling-Allerød and Holocene), and weakened upwelling and summer winds during the glacial and stadial ones. On interannual and decadal timescales, the Indian monsoon system and thus, the AS, is particularly sensitive to fluctuations in the ocean-atmosphere coupled system with remote connections to the El Niño Southern Oscillation (ENSO) and the Indian Ocean Dipole (IOD). (Kumar

et al., 1999; Ashok et al., 2001; Krishnamurthy and Kirtman, 2003; Hong et al., 2005; Kumar et al., 2006; Abram et al., 2007; Liu et al., 2007; Charabi et al., 2009). On centennial and millennial timescales, paleoclimatic studies have shown that the Indian monsoon is mainly influenced by oscillations of the Atlantic Meridional Overturning Circulation (AMOC) strength (Overpeck et al., 1996; Barber et al., 1999; Fleitmann et al., 2003; Gupta et al., 2003; Murton et al., 2010; Yu et al., 2010; Cai et al., 2012; Kageyama et al., 2013; Marzin et al., 2013; Zhou et al., 2020). However, relationships between paleo-PP and monsoon patterns in different regions of the AS are still improperly understood as several synergistic mechanisms are involved and paleo-PP records may be linked to different paleoclimate interpretations depending on the proxies they are based upon. A proxy-model study recently weakens the usual paradigm that a stronger summer monsoon should induce a stronger upwelling and thus increased PP in the AS (Le Mézo et al., 2017). In the eastern AS where both summer and winter monsoons influence PP changes, the interpretations of the paleo-PP records are with uncertainties. Some records show a summer monsoon pattern, while the others have contrasting results suggesting a winter monsoon control (Schulz et al., 1998; Banakar et al., 2005; Singh et al., 2011; Cabarcos et al., 2014; Naik et al., 2017).

Organic proxies (total organic carbon, biomarkers) (e.g., Schulz et al., 1998; Schulte and Müller, 2001; Pourmand et al., 2007) or inorganic proxies (biogenic silica, biogenic barium, planktonic foraminifera) (e.g., Shimmield et al., 1990; Naidu and Malmgren, 1996; Reichart et al., 1997; Schulz et al., 2002; Pattan et al., 2003; Invanochko et al., 2005; Balaji et al., 2018) that are used for PP reconstructions provide important insights into specific oceanic nutrient dynamics and particulate carbon exports, but they might not be representative of quantitative PP that is a signal restricted to the euphotic zone. In 1997, Beaufort et al. provided an empirical function to transfer the relative abundance of coccolith *Florisphaera profunda* (Fp%) from sediments into quantitative annual PP, based on the study of surface sediments and satellite chlorophyll data from the AS and the western Indian Ocean. Lately, Rogalla and Andruleit (2005) and Cabarcos et al. (2014) showed that the Fp% is lower (indicating higher PP) during the LGM than during the Holocene in the northern, western, and eastern AS. High-resolution, quantitative PP reconstructions using this Fp% proxy have never been obtained in the northwestern AS where PP is strongly influenced by both summer and winter monsoons. As for modelling studies, those of Bassinot et al. (2011) and Le Mézo et al. (2017) are the only ones to simulate PP patterns in response to changed boundary conditions in the past (e.g., Mid-Holocene and Last Glacial Maximum) considering both summer and winter monsoons, based on the IPSL-CM4 and IPSL-CM5 models with biogeochemical components.

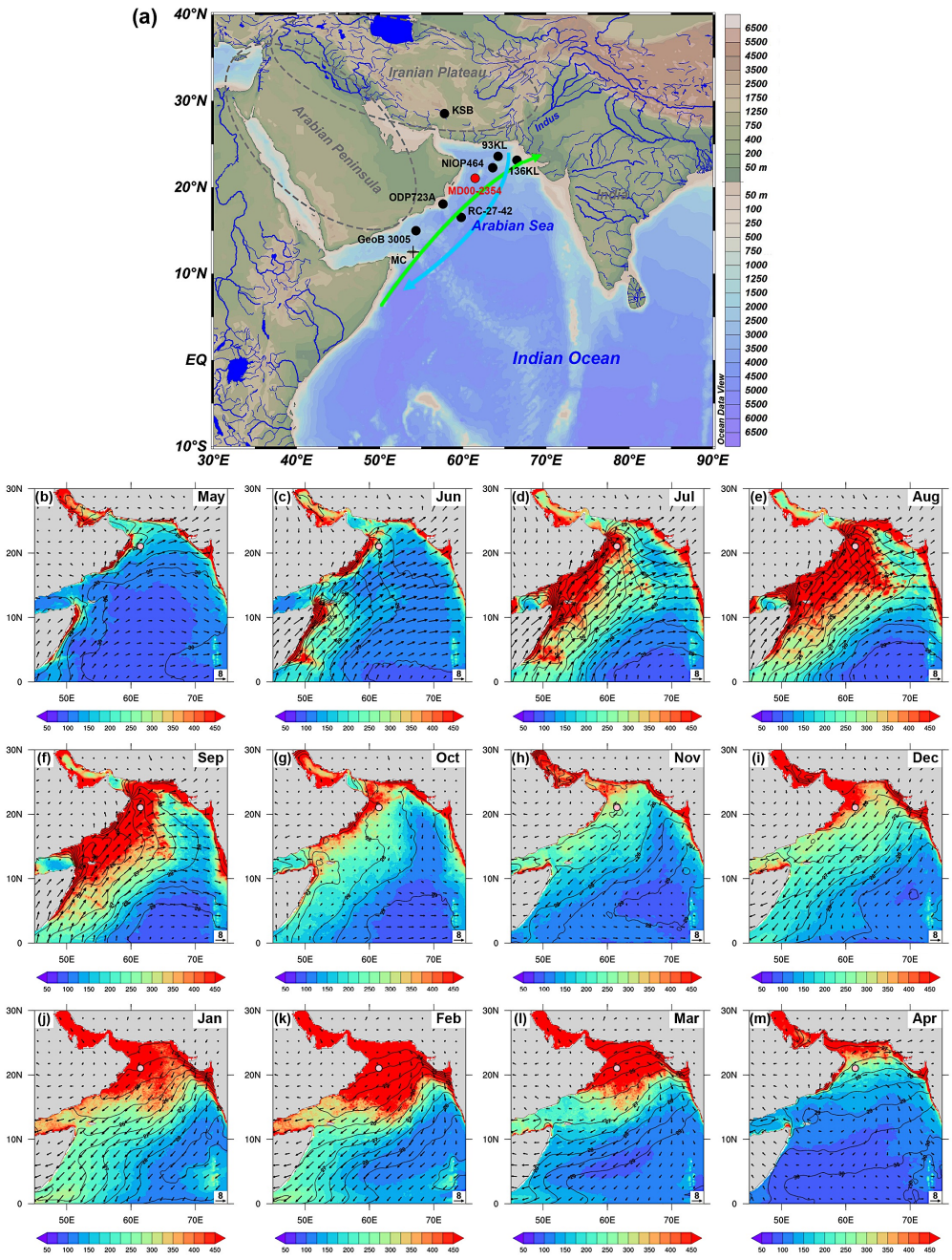

Fig. 4.1. (a) Geographic setting and bathymetric map created by the Ocean Data View software (©Reiner Schlitzer, Alfred Wegener Institute) with its built-in global high-resolution bathymetric data (GlobHR). The red dot marks the location of core MD00-2354 for PP reconstruction in this study. The black dots and cross mark the locations of sediment cores and speleothem with published paleoenvironmental records discussed in this study. The green and blue arrows schematically depict the summer southwesterly (Findlater Jet) and winter northeasterly. The dash line cycles show the potential source areas of the aeolian dust transported to the Arabian Sea. The Indus River injects the northeastern Arabian Sea. KSB = Konor Sandal peat boot; MC = Mooni Cave. (b)−(m) Climatology (period 2003−2019) of PP (color, gC m^{-2} yr^{-1}), SST (contours, ℃), and surface wind (vectors, m s^{-1}). PP was calculated by VGPM model based on MODIS chlorophyll-a concentration dataset (Behrenfeld and Falkowski, 1997). PP data are from the "Ocean Productivity" website (http://sites.science.oregonstate.edu/ocean.productivity). SST data are from the NOAA OI SST V2 High-Resolution Dataset (https://psl.noaa.gov/data/gridded/data.noaa.oisst.v2.highres.html). Wind speed data are from the ERA5 reanalysis dataset (https://www.ecmwf.int/en/forecasts/datasets/reanalysis-datasets/era5).

In this study, we provide the first millennial-scale record of paleo-PP in the northwestern AS over the last ~23 kyr, based on the analysis of the coccolith assemblages of sediment core MD00-2354 (61.48°E, 21.04°N). This time interval witnesses a glacial-interglacial transition and covers an entire precession cycle together with important fluctuations in the AMOC during the last deglaciation (McManus et al., 2004). It is therefore a perfect case study to explore the impact of key Earth's climate forcing mechanisms on PP for both, past and future climate conditions, such as ice volume, sea level, and atmospheric CO_2 concentration. We combine our PP estimates with published records of exported PP (mass accumulation rate of total organic carbon), upwelling in western AS (percentage of foraminifer *Globigerina bulloides*), sea surface temperature (SST) in the northern AS, and aeolian input. We also compare the reconstructed PP with outputs of the Earth System model IPSL-CM5A-LR (IPSL-CM5A in the following) and the transient simulation TraCE-21 (termed TraCE in the following). This allows us to evaluate the response of PP to changing surface oceanic and atmospheric conditions over the last ~23 kyr, with special a focus on the Last Glacial Maximum (LGM, 21 ka) and the Mid-Holocene (MH, 6 ka).

2. Materials and methods

2.1 Core location and age model

Core MD00-2354 was collected in the northwestern AS on board the *R.V. Marion Dufresne,* in 2000. It is located on the southwestern slope of the Murray Ridge, at 2740 m water depth i.e., above the modern lysocline (~3300 m; Cullen and Prell, 1984) (Fig. 4.1a). The surface waters at that site, about 210 km off the Oman Margin, are under the direct influence of the upwelling off Oman and the convective mixing cell off Iran/Pakistan that drive high PP during summer and winter, respectively (Figs. 4.1b–m). The site is also far from the influence of rivers that flow mainly in the south of Sindh Province in Pakistan, especially the Indus river which flows into the northeastern Arabian Sea (Shimmield et al., 1990) (Fig. 4.1a). The lithology of this sediment core mainly consists of homogenous grey clay and foraminifera- and nannofossil-bearing oozes. Its age model has been established by Böll et al. (2015) based on the correlation of the $\delta^{18}O$ signal obtained on foraminifera *Globigerinoides ruber* ($\delta^{18}O_{G.\ ruber}$) to the $\delta^{18}O_{G.\ ruber}$ record of 74KL sediment core retrieved in the western Arabian Sea, in turn, correlated to the $\delta^{18}O$ signal of GISP2 ice core. The upper 3 m of the sediments span the last 23.3 kyr, with sedimentation rate ranging between ~10 to 110 $cm.kyr^{-1}$ (Fig. 4.S1).

2.2 Coccolith analysis

Coccoliths are the calcite scales produced by coccolithophores, the only phytoplankton group responsible for the export of both organic and carbonate particles to the sedimentary reservoir. Because of their abundance in marine sediments as fossil remains, they have been widely used to infer physio-chemical conditions of the euphotic zone in the past, and this is particularly the case when dealing with the species *Florisphaera profunda* and *Calcidiscus leptoporus*. *F. profunda* is restricted to the lower euphotic zone and has been used to reconstruct variations in the nutricline depth (McIntyre and Molfino, 1990, 1996; Castradori, 1993; Bassinot et al., 1997; Cheng and Wang, 1998; Okada and Matsuoka, 1996; Kinkel et al., 2000; Liu et al., 2008; Su et al., 2013), and hence in PP (e.g. Beaufort et al. 1997; de Garidel-Thoron et al., 2001; Beaufort et al., 2010; Zhang et al., 2016; Zhou et al., 2020). *C. leptoporus* flourishes in mixed and nutrient-rich waters and has therefore been used to reflect nutrient contents in surface layers, either in coastal upwelling from low to mid-latitude settings (Fincham and Winter, 1989; Giraudeau, 1992; Cachão and Moita, 2000), or in frontal zone settings from high-latitudes (Flores et al., 1999; Findlay and Giraudeau; 2000; Flores et al., 2003; Baumann et al., 2004; Malinverno et al., 2005; Boeckel et al., 2006; Marino et al., 2008; Saavedra-Pellitero et al., 2017).

In this study, we use the relative abundance of *F. profunda* (Fp% = 100 × (Fp number / total coccolith number) from sediment core MD00-2354 to reconstruct PP variations in the northwestern Arabian Sea over the last ~23 kyr. The 95% confidence interval for Fp% was calculated following the method of Patterson and Fishbein (1984), and the errors are smaller than ±5 %. We converted Fp% into PP by using the tropical Indian Ocean empirical equation proposed by Hernández-Almeida et al. (2019): $PP = [10^{(3.27-0.01\times Fp\%)}] \times 365/1000$. The unit of estimated PP is grams of carbon per square meter per year (gC m^{-2} yr^{-1}). We also propose that the absolute abundance of *C. leptoporus* (n/g of sediment) is an indicator of the upwelling dynamic off Oman. In the same way, as for the planktonic foraminifera *G. bulloides* (Curry et al., 1992; Naidu and Malmgren, 1996; Schulz et al., 2002; Conan et al., 2000; Bassinot et al., 2011), we interpret its variations as changes in summer southwesterly intensity.

A total of 300 samples at 1 cm interval was analysed at the Geoscience Paris-Saclay laboratory (GEOPS, Orsay, France) for coccolith data, with time resolutions ranging from ~20 to 100 years. The "settling" technique of Duchamp-Alphonse et al. (2018) after Beaufort et al. (2014) was used to prepare coccolith smear slides. For each slide, at least 500 coccolith specimens were counted by human eyes, under at least 3 random fields of view using a polarized light microscope (Leica DM6000B) at

×1000.

2.3 Climate model and simulations

2.3.1 IPSL-CM5A-LR

Paleoclimate simulations were run with the IPSL-CM5A coupled model (Dufresne et al., 2013), which has three model components: the atmospheric general circulation and physics LMDZ5A model (Hourdin et al., 2013), the land surface ORCHIDEE model (Krinner et al., 2005), and the ocean-biogeochemistry NEMO-PISCES model (Aumont and Bopp, 2006; Madec, 2008). Simulations were run for the pre-industrial control (CTRL) in the framework of the Coupled Modelling Intercomparison Project phase 5 (CMIP5; Taylor et al., 2012) and for the LGM and the MH in the framework of Paleoclimate Modelling Intercomparison Project phase 3 (PMIP3; Braconnot et al., 2012). The comparison of LGM and MH mean states with CTRL are expressed in terms of experiment differences (LGM−CTRL and MH−CTRL) to highlight specific atmospheric and oceanic responses under LGM and MH conditions. Compared to CTRL, MH is characterized by a smaller precession parameter, while larger ice sheets, lower greenhouse gases concentrations, and lower sea level are set for the LGM. Nutrient supply from dust, rivers, and sediments to the ocean is assumed to be constant during LGM, MH, and CTRL. Details of the model and the boundary conditions for these three experiments can be found in Dufresne et al. (2013) and Le Mézo et al. (2017).

In brief, surface wind speed (m s^{-1}) and wind stress curl (N m^{-3}) were extracted to describe atmospheric conditions, while net evaporation (evaporation minus precipitation, mm day^{-1}), surface nutrient content (mmol m^{-3}), mixed-layer depth (m), seawater vertical mass transport (upper 200 m mean, kg s^{-1}; Lee et al., 2000), together with temperature (°C), salinity (psu) and potential density (kg m^{-3}) were extracted to infer oceanic conditions. Temperature (salinity) gradients were calculated based on the difference between 0 m (200 m) and 200m (0 m) water depths, termed $\Delta T_{0\text{-}200m}$ ($\Delta S_{200\text{-}0m}$) in the following. The vertically averaged stable stability of the upper 200 m (termed $E_{0\text{-}200m}$, m^{-1}) was calculated based on the normalized vertical density gradient: $E = -(1/\rho)\cdot(\partial\rho/\partial z)$, where z is the water depth (m), which represents the upper seawater stratification (Prasanna Kumar et al., 2002). The variables used here are in the seasonal and annual mean.

2.3.2 TraCE-21

TraCE-21 is a transient simulation of global climate evolution over the last 22 kyr run with Community Climate System Model version 3 (Collins et al., 2006; Liu et al., 2009). The simulation was initialized from a previous LGM equilibrium simulation of CCSM3 (Otto-Bliensner et al., 2006)

and is then forced by a set of realistic transient climate forcing including orbital parameters, greenhouse gases concentration, continental ice sheets, and glacial meltwater discharge. The last one can force the AMOC strength to change. Outputs of the single forcing experiments are available (Liu et al., 2009). We extracted annual mean temperature and salinity at 0 and 200 m, and calculate annual mean vertically averaged stable stability of the upper 200 m ($E_{0\text{-}200m}$, m^{-1}) to describe oceanic conditions around the MD00-2354 site (21°N−23°N, 60°E−65°E).

3. Results

3.1. Coccolith assemblage and reconstructed PP

At site MD00-2354, *Gephyrocapsa* spp. (including *G. oceanica* and small *Gephyrocapsa*), *Emiliania huxleyi* and *F. profunda* together represent more than 70 % of the coccolith assemblage (Fig. 4.2), while *Calcidiscus leptoporus*, *Umblicosphaera sibogae*, and *Helicosphaera. carteri* account for up to ~25 %.

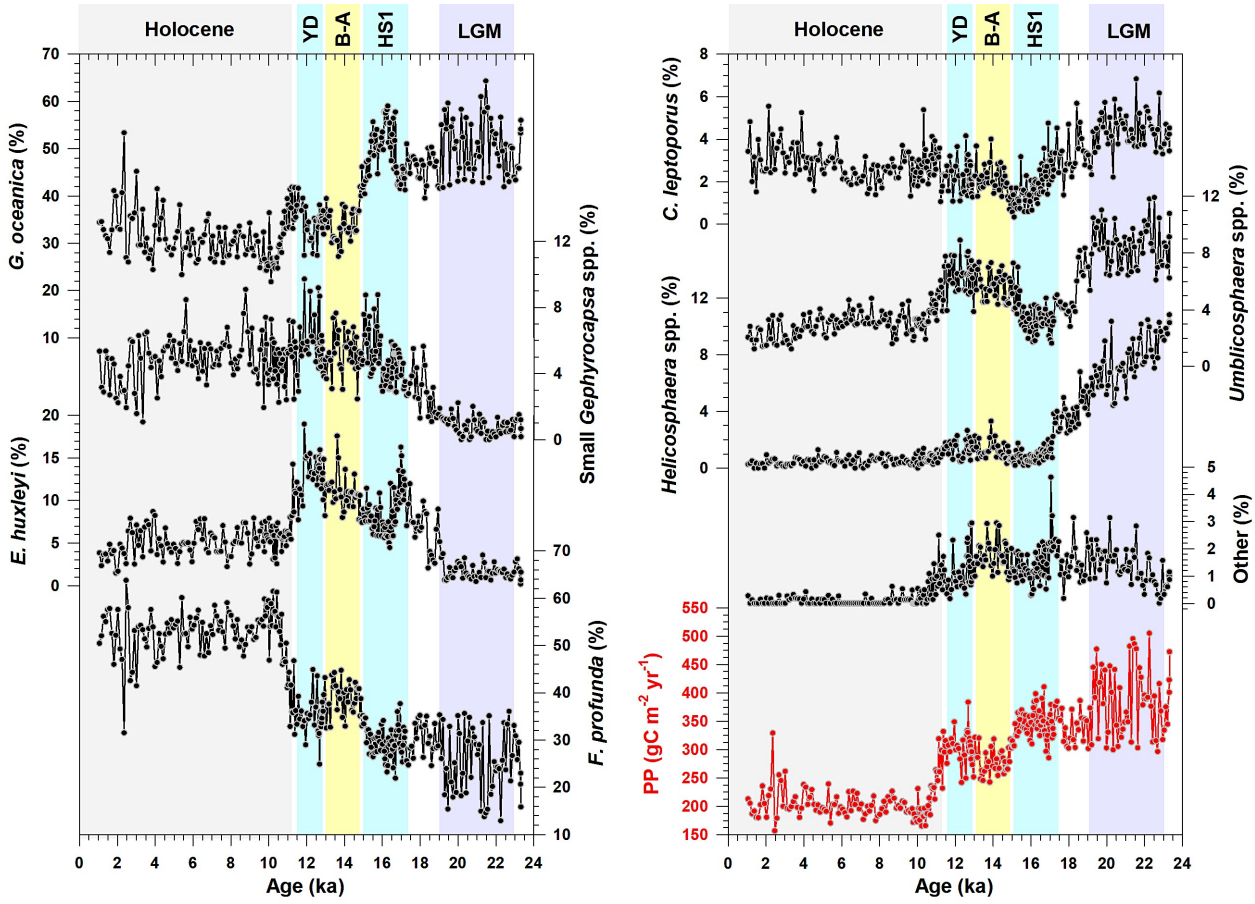

Fig. 4.2. Relative abundances (%) of coccolith species in core MD00-2354 (black), and the estimated PP (red) calculated by the Indian Ocean empirical equation (Hernández-Almeida et al., 2019).

Other species such as *Syracosphaera* spp. and *Rhabdosphaera* spp. are rare and altogether, never exceed 5 %. The most striking patterns are those of *F. profunda* and *G. oceanica* i.e., the two most abundant species, that depict opposite trends over the last 23 kyr. While *F. profunda* shows a minimum (~15 %) during the LGM, a two-step increase during the deglaciation, and a maximum (~60 %) during the Holocene, *G. oceanica* shows its maximum (~60 %) during LGM, a two-step decrease during the deglaciation and a minimum (~25 %) during the Holocene. Overall, *small Gephyrocapsa* and *E. huxleyi* depict lower percentages during the LGM (averages of ~1 % and 1.5 %, respectively) compared to the Holocene (averages of ~4.5 % and 5 %, respectively), while *C. leptoporus*, *U. sibogae* and *H. carteri* show higher proportions during the LGM than during the Holocene. Interestingly, during the deglaciation, *G. oceanica* and *F. profunda* have opposite millennial-scale variations. *F. profunda* (*G. oceanica*) shows averaged abundances of ~30 % (~52 %) and ~35 % (~35 %) during HS1 and YD and of ~39 % (~30%) during B-A. *C. leptoporus* shows values as low as 0.5 % during HS1 and depicts an increasing trend during the B-A with proportions as high as 2.5%.

Reconstructed PP varies between 150 and 500 gC m^{-2} yr^{-1} (Fig. 4.2). Despite rather scattered values during the LMG, it appears that PP during this period (average of ~382 gC m^{-2} yr^{-1}) is about ~90 % higher than during the Holocene (average of ~203 gC m^{-2} yr^{-1}). Indeed, maximum and minimum are found during the LGM and the Early-Holocene, respectively. During the deglaciation, PP averages are 346 gC m^{-2} yr^{-1} and 305 gC m^{-2} yr^{-1} during HS1 and YD, and neither exceed 300 gC m^{-2} yr^{-1} during the B-A.

3.2 Simulated PP

The results of simulated PP (CTRL, LGM−CTRL, and MH−CTRL) are shown in Fig. 4.3. According to the CTRL, the coastal areas off Somalia-Oman and off Northern Oman and Pakistan appear to be the most productive areas during preindustrial summer and winter (> 400 gC m^{-2} yr^{-1}) which is consistent with the VGPM modern features (Figs. 4.3a−f) (Behrenfeld and Falkowski, 1997). The difference in annual PP between LGM and CTRL reveals a strong increase (> 50 gC m^{-2} yr^{-1}) in the northern and northeastern parts of the basin and a strong decrease (< -50 gC m^{-2} yr^{-1}) along the coastal areas off Somalia and Oman (Fig. 4.3g). The PP increase in the northern part of the basin is mainly related to the winter pattern (Fig. 4.3i), while the PP decrease in the western part is mainly associated to the summer one (Fig. 4.3h; Le Mézo et al. 2017).

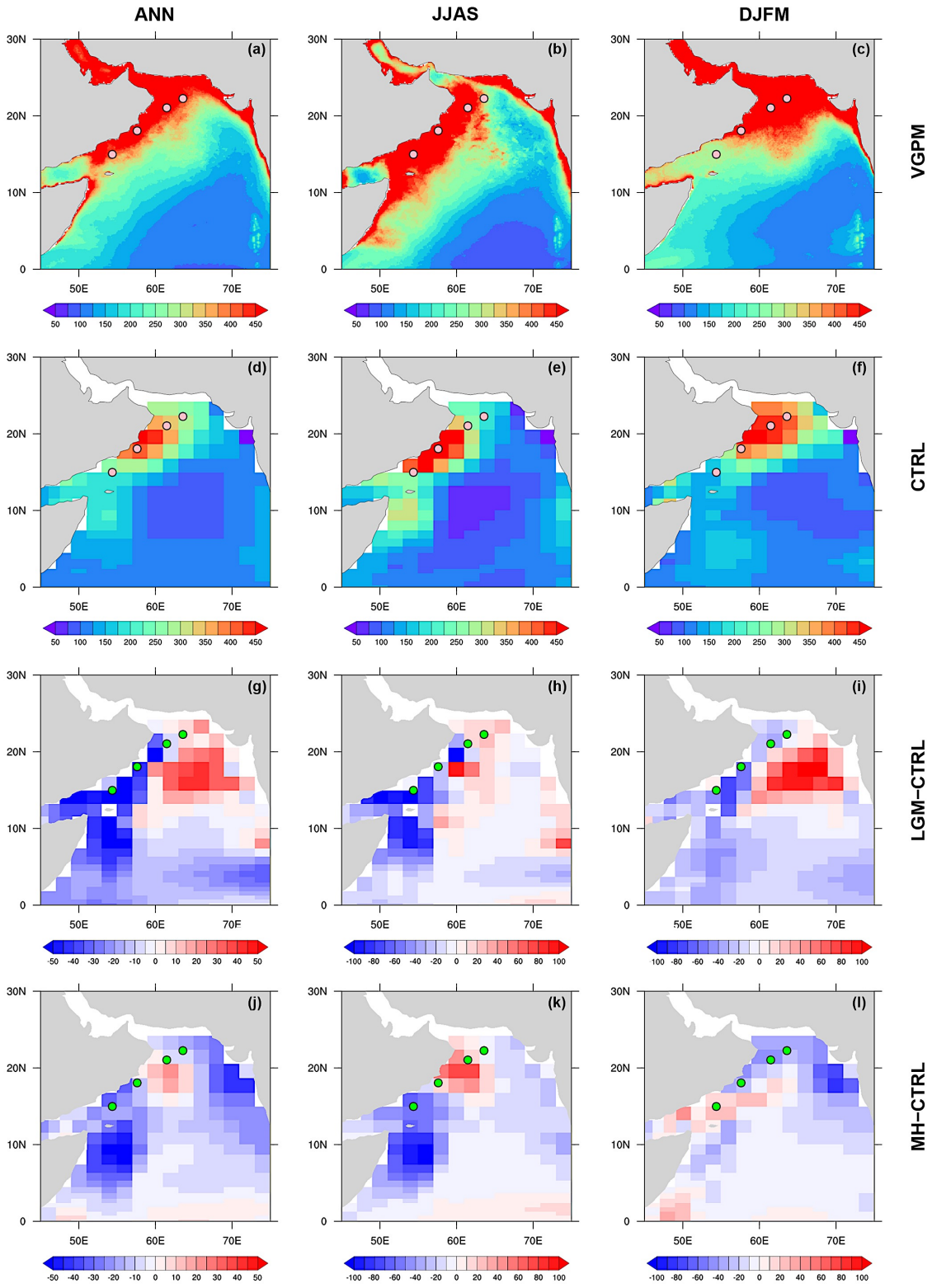

Fig. 4.3. (a)−(c) Annual mean (ANN), summer (June−July−August−September, JJAS), and winter December−January−February−March, DJFM) integrated PP (gC m^{-2} yr^{-1}) calculated by VGPM model based on MODIS chlorophyll concentration data (Behrenfeld and Falkowski, 1997). (d)−(f) Annual mean, summer, and winter integrated PP simulated by CTRL experiment. (g)−(i) Differences of annual mean, summer, and winter integrated PP between LGM and CTRL experiments. (j)−(l) Differences of annual mean, summer, and winter integrated PP between MH and CTRL experiments. The dots mark the locations of cores MD00-2354, OPD723A, NIOP464, and GeoB 3005 (see Fig. 4.1a).

The difference in annual PP between MH and CTRL shows an overall decrease in annual PP. It is only in the northwestern AS off Oman that a PP increase (10−25 gC m^{-2} yr^{-1}) is simulated as a result of a strong signal of higher PP in that area during summer (Figs. 4.3j, k; Le Mézo et al., 2017). The annual pattern also reflects at some points, the high PP simulated by CTRL and VGPM off northern Oman during summer.

4. Discussion: atmospheric and oceanographic implications behind PP patterns

4.1. Today

During summer, southwesterly winds alongshore Oman and Somalia, are accompanied by positive wind stress curls and upward seawater movements related to the coastal upwelling system (Figs. 4.4a−h). This mechanism increases the nutrients contents in surface layers and results in relatively high PP (Figs. 4a−d). This high PP pattern is clearly not related to a weaker upper seawater stratification in the northwestern AS as no stronger net evaporation, no deeper mixed-layer, no lower stable stability, and no smaller temperature and salinity gradients are observed (Figs. 4.4e−h). During winter, no important positive wind stress curls and upwelling are found (Figs. 4.4l). During that season, northeasterly winds across AS, are associated with strong net evaporation in the northern part of the basin that, together with an important sea surface cooling, causes the temperature gradient and hence the upper seawater stratification to collapse (Figs. 4.4m−o). These processes help to sustain a substantial amount of nutrients in the upper layers which appears to drive high PP (Figs. 4.4i−k).

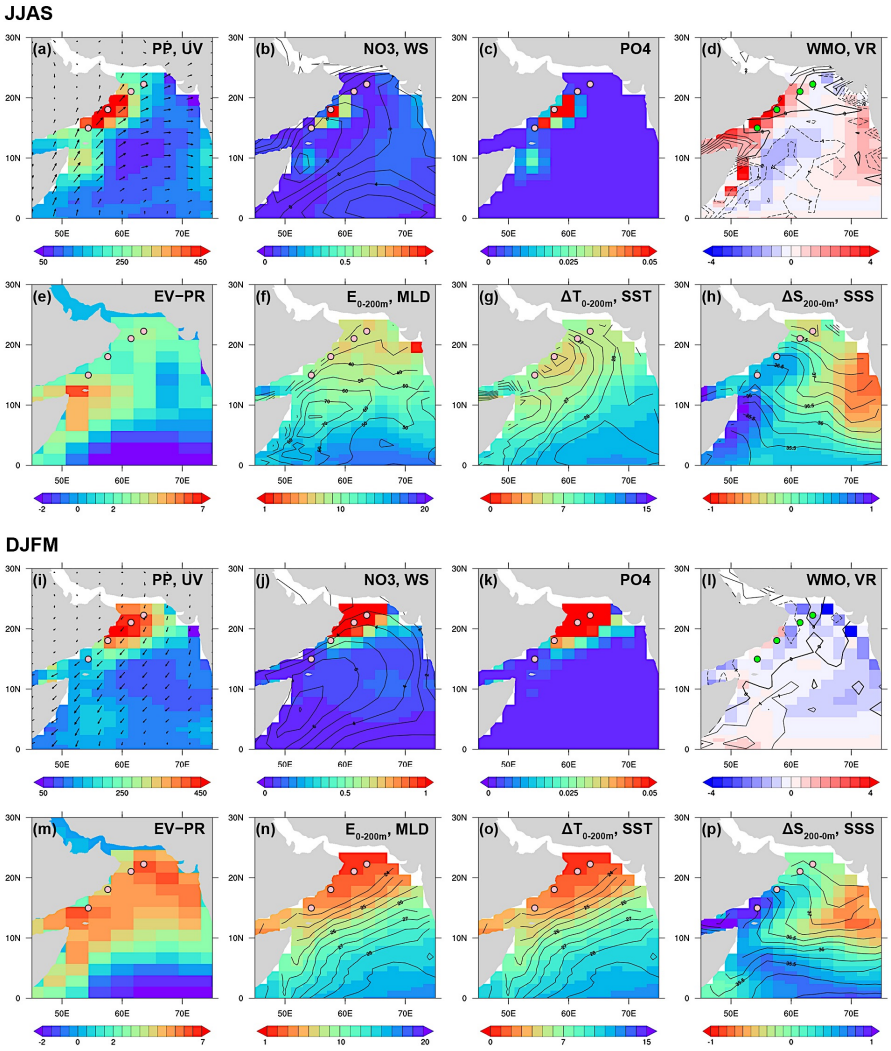

Fig. 4.4. Analysis of PP using CTRL outputs in (a)−(h) summer (JJAS) and (i)−(p) winter (DJFM). (a) and (i) Integrated PP (color, gC m^{-2} yr^{-1}) and surface wind (vectors, m s^{-1}). (b) and (j) Surface concentration of nitrate (NO3, mmol m^{-3}) and surface wind intensity (contours, m s^{-1}). (c) and (k) Surface concentration of phosphate (PO4, mmol m^{-3}). (d) and (l) Mean vertical mass transport of the upper 200 m seawater (VMO, color, kg s^{-1}) and wind stress curl (VR, contours, 10^7 N m^{-3}). (e) and (m) Net evaporation (EV−PR, mm day^{-1}). (f) and (n) Upper seawater stratification quantified by mean stable stability of the upper 200 m ($E_{0\text{-}200m}$, color, 10^6 m^{-1}) and mix-layer depth (contours, m). (g) and (o) Upper seawater temperature gradient quantified by the difference between the surface and 200 m ($\Delta T_{0\text{-}200m}$, color, ℃) and sea surface temperature (contours, ℃). (h) and (p) Upper seawater salinity gradient quantified by the difference between 200 m and the surface ($\Delta S_{200\text{-}0m}$, color, psu) and sea surface salinity (contours, psu). The dots mark the locations of cores MD00-2354, OPD723A, NIOP464 and GeoB 3005 (see Fig. 4.1a).

The results of CTRL simulations document well the processes encountered in the upper layers of the AS during summer and winter seasons, when wind-driven coastal upwelling off Somalia and Oman, and surface cooling-driven convective mixing off North Oman and Pakistan drive high PP, respectively. They are also consistent with the findings of previous studies based on in-situ data (e.g. Lee et al., 2000; Prasanna Kumar et al., 2001a). As a result, the annual PP is relatively important in the northwestern AS off Oman i.e., where the studied core has been retrieved. The seawater is therefore under the direct influences of the major seasonal phytoplankton blooms of the basin.

4.2 During the LGM

At MD00-2354, high PP signal (~380 gC m^{-2} kyr^{-1}) associated with low *C. leptoporus* abundance (0.8 10^9 n/g) confirm previous evidence of high sedimentary TOC (~0.1 gC cm^{-2} kyr^{-1}) associated with low *G. bulloides* abundance (~32 %; weak upwelling) on sites GeoB 3005, NIOP464 and ODP723A, respectively (Naidu and Malmgren, 1996; Reichart et al., 1997; Budziak et al., 2000; Figs. 4.5c, e–h).

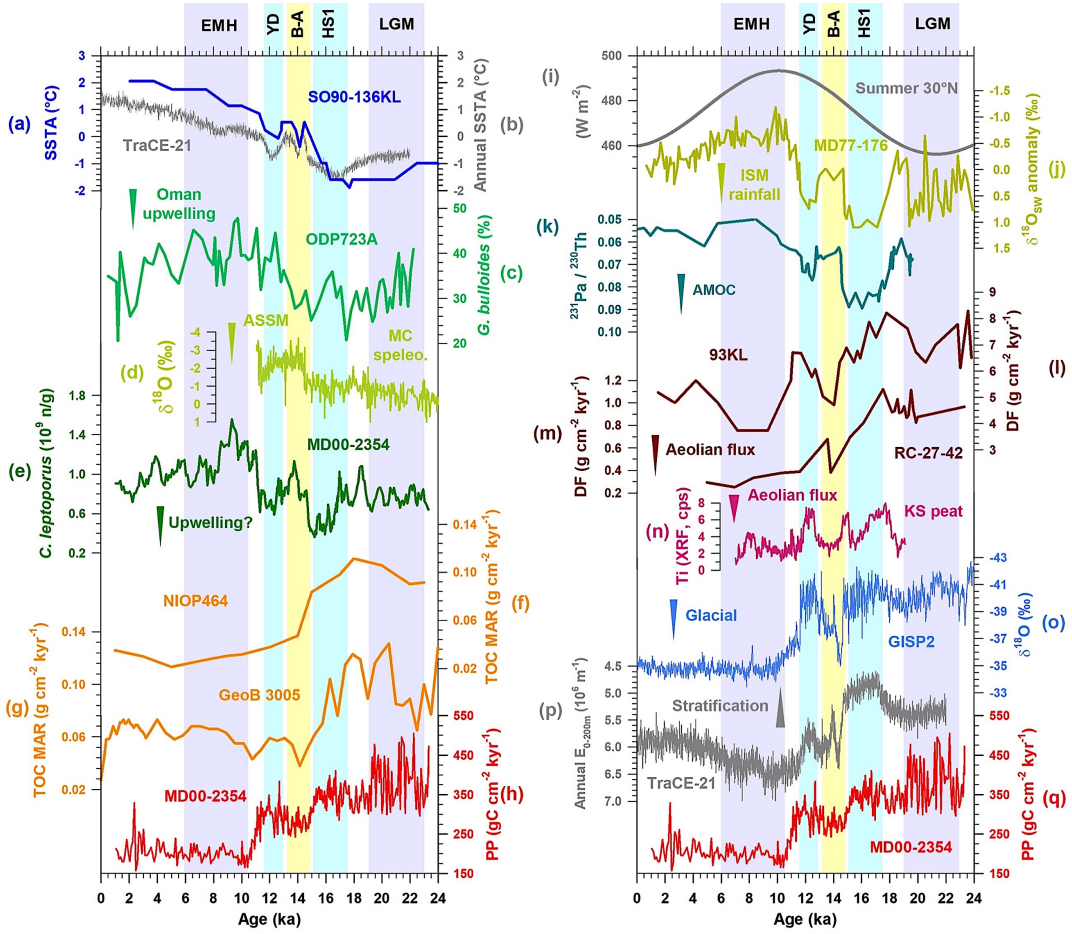

Fig. 4.5. (a) Alkenone-derived SST in core SO90-136KL (Böll et al., 2015). (b) Annual sea surface temperature (SST) in the northern Arabian Sea (AS) (21°N–23°N, 60°E–68°E) simulated by TraCE-21 (c) Relative abundance of *G. bulloides* in core OPD723A indicating the variations of Oman upwelling intensity (Naidu and Malmgren, 1996). (d) Speleothem $\delta^{18}O$ record from the Mooni Cave indicating the variations of summer surface winds in the western AS (Shakun et al., 2007). (e) Absolute abundance (n/g) of *Calcidiscus leptoporus* in core MD00-2354 (5-point moving average). Mass accumulation rates (MAR) of total organic carbon (TOC) of cores (f) NIOP464 from the northern AS (Reichart et al., 1997) and (g) GeoB 3005 from the western AS (Budziak et al., 2000). (h) Reconstructed PP in core MD00-2354. (i) Summer (June-July-August) insolation at 30° N (Laskar et al., 2004). (j) Seawater $\delta^{18}O$ anomaly record of core MD77-176 indicating the variations of South Asian summer monsoon rainfall (Marzin et al., 2013). (k) AMOC strength revealed by the $^{231}Pa/^{230}Th$ ratio in marine sediments from the western subtropical Atlantic Ocean (McManus et al., 2004). ^{230}Th-normalized detrital flux of cores (l) 93KL from the northern AS (Pourmand et al., 2004) and (m) RC-27-24 from the western AS (Pourmand et al., 2007), both indicating aeolian dust flux. (n) Downcore Ti abundance measured by XRF of a sediment core from the Konar Sandal peat bog, southeastern Iran (Safaierad et al., 2020). (o) GISP2 ice core $\delta^{18}O$ record (Stuiver and Grootes, 2000). (p) Annual mean seawater stratification in the northwestern AS simulated by TraCE-21. (q) Reconstructed PP in core MD00-2354.

These results reveal the occurrence of an extended high (exported-) PP cell in the northern and northwestern parts of the AS and are in agreement with the low-resolution Fp% data previously obtained by Rogalla and Andruleit (2005). These data also indicate that relatively high PP in that area during the LGM is not associated to the development of a strong upwelling system off Somalia and Oman, as the Indian summer monsoon was probably weaker during that period. Such assumption is confirmed by the positive $\delta^{18}O_{sw}$ anomaly from core MD77-176 in northeastern BoB, which indicates lower Indian summer monsoon rainfall during the LGM (Fig. 4.5j). In parallel, the alkenone-SST data from core SO90-136KL documents a stronger surface cooling in the northern AS during the LGM (Fig. 4.5a), which suggests that forcing factors driving this higher PP might therefore be found within mechanisms involved under stronger winter monsoon conditions. Such an assumption is coherent with the extended ice sheets and the lower greenhouse gas concentrations that characterize the LGM and make Eurasia much colder than the northern Indian ocean (e.g., Peltier, 2004; Braconnot et al., 2007; Joos and Spahni, 2008; Jiang et al., 2015; Tierney et al., 2020). It is also well expressed by the LGM−CTRL experiments that document northwesterly and northeasterly anomalies during winter and summer, respectively (Figs. 4.6a, d), and by TraCE that simulates the exact same SST trends as those obtained in the area, especially at site SO90-136KL (Figs. 4.5a, b).

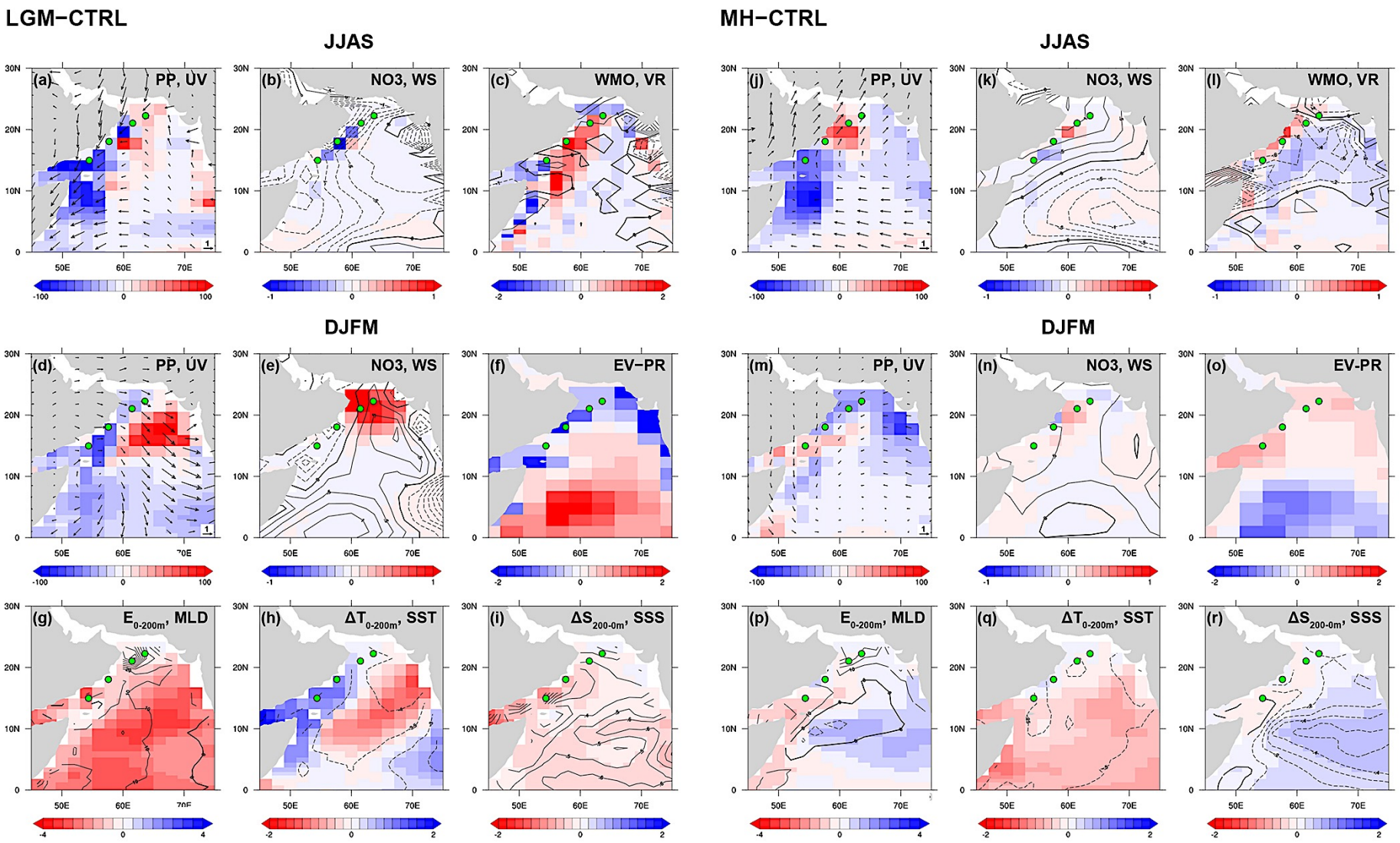

Fig. 4.6. Differences between LGM and CTRL experiments in (a) –(c) summer and (d)–(i) winter. Differences between MH and CTRL experiments in (j)–(l) summer and (m)–(r) winter. The parameters are the same as those in Fig. 4.5.

Under such cold and dry conditions, another plausible explanation behind the aforementioned PP patterns is the fertilization of the euphotic zone by windblown nutrient-rich dust during a glacial period favorable for the increase of global dust emission and deposition (e.g., Winckler et al., 2008; Martínez-García et al., 2009; Maher et al., 2010; Lambert et al., 2013; Lamy et al., 2014; Albani et al., 2016, 2018). Stronger aeolian inputs are documented in the northern and western AS by the ^{230}Th-normalized detrital flux records obtained at sites 93KL and RC-27-42 (Poumand et al., 2004; 2007; Figs. 4.5l, m). In addition, sensitive experiments of dust deposition from the biogeochemical model PISCES have recently demonstrated that the aeolian flux could influence PP in a large area including the northern and western AS, and that null dust accumulation could reduce PP by 50 % (Guieu et al., 2019). However, the 40% stronger aeolian flux recorded during the LGM relative to the Holocene cannot fully account for the observed ~90 % higher PP (Figs. 4.5l, m).

Another plausible cause might be a stronger convective mixing and a weaker stratification in the euphotic zone as suggested by the LGM−CTRL winter experiments (Figs. 4.6d−i). According to the results of LGM−CTRL, stronger winter surface winds are accompanied by stronger surface cooling, stronger net evaporation (Figs. 4.6d−f), and hence, a smaller temperature gradient leading to a weaker stratification in the northern part of the AS (Figs. 4.6g−i). This winter pattern dominates the annual mean of LGM−CTRL (Figs. 4.7a−c), which is also simulated by TraCE that shows low values of annual mean seawater stratification corresponding to a smaller temperature gradient in the studied area (Figs. 4.5p, 4.7d−f). It is worth mentioning that in the LGM−CTRL experiment, the summer season appears to be associated with northeasterly anomalies along the coastal area off Somalia and Oman, that drive positive wind stress curl anomalies over the western AS and a slight increase of PP (Le Mézo et al., 2017; Figs. 4.6a−c). However, as previously highlighted, the annual mean of PP mainly reflects PP patterns of the winter season, and summer mechanisms are of minor importance (Figs. 4.3g−i).

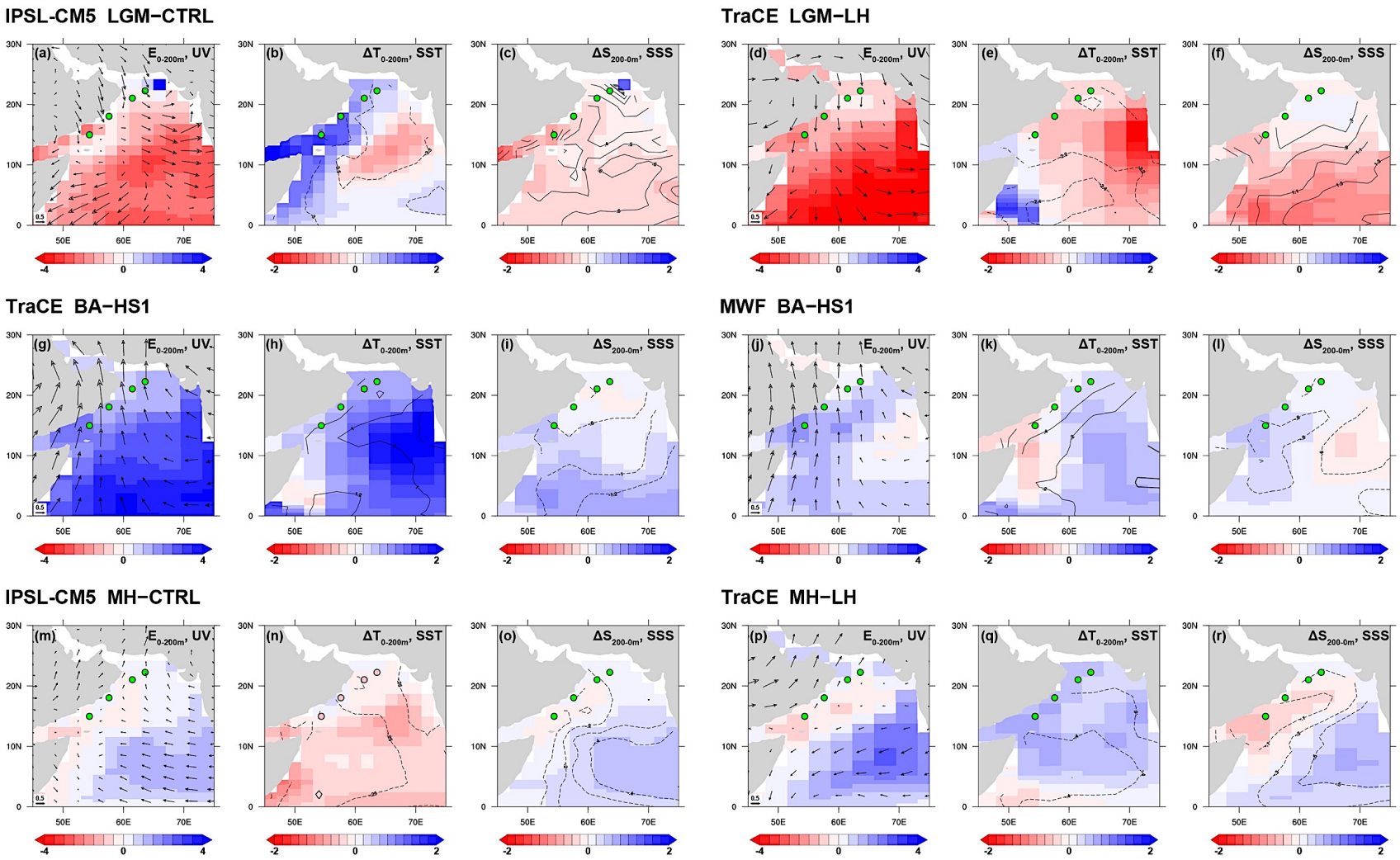

Fig. 4.7. Differences of annual mean $E_{0\text{-}200m}$ (10^6 m^{-1}), surface wind (vectors, m s^{-1}), $\Delta T_{0\text{-}200m}$ (° C), and $\Delta S_{200\text{-}0m}$ (psu) between (a)−(c) LGM and CTRL experiments of IPSL-CM5, between (d)−(f) LGM and Late Holocene of TraCE-21, between (g)–(i) BA and HS1 of TraCE-21, between (j)–(l) BA and HS1 of MWF, between (m)–(o) MH and CTRL experiments of IPSL-CM5, and between (p)–(r) LGM and CTRL experiments of IPSL-CM5.

In summary, the high PP observed in the northern part of the basin during LGM most likely reflects the combined effects of stronger aeolian input and stronger surface cooling-driven mixing. The LGM conditions can enhance the impact of dust supply, and lead to a more "winter monsoon-like" interval.

4.3 During the deglaciation

The long-term decreasing trend of PP (from 400 to 200 gC m^{-2} kyr^{-1}) and the long-term increasing trend of *C. leptoporus* abundance (from 0.8 to 1.2 10^9 n/g) mimic TOC and *G. bulloides* signals previously obtained in the studied area (Figs. 4.5c, e−h). In the same way, as for the LGM period, these results most likely indicate a reduction of PP in the northern part of the AS as the winter monsoon decreased, while the coastal upwelling off Somalia-Oman strengthens as the summer monsoon reinforced. Together with the overall increase in SST in the area (Figs. 4.5a, b), and the general decrease in the aeolian flux (Figs. 4.5l, m), these findings confirm terrestrial and marine climatic records that point to a transition from cold and dry LGM conditions to warm and wet Holocene conditions. This is expected when the North Hemisphere summer insolation increased (e.g. Sowers and Bender, 1995; Renssen and Isarin., 2001; Tierney et al., 2008; Blaga et al., 2013; Cheng et al., 2016), which together with the retreat of ice sheets and the increase of greenhouse gas concentrations, induced faster warming of Eurasia with respect to the northern Indian ocean (Peltier, 2004; Joos and Spahni, 2008; Clark et al., 2012; Shakun et al., 2012).

Interestingly, millennial-scale PP and *C. leptoporus* records change in concert with regional climate data, particularly those related to aeolian supply from the Iranian Plateau and summer wind intensity over the western AS (Shakun et al., 2007; Safaierad et al., 2020; Figs. 4.5d, n). They highlight the HS 1 (17.5−15 ka), the B-A (14.8−13 ka), and the YD (12.8−11.5 ka) climate periods i.e., the three stages that correspond to significant changes in the AMOC strength (Figs. 4.5k, q; Elliot et al., 2002; McManus et al., 2004). During the cold HS1 and YD, relatively high PP are accompanied by relatively low Indian summer monsoon rainfall and high aeolian dust deposition over the AS and the Iranian Plateau (Figs 4.5j, l−m), while SST is lower (Figs. 4.5a, b) and the summer southwesterly winds and coastal upwelling are weaker (Figs. 4.5c−e). Conversely, during the warm B-A, low PP is associated with high monsoon rainfall and low aeolian supply, while SST increases, and the summer winds and coastal upwelling strengthen. TraCE, which is forced by North Atlantic melt water fluxes during the deglaciation, simulates a weaker (stronger) upper seawater stratification driven by stronger (weaker) surface cooling during the HS1 and YD (B-A) (Figs. 4.5a, p; Fig. 4.S2). When considering the annual surface winds and seawater stratification, TraCE shows that during the B-A, anomalous southerly winds prevail over the AS, and the stratification gets stronger corresponding to a larger temperature

gradient compared to HS1 (Figs. 4.7g–l). Therefore, it appears that the stratification could be mainly controlled by temperature rather than salinity conditions. Indeed, the temperature gradient fluctuates up to 1 ° C, thanks to significant changes in SST, while changes in salinity gradient are limited within 0.25 psu (Fig. 4.8).

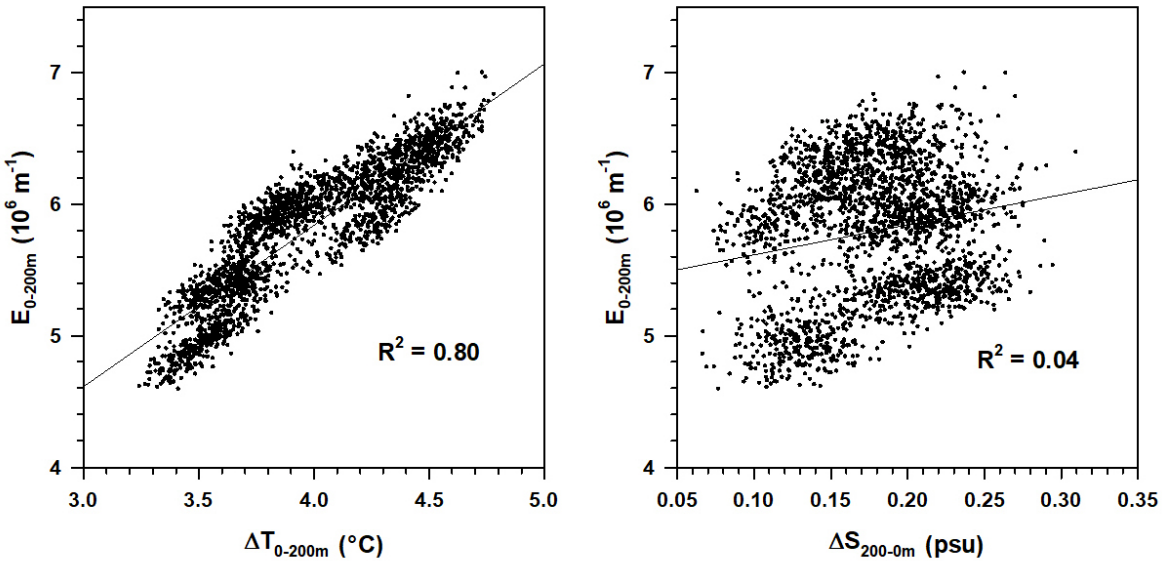

Fig. 4.8. Cross plots showing correlations between $\Delta T_{0\text{-}200m}$ and $E_{0\text{-}200m}$, and between $\Delta S_{200\text{-}0m}$ and $E_{0\text{-}200m}$. The data are the TraCE-21 simulation in the northern Arabian Sea (21°N−23°N, 60°E−68°E) over the past 22 kyr.

These findings suggest that the AMOC controls the inter-hemisphere heat transport (e.g., Liu et al., 2009, Kageyama et al., 2013; Marzin et al., 2013; Obase and Abe-Ouchi, 2019), and hence, millennial-scale climatic changes in the AS (e.g., Schulz et al., 1998; Ivanochko et al., 2005; Shakun et al., 2007). During the HS1 and the YD, weakened AMOC and northward heat transport from the tropical Atlantic made the Euro-Asian continent cooler throughout the year. They reduced and enhanced the land-sea thermal contrasts over the African-Asian monsoon regions during summer and winter respectively, and thus, drove a weaker summer monsoon and a stronger winter one (Fig. 4.S3; Huang et al., 2011; Marzin et al., 2013; Otto-Bliesner et al., 2014; Liu et al., 2014; Wen et al., 2016). It is most probable that colder and dryer surface winds help providing higher bioavailable nutrients to PP through both, stronger aeolian inputs and weaker stratification (Figs. 4.5n, p). During the B-A, when the AMOC recovered, winter monsoon and dust supply were weaker compared to the HS1 and YD, and thus, lower PP is found due to stronger stratification and lower aeolian nutrient input.

Previous studies have demonstrated that the variations of East Asian winter and summer monsoons were anti-phased during the last deglaciation (Huang et al., 2011; Wen et al., 2016). Here, such an anti-phased pattern is revealed by PP that seems, in the same way as during LGM, representative of changes

in winter monsoon intensity (Figs. 4.5c–e; Fig. 4.S3). Indeed, one could have expected an increase of PP during the warm period as SST raised and the coastal upwelling off Somalia and Oman reinforced. However, it clearly appears that fertilization of the euphotic zone under stronger winter monsoon conditions is much more efficient on PP.

4.4 During the Holocene

Values of PP (average of ~200 gC m^{-2} yr^{-1}) and TOC (averages of 0.03 gC cm^{-2} kyr^{-1} and 0.06 gC cm^{-2} kyr^{-1}) obtained at sites MD00-2354 and GEOB 3005 and NIOP464, together with the abundances of *C. leptoporus* (1.2 10^9 n/g) and *G. bulloides* recorded at sites MD00-2354 and ODP723A, show that the Holocene is characterized by the lowest PP values and the highest intensity of coastal upwelling off Somalia-Oman over the past 23 kyr (Figs. 4.5c, e–f). Together with relatively high SST, low aeolian flux, and high monsoon rainfall conditions, they reveal that the warm and humid conditions took place and reached their maximum as the summer monsoon intensified and the winter monsoon weakened compared to the glacial period (Figs. 4.5a, l, m). Overall, the Holocene conditions are well expressed by the MH-CTRL experiments. In particular, it appears that the annual mean atmospheric and ocean simulations reflect summer season patterns that are characterized by stronger southwesterly winds (Figs. 4.6j, 7m, p). The negative wind stress curl anomalies during summer in the western AS can limit the advection of the stronger coastal upwelling off Somalia and Oman resulting in a small area with higher PP (Figs. 4.6j–l; Le Mézo et al., 2017), while PP is generally low elsewhere (Fig. 4.5j). The winter winds simulated by IPSL-CM5 are only slightly stronger in the northern AS (Fig. 6j), and the changes of stratification are limited in both winter and annual mean (Figs. 4.5p–r, 4.7m–r).

In detail, PP and *C. leptoporus* reach minima and maxima values during the EMH (10–8 ka), before showing slightly increasing and decreasing trends, respectively (Figs. 4.5e, h). Such features are consistent with TOC and *G. bulloides* records (Figs. 4.5c, g), as well as with the aforementioned PP and climate data, that testify for slightly lower annual PP and a paroxysmal phase in summer monsoon conditions with stronger coastal upwelling dynamics off Oman and Somalia, and weaker aeolian inputs during the EMH (Fig. 4.5l) (e.g., Gupta et al., 2003; Ivanochko et al., 2005; Jiménez-Espejo et al., 2014). This time interval is probably characterized by an enhanced vegetation cover in today's arid regions surrounding the AS, that reduces the aeolian supply (e.g., Hoelzmann et al., 1998; Davies, 2006; Kuper and Kröpelin, 2006; Engel et al., 2012; Swann et al., 2014). In all cases, these conditions are expected as the result of smaller precession leading to higher Norther Hemisphere summer insolation, and stronger summer monsoon intensity. As such, because of the restricted extension of coastal upwelling cell due to the negative wind stress curl anomalies, the nearly unchanged convective

mixing associated to the slight increase of winter wind intensity, and the weaker aeolian input associated to a wetter period, the annual PP was at a minimum in the northwestern AS. From 8 ka to present, such conditions gradually changed to let the winter monsoon conditions better express and dust supply strengthen, as slightly higher aeolian inputs and slightly higher PP are observed, particularly between 4 and 2 ka.

5. Conclusions

We have provided a record of PP variations in the northwestern AS over the last 23 kyr, reconstructed from the coccolith assemblages of core MD00-2354. Our data show the influence of several processes taking place during both summer and/or winter monsoon seasons and controlling the supply of nutrients in the ocean surface layers either from the subsurface or from surrounding continents. During the LGM, the summer monsoon was weaker and PP was higher relative to the Holocene. This high PP under stronger glacial conditions resulted from the increase of aeolian input, and the strengthened surface cooling-driven mixing associated to a stronger winter monsoon. Our PP record clearly shows millennial-scale variations corresponding to the fluctuations of AMOC and high-latitude climate events. The higher PP during the HS1 and YD cold periods was linked to the strengthened winter monsoon processes under weaker AMOC, while the lower PP during the B-A warm periods was due to an inverse pattern. PP is generally low during the Holocene as the winter monsoon was weaker. During the EMH, the summer monsoon was at maximum but the PP was at minimum. This is because of the restricted advection of summer upwelling cell under negative wind stress curls, limited winter mixing, and lower aeolian input.

References

Agnihotri, R., Dutta, K., Bhushan, R., Somayajulu, B. L. K., 2002. Evidence of solar forcing on the Indian monsoon during the last millennium. Earth and Planetary Science Letter 198, 521−527.

Albani, S., Mahowald, N. M., Murphy, L. M., Raiswell, R., Moore, J. K., Anderson, R. F., McGee, D., Bradtmiller, L. I., Delmonte, B., Hesse, P. P., Mayewski, P. A., 2016. Paleodust variability since the Last Glacial Maximum and implications for iron inputs to the ocean. Geophysical Research Letters 43, 3944–3954, https://doi.org/10.1002/ 2016GL067911.

Albani, S., Balkanski, Y., Mahowald, N., Winckler, G., Maggi, V., Delmonte, B., 2018. Aerosol-climate interactions during the Last Glacial Maximum. Current Climate Change Reports 4, 99–114.

Anderson, D. M., Prell, W. L., 1993. A 300 kyr record of upwelling off Oman during the Late Quaternary: evidence of the Asian Southwest Monsoon. Paleoceanography 8, 193−208.

Abram, N. J., Gagan, M. K., Liu, Z., Hantoro, W. S., McCulloch, M. T., Suwargadi, B. W., 2007. Seasonal characteristics of Indian Ocean Dipole during the Holocene epoch. Nature 445, 299–302.

Ashok, K., Guan, Z., Yamagata, T., 2001. Impacts of the Indian Ocean Dipole on the relationship between the Indian Monsoon rainfall and ENSO. Geophysical Research Letter 28, 4499−4502.

Aumont, O., Bopp, L., 2006. Globalizing results from ocean in situ iron fertilization studies. Global Biogeochemical Cycles 20, GB2017.

Balaji, D., Bhushan, R., Chamyal, L. S., Variations of the Somali upwelling since 18.5 ka BP and its relationship with southwest monsoon rainfall. Climate of the Past 14, 1331−1343.

Bali, K., Mishra, A. K., Singh, S., Chandra, S., Lehahn, Y., 2019. Impact of dust storm on phytoplankton bloom over the Arabian Sea: a case study during March 2012. Environmental Science and Pollution Research 26, 11940−11950.

Banakar, V. K., Oba, T., Chodankar, A. R., Kuramoto, T., Yamamoto, M., Minagawa, M., 2005. Monsoon related changes in sea surface productivity and water column denitrification in the Eastern Araian Sea during the last glacial cycle. Marine Geology 219, 99−108.

Banerjee, P., Prasanna Kumar, S., 2014. Dust-induced episodic phytoplankton blooms in the Arabian Sea during winter monsoon. Journal of Geohysical Research: Oceans 119, 7123–7138.

Barber, D. C., Dyke, A., Hillaire-Marcel, C., Jennings, A. E., Andrews, J. T., Kerwin, M. W., Bilodeau, G., McNeely, R., Southon, J., Morehead, M. D., Gagnon, J.-M., 1999. Forcing of the cold event of 8200 years ago by catastrophic drainage of Laurentide lakes. Nature 400, 344–348.

Bartolacci, D. M., Luther, M. E., 1999. Patterns of co-variability between physical and biological parameters in the Arabian Sea. Deep-Sea Research Ⅱ 47, 1933−1964.

Bassinot, F. C., Beaufort, L., Vincent, E., Labeyrie, L., 1997. Changes in the dynamics of western equatorial Atlantic surface currents and biogenic productivity at the “Mid-Pleostocene Revolution” (~930 ka), in: Shackleton, N. J., Curry, W. B., Richter, C., Bralower, T. J. (Eds.), *Proceedings of the Ocean Drilling Program, Scientific Results*, vol. 154, pp. 269−284.

Bassinot, F. C., Marzin, C., Braconnot, P., Marti, O., Mathien-Blard, E., Lombard, F., Bopp, L., 2011. Holocene evolution of summer winds and marine productivity in the tropical Indian Ocean in response to insolation forcing data-model comparison. Climate of the Past 7, 815−829.

Baumann, K.-H., Freitag, T., 2004. Pleistocene fluctucations in the northern Benguela Current system as revealed by coccolith assemblages. Marine Micropaleontology 52, 195–215.

Bialik, O. M., Auer, G., Ogawa, N. O., Kroon, D., Waldmann, N. D., Ohkouchi, N., 2020. Monsoon, upwelling, and the deoxygenation of the northwestern Indian Ocean in response to Middle to

Late Miocene global climatic shifts. Paleoceanography and Paleoclimatology 35, e2019PA003762. https://doi.org/10.1029/2019PA003762.

Beaufort, L., Barbarin, N., Gally, Y., 2014. Optical measurements to determine the thickness of calcite crystals and the mass of thin carbon particles such as coccoliths, Nature Protocols, 9, 633–642.

Beaufort, L., Lancelot, Y., Camberlin, P., Cayre, O., Vincent, E., Bassinot, F., Labeyrie, L., 1997. Insolation cycles as a major control of Equatorial Indian Ocean primary production, Science, 278, 1451–1454.

Beaufort, L., van der Kaars, S. Bassonot, F. C., Moron, V., 2010. Past dynamics of the Australian monsoon: precession, phase and links to the global monsoon concept. Climate of the Past 6, 695–706.

Behrenfeld, M. J., Falkowski, P. G., 1997. Photosynthetic rates de- rived from satellite-based chlorophyll concentration, Limnology and Oceanography 42, 1–20, 1997.

Blaga, C., Reichar, G.-J., Lotter, A. F., Anselmetti, F. S., Damsté, J. S. S., 2013. A TEX_{86} lake record suggests simultaneous shifts in temperature in Central Europe and Greenland during the last deglaciation. Geophysical Research Letters 40, 948–953.

Boeckel, B., Baumann, K.-H., Henrich, R., Kinkel, H., 2006. Coccolith distribution patterns in South Atlantic and Southern Ocean surface sediments in relation to environmental gradients. Deep-Sea Research Ⅰ 53, 1073–1099.

Böll, A., Schulz, H., Munz, P., Rixen, T., Gaye, B., Emeis, K.-C., Contrasting sea surface temperature of summer and winter monsoon variability in the northern Arabian Sea over the last 25 ka. Palaeogeography, Palaeoclimatology, Palaeoecology 426, 10−21.

Braconnot, P., Harrison, S. P., Kageyama, M., Bartlein, P. J., Masson-Delmotte, V., Abe-Ouchi, A., Otto-Bliesner, B., and Zhao, Y., 2012. Evaluation of climate models using palaeoclimatic data, Nature Climate Change 2, 417–424.

Braconnot, P., Otto-Bliesner, B., Harrison, S., Joussaume, S., Peterchmitt, J.-Y., Abe-Ouchi, A., Crucifix, M., Driesschaert, E., Fichefet, Th., Hewitt, C. D., Kageyama, M., Kitoh, A., Loutre, M.-F., Marti, O., Merkel, U., Ramstein, G., Valdes, P., Weber, L., Yu, Y., and Zhao, Y., 2007 Results of PMIP2 coupled simulations of the Mid-Holocene and Last Glacial Maximum–Part 2: feedbacks with emphasis on the location of the ITCZ and mid- and high latitudes heat budget. Climate of the Past 3, 279–296.

Budziak, D., Schneider, R. R., Rostek, F., Müller, P. J., Bard, E., Wefer, G., 2000. Late Quaternary insolation forcing on total organic carbon and C_{37} alkenone variations in the Arabian Sea. Paleoceanography 15, 307-321.

Cabarcos, E., Flores, J. A., Singh, A. D., Sierro, F. J., 2014. Monsoonal dynamics and evolution of the primary productivity in the eastern Arabian Sea over the past 30 ka. Palaeogeography, Palaeoclimatology, Palaeoecology 411, 249–256.

Cachão, M., Moita, M. T., 2000. *Coccolithus pelagicus*, a productivity proxy related to moderate fronts off Western Iberia. Marine Micropaleontology 39, 131–155.

Cai, Y., Zhang, H., Cheng, H., An, Z., Edwards, R. L., Wang, X., Tan, L., Liang, F., Wang, J., Kelly, M., 2012. The Holocene Indian Monsoon variablility over the southern Tibetan Plateau and its teleconnections. Earth and Planetary Science Letters 335–336 135–144.

Castradori, D., 1993. Calcareous nannofossils and the origin of eastern Mediterranean sapropels. Paleoceanography 8, 459–471.

Charabi, Y., 2009. Arabian summer monsoon variability: Teleconexion to ENSO and IOD. Atmospheric Research 91, 105–107.

Chen, X., Wang, P., 1998. Variations in late Quaternary upper ocean structure of Okina Trough: A nannofossil approach. Science in China (Series D) 41, 290–296.

Cheng, H., Edwards, R. L., Sinha, A., Spötl, C., Yi, L., Chen, S., Kelly, M., Kathayat, G., Wang, X., Li, X., Kong, X., Wang, Y., Ning, Y., Zhang, H., 2016. The Asian monsoon over the past 640,000 years and ice age terminations. Nature 534, 640–646.

Clark, P. U., Shakun, J. D., Baker, P. A., Bartlein, P. J., Brewer, S., Brook, E., Carlson, A. E., Cheng, H., Kaufman, D. S., Liu, Z., Marchitto, T. M., Mix, A. C., Morrill, C., Otto-Bliesner, B. L., Pahnke, K., Russell, J. M., Whitlock, C., Adkins, J. F., Blois, J. L., Clark, J., Colman, S. M., Curry, W. B., Flower, B. P., He, F., Johnson, T. C., Lynch-Stieglitz, J., Markgraf, V., McManus, J., Mitrovica, J. X., Moreno, P. I., Williams, J. W., 2012. Global climate evolution during the last deglaciation. Proceedings of the National Academy of Sciences 109, E1134–E1142.

Collins, W. D., Bitz, C. M., Blackmon, M. L., Bonan, G. B., Bretheton, C. S., Carton, J. A., Chang, P., Doney, S. C., Hack, J. J., Henderson, T. B., Kiehl, J. T., Large, W. G., McKenna, D. S., Santer, B. D., and Smith, R. D., 2006. The Community Climate System Model Version 3 (CCSM3). Journal of Climate 19, 2122–2143.

Conan, S. M.-H., Brummer, G.-J. A., 2000. Fluxes of planktic foraminifera in response to monsoonal upwelling on the Somalia Basin margin. Deep-Sea Research Ⅱ 47, 2207–2227.

Cullen, J. L., Prell, W. L., 1984. Planktonic foraminifera of the north- ern Indian Ocean: Distribution and preservation in surface sediments. Marine Micropaleontology 9, 1–52.

Curry, W. B., Ostermann, D. R., Guptha, M. V. S., Ittekkot, V., 1992. Foraminiferal production and monsoonal upwelling in the Arabian Sea: evidence from sediment traps, in: Prell, C. P., Emeis,

K. C. (Eds.), Upwelling systems: evolution since the Early Miocene. Geological Society Special Publication, vol. 64, pp. 93−106.

Davies, C. P., 2006. Holocene paleoclimates of southern Arabian from lacustrine deposits of the Dhamar highlights, Yemen. Quaternary Research 66, 454–464.

de Garidel-Thoron, T., Beaufort, L., Linsley, B. K., Dannenmann, S., 2001. Millennial-scale dynamics of the East Asian winter monsoon during the last 200,000 years. Paleoceanography 16, 491–502.

Duchamp-Alphonse, S., Siani, G, Michel, E., Beaufort, L, Gally, Y., Jaccard, S. L., 2018. Enhanced ocean-atmosphere carbon partitioning via the carbonate counter pump during the last deglacial. Nature Communications 9, 2396. https://doi.org/ 10.1038/s41467-018-04625-7.

Dufresne, J.-L., Foujols, M.-A., Denvil, S., Caubel, A., Marti, O., Aumont, O., Balkanski, Y., Bekki, S., Bellenger, H., Benshila, R., Bony, S., Bopp, L., Braconnot, P., Brockmann, P., Cadule, P., Cheruy, F., Codron, F., Cozic, A., Cugnet, D., de Noblet, N., Duvel, J.-P., Ethé, C., Fairhead, L., Fichefet, T., Flavoni, S., Friedlingstein, P., Grandpeix, J.-Y., Guez, L., Guilyardi, E., Hauglustaine, D. A., Hourdin, F., Idelkadi, A., Ghattas, J., Jous- saume, S., Kageyama, M., Krinner, G., Labetoulle, S., Lahel- lec, A., Lefebvre, M.-P., Lefevre, F., Levy, C., Li, Z. X., Lloyd, J., Lott, F., Madec, G., Mancip, M., Marchand, M., Masson, S., Meurdesoif, Y., Mignot, J., Musat, I., Parouty, S., Polcher, J., Rio, C., Schulz, M., Swingedouw, D., Szopa, S., Talandier, C., Terray, P., Viovy, N., and Vuichard, N., 2013. Climate change projections using the IPSL-CM5 Earth System Model: from CMIP3 to CMIP5. Climate Dynamics 40, 2123–2165.

Elliot, M., Labeyrie, L., and Duplessy, J.-C.,2002. Changes in North Atlantic deep-water formation associated with the Dansgaard- Oeschger temperature oscillations (60–10ka). Quaternary Science Reviews 21, 1153–1165.

Engel, M., Brückner, H., Pint, A., Wellbrock, K., Ginau, A., Voss, P., Grottker, M., Klasen, N., Frenzel, P., 2012. The early Holocene humid period in NW Saudi Arabia – Sediments, microfossils and palaeo-hydrological modelling. Quaternary International 266, 131–141.

Fincham, M., Winter, A., 1989. Paleoceanographic interpretations of coccliths and oxygen-isotope from the sediment surface of the southwest Indian Ocean. Marine Micropaleontology 13, 325–351.

Findlay, C. S., Giraudeau, J., 2000. Extant calcareous nannoplankton in the Australian Sector of the Southern Ocean (austral summers 1994 and 1995). Marine Micropaleontology 40, 417–439.

Flores, J.-A., Gersonde, R., Sierro, F. J., 1999. Pleistocene fluctuations in the Agulhas Current Retroflection based on the calcareous plankton record. Marine Micropaleontology 37, 1–22.

Flores, J.-A., Marino, M., Sierro, F. J., Hodell. D. A., Charles, C. D., 2003. Calcareous plankton

dissolution pattern and coccolithophore assemblages during the last 600 kyr at ODP Site 1089 (CapeBasin, South Atlantic): paleoceanographic implications. Palaeogeography, Palaeoclimatology, Palaeoecology 196, 409–426.

Fleitmann, D., Burns, S. J., Mudelsee, M., Neff, U., Kramers, J., Mangini, A., Matter, A., 2003. Holocene forcing of the Indian Monsoon recorded in a stalagmite from southern Oman. Science 300, 1737–1739.

Giraudeau, J., 1992. Distribution of recent nannofossil beneath the Benguela system: southwest African continental margin. Marine Geology 108, 219–237.

Guieu, C., Al Azhar, M., Aumont, O., Mahowald, N., Levy, M., Ethé, C., Lachkar, Z., 2019. Major impact of dust deposition on the productivity of the Arabian Sea. Geophysical Research Letters 46, 6736–6744.

Gupta, A. K., Anderson, D. M., Overpeck, J. T., 2003. Abrupt changes in the Asian southwest monsoon during the Holocene and their links to the North Atlantic Ocean. Nature 421, 354−357.

Gupta, A. K., Yuvaraja, A., Prakasam, M., Clemens, S. C., Velu, A., 2015. Evolution of the South Asian monsoon wind system since the late Middle Miocene. Palaeogeography, Palaeoclimatology, Palaeoecology 438, 160−167.

Hernández-Almeida, I., Ausín, B., Saavedra-Pellitero, M., Baumann, K.-H., Stoll, H. M., 2019. Quantitative reconstruction of primary productivity in low latitudes during the last glacial maximum and the mid-to-late Holocene from a global *Florisphaera profunda* calibration dataset, Quaternary Science Reviews, 205, 166–181.

Hoelzmann, P., Jolly, D., Harrison, S. P., Laarif, F., Bonnefille, R., Pachur, H.-J., 1998. Mid-Holocene land-surface conditions in northern Africa and the Arabian peninsula: A dataset for the analysis of biogeophysical feedbacks in the climate system. Global Biogeochemical Cycles 12, 35–51.

Hong, Y. T., Homh, B., Lin, Q. H., Shibata, Y., Hirota, M., Zhu, Y. Y., Leng, X. T., Wang, Y., Wang, H., Yi, L., 2005. Inverse phase oscillations between the East Asian and Indian Ocean summer monsoons during the last 12000 years and paleo-El Niño. Earth and Planetary Science Letters 231, 337–346.

Hourdin, F., Foujols, M.-A., Codron, F., Guemas, V., Dufresne, J.- L., Bony, S., Denvil, S., Guez, L., Lott, F., Ghattas, J., Braconnot, P., Marti, O., Meurdesoif, Y., Bopp, L., 2013. Impact of the LMDZ atmospheric grid configuration on the climate and sensitivity of the IPSL-CM5A coupled model. Climate Dynamics 40, 2167–2192.

Huang, E., Tian, J., Steinke, S., 2011. Millennial-scale dynamics of the winter cold tongue in the southern South China Sea over the past 26 ka and the East Asian winter monsoon. Quaternary

Research 75, 196–204.

Ivanochko, T. S., Ganeshram, R. S., Brummer, G.-J. A., Ganssen, G., Jung, S. J. A., Moreton, S. G., Kroon, D., 2005. Variations in tropical convection as an amplifier of global climate change at the millennial scale. Earth and Planetary Science Letter 235, 302−314.

Jiang, D., Tian, Z., Lang, X, Kageyama, M., Ramstein, G., 2015. The concept of global monsoon applied to the last glacial maximum: A multi-model analysis. Quaternary Science Reviews 126, 126−139.

Jickells, T. D., An, Z. S., Andersen, K. K., Baler, A. R., Bergametti, G., Brooks, N., Cao, J. J., Boyd, P. W., Duce, R. A., Hunter, K. A., Kawahata, H., Kubilay, N., LaRoche, H., Liss, P. S., Mahowald, N., Prospero, J. M., Ridgwell, A. J., Tegan, I. Torres, R., 2005. Global iron connections between desert dust, ocean biogeochemistry, and climate. Science 308, 67−71.

Jiménez-Espejo, F. J., García-Alix, A., Jiménez-Moreno, G., Rodrigo-Gámiz, M., Anderson, R. S., Rodríguez-Tovar, F. J., Martínez-Ruiz, F., Giralt, S., Huertas, A. D., Pardo-Igúzquiza, E., 2014. Saharan aeolian input and effective humidity variations over western Europe during the Holocene from a high altitude record. Chemical Geology 374−375, 1−12.

Joos, F., Spahni, R., 2008. Rates of change in natural and anthropogenic radiative forcing over the past 20,000 years. Proceedings of the National Academy of Sciences of the United States of America 105, 1425−1430.

Jung, S. J. A., Davies, G. R., Ganssen, G., Kroon, D., 2002. Decadal-centennial scale monsoon variations in the Arabian Sea during the Early Holocene. Geochemistry, Geophysics, Geosystems 3, 1060. https://doi.org/10.1029/2002GC000348.

Kageyama, M., Merkel, U., Otto-Bliesner, B., Prange, M., Abe-Ouchi, A., Lohmann, G., Ohgaito, R., Roche, D. M., Singarayer, J., Swingedouw, D., X Zhang, 2013. Climatic impacts of fresh water hosing under Last Glacial Maximum conditions: a multi-model study. Climate of the Past 9, 935–953.

Kinkel, H., Baumann, K.-H., Cepek, M., 2000. Coccolithophores in the equatorial Atlantic Ocean: response to seasonal and Late Quaternary surface water variability. Marine Micropaleontology 39, 87–112.

Krinner, G., Viovy, N., de Noblet-Ducoudré, N., Ogée, J., Polcher, J., Friedlingstein, P., Ciais, P., Sitch, S., and Prentice, I. C., 2005. A dynamic global vegetation model for studies of the cou- pled atmosphere-biosphere system. Global Biogeochemical Cycles 19, GB1015.

Krishnamurthy, V., Kirtman, B. P., 2003. Variability of the Indian Ocean: Relation to monsoon ENSO. Q. J. R. Meteorol. Soc. 129, 1623−1646.

Kumar, K. K., Rajagopalan, B., Cane, M. A., 1999. On the weakening relationship between Indian Monsoon and ENSO. Science 284, 2156−2159.

Kumar, K. K., Rajagopalan, B., Hoerling, M., Bates, G., Cane, M., 2006. Unraveling the mystery of Indian Monsoon failure during El Niño. Science 314, 115−119.

Kuper, R., Kröpelin, S., 2006. Climate-controlled Holocene occupation in the Sahara: Motor of Africa's evolution. Science 313, 803−807.

Lambert, F., Kug, J-S., Park, R. J., Mahowald, N., Winckler, G., Abe-Ouchi, A., O'ishi, R., Takemura, T., Lee, J-H., 2013. The role of mineral-dust aerosols in polar temperature amplification. Nature Climate Change 3, 487−491.

Lamy, F., Gersonde, R., Winckler, G., Esper, O., Jaeschke, A., Kuhn, G., Ullermann, J., Martinez-Garcia, A., Lambert, F., Kilian, R., 2014. Increased dust deposition in the Pacific Southern Ocean during glacial periods. Science 343, 403−407.

Laskar, J., Robutel, P., Joutel, F., Gastineau, M., Correia, A. C. M., and Levrard, B., 2004. A long-term numerical solution for the insola- tion quantities of the Earth, Astronomy and Astrophysics, 428, 261–285.

Lee, C. M., Jones, B. H., Brink, K. H., Fischer, A. S., 2000. The upper-ocean response to monsoonal forcing in the Arabian Sea: seasonal and spatial variability. Deep-Sea Research II 47, 1177−1226.

Le Mézo, P., Beaufort, L., Bopp, L., Braconnot, P., Kageyama, M., 2017. From monsoon to marine productivity in the Arabian Sea: insights from glacial and interglacial climates. Climate of the Past 13, 759−778.

Liu, C., Wang, P., Tian, J., Cheng, X., 2008. Coccolith evidence for Quaternary nutricline variations in the southern South China Sea. Marine Micropaleontology 69, 42–51.

Liu, X., Liu, Z., Clemens, S., Prell, W., Kutzbach, J., 2007. A coupled model study of glacial Asian Monsoon variability and Indian Ocean Dipole. Journal of the Meteorological Society of Japan 85, 1–10.

Liu, Z., Otto-Bliesner, B. L., He, F., Brady, W. C., Tomas, R., Clark, P. U., Carlson, A. E., Lynch-Stieglitz, J., Curry, W., Brook, E., Erickson, D., Jacob, R., Kutzbach, J., and Cheng, J., 2009. Transient Simulation of Last Deglaciation with a new mechanism for Bølling-Allerød Warming. Science 325, 310–314

Liu, Z., Wen, X., Brady, E. C., Otto-Bliesner, B., Yu, G., Lu, H., Cheng, H., Wang, Y., Zheng, W., Ding, Y., Edward, R. L., Cheng, J., Liu, W., Yang, H., 2014. Chinese cave records and the East Asia Summer Monsoon. Quaternary Science Reviews 83, 115–128.

Madec, G., 2008. NEMO ocean engine, Note du pôle de modélisation, Institut Pierre-Simon Laplace (IPSL), Paris, France, No. 27, ISSN 1288-1619.

Maher, B. A., Prospero, J. M., Mackie, D., Gaiero, D., Hesse, P. P., Balkanski, Y., 2010. Global connections between aeolian dust, climate and ocean biogeochemistry at the present day and at the last glacial maximum. Earth-Science Reviews 99, 61–97.

Malinverno, E., Ziveri, P., Corselli, C., 2003. Coccolithophorid distribution in the Ionian Sea and its relationship to eastern Mediterranean circulation during late fall to early winter 1997. Journal of Geophysical Research 108, C98155.

Marino, M., Maiorano, P., Lirer, F., 2008. Changes in calcareous nannofossil assemblages during the Mid-Pleistocene Revolution. Marine Micropaleontology 69, 70–90.

Martínez-García, A., Rosell-Melé, A., Geibert, W., Gersonde, R., Masqué. P., Gaspari, V., Barbante, C., 2009. Links between iron supply, marine productivity, sea surface temperature, and CO_2 over the last 1.1 Ma. Paleoceanography 24, PA1207, https://doi.org/ 10.1029/2008PA001657.

Marzin, C., Kallel, N., Kageyama, M., Duplessy, J.-C., and Braconnot, P., 2013. Glacial fluctuations of the Indian monsoon and their rela- tionship with North Atlantic climate: new data and modelling experiments. Climate of the Past 9, 2135–2151.

Mashat, A.-W. S., Alamoudi, A. O., Awad, A. M., Assiri, M. E., 2018. Seasonal variability and synoptic characteristics of dust cases over southwestern Saudi Arabia. International Journal of Climatology 38, 105–124.

McManus, J. F., Francois, R., Gherardi, J.-M., Keigwin, L. D., and Brown-Leger, S., 2004. Collapse and rapid resumption of Atlantic meridional circulation linked to deglacial climate changes. Nature 428, 834–837.

Molfino, B., McIntyre, A., 1990. Precessional forcing of nutricline dynamics in the Equatorial Atlantic. Science 249, 766–769.

Molfino, B., McIntyre, A., 1996. Forcing of Atlantic equatorial and subpolar millennial cycles by precession. Science 274, 1867–1870.

Murton, J. B., Bateman, M. D., Dallimore, S. R., Teller, J. T., Yang, Z., 2010. Identification of Younger Dryas outburst flood path from Lake Agassiz to the Arctic Ocean. Nature 464, 740–743.

Naidu, P. D., Malmgren, B. A., 1996. A high-resolution of late Quaternary upwelling along the Oman Margin, Arabian Sea based on planktonic foraminifera. Paleoceanography 11, 129−140.

Naik, D. K., Saraswat, R., Lea, D. W., Kurtarkar, S. R., Mackensen, A., 2017. Last glacial-interglacial productivity and associated changes in the eastern Arabian Sea. Palaeogeography, Palaeoclimatology, Palaeoecology 483, 147−156.

Notaro, M., Yu, Y., Kalashnikova, O. V., Regime shift in Arabian dust activity, triggered by persistent Fertile Crescent drought. Journal of Geophysical Research: Atmospheres 120, 10299−10249.

Obase, T., Abe-Ouchi, A., 2019. Abrupt Bølling-Allerød warming simulated under gradual forcing of the last deglaciation. Geophysical Research Letters, 46, 11397–11405.

Okada, H., Mastsuoka, M., 1996. Lower-photic nannoflora as an indicator of the late Quaternary monsoonal palaeo-record in the tropical Indian Ocean, in: *Proceedings of the "ODP and the Marine Biosphere" International Conference, 1994*.

Otto-Bliesner, B. L., Brady, E. C., Clauzet, G., Tomas, R., Levis, S., & Kothavala, Z., 2006. Last Glacial Maximum and Holocene climate in CCSM3. Journal of Climate 19, 2526–2544.

Otto-Bliesner, B. L., Russell, J. M., Clark, P. U., Liu, Z., Overpeck, J. T., Konecky, B., deMenocal, P., Nicholson, S. E., He, F., Lu, Z., 2014. Coherent changes of southeastern equatorial and northern African rainfall during the last deglaciation. Science 346, 1223–1227.

Overpeck, J., Anderson, D., Trumbore, S., Prell, W., 1996. The south-west Indian Monsoon over the last 18 000 year. Climate Dynamics 12, 213–225.

Pattan, J. N., Masuzawa, T., Naidu, P. D., Parthiban, G., Yamamoto, M., 2003. Productivity fluctuations in the southeastern Arabian Sea during the last 140 ka. Palaeogeography, Palaeoclimatology, Palaeoecology 193, 575−590.

Patterson, R. T., Fishbein, E., 1984. Re-examination of the statistical methods used to determine the number of point counts needed for micropaleontological quantitative research, J. Paleontol., 63, 245–248.

Patra, P. K., Dileep Kumar, M., Mahowald, N., Sarma, V. V. S. S., 2007. Atmospheric deposition and surface stratification as controls of contrasting chlorophyll abundance in the North Indian Ocean. Journal of Geophysical Research 112, C05029, https://doi.org/10.1029/2006JC003885.

Peltier, W. R., 2004. Global glacial isostasy and the surface of the ice-age earth: The ICE-5G (VM2) model and grace. Annual Review of Earth and Planetary Sciences 32, 111–149.

Pourmand, A., Marcantonio, F., Schulz, H., 2004. Variations in productivity and eolian fluxes in the northeastern Arabian Sea during the past 110 ka. Earth and Planetary Science Letters 221, 39−54.

Pourmand, A., Marcantonio, F., Bianchi, T. S., Canuel, E. A., Waterson, E. J., 2007. A 28-ka history of sea surface temperature, primary productivity and planktonic community variability in the western Arabian Sea. Paleoceanography 22, PA4208, https://doi.org/10.1029/2007PA001502.

Prasanna Kumar, S., Madhupratap, M., Dileep Kumar, M., Muraleedharan, P. M., de Souza, S. N., Ganus, M., Sarma, V. V. S. S., 2001a. High biological productivity in the central Arabian Sea during the summer monsoon driven by Ekman pumping and lateral advection. Current Science

81, 1633−1638.

Prasanna Kumar, S., Ramaiah, N., Ganus, M., Sarma, V. V. S. S., Muraleedharan, P. M., Raghukumar, S., Dileep Kumar, M., Madhupratap, M., 2001b. Physical forcing of biological productivity in the Northern Arabian Sea during the Northeast Monsoon. Deep-Sea Research Ⅱ 48, 1115−1126.

Prasanna Kumar, S., Muraleedharan, P. M., Prasad, T. G., Ganus, M., Ramaiah, N., de Souza, S. N., Sardesai, S., Madhupratap, M., 2002. Why is the Bay of Bengal less productive during summer monsoon compared to the Arabian Sea? Geophysical Research Letter 29, 2235, https://doi.org/ 10.1029/2002GL016013.

Prasanna Kumar, S., Narvekar, J., 2005. Seasonal variability of the mixed layer in the central Arabian Sea and its implication on nutrients and primary productivity. Deep-Sea Research Ⅱ 52, 1848−1861.

Ramaswamy, V., Muraleedharan, P. M., Prakash Babu, C., 2017. Mid-troposphere transport of Middle-East dust over the Arabian Sea and its e ect on rainwater composition and sensitive ecosystems over India. Scientific Reports 7, 13676, https://doi.org/ 10.1038/s41598-017-13652-1.

Reichart, G. J., den Dulk, M., Visser, H. J., van der Weijden, C. H., Zachariasse, W. J., 1997. A 225 kyr record of dust supply, paleoproductivity and the oxygen minimum zone from the Murray Ridge (northern Arabian Sea). Palaeogeography, Palaeoclimatology, Palaeoecology 134, 149−169.

Renssen, H., Isarin, R. F., B., 2001. The two major warming phases of the last deglaciation at ~ 14.7 and ~ 11.5 ka cal BP in Europe: climate reconstructions and AGCM experiments. Global and Planetary Change 30, 117−153.

Rezazadeh, M., Irannejad, P., Shao, Y., 2013. Climatology of the Middle East dust events. Aeolian Research 10, 103−109.

Rogalla, U., Andruleit, H., 2005. Precessional forcing of coccolithophore assemblages in the northern Arabian Sea: Implications for monsoonal dynamics during the last 200,000 years. Marine Geology 217, 31−48.

Saavedra-Pellitero, M., Baumann, K.-H., Ullermann, J., 2017. Marine Isotope Stage 11 in the Pacific sector of the Southern Ocean; a coccolithophore perspective. Quaternary Science Reviews 158, 1–14.

Safaierad, R., Mohtadi, M., Zolitschka, B., Yokoyama, Y., Vogt, C., Schefuß, E., 2020. Elevated dust depositions in West Asia linked to ocean–atmosphere shifts during North Atlantic cold events. Proceedings of the National Academy of Sciences of the United States of America 117, 18272−18277.

Schott, F. A., McCreary, J. P., 2001. The monsoon circulation of the Indian Ocean. Progress in

Oceanography 52, 1−123.

Schulz, H., von Rad, U., Erlenkeuser, H., 1998. Correlation between Arabian Sea and Greenland climate oscillations of the past 110,000 years. Nature 393, 54−57.

Schulz, H., von Rad, U., Ittekkot, V., 2002. Planktic foraminifera, particle flux and oceanic productivity off Pakistan, NE Arabian Sea: modern analogues and application to the paleoclimatic record, in: Clift, P. D., Kroon, D., Gaedicke, D., Craig, J. (Eds.), The tectonic and climatic evolution of the Arabian Sea region. Geological Society, London, Special Publication, vol. 195, pp. 499−516.

Schulte, S., Müller, P. J., 2001. Variations of sea surface temperature and primary productivity during Heinrich and Dansgaard-Oeschger events in the northwestern Arabian Sea. Geo-Marine Letters 21, 168−175.

Shakun, J. D., Burns, S. J., Fleitmann, D., Kramers, J., Matter, A., Al-Subary, A., 2007. A hgh-resolution, absolute dated deglacial speleothem record of Indian Ocean climate from Socotra Island, Yemen, Earth and Planetary Science Letters 259, 442−456.

Shakun, J. D., Clark, P. U., He, F., Marcott, S. A., Mix, A. C., Liu, Z., Otto-Bilesner, B., Schmittner, A., Bard, E., 2012. Global warming preceded by increasing carbon dioxide concentrations during the last deglaciation. Nature 484, 49−54.

Shimmield, G. B., Mowbray, S. R., Weedon, G. P., 1990. A 350 ka history of the Indian Southwest Monsoon—evidence from deep-sea cores, northwest Arabian Sea. Transactions of the Royal Society of Edinburgh: Earth Science 81, 289−299.

Singh, R. P., Prasad, A. K., Kayetha, V., K., Kafatos, M., 2008. Enhancement of oceanic parameters associated with dust storms using satellite data. Journal of Geophysical Research 113, C11008. https://doi.org/10.1029/2008JC004815.

Singh, A. D., Jung, S. J. A., Darling, K., Ganeshram, R., Ivanochko, T., Kroon, D., 2011. Productivity collapses in the Arabian Sea during glacial cold phases. Paleoceanography 26, PA3210. https://doi.org/10.1029/2009PA001923.

Sowers, T., Bender, M., 1995. Climate records covering the last deglaciation. Science 269, 210−214.

Stuiver, M., Grootes, P. M., 2000. GISP2 oxygen isotope ratios. Quaternary Research 53, 277−284.

Su, X., Liu, C., Beaufort, L., Tian, J., Huang, E., 2013. Late Quaternary coccolith records in the South China Sea and East Asian monsoon dynamics. Global and Planetary Change 111, 88−96.

Swann, A. L. S., Fung, I. Y., Liu, Y., Chiang, J. C. H., 2014. Remote vegetation feedbacks and the Mid-Holocene Green Sahara. Journal of Climate 27, 4857−4870.

Taylor, K. E., Stouffer, R. J., and Meehl, G. A.,2012. An overview of CMIP5 and the experiment design, Bulletin of the American Meteorological Society 93, 485–498.

Tierney, J. E., Russel, J. M., Huang, Y., Damsté, J. S. S., Hapmans, E. C., Cohen, A. S., 2008. Northern Hemisphere controls on tropical southeast African climate during the Past 60,000 years. Science 322, 252–255.

Tierney, J. E., Zhu, J., King, J., Malevich, S. B., Hakim, G. J., Poulsen, C. J., 2020. Glacial cooling and climate sensitivity revisited. Nature 584, 569−573.

Jung, S. J. A., Davies, G. R., Ganssen, G., Kroon, D., 2002. Decadal-centennial scale monsoon variations in the Arabian Sea during the Early Holocene. Geochemistry, Geophysics, Geosystems 3, 1060. https://doi.org/10.1029/2002GC000348.

Wang, B., Ding, Q., 2008. Global monsoon: Dominant mode of annual variation in the tropics. Dynamics of Atmospheric and Oceans 44, 165−183.

Wen, X., Liu, Z., Wang, S., Cheng, J., Zhu, J., Correlation and anti-correlation of the East Asian summer and winter monsoons during the last 21,000 years. Nature Communications 7, 11999, https://doi.org/ 10.1038/ncomms11999.

Winckler, G., Anderson, R. F., Fleisher, M. Q., McGee, D., Mahowald, N., 2008. Covariant glacial-interglacial dust fluxes in the equatorial Pacific and Antarctica. Science 320, 93−96.

Yu, S.-Y., Colman, S. M. Lowell, T. V., Milne, G. A., Fisher, T. G., Breckenridge, A., Boyd, M., Teller, J. T., 2010. Freshwater outburst from Lake Superior as a trigger for the cold event 9300 years ago. Science 328, 1262–1266.

Yu Y., Notaro, M., Liu, Z., Kalashnikova, O., Alkolibi, F., Fadda, E., Bakhrjy, F., 2013. Assessing temporal and spatial variations in atmospheric dust over Saudi Arabian through satellite, radiometric, and station data. Journal of Geophysical Research: Atmospheres 118, 13253−13264.

Zhang, H., Liu, C., Jin, X., Shi, J., Zhao, S., Jian, Z., 2016. Dynamics of primary productivity in the northern S outh C hina S ea over the past 24,000 years. Geochemistry, Geophysics, Geosystems 17, 4878–4891.

Ziegler, M., Lourens, L. J., Tuenter, E., Reichart, G.-J., 2010a. High Arabian Sea productivity conditions during MIS 13 – odd monsoon event or intensified overturning circulation at the end of Mid-Pleistocene transition? Climate of the Past 6, 63−76.

Ziegler, M., Lourens, L. J., Tuenter, E., Hilgen, F., Reichart, G.-J., 2010b. Precession phasing offset between Indian summer monsoon and Arabian Sea productivity linked to changes in Atlantic overturning circulation. Paleoceanography 25, PA3213, https://doi.org/10.1029/2009PA001884.

Zhou, X., Duchamp-Alphonse, S., Kageyama, M., Bassinot, F., Beaufort, L., Colin, C., 2020. Dynamics of primary productivity in the northeastern Bay of Bengal over the last 26 000 years. Climate of the Past 16, 1969−1986.

Supplementary figures

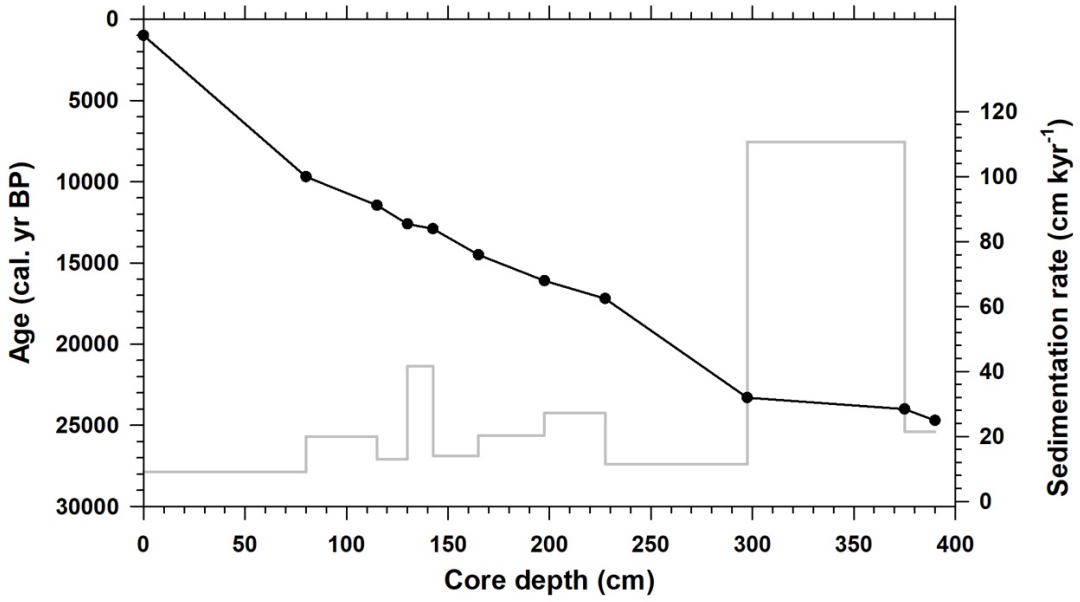

Fig. 4.S1. Age model and linear sedimentation rates of core MD00-2354. Dots are the calendar age in GISP2 ice core oxygen isotope record (Böll et al., 2015).

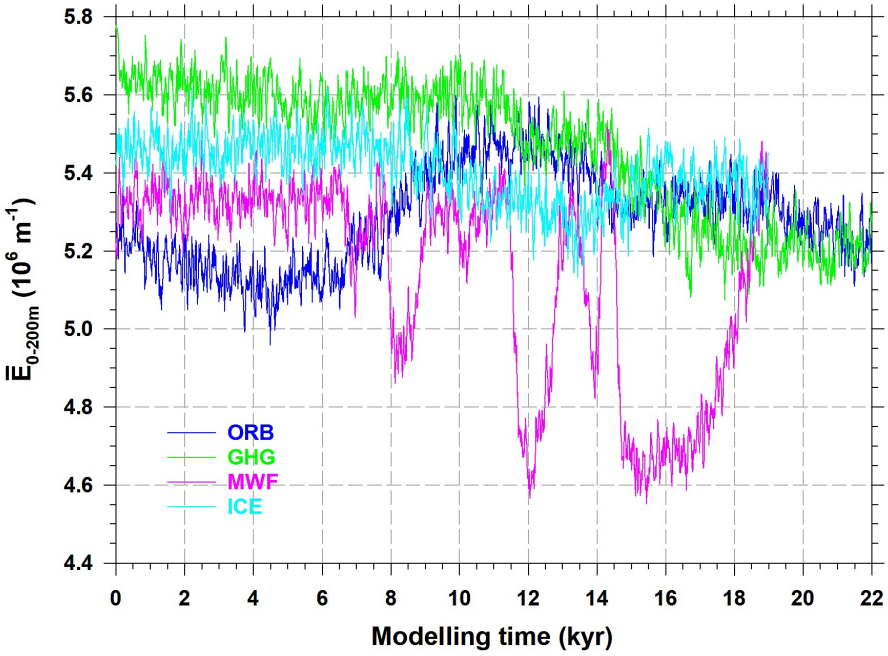

Fig. 4.S2. Results of $E_{0\text{-}200m}$ simulated by TraCE-21 single forcing experiments: (ORB) orbital parameter, (GHG) greenhouse gases concentrations, (MWF) melt water flux that can drive the AMOC to change, and (ICE) ice sheets volumes.

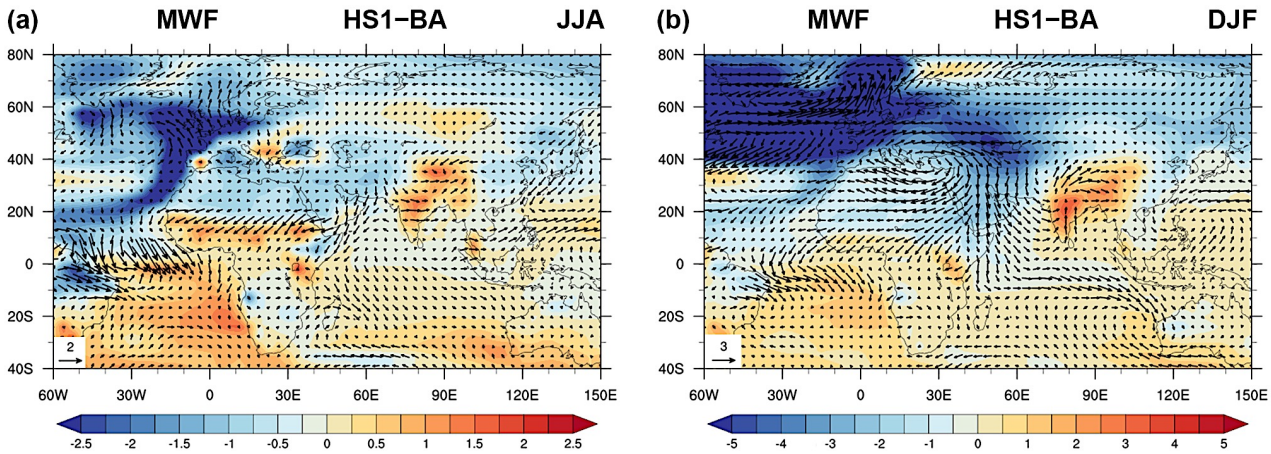

Fig. 4.S3. Differences of surface temperature (color, °C) and surface wind (vector, m s^{-1}) between the Heinrich Stadial 1 (HS1, 17−15.5 ka) and Bølling–Allerød (BA, 14.7−13 ka during (a) winter and (b) summer in the MWF single forcing experiment. These differences indicate the responses of meridional and land-sea thermal gradients, and summer and winter monsoons a ~6 Sv weakening of the AMOC.

Chapter 5

Evolution of the upper seawater stratification in the northern Indian Ocean since the Last Glacial Maximum and its relationship with the dynamics of summer and winter monsoons

In this chapter, I combine the two records of Florisphaera profunda (%) previously obtained in the northeastern Bay of Bengal (Chapter 3) and the northwestern Arabian Sea (Chapter 4) to provide a regional overview of the evolution of the upper seawater stratification over the last 22 kyr. Modern observations reveal that the stratification patterns of these two basins are linked to the Indian summer and winter monsoons, respectively. Therefore, these two records, combined with published data, and compared to outputs from TraCE-21, have the potential to help better understanding summer vs winter monsoons dynamics in the past. I suggest that the Indian summer and winter monsoons intensities have in-phased responses to the glacial-interglacial difference and orbital forcing, and for the responses to the AMOC strength during the last deglaciation, they are anti-phased on millennial scale.

1. Introduction

Modern observations show that the upper seawater stratification of the northern Bay of Bengal (BoB) and Arabian Sea (AS) are highly controlled by Indian summer and winter monsoons, respectively (Prasanna Kumar et al., 2002; Vinayachandran et al., 2002; Prasad et al., 2004). During summer, the southwesterly winds blowing from the ocean transport a huge amount of moisture that result in heavy rainfall over South Asia (Wang and Ding, 2008). This rainfall leads to an important amount of freshwater input to the northern BoB and Andaman Sea (ADS), either from the direct rainfall over the seas or from the runoffs of Ganges-Brahmaputra-Meghna and Irrawaddy–Salween river systems. The strong freshwater input results in low SSS that forms a barrier layer making the upper seawater very stable in the BoB and ADS (Howden and Murtugudde, 2001; Vinayachandran et al., 2002; Sengupta et al., 2006; Thadathil et al., 2007; Akhil et al., 2014). Conversely, in the northern and western AS, rainfall is much weaker, and strong surface evaporation occurs, which together result in high SSS (Prasanna Kumar and Prasad, 1999; Rao and Sivakumar, 2003). During winter, the northeasterly winds blow from Eurasia driven by the Siberian high pressure, resulting in relatively dry conditions over the northern Indian Ocean. They are accompanied by a strong surface cooling in the northern AS, which makes the upper seawater very instable (Prasanna Kumar and Prasad, 1996; Prasanna Kumar et al., 2001; Prasanna Kumar and Narvekar, 2005). Remarkably, previous studies revealed that the stability of the upper seawater in the northern AS is one order of magnitude lower than in the northern BoB (Prasanna Kumar et al., 2002). Additionally, the Siberian high pressure during winter has significant impacts on the Northern Hemisphere climate over a large area of Eurasia (Cohen et al., 2001; Hasanean et al., 2013; Riaz et al., 2017; Labban et al., 2020; Salahi et al., 2020).

As previously highlighted in Chapters 1, 3, and 4, the Indian summer monsoon variability since the LGM, is better documented than the winter monsoon, thanks to the occurrence of numerous proxies associated to rainfall (see Chapters 1, 3, and 4) (e.g. Kudrass et al., 2001; Rashid et al., 2007; Contreras-Rosales et al., 2014; Dutt et al., 2015; Kathayat et al., 2016). Indeed, proxies related to winter monsoon are lacking and only a very few low-resolution records exist in the AS, showing stronger winter monsoon during the LGM with respect to the Holocene (Fig. 1.15 in Chapter 1) (e.g., Sarkar et al., 1990; Mahesh and Banakar, 2014). Compared to Indian winter monsoon over the northern Indian Ocean, the variability of East Asian winter monsoon in the past is better studied (e.g. Huang et al., 2011; Wang et al., 2012; Zhang et al., 2016). Wen et al., (2016) have proposed that the East Asian summer and winter monsoons are anti-phased on millennial-scale during the deglaciation in response to the oscillations of AMOC. They have shown that the winter (summer) monsoon was stronger during

HS1 and YD (B-A). However, the relationship between Indian summer and winter monsoons is seldom studied. In parallel, *Florisphaera profunda* (Fp%) records previously obtained in the northeastern BoB (Chapter 3) and the northwestern AS (Chapter 4) appear to be directly associated to the position of the nutricline during summer and winter monsoons, respectively. Studied together, they open the field of possibilities when referring to these climate conditions since the LGM.

Here, I discuss Fp% data from marine sediment cores MD77-176 and MD00-2354 in terms of upper seawater stratification in the northeastern BoB and northwestern AS since the LGM, respectively. Together with published records of South Asian rainfall, SSS, and SST, as well as paleoclimate simulations of TraCE-21 (termed TraCE in the following) they are helpful to understand the mechanisms that control stratifications of both basins, reconstruct summer and winter monsoon dynamics, and discuss the processes at play. Particularly, the millennial resolution of the datasets during the deglaciation offers the possibility to discuss the relationship between seawater stratification, summer/winter Indian monsoon, and the AMOC.

2. Data

2.1. Empirical data

Information about age models of sites MD77-176 (14.52°N, 93.13°E) and MD00-2354 (21.04°N, 61.48°E), together with their Fp% records, are available in Chapters 3 (Zhou et al., 2020) and 4 (Zhou et al., in preparation), respectively. Fp% data of core MD77-176 have been compared with SSS and SST data from core SO93-126KL from the northern BoB and core RC12-344 from the ADS (Kudrass et al., 2001; Rashid et al., 2007). SST in core SO93-126KL was estimated by alkenones ($U_{37}^{K'}$), while SST in core RC12-344 was based on the Mg/Ca ratio obtained on planktonic foraminifera. SSS in both cores is quantified by the seawater $\delta^{18}O$ anomaly ($\delta^{18}O_{SW}$) i.e. the temperature- and ice volume-correlated planktonic foraminifera $\delta^{18}O$. Such pair-measurements of SST and $\delta^{18}O$ are not available in the northern Arabian Sea. Fp% data of core MD00-2354 have been compared to the alkenone-SST record of core 136KL from the northern AS (Schulz and Müller, 2001), and the $\delta^{18}O_{SW}$−SSS record of core 905 from western AS (Anand et al., 2008). The south Asian rainfall signals come from the speleothem $\delta^{18}O$ record from the Mawnluh Cave, located in northeastern India (Dutt et al., 2015), and the hydrogen isotope (δD) signal of terrestrial plant waxes of core SO188-342KL, retrieved in the northern BoB (Contreras-Rosales et al., 2014). All the locations of the records are shown in Fig. 5.1.

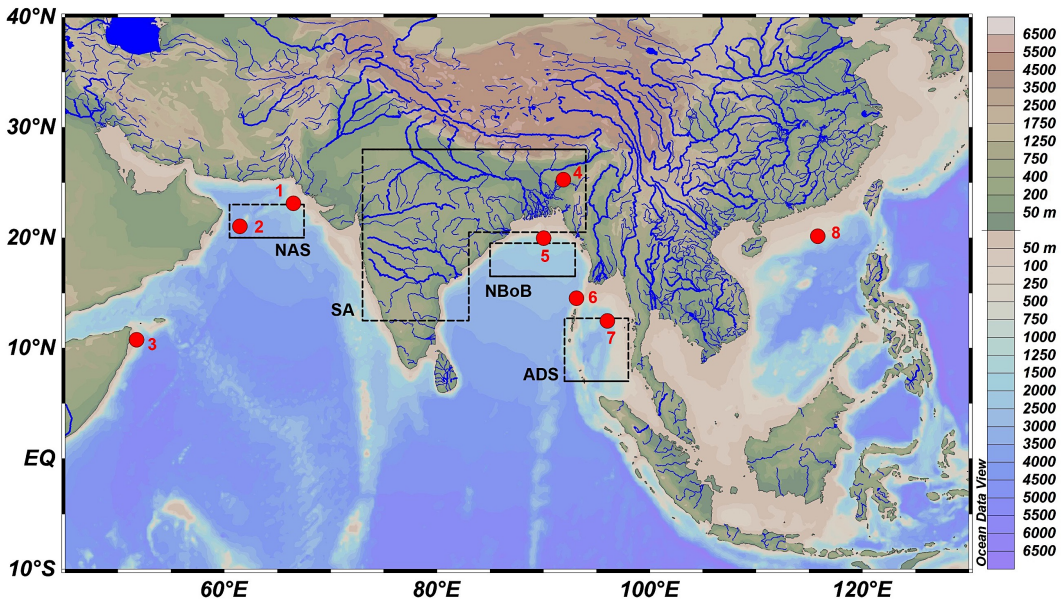

Fig. 5.1. Geographic setting and bathymetric map created by the Ocean Data View software (©Reiner Schlitzer, Alfred Wegener Institute) with its built-in global high-resolution bathymetric data (GlobHR). The red dot marks the location of core MD00-2354 for PP reconstruction in this study. The red dots and cross mark the locations of sediment cores and speleothem with published paleoenvironmental records discussed in this study: 1 = 136KL, 2 = MD00-2354, 3 = 905, 4 = Mawmluh Cave; 5 = SO93-126KL and SO188-342KL, 6 = MD77-176, 7 = RC12-344, and 8 = MD12-3428. The black rectangles or polygon mark the regions with modelling data extraction.

2.2. Modelling data

Information about TraCE-21 is provided in Chapter 1. Here, I focus on three oceanic regions (Fig. 5.1): the northern BoB (NBoB; 16°N−19°N, 85°E−93°E), the ADS (7°N−12°N, 92.5°E−96.5°E), and the northern AS (NAS; 20°N−23°N, 60°E−68°E). The extracted variables are SST, SSS, the temperature at 200 m (T_{200m}), salinity at 200 m (S_{200m}), and the upper seawater stratification. The salinity (temperature) gradient of the upper seawater is quantified by the difference between 200 m (the surface) and the surface (200 m), termed $\Delta S_{200\text{-}0m}$ ($\Delta T_{0\text{-}200m}$). The stratification is calculated by the vertically averaged stable stability of the upper 200 m ($E_{0\text{-}200m}$, m^{-1}; Prasanna Kumar et al., 2002). E is the stable stability at single depths: $E = -(1/\rho)\cdot(\partial\rho/\partial z)$, where z is the water depth, and ρ is seawater in-situ density.

The South Asian rainfall is represented by the area of average precipitation in the polygonal region (SA; Fig. 5.1). I also use the Indian summer monsoon index quantified by the area of average vertical shear of southerly winds (ISMVI; difference of V winds between 850 and 200 hPa levels) over the region between 10°N−30°N and 70°E−110°E (Goswami et al., 1999), and the Siberian High index quantified by the area of average sea level pressure (SLP minus 1000 hPa) over the region between 40°N−60°N and 80°E−120°E (Wu and Wang, 2002) to evaluate the dynamics of Indian summer and winter monsoons.

3. Evolution of the stratification over the last 22 kyr

3.1. The northeastern Indian Ocean

Core MD77-176 has been retrieved at the junction between the BoB and the ADS, and seawater conditions from both basins could have significant influences on the stratification pattern over the site. However, when comparing the Fp% record to TraCE stratification simulations for both basins, it appears that it is rather consistent with the patterns of the ADS, particularly consider the offset between the LGM and the Holocene (Fig. 5.2c). In the NBoB, TraCE simulates significantly stronger stratification during the LGM with respect to the Holocene (Fig. 5.2b).

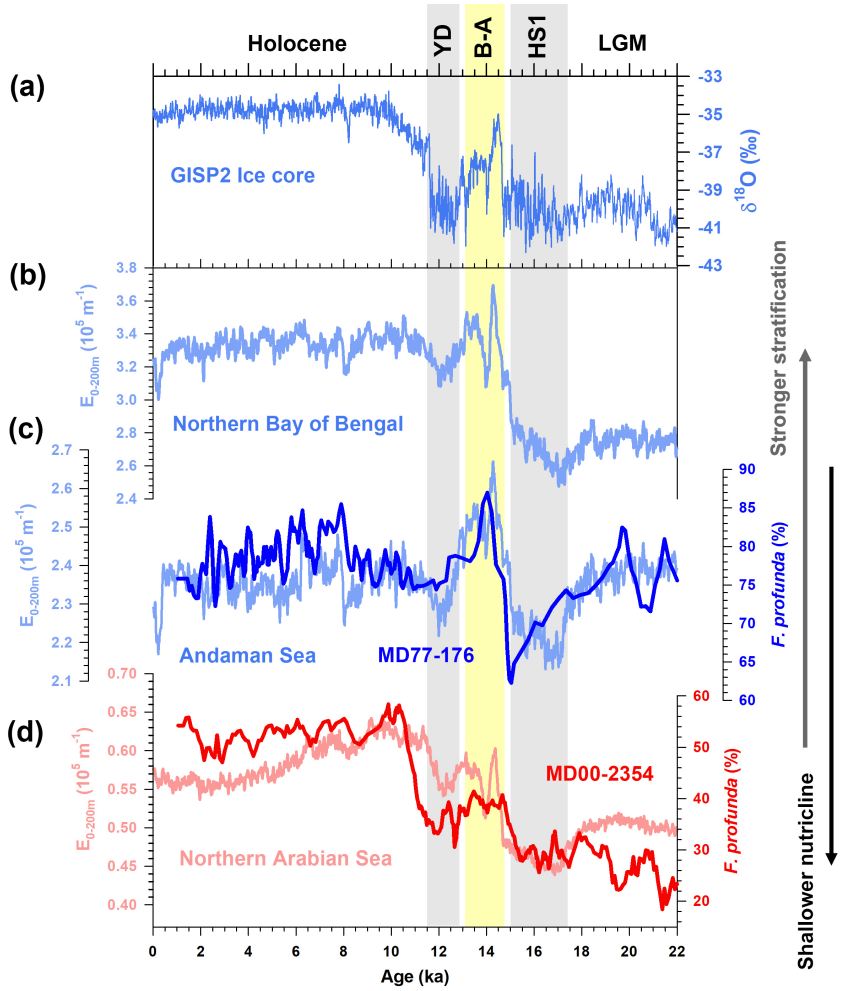

Fig. 5.2. (a) GISP2 ice oxygen isotope record (Stuiver and Grootes, 2000). (b) TraCE-21 simulated annual mean $E_{0\text{-}200m}$ (upper seawater stratification) in the northern Bay of Bengal (NBoB; Fig. 1). (c) TraCE-21 simulated annual mean $E_{0\text{-}200m}$ in the Andaman Sea (ADS; Fig. 1) and the *F. profunda* % record of core MD77-176 (Zhou et al., 2020). (d) TraCE-21 simulated annual mean $E_{0\text{-}200m}$ in the northern Arabian Sea (NAS; Fig. 1) and the *F. profunda* % record of core MD00-2354 (Zhou et al., in preparation). The larger value of $E_{0\text{-}200m}$ indicates stronger upper seawater stratification. The lower value of *F. profunda* % indicates shallower nutricline and weaker upper seawater stratification. HS1 = Heinrich Stadial 1; B-A = Bølling–Allerød; YD = Younger Dryas; LGM = Last Glacial Maximum.

In detail, Fp% average values, and thus the ADS stratification are comparable between the LGM (~ 78 % and 2.4×10^5 m^{-1}) and the Holocene (~ 78 % and 2.37×10^5 m^{-1}). The strongest variability occurs during the last deglaciation and is in phase with the abrupt climate changes recorded in northern high latitudes, as revealed by the Greenland GISP2 ice core $\delta^{18}O$ (Fig. 5.2a). Lower Fp%, which indicates a shallower nutricline and a weaker upper seawater stratification, is found during the cold periods of HS1 and YD, while higher Fp%, which reflects a deeper nutricline and a stronger stratification, is recorded during the warm period of B-A (Fig. 5.2c). During the Holocene, the Fp% maximum is recorded at ~8 ka.

3.2. Upper seawater stratification in the northern Arabian Sea

In general, the Fp% curve obtained at site MD00-2354 shows similar a trend as the simulated stratification in NAS, and particularly during the deglaciation that, as for site MD77-176, is associated with significant variations (Fig. 5.2d). The simulated stratification during LGM (0.5×10^5 m^{-1}) is stronger than during the Holocene (0.6×10^5 m^{-1}). Although this difference also reflects in the Fp% curve, the patterns of simulated stratification and Fp% show discrepancies with each other. For example, Fp% during the LGM is lower than during the HS1, which is opposite to the simulated stratification. Such discrepancies are probably linked to the fact that coccolith assemblages and thus, *F. profunda* can be modulated by secondary factors than the upper sea water stratification. It is not excluded that relatively low Fp% during LGM testify for higher aeolian input to the AS during the LGM (Pourmand et al., 2004, 2007), as previously documented in chapter 4. Indeed, it might be associated with higher nutrient supplies to surface waters and higher proportions of upper dweller forms such as *Gephyrocapsa* spp. and *Emiliania huxleyi* at the expense of *F. profunda*. In all cases, during the deglaciation, Fp% are relatively low during HS1 and YD, and relatively high during the B-A. Fp% maximum is found during the Holocene (up to 56 %), at ~10 ka, which is consistent with the simulated stratification maximum (0.63×10^5 m^{-1}; Fig. 5.2d).

3.3. Inter-basin discrepancy of control factors

As highlighted by reconstructed records and revealed by TraCE outputs shown here, changes in SSS are the largest in BoB, and the weakest in the AS over the last 22 kyr, especially during the deglaciation (Kudrass et al., 2001; Anand et al., 2008; Figs. 5.3a, c). The limited variability of the signal from the AS shows that SSS is not the major forcing factor behind seawater structure in this basin (Fig. 5.3c). Changes in SST are significant in both basins. However, the AS registers variations with a higher magnitude between the LGM and the Holocene, but also during the HS1, B-A, and YD

climate periods (Fig. 5.3f). This is mainly associated to the fact that the LGM and the HS1 both witness a ~ 3 ° C surface cooling in the NAS, which is larger than the cooling in the NBoB and ADS (Fig. 5.3d–f).

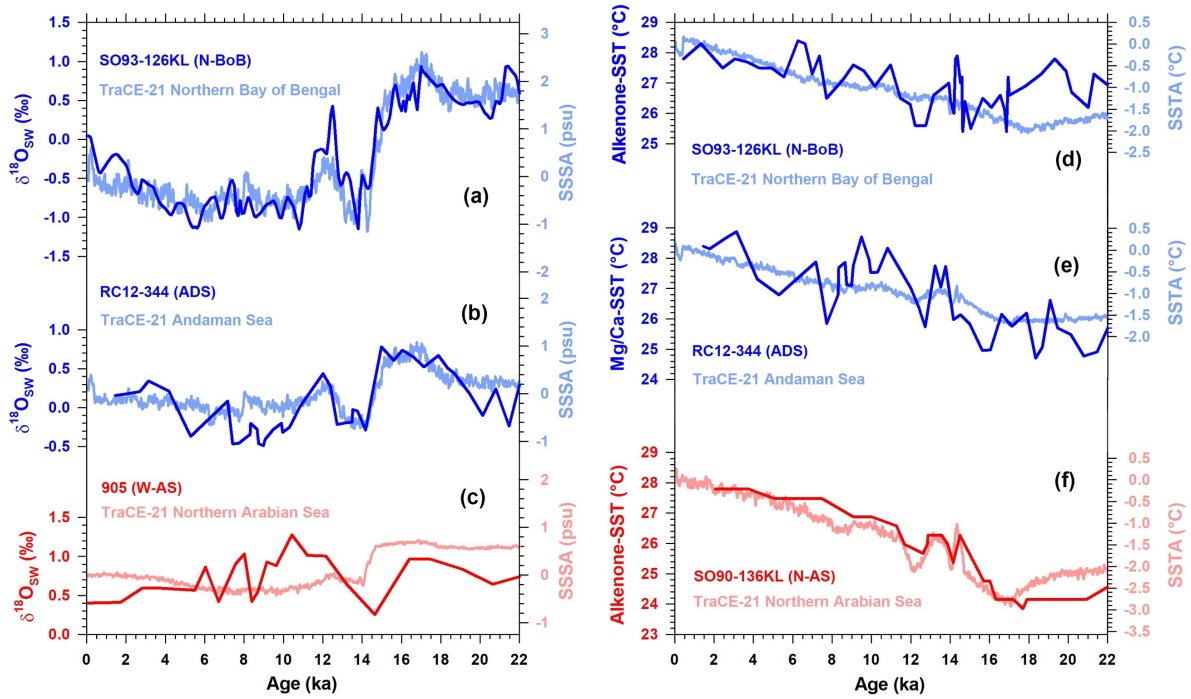

Fig. 5.3. The and reconstructed TraCE-21 simulated (a–c) SSS and (d–f) SST in studied areas (see sections 2.1 and 2.2) (Kudrass et al., 2001; Schulz and Müller, 2001; Rashid et al., 2007; Anand et al., 2008). The regions of modelling data extraction are marked in Fig.5.1.

TraCE cross plots between the seawater temperature/salinity and the upper layer stratification are provided in Fig. 5.4. In the NBoB and ADS, as revealed by R^2 values of 0.97 and 0.81 between $\Delta S_{200\text{-}0m}$ and $E_{0\text{-}200m}$, and by R^2 values of 0.19 and 0.24 between $\Delta T_{0\text{-}200m}$ and $E_{0\text{-}200m}$, it appears that the upper seawater stratification is correlated to the salinity gradient rather than the temperature one in these regions (Figs. 5.4a, b, e, f, 5.S1). Notably, the salinity gradient is mainly controlled by SSS changes rather than the subsurface salinity (Figs. 5.4c, d, g, h). In the AS, according to the R^2 values of 0.09 between $\Delta S_{200\text{-}0m}$ and $E_{0\text{-}200m}$, and by R^2 values of 0.82 between $\Delta T_{0\text{-}200m}$ and $E_{0\text{-}200m}$, it appears that the stratification is correlated to the temperature gradient, rather than the salinity one (Figs. 5.4, 5.S1). However, changes in the temperature gradient are complex. While it seems mainly controlled by SST during the LGM and the deglaciation, lower SST does not correspond to weaker stratification over the Holocene (Figs. 5.4k, l). The subsurface temperature has a larger range of variations during that period: when the cooling at the subsurface is stronger than the surface, the temperature gradient is larger, and this is accompanied by a stronger stratification (Fig. 5.S1).

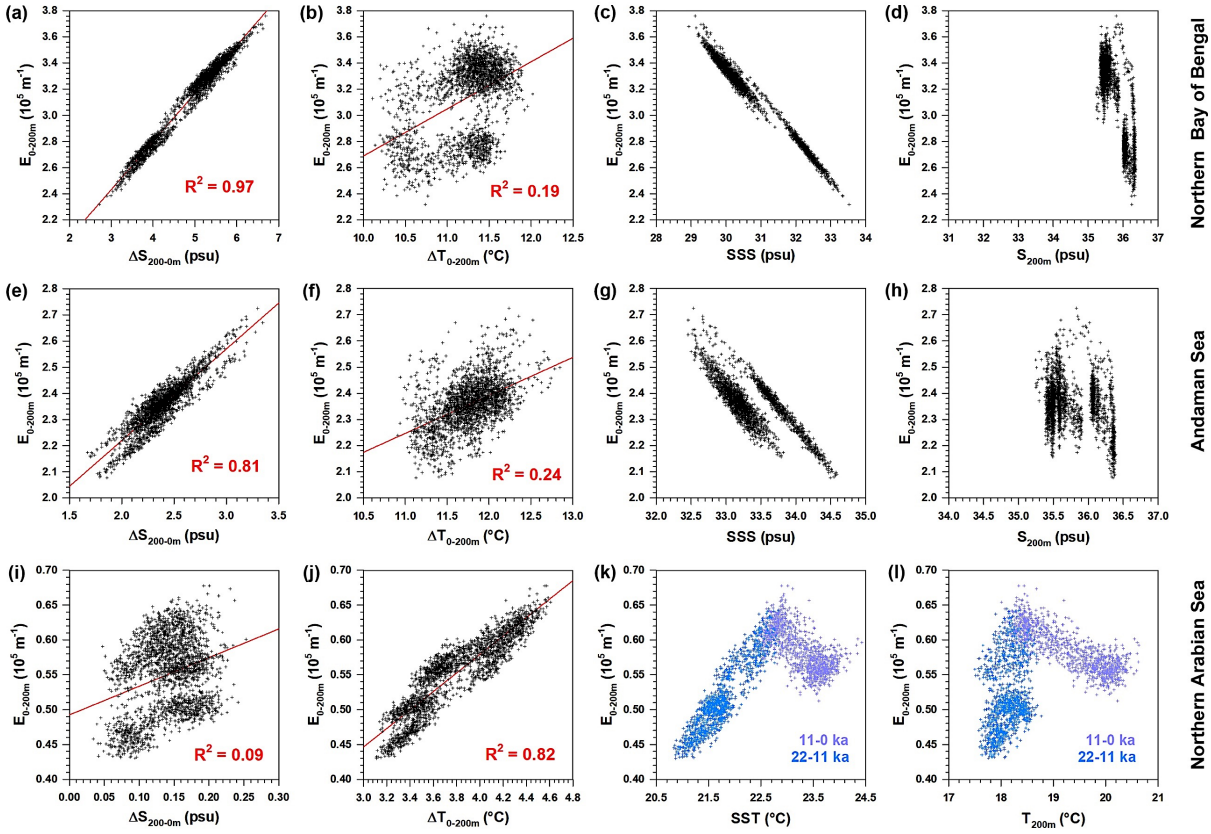

Fig. 5.4. Cross plots showing correlations between TraCE-21 simulated oceanic variables over the last 22 kyr in (a−d) the northern Bay of Bengal (NBoB; Fig. 5.1), (e−h) the Andaman Sea (ADS; Fig. 5.1), and northern Arabian Sea (NAS; Fig. 5.1). The variables are described in section 2.2.

3.3.2 Relationship between upper seawater stratification and Indian monsoon

3.3.2.1. During summer

Simulated annual and summer precipitation curves obtained by TraCE in South Asia since the LGM are well in agreement with the reconstructed ones based on sedimentary plant wax δD and speleothem $\delta^{18}O$ (Fig. 5.5), and confirm that summer monsoon rainfall mainly contributes to the annual mean (Fig. 5.5h). It also clearly appears that when South Asian rainfall is stronger, SSS in the BoB/ADS is lower due to higher river runoff and freshwater input (Figs. 5.5i, j), while Fp% (and thus, stratification) is higher (stronger) (Fig. 5.2c). In other words, summer monsoon rainfall drives stratification patterns in the BoB. The TraCE simulation reveals a stronger correlation (R^2=0.94) between annual precipitation and SSS in the BoB than in the ADS (R^2=0.66) (Figs. 5.5d, e). In ADS, the SSS during LGM is not significantly higher when the summer monsoon is weaker (Figs. 5.3b). This is probably because of a relative freshness in this region, a result of basin morphology during sea-level low stand as proposed by Sijinkumar et al. (2016). As highlighted above (section 3.1), the result of Fp% of MD77-176 implies that during the LGM the core site is probably more influenced by the seawater from the ADS.

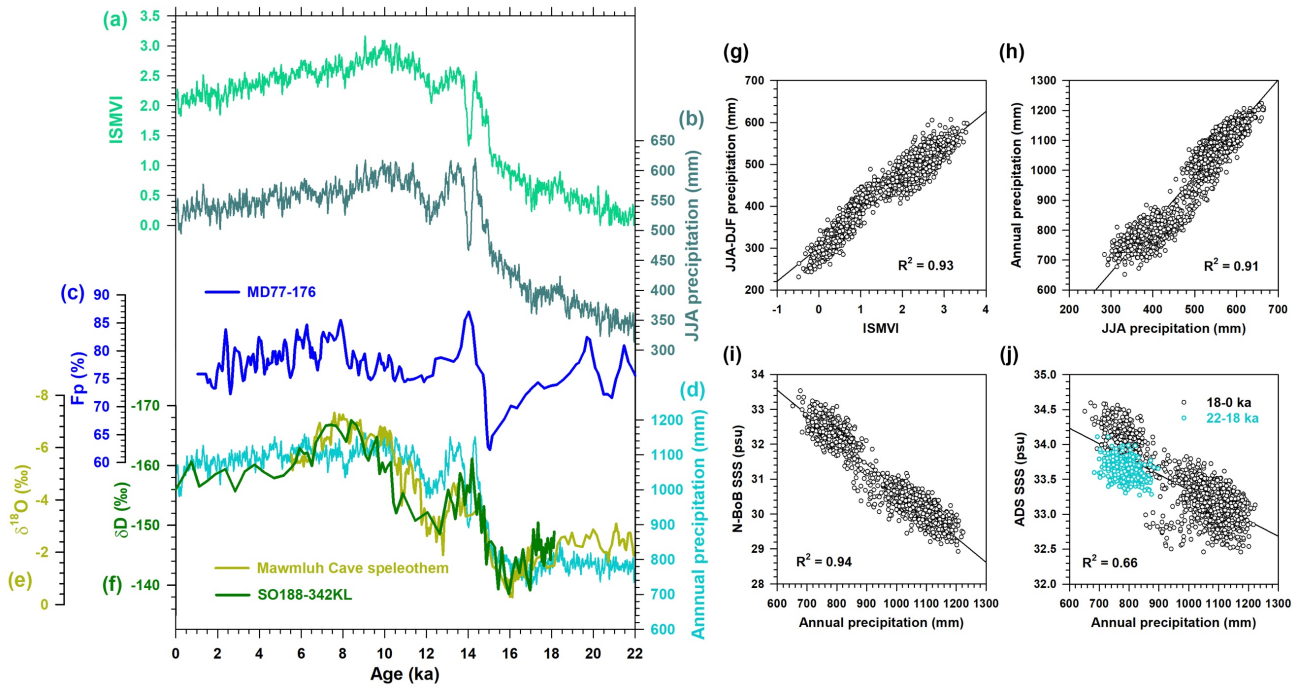

Fig. 5.5. (a) TraCE-21 simulated Indian summer monsoon index and (b) summer precipitation over South Asia. (c) *F. profunda* % record of MD77-176 (Zhou et al., 2020). (d) TraCE-21 simulated annual precipitation over South Asia. (e) Mawmluh cave speleothem δ18O and (f) core SO188-342KL plant was δD both indicating precipitation (Dutt et al., 2015; Contreras-Rosales et al., 2014). Cross plots show correlations of TraCE-21 simulate variables: (b) Indian summer monsoon index vs the precipitation discrepancy between summer and winter (seasonality), (c) summer precipitation vs annual precipitation, (d) annual precipitation vs SSS in the northern Bay of Bengal, and (d) annual mean precipitation vs SSS in the Andaman Sea. The regions of modelling data extraction are marked in Fig.5.1.

Consequently, the Fp% record of MD77-176 reflects local SSS-related stratification, and it can represent the summer monsoon variations, particularly from 19 ka to the present. The record indicates stronger summer monsoon during B-A and Early-Mid Holocene, and weaker summer monsoon during HS1 and YD (Fig. 5.5c).

3.3.2.2. During winter

The Siberian High Index (SHI) simulated by TraCE that represents the Asian winter monsoon forcing, has the same glacial-interglacial trend as the SST anomaly and the Fp% record of MD00-2354 obtained in the northern AS (Figs. 5.6a–c). This confirms that winter monsoonal winds mainly contribute to the stratification of the AS since the LGM. It needs to be pointed out that the maximum in stratification documented at the Early Holocene by an Fp% peak does not correspond to a minimum in surface cooling (Figs. 5.6b, c). Since the winter monsoon-related Fp% record obtained in the northern South China Sea shows relatively high values at that time, particularly when comparing to the Late Holocene (Liu et al., 2002; Chen, 2005; Zhang et al., 2006; Fig. 5.6d), it implies that the winter monsoon is not the only control factor of seawater stratification in the northern AS during the

Holocene. As documented above (section 3.3.1), the stratification pattern of the AS that is well correlated to the temperature gradient during the LGM and the deglaciation seems complex during the Holocene. TraCE provides an interpretation that the subsurface cooling at Early Holocene is stronger than the surface cooling resulting in a larger temperature gradient (Figs. 5.6e, f). However, such a mechanism has not been documented by empirical data so far. It could be linked to an anomalous shallow overturning circulation in the western AS (Schott, 2005; Meng et al., 2020), but further studies are needed to better understand the mechanisms.

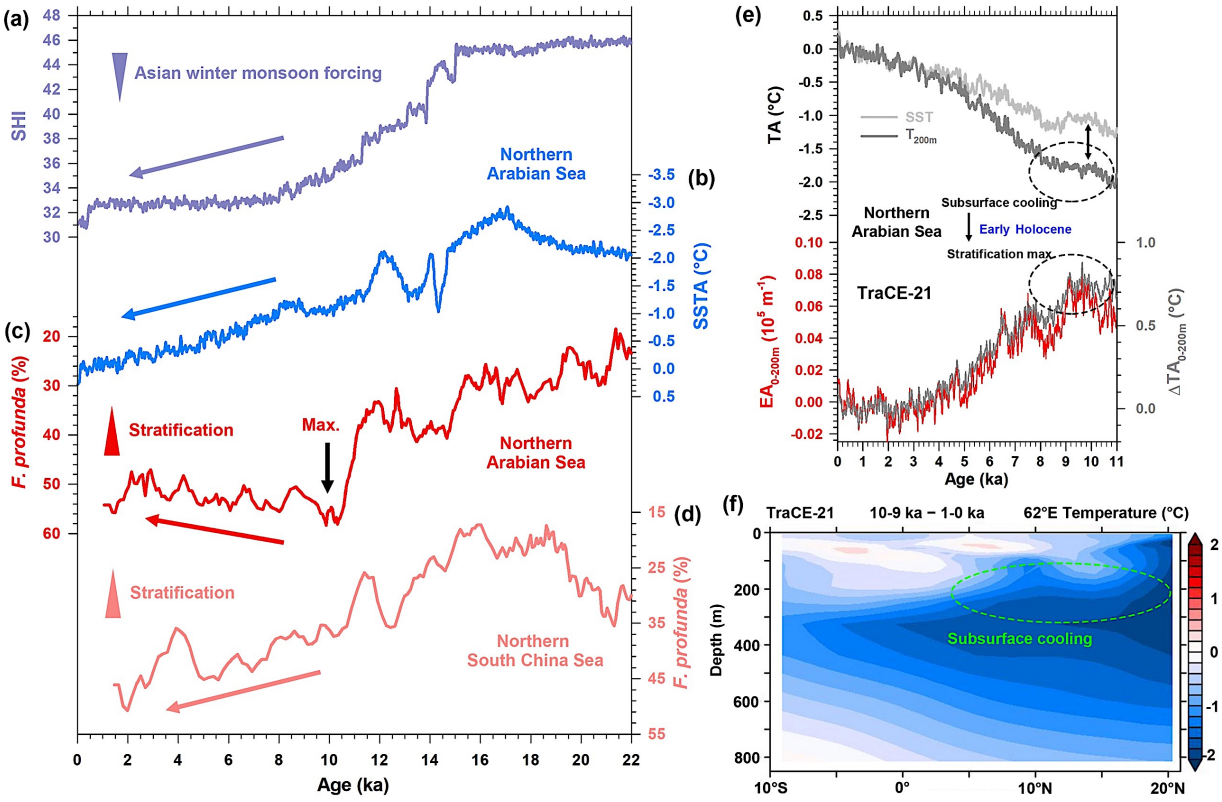

Fig. 5.6. (a−d) The TraCE-21 simulated Siberian High index (SHI), surface cooling in the northern Arabian Sea quantified by the SST values minus the Late Holocene mean (1−0 ka), and *F. profunda* % records of cores MD00-2354 from the northern Arabian Sea (Zhou et al., in preparation) and core MD12-3428 from the northern South China Sea (Zhang et al., 2016). The stratification maximum in the northern Arabian Sea is found during the Early Holocene. (e) The anomalies of surface temperature, subsurface temperature cooling, temperature gradient, and stratification in the northern Arabian Sea simulated by the TraCE-21. The anomalies are calculated by the values minus the Late Holocene means. (f) The 62° E longitude slice of annual mean seawater temperature simulated by TraCE-21. The values are the differences between the Early (10−9 ka) and Late Holocene (1−0 ka).

Consequently, at least for the LGM and the deglaciation, the Fp% record of MD00-2354 mainly reflects SST-related stratification in the northern AS, and represents winter monsoon variations, particularly before the Holocene. The record indicates stronger winter monsoon during the LGM, HS1, and YD, and weaker winter monsoon during the B-A.

3.3.3. Relationship between the meridional thermal contrast and Indian summer/winter monsoon dynamics

The simulation of surface temperature and sea level pressure by TraCE show that changing meridional/land-sea contrast is in phase with the winter vs summer monsoon dynamics documented above (section 3.3.2) (Figs. 5.7 and 5.8).

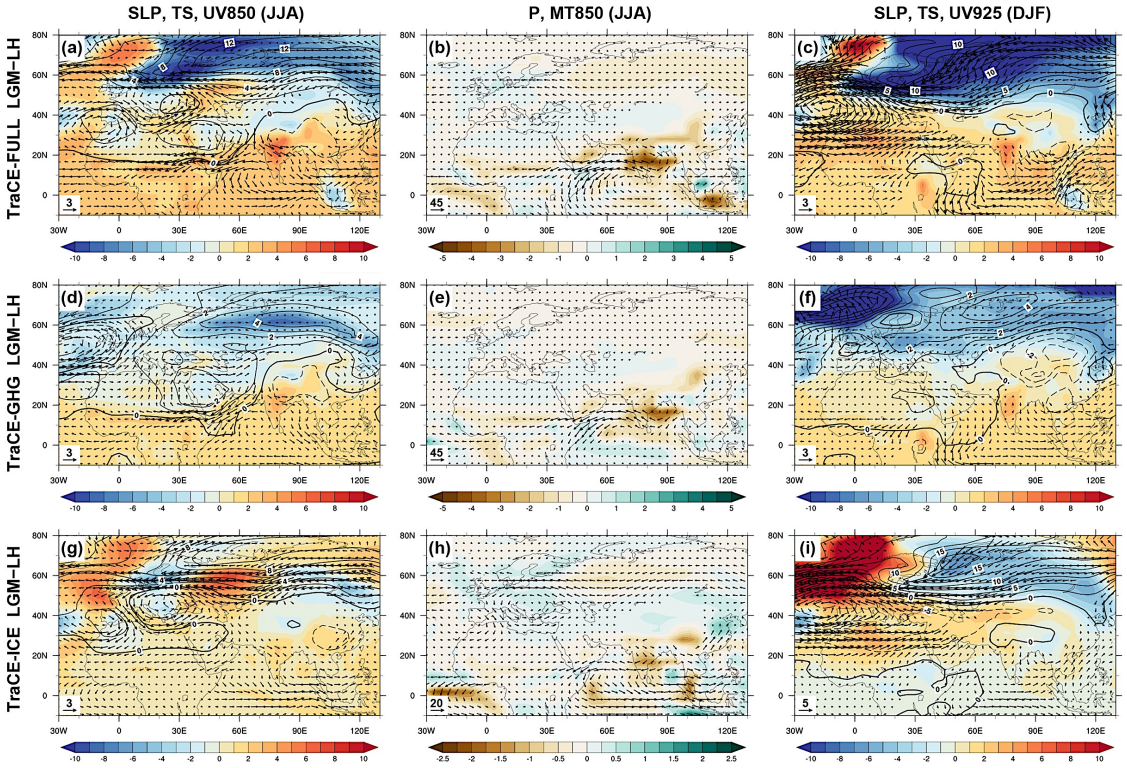

Fig. 5.7. Differences between LGM (21−20 ka or 19−18 ka) and Late Holocene (1−0 ka) in (a−c) TraCE-21 full simulation, (d−f) TraCE-21 greenhouse gas single forcing experiment, and (g−i) TraCE-21 ice sheet single forcing experiment. (Left column) Summer (JJA) sea level pressure (SLP, contours, hPa), surface temperature (TS, shaded, ° C), and wind vectors at 850 hPa level (UV850, vectors, m s^{-1}). (Middle column) Summer precipitation rate (P, shaded, mm day^{-1}) and moisture transport at 850 hPa level (MT850, vectors, g kg^{-1} m s^{-1}). (Right column) Winter (DJF) sea level pressure, surface temperature, wind vectors at 925 hPa level (UV925). The SLP and TS differences are subtracted by the globally averaged differences.

Differences between the LGM and the Late Holocene show that under LGM conditions that are characterized by larger ice sheets and lower greenhouse gases concentrations (Peltier, 2004; Joos and Spahni, 2008), a strong cooling occurs over North Europe throughout the year, with an extension westward and northward to Mongolia-Siberia and the subtropics (Figs. 5.7a, c). It results in a smaller meridional gradient of sea level pressure during summer and a larger one during winter, thanks to the redistribution of heat. The strengthening of the Siberian High is much stronger than the pressure over the Indian Ocean, which drives northerly wind anomalies over the northern Indian Ocean in both

summer and winter seasons. The moisture transport over the AS during summer is, therefore, weaker leading to a drier climate over South Asia (Fig. 5.7b). Interestingly, the single forcing experiments of TraCE indicate that the lower greenhouse gas condition (and not necessarily larger ice sheets) mainly drive the meridional gradients and the anomalous winds over the AS blowing from the lands (Figs. 5.7d–i).

The main forcing factor influencing Indian summer and winter monsoons dynamics during the Holocene is the precession parameter. During the Early Holocene, precession is smaller than during the Late Holocene, resulting in higher North Hemisphere summer isolation and lower winter insolation (Marzin et al., 2009; Wen et al., 2016). Because of the land-sea discrepancy of heat capacity, the meridional thermal and sea level pressure gradients are larger both, in summer and winter, and thus the summer and winter monsoons are stronger (Figs. 5.8a–c). The stronger summer southwesterly winds over the AS drive a stronger moisture transport and a wetter climate over South Asia, while the stronger winter northerly winds are associated with stronger surface cooling.

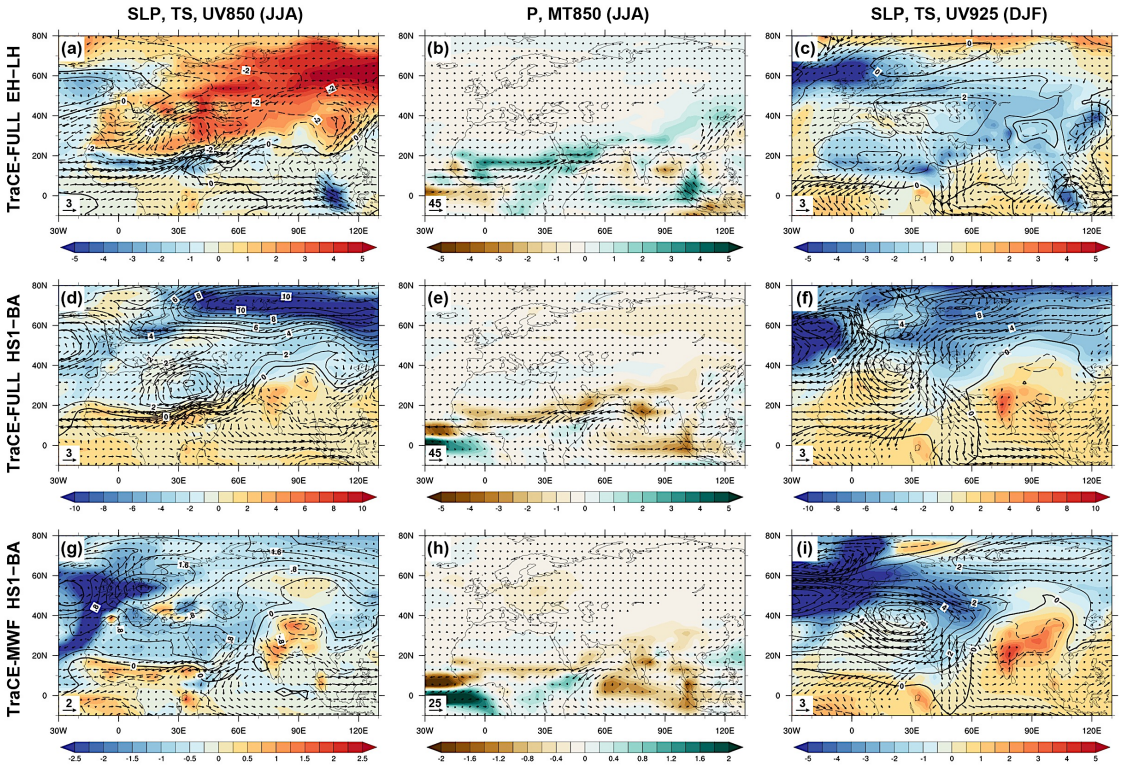

Fig. 5.8. (a–c) Differences between Early Holocene (10–8 ka) and Late Holocene (1–0 ka) in TraCE-21 full simulation. (d–f) Differences between Heinrich Stadial 1 (17–15.5 ka) and Bølling–Allerød (14.7–13 ka) in TraCE-21 full simulation. (g–i) Differences between Heinrich Stadial 1 (17–15.5 ka) and Bølling–Allerød (14.7–13 ka) in TraCE-21 melt water flux experiment. (Left column) Summer (JJA) sea level pressure (SLP, contours, hPa), surface temperature (TS, shaded, °C), and wind vectors at 850 hPa level (UV850, vectors, m s^{-1}). (Middle column) Summer precipitation rate (P, shaded, mm day^{-1}) and moisture transport at 850 hPa level (MT850, vectors, g kg^{-1} m s^{-1}). (Right column) Winter (DJF) sea level pressure, surface temperature, wind vectors at 925 hPa level (UV925). The SLP and TS differences are subtracted by the globally averaged differences.

The last deglaciation witnesses the millennial-scale fluctuations of the AMOC corresponding the abrupt meltwater flux events (McManus et al., 2004; Clement et al., 2008) (Fig. 5.9a). The two Fp% records well in agreement with the simulated ISMVI and SHI during this period, indicate the phases on millennial scale between the Indian summer and winter monsoons (Figs. 5.9b, c). Obviously, they are anti-correlated.

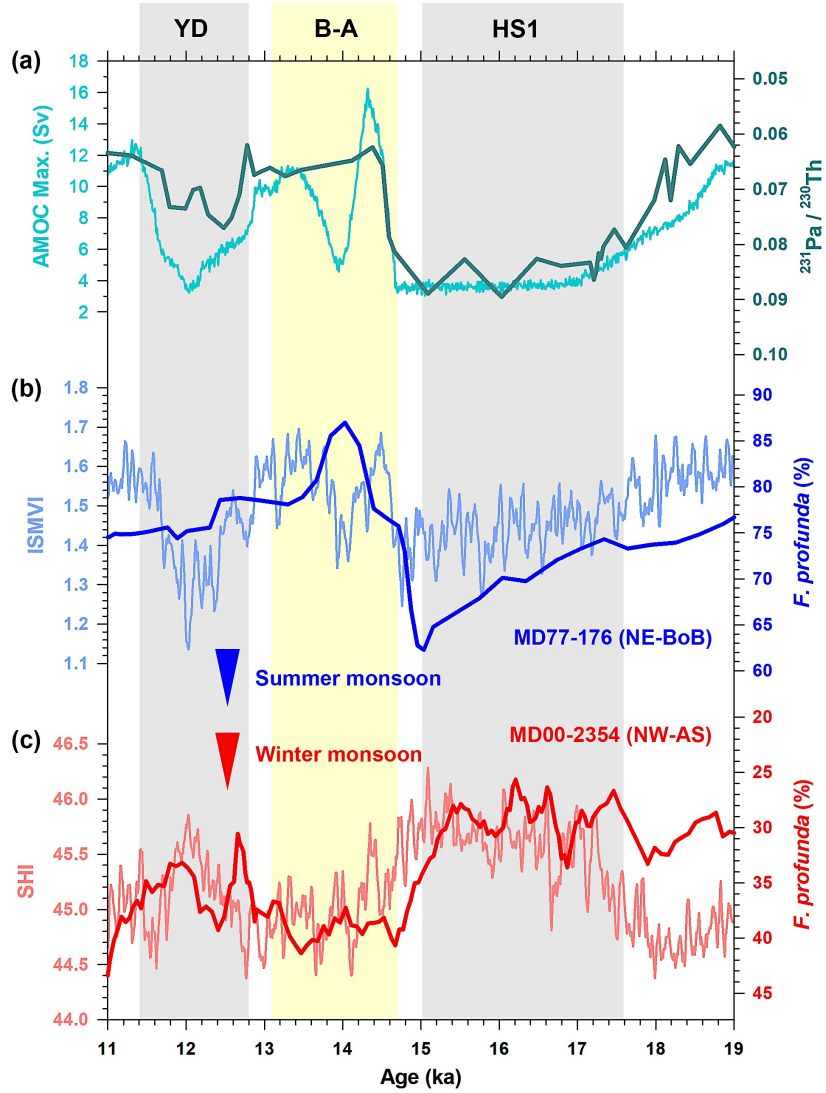

Fig. 5.9. Paleoclimate variations during the last deglaciation (19−11 ka). The simulated results are from the TraCE-21 meltwater flux single forcing experiment. (a) Simulated AMOC strength and $^{231}Pa/^{230}Th$ ratio in marine sediments from the western subtropical Atlantic Ocean indicating the AMOC strength (McManus et al., 2004). (b) Simulated Indian summer monsoon index (ISMVI) and the *F. profunda* % records of core MD77-176 representing the Indian summer monsoon intensity (Zhou et al., 2020). (c) Simulated Siberian High index (SHI) and the *F. profunda* % records of core MD00-2354 indicating the winter monsoon intensity (Zhou et al. in preparation).

During the HS1 and YD, when the AMOC shutdown, the poleward heat transport in the Atlantic is weaker resulting in the cooling over Eurasia throughout the year. Like the LGM patterns, the heat redistribution results in the smaller meridional gradient of sea level pressure during summer and the

larger gradient during winter, and thus weaker summer monsoon and stronger winter monsoon relative to the B-A (Figs. 5.8d, f). Drier climate prevails over South Asia due to weaker moisture transport in summer (Fig. 5.8e). The results of the single forcing experiment reveal that the differences between HS1 and B-A are mainly the responses to the changed AMOC strengths induced by meltwater flux (Figs. 5.8j–l).

4. Summary and perspectives

The upper seawater stratification in the northeastern and northwestern Indian Ocean are respectively controlled by the freshwater input and the surface cooling. Therefore, the evolution of stratification in these two basins can respectively represent the dynamics of Indian summer monsoon and winter monsoon. The comparison of proxy results and modelling data proves that the *F. profunda* % records, which indicate the stratification, of cores MD77-176 and MD00-2354 can respectively be seen as summer and winter monsoon proxies. However, there are two special cases in these two records. The LGM values of MD77-176 are similar to the Late Holocene values, which reflects a relative freshness of the Andaman Sea, rather than an unchanged summer monsoon. Stratification maximum during the Early Holocene is found in MD00-2354 despite the surface cooling and winter monsoon are strong. This strong stratification in the Arabian Sea is probably due to a strong subsurface cooling making a larger temperature gradient. The anti-correlation of the two *F.profunda* % records during the last deglaciation indicates the anti-phased responses of summer and winter monsoons to the AMOC fluctuations. The model-proxy comparison reveals that the Indian summer monsoon has a significant response to the LGM conditions, and implies that the proxies related to SSS in the northern Bay of Bengal closed to the river mouth are more sensitive to the glacial-interglacial cycles. Salinity budget and regional discrepancy in the northeastern Indian Ocean are important for the interpretations of SSS records. The stratification and SST in the northwestern Indian Ocean are strongly influenced by the glacial-interglacial cycles. But in the precession band, other factors, such as the subsurface temperature, in addition to the winter monsoon can influence the upper seawater stratification and nutrient contents in the euphotic zone. Records of *F. profunda* % are not reported in the northern Bay of Bengal, and such a record compared with the MD77-176 one is important to further support the interpretation of regional discrepancy of SSS changes. The lack of subsurface temperature in the Arabian Sea hampers our understanding of the changes in upper seawater stratification. The subsurface cooling during the Early Holocene shown by TraCE-21 needs results of multi-model to support.

References

Akhil, V. P., Durand, F., Lengaigne, M., Vialard, J., Keerthi, M. G., Gopalakrishna, V. V., Deltel, C., Papa, F., and de Boyer Montegut, C., 2014. A modeling study of the processes of surface salinity seasonal cycle in the Bay of Bengal. Journal of Geophysical Research-Oceans 119, 3926–3947.

Anand, P., Kroon, D., Singh, A. D., Ganeshram, R. S., Ganssen, G., Elderfield, H., 2008. Coupled sea surface temperature-seawater $\delta^{18}O$ reconstructions in the Arabian sea at the millennial scale for the last 35 ka. Paleoceanography 23, PA4207.

Böll, A., Schulz, H., Munz, P., Rixen, T., Gaye, B., Emeis, K.-C., 2015. Contrasting sea surface temperature of summer and winter monsoon variability in the northern Arabian Sea over the last 25 ka. Palaeogeography, Palaeoclimatology, Palaeoecology 426, 10−21.

Chen, Y.-l. L., 2005. Spatial and seasonal variations of nitrate-based new production and primary production in the South China Sea. Deep-Sea Research I 52, 319–340.

Clement, A. C., Peterson, L. C., 2008. Mechanisms of abrupt climate change of the last glacial period. Reviews of Geophysics. Reviews of Geophysics 46, RG4002.

Cohen, J., Saito, K., Entekhabi, D., 2001. The role of the Siberian high in Northern Hemisphere climate variability. Geophysical Research Letters 28, 299–302.

Collins, W. D., Bitz, C. M., Blackmon, M. L., Bonan, G. B., Bretheton, C. S., Carton, J. A., Chang, P., Doney, S. C., Hack, J. J., Henderson, T. B., Kiehl, J. T., Large, W. G., McKenna, D. S., Santer, B. D., Smith, R. D., 2006. The Community Climate System Model Version 3 (CCSM3). Journal of Climate 19, 2122–2143.

Contreras-Rosales, L. A., Jennerjahn, T., Tharammal, T., Meyer, V., Lückge, A., Paul, A., Schefuß, E., 2014. Evolution of the Indian Summer Monsoon and terrestrial vegetation in the Bay of Bengal region during the past 18 ka. Quaternary Science Review 102, 133–148.

Dutt, S., Gupta, A. K., Clemens, S. C., Cheng, H., Singh, R. K., Kathayat, G., Edwards, R. L., 2015. Abrupt changes in Indian summer monsoon strength during 33,800 to 5500 years B.P. Geophysical Research Letters 42, 5526–5532.

Goswami, B. N., Krishnamurthy, V., Annamalai, H., 1999. A broad-scale circulation index for the interannual variability of the Indian summer monsoon. Quarterly Journal of the Royal Meteorological Society 125, 611–633.

Hasanean, H. M., Almazroui, M., Jones, P. D., Alamoudi, A. A., 2013. Siberian high variability and its teleconnections with tropical circulations and surface air temperature over Saudi Arabia. Climate Dynamics 41, 2003–2018.

Howden, S. D., Murtugdde, R., 2001. Effects of river inputs into the Bay of Bengal. Journal of Geophysical Research 106, 19825–19843.

Joos, F., Spahni, R., 2008. Rates of change in natural and anthropogenic radiative forcing over the past 20,000 years. PNAS 105, 1425−1430.

Kathayat, G., Cheng, H., Sinha, A., Spötl, C., Edwards, R. L., Zhang, H., Li, X., Yi, L., Ning, Y., Cai, Y., Lui, W. L., Breitenbach, S. F. M., 2016. Indian monsoon variability on millennial-orbital timescales. Scientific Reports 6, 24374.

Kudrass, H. R., Hofmann, A., Doose, H., Meis, K., Erlenkeuser, H., 2001. Modulation and amplification of climatic changes in the Northern Hemisphere by the Indian summer monsoon during the past 80 k.y. Geology 29, 63−66.

Labban, A. H., Mashat, A.-W. S., Awad, A. M., 2019. The variability of the Siberian high ridge over the Middle East. International Journal of Climatology 41, 104−130.

Liu, K.-K., Chao, S.-Y., Shaw, P.-T., Gong, G.-C., Chen, C.-C., Tang, T., 2002. Monsoon-forced chlorophyll distribution and primary production in the South China Sea: Observations and a numerical study. Deep-Sea Research I 49, 1387–1412.

Liu, Z., Otto-Bliesner, B. L., He, F., Brady, W. C., Tomas, R., Clark, P. U., Carlson, A. E., Lynch-Stieglitz, J., Curry, W., Brook, E., Er- ickson, D., Jacob, R., Kutzbach, J., and Cheng, J., 2009. Transient Simulation of Last Deglaciation with a new mechanism for Bølling- Allerød Warming. Science 325, 310–314, 2009.

Mahesh, B. S., Banakar, V. L., 2014. Change in the intensity of low-salinity water inflow from the Bay of Bengal into the Eastern Arabian Sea from the Last Glacial Maximum to the Holocene: Implications for monsoon variations. Palaeogeography, Palaeoclimatology, Palaeoecology 397, 31–37.

Marzin, C., Braconnot, P., 2009. The role of the ocean feedback on Asian and African monsoon variations at 6 kyr and 9.5 kyr BP. C. R. Geoscience 341, 643–655.

Marzin, C., Kallel, N., Kageyama, M., Duplessy, J.-C., and Braconnot, P., 2013. Glacial fluctuations of the Indian monsoon and their rela- tionship with North Atlantic climate: new data and modelling experiments. Climate of the Past 9, 2135–2151.

Meng, L., Zhuang, W., Zhang, W., Yan, C., Yan, X.-H., 2020. Variability of the shallow overturning circulation in the Indian Ocean. Journal of Geophysical Research-Oceans 125, e2019JC015651.

McManus, J. F., Francois, R., Gherardi, J.-M., Keigwin, L. D., and Brown-Leger, S., 2004. Collapse and rapid resumption of Atlantic meridional circulation linked to deglacial climate changes. Nature 428, 834–837.

Molfino, B., McIntyre, A., 1990. Precessional forcing of nutricline dynamics in the Equatorial Atlantic. Science 249, 766–769.

Otto-Bliesner, B. L., Brady, E. C., Clauzet, G., Tomas, R., Levis, S., & Kothavala, Z., 2006. Last Glacial Maximum and Holocene climate in CCSM3. Journal of Climate 19, 2526–2544.

Peltier, W. R., 2004. Global glacial isostasy and the surface of the ice-age earth: The ICE-5G (VM2) model and GRACE. Annual Review of Earth and Planetary Sciences 32, 111–149.

Pourmand, A., Marcantonio, F., Schulz, H., 2004. Variations in productivity and eolian fluxes in the northeastern Arabian Sea during the past 110 ka. Earth and Planetary Science Letters 221, 39−54.

Pourmand, A., Marcantonio, F., Bianchi, T. S., Canuel, E. A., Waterson, E. J., 2007. A 28-ka history of sea surface temperature, primary productivity and planktonic community variability in the western Arabian Sea. Paleoceanography 22, PA4208.

Prasad, T. G., 2004. A comparison of mixed-layer dynamics between the Arabian Sea and Bay of Bengal: One-demensional model results. Journal of Geophysical Research 109, C03025.

Prasanna Kumar, S., Muraleedharan, P. M., Prasad, T. G., Ganus, M., Ramaiah, N., de Souza, S. N., Sardesai, S., Madhupratap, M., 2002. Why is the Bay of Bengal less productive during summer monsoon compared to the Arabian Sea? Geophysical Research Letter 29, 2235.

Prasanna Kumar, S., Prasad, T. G., 1996. Winter cooling in the northern Arabian Sea. Current Science 71, 834–841.

Prasanna Kumar, S., Prasad, T. G., 1999. Formation and spreading of Arabian Sea high-salinity water mass. Journal of Geophysical Research 104, 1455–1464.

Prasanna Kumar, S., Madhupratap, M., Dileep Kumar, M., Muraleedharan, P. M., de Souza, S. N., Ganus, M., Sarma, V. V. S. S., 2001a. High biological productivity in the central Arabian Sea during the summer monsoon driven by Ekman pumping and lateral advection. Current Science 81, 1633−1638.

Prasanna Kumar, S., Narvekar, J., 2005. Seasonal variability of the mixed layer in the central Arabian Sea and its implication on nutrients and primary productivity. Deep-Sea Research II 52, 1848−1861.

Rao, R. R., Sivakumar, R., 2003. Seasonal variability of sea surface salinity and salt budget of the mixed layer of the north Indian Ocean. Journal of Geophysical Research 108, C13009.

Rashid, H., Flower, B. P., Poore, R. Z., Quinn, T. M., 2007. A ~25 ka Indian Ocean monsoon variability record from the Andaman Sea. Quaternary Science Reviews 26, 2586−2597.

Riaz, S. M. F., Iqbal, M. J., Baig, M .J., 2017. Influence of Siberian High on temperature variability over northern areas of South Asia. Meteorology and Atmospheric Physics 130, 441−457.

Salahi, B., Kashani, A., Safarianzengir, V., 2020. Investigation and analysis of climate change and Siberian high-pressure system during drought and wet periods in the Iranian plateau. Modelling Earth Systems and Environment 6, 1695−1706.

Sarkar, A., Ramesh, R., Bhattacharya, S. K., Rajagopalan, G., 1990. Oxygen isotope evidence for a stronger winter monsoon current during the last glaciation. Nature 343, 549–551.

Sengupta, D., Raj, G. N. B., Shenoi, S. S. C., 2006. Surface freshwater from Bay of Bengal runoff and Indonesian Throughflow in the tropical Indian Ocean. Geophysical Research Letters 33, L22609.

Schott, F. A., 2005. Shallow overturning circulation of the Western Indian Ocean. Philosophical Transactions of the Royal Society A 363, 143–149.

Schulte, S., Müller, P. J., 2001. Variations of sea surface temperature and primary productivity during Heinrich and Dansgaard-Oeschger events in the northwestern Arabian Sea. Geo-Marine Letters 21, 168−175.

Sijinkumar, A. V., Clemens, S., Nath, B. N., Prell, W., Benshila, R., and Lengaigne, M., 2016. δ18O and salinity variability from the Last Glacial Maximum to Recent in the Bay of Bengal and Andaman Sea. Quaternary Science Reviews 135 79–91.

Stuiver, M., Grootes, P. M., 2000. GISP2 oxygen isotope ratios. Quaternary Research 53, 277−284.

Thadathil, P., Muraleedharan, P. M., Rao, R. R., Somayajulu, Y. K., Reddy, G. V., Revichandran, C., 2007. Observed seasonal variability of barrier layer in the Bay of Bengal. Journal of Geophysical Research 112, C02009.

Vinayachandran, P. N., Murty, V. S. N., and Ramesh Bahu, V., 2002. Observations of barrier layer formation in the Bay of Bengal during summer monsoon, Journal of Geophysical Research 107, 8018.

Wang, B., Ding, Q., 2008. Global monsoon: Dominant mode of annual variation in the tropics. Dynamics of Atmospheric and Oceans 44, 165−183.

Webster, P. J., Magaña, V. O., Palmer, T. N., Shukla, J. Tmas, R. A., Yanai, M., and Yasunari, T., 1998. Monsoons: Processes, predictability, and the prospects for prediction. Journal of Geophysical Research 103, 14451–14510.

Wen, X., Liu, Z., Wang, S., Cheng, J., Zhu, J., 2016. Correlation and anti-correlation of the East Asian summer and winter monsoons during the last 21,000 years. Nature Communications 7, 11999.

Wu, B., Wang, J., 2002. Winter Arctic Oscillation, Siberian High and East Asian Monsoon. Geophysical Research Letters 29, 1897.

Zhang, H., Liu, C., Jin, X., Shi, J., Zhao, S., Jian, Z., 2016. Dynamics of primary productivity in the northern South China Sea over the past 24,000 years. Geochemistry, Geophysics, Geosystems

17, 4878−4891.

Zhou, X., Duchamp-Alphonse, S., Kageyama, M., Bassinot, F., Beaufort, L., Colin, C., 2020. Dynamics of primary productivity in the northeastern Bay of Bengal over the last 26 000 years. Climate of the Past 16, 1969–1986.

Supplementary figure

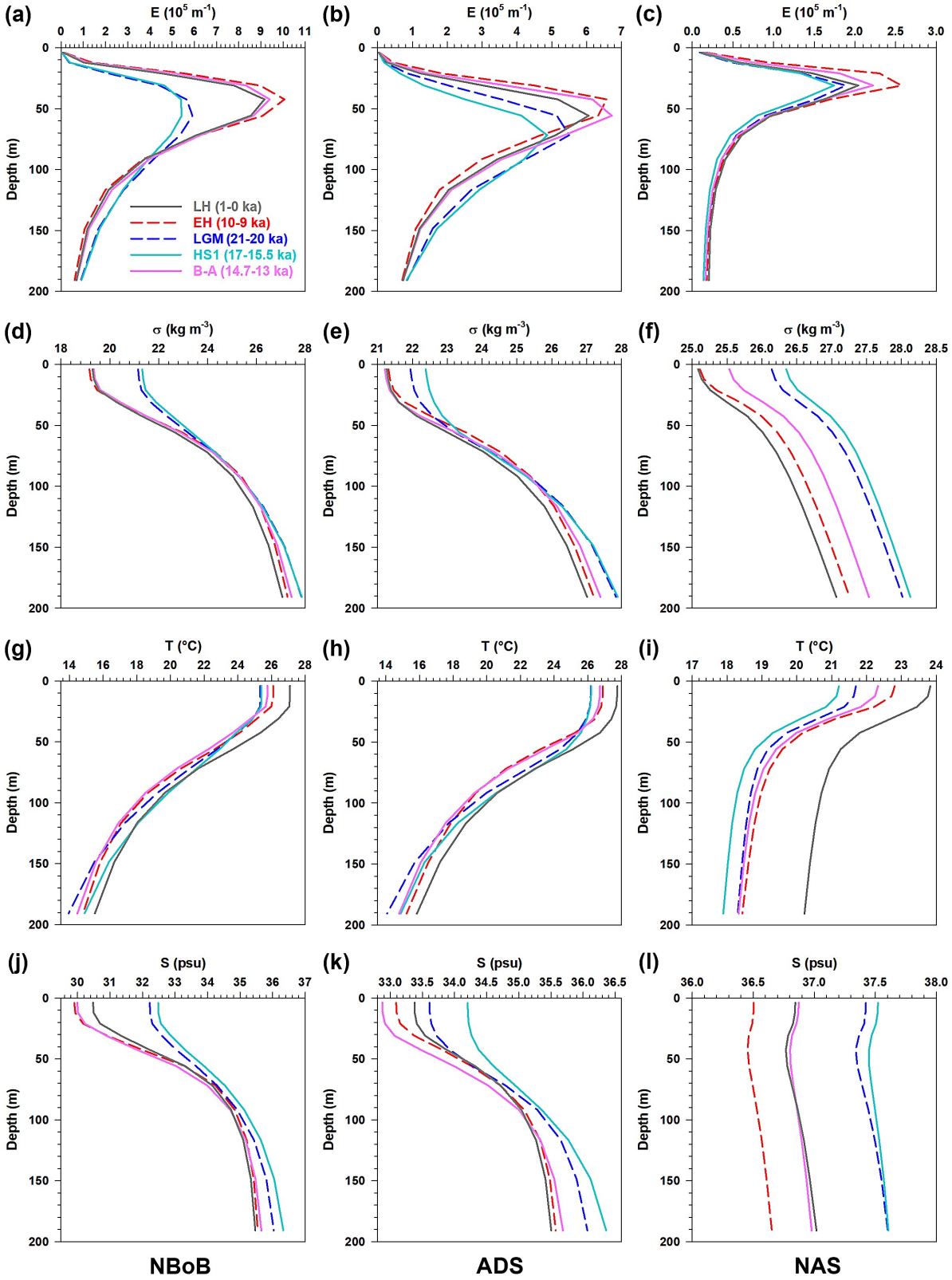

Fig. 5.S1. TraCE-21 simulated profiles between 0 and 200 m water depth in (left column) the northern Bay of Bengal (NBoB), (middle column) the Andaman Sea (ADS), and (right column) the northern Arabian Sea (NAS). The regions for data extractions are shown in Fig. 5.1.

Chapter 6

Variations of the Indian Ocean Walker circulation since the Last Glacial Maximum revealed by reconstructed and simulated zonal wind intensity

No paleo-PP records have been provided within the equatorial Indian Ocean so far. It is probably because most of the palaeoceanographic studies (and particularly those dealing with PP) focus on the Indian Monsoon dynamic and its link to the AMOC in the past, thus, usually neglecting the Walker circulation despite its crucial role in the ocean-atmosphere system of the area. Here, I provide two high-resolution quantitative PP records in the Northern tip of Sumatra and the Southern tip of India, based on the Florisphaera profunda (%) signals obtained on cores BAR94-24 and MD77-191, respectively. As they are located within equatorial coastal wind-driven upwelling systems, they present great potentials to reflect Walker circulation dynamic in the past. For the first time, I interpret Fp% data as a zonal wind intensity proxy. Combined with the use of AWI-ESM model outputs, I show that the Indian Ocean Walker circulation was weaker than present during both the LGM and Early-Mid Holocene.

Variations of the Indian Ocean Walker circulation since the Last Glacial Maximum revealed by reconstructed and simulated zonal wind intensity

Xinquan Zhou[1*], Stéphanie Duchamp-Alphonse[1], Franck Bassinot[2], Masa Kageyama[2], Xiaoxu Shi[3], Luc Beaufort[4], Gerrit Lohmann[3]

[1]Université Paris-Saclay, Géosciences Paris Saclay, CNRS, Rue du Belvédère, 91405 Orsay, France

[2]Laboratoire des Sciences du Climat et de l'Environnement, CEA/CNRS/UVSQ, Université Paris-Saclay, Centre CEA-Saclay, Orme des Merisiers, 91191 Gif-sur-Yvette, France

[3]Alfred Wegener Institute Helmholtz Center for Polar and Marine Research, Bussestr. 24, 275070 Bremerhaven, Germany

[4]Centre Européen de Recherche et d'Enseignement des Géosciences de l'Environnement, CNRS/IRD/Aix-Marseille Université, Av. Louis Philibert, BP80, 13545 Aix-en-Provence, France

*Corresponding author: xinquan.zhou@universite-paris-saclay.fr

In preparation

Abstract: The zonal Walker circulation, characterized by seasonal to interannual variability associated with the Indian Ocean Dipole mode (IOD), has a strong impact on the climate over the equatorial Indian Ocean and its surrounding realm. Despite its crucial role in the modern climate, its future evolution is still under debate and requires that we better understand its variability and changes over timescales exceeding those available with recent meteorological data. Here, we reconstruct coastal upwelling dynamics over the equatorial Indian Ocean (10°S−10°N) to document the evolution of the zonal wind intensity associated with the Walker circulation since the Last Glacial Maximum (LGM) based on: i) coccolith related primary productivity anomalies (PPA) from two sediment cores collected off the southern tip of India (MD77-191) and off the north-western tip of Sumatra (BAR94-24), and ii) latitudinal differences of sea surface temperature anomalies (SSTA) calculated based on published SST data previously obtained from three sediment cores retrieved off western (SO189-39KL and GeoB10029-4) and southwestern (GeoB10038-4) Sumatra (Mohtadi et al., 2010; 2014). A comparison of reconstructed PPA and SSTA to published records, in conjunction with the analysis of the coupled climate model AWI-ESM, reveals anomalous (south-) easterly winds associated with a relatively weak Indian Ocean Walker circulation from the LGM to the Early-Mid Holocene and anomalously strong

westerly winds associated with a well-established Indian Ocean Walker circulation during the Late Holocene. The LGM and the Early-Mid Holocene periods were both associated with "positive IOD-like" modes. The LGM mean state bears similarities with the 1997 episode, when a broad coastal upwelling system developed off (north-) western Sumatra, related to strong equatorial easterlies during winter. The Early-Mid Holocene mean state has similarities with the 2006 situation, when a coastal upwelling developed off southwestern Sumatra occurred, associated to both, equatorial easterlies and vigorous southeasterlies alongshore southwestern Sumatra and Java during summer.

Key words: Indian Ocean Walker circulation, coastal upwelling, equatorial zonal wind, Last Glacial Maximum, Early-Mid Holocene

1. Introduction

At present, the Walker circulation over the tropical Indian Ocean is a zonal atmospheric overturning cell characterized by an updraught (relatively low sea-level pressure) over Indonesia and a downdraught (relatively high sea-level pressure) over eastern Africa (Fig. 6.1; Bjerknes, 1969; Lau and Yang, 2015). It is accompanied by annual mean surface westerlies along the equatorial Indian Ocean and results in relatively wet conditions in the eastern Indian Ocean, and relatively dry ones over the western Indian Ocean. On seasonal-to-interannual timescales, it is closely tied to the east-west SST gradient along the equator and is therefore coupled with the Indian Ocean Dipole (IOD) (Saji et al., 1999; Webster et al., 1999). The negative IOD mode is characterized by warmer than normal seawater in the east, and cooler than normal seawater in the west (Saji et al., 1999), generating a stronger and broader east-west gradient of sea-level pressure (SLP) anomaly and more intense convection in the east (Behera and Yamagata, 2003). It is associated with enhanced westerly winds along the equator and stronger rainfall over Indonesia and western Australia (D' Arrigo and Wison, 2008; Ummenhofer et al., 2009; Cai et al., 2009; Trewin and Ganter, 2019). The positive IOD mode features opposite anomalies over these areas, as the east-west sea surface temperature (SST) anomaly gradient reverses. It is accompanied by the positive SLP anomaly in the east that creates anomalous easterly winds along the equator and results in anomalously dry conditions in the eastern Indian Ocean and wet conditions in central and western parts. As an example, the 1997 positive IOD event caused disastrous droughts in Indonesia and Australia and catastrophic floods in eastern Africa (Abram et al., 2003; Ummenhofer et al., 2009; Cai et al., 2009; Brown et al., 2009; Lim and Hendon, 2015).

Interestingly, it appears that the anomalous physical structures associated with the IOD, and particularly those related to zonal wind intensity, are accompanied by profound biological reorganizations over the entire tropical Indian Ocean, and particularly within phytoplankton biomass and primary productivity (PP), as they directly react to changes in surface ocean dynamics and more particularly in thermocline (nutricline) depth (Wiggert et al., 2009; Currie et al., 2013). During the intense 1997, 2006, and 2019 positive IOD modes, when anomalous easterly and southeasterly winds were accompanied by a rising thermocline in the eastern part of the basin and a deepening one in its central and western parts, stronger than normal chlorophyll blooms were observed in the coastal upwelling area off Sumatra and Java, whereas weaker than normal ones were documented in the coastal upwelling systems off southern India and eastern Africa/Oman (e.g. Murtugudde et al., 1999, 2000; Vinayachandran et al., 2002; Iskandar et al., 2009; Wiggert et al., 2009; Girishkumar et al., 2012; Currie et al., 2013; Shi and Wang, 2021). Conversely, during the recent 2016 negative IOD mode,

when anomalous westerly winds triggered a deepened thermocline in the eastern part of the basin and a shallower one in its central and western parts, weaker and stronger chlorophyll blooms were documented off Sumatra and Java and off southern India, respectively (Thushara and Vinayachandran, 2020). Therefore, it appears that physical and biological structures of the tropical Indian Ocean react in concert to changes in the Walker circulation. However, the future response of the Walker circulation to global warming and its influence on the climate and ecosystems of the Indian Ocean realm is still under debate, and studies of its dynamics in the past, particularly those related to the IOD-like modes, are required to better constraint projections (e.g., Vecchi et al., 2007; L'Heureux et al., 2013).

The impacts of Walker circulation and IOD variability on the physical structure of the Indian Ocean during the Last Glacial Maximum (LGM) and the Early-Mid Holocene (EMH) have been the focus of numerous studies. Both periods are perfect study cases to explore the impact of key internal or external Earth's climate forcing mechanisms and boundary conditions. The LGM makes it possible to study the Indian Ocean Walker circulation response to larger ice volume, lower sea-level, and lower greenhouse gases concentrations than today, while the EMH, which is characterized by a lower precession parameter, making it possible to decipher the impact of a strong Northern Hemisphere summer solar insolation and stronger seasonality in a period with high sea-level and low ice volume. Several sea surface salinity (SSS) and precipitation proxies derived from terrestrial and marine records point to a drier Indonesia and wetter eastern Africa during both periods (e.g., Tierney et al., 2011, 2012; DiNezio and Tierney, 2013; Bloszies et al., 2015; Chevalier et al., 2017; DiNezio et al., 2018) and suggest, therefore, anomalous easterlies and a weaker Walker circulation during LGM and EMH (Tierney et al., 2012; DiNezio et al., 2018). However, the debate is still opened since another study, from Mohtadi et al. (2017), concluded about a stronger Walker circulation during the LGM, based on its reconstruction of a deeper thermocline in the eastern Indian Ocean. Paleoclimate simulations under LGM conditions show a broad range of contrasting Walker circulation scenarios (see DiNezio and Tierney, 2013; Chevalier et al., 2017; Mohtadi et al., 2017; DiNezio et al., 2018), with the HadCM3 and CESM1.2 models simulating a weaker Indian Ocean Walker circulation, while the CCSM3 and FGOALS-g1.0 models simulate a stronger one and other models do not show significant changes in the zonal gradient over the Indian Ocean between the two periods. Besides, only a few studies focus on the reconstruction of zonal wind anomalies over the equatorial Indian Ocean despite their close relationship with the Walker circulation and their direct impact on coastal upwelling dynamics, well characterized by in-situ PP and/or SST patterns (e.g., Mohtadi et al., 2014; Bassinot et al., 2011).

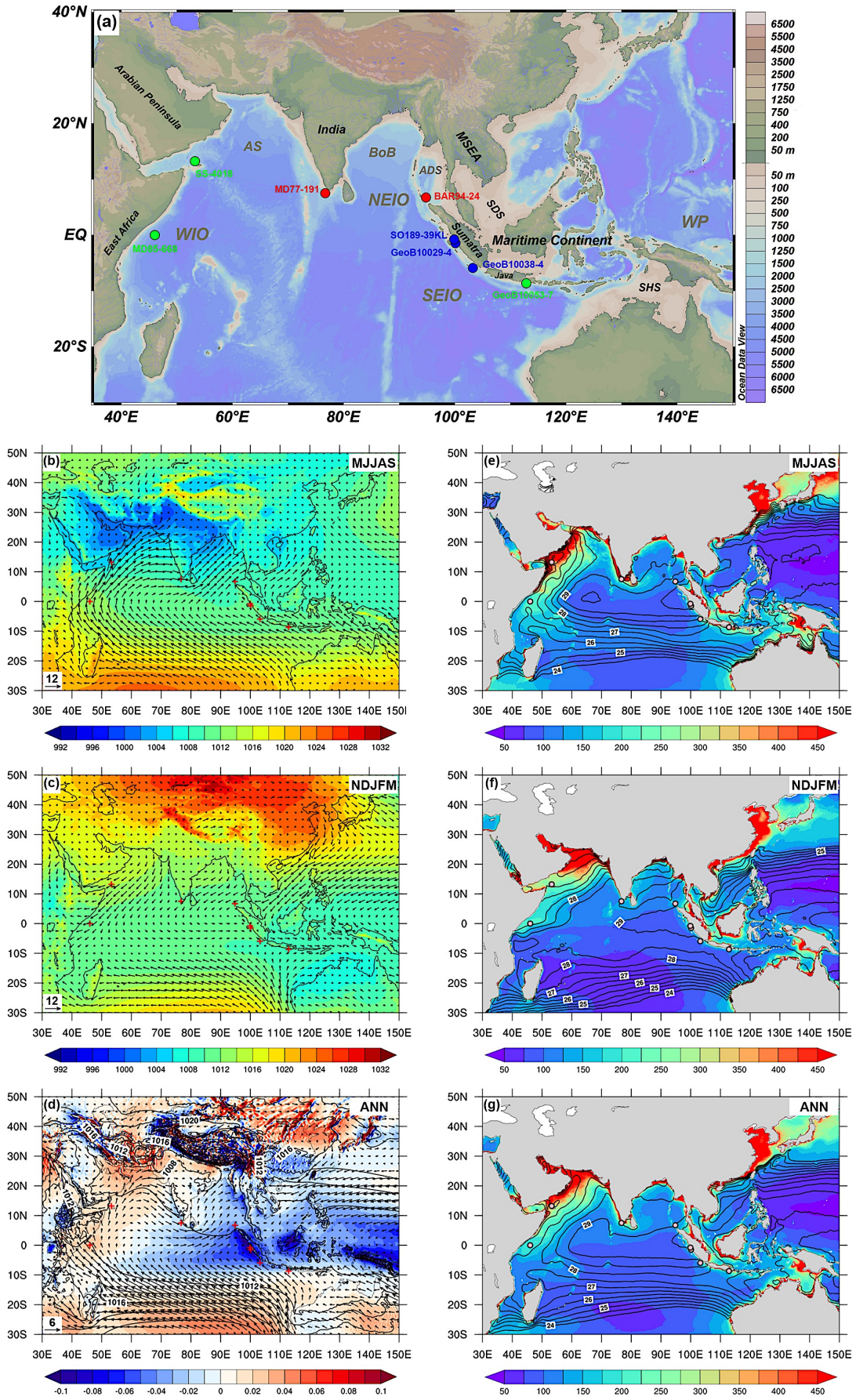

Fig. 6.1. (see next page)

Fig. 6.1. (a) Geographic setting and bathymetric map created by the Ocean Data View software (©Reiner Schlitzer, Alfred Wegener Institute) with its built-in global high-resolution bathymetric data (GlobHR). The locations of the sediment cores retrieved in the coastal upwelling systems studied here are marked by red (PP reconstruction) blue (SST anomalies) and green (published PP-related records) circles. Climatology (period 1979−2019) of surface wind (vectors, m s^{-1}) and sea level pressure (color, hPa) during (b) the summer monsoon season (May−June−July−August−September) and (c) the winter monsoon season (November−December−January−February−March). (d) Annual mean vertical velocity at 500 hPa level (Pa s^{-1}, with blue (red) colors indicating ascending (descending) air motion), surface wind (vectors, m s^{-1}), and SLP (contours between 992 and 1032 hPa with 2 hPa spacing). Climatology (period 2003−2019) of PP (color, gC m^{-2} yr^{-1}), surface wind (vectors, m s^{-1}), and SST (contours, ℃) during the (e) summer (May−June−July−August−September), (f) winter (November−December−January−February−March), and (g) the annual mean. Atmospheric data are from ERA5 reanalysis dataset (monthly; https://www.ecmwf.int/en/forecasts/datasets/reanalysis-datasets/era5; Hersbach et al., 2020). PP data are from the "Ocean Productivity" website (http://sites.science.oregonstate.edu/ocean.productivity), that were calculated by the Vertically Generalized Production Model (VGPM, Behrenfeld and Falkowski, 1997), based on the MODIS satellite chlorophyll concentration data. AS = Arabian Sea; BoB = Bay of Bengal; ADS = Andaman Sea;; MSEA = Mainland Southeast Asia; SDS = Sunda Shelf; SHS = Sahul Shelf; WIO = West Equatorial Indian Ocean; NEIO = Northeast Indian Ocean; SEIO = Southeast Indian Ocean; WP = West Pacific.

In this study, we provide reconstructed PPA records of the north-western Sumatra and southern India upwelling systems based on coccolith assemblages in marine sediment cores BAR94-24 (6.73°N, 94.83°E) and MD77-191 (7.5°N, 76.717°E), respectively. Together with calculated SST anomaly (SSTA) difference between southwestern and western Sumatra obtained based on published SST records from cores SO189-39KL (0.79°S, 99.91°E), GeoB10029-4 (1.49°S, 100.13°E), and GeoB10038-4 (5.94°S, 103.25°E) (Mohtadi et al., 2010, 2014), it allows us to unravel the variations of zonal wind along the equatorial Indian Ocean and identify the changes in Walker circulation strength since the LGM. These study sites appear to be suitable candidates to fulfil these objectives, as they document clear relationships between PP, SST, coastal upwelling, and zonal wind anomalies today and are likely to remain so in the past (e.g. Wiggert et al., 2009; Thushara and Vinayachandran, 2020; Shi and Wang, 2021). Our results are also compared with published PP-related records and outputs from the coupled Earth system model AWI-ESM-1-1-LR (Alfred Wegener Institute Earth System Model) to evaluate the signature of SLP, surface wind, and vertical velocity dynamics of the studied area under LGM and Mid Holocene (MH) conditions. This model is designed to work on unstructured meshes (Sidorenko et al., 2011), with a finite-element approach that increases spatial resolutions in coastal and equatorial areas (Shi et al., 2020). It is therefore particularly accurate for near-shore processes and ocean-atmosphere feedbacks, which are keys to simulate the changes of Walker circulation in the past (DiNezio et al., 2016).

2. Core locations and oceanic settings

Cores MD77-191 and BAR94-24 were collected to the north of the equator, off the southern tip of India and the northwestern tip of Sumatra aboard the N/O *Marion Dufresne* and the N/O *Baruna Jaya*, during the OSIRIS 3 (1977) and BARAT cruises (1994), respectively (Fig. 6.1a). Cores SO189-39KL, GeoB10029-4, and GeoB10038-4 were retrieved to the south of the equator, off western and southwestern Sumatra (Fig. 6.1a; Mohtadi et al., 2010, 2014). These all have been collected above the modern lysocline (Cullen and Prell, 1984), within coastal upwelling systems. Therefore, PP and SST records from all these sites are closely related to surface wind patterns, as cold and nutrient-rich waters seasonally resurface by Ekman transport and feed phytoplankton (e.g. Susanto et al., 2001; Rao et al., 2006). In detail, PP off the southern tip of India and off southwestern Sumatra are relatively high, and SST are relatively low from June to September i.e., broadly during boreal summer, when alongshore westerlies and alongshore southeasterlies prevail, respectively (Figs. 6.1b, e, 6.S1). Conversely, PP off the northwestern tip of Sumatra is moderately high, and SST is low from December to March i.e., during boreal winter when equatorial easterlies dominate (Figs. 6.1c, f, 6.S1). Overall, these seasonal trends are reflected in the annual mean states, when annual PP and SST in southern India and western Sumatra are closely related to annual mean states of equatorial westerlies and (south-) easterlies, respectively (Figs.6.1d, g). Remarkably, upwelling and PP near the equator i.e., at sites SO189-39KL and GeoB10029-4, are relatively weak and low as the Coriolis force is relatively small (Fig. 6.S1).

The relationships between PP, SST, and zonal wind intensities within these upwelling systems are strengthened under IOD events that develop from summer to early winter and dominate the annual mean anomalies. During the recent 1997, 2006, and 2019 positive modes i.e., when anomalous equatorial easterlies and southeasterlies over the tropical southeastern Indian Ocean prevailed, PP along (south-) western Sumatra increased while SST decreased (Figs. 6.S2, 6.S3), highlighting enhanced upwelling in the area, and an overall shallower thermocline (nutricline) in the eastern Indian Ocean (Murtugudde et al., 1999, 2000; Vinayachandran et al., 2002; Girishkumar et al., 2012; Currie et al., 2013; Shi and Wang, 2021). Reversed trends are observed off the southern tip of India, with decreased PP, increased SST, and a reduced coastal upwelling system that reflects an overall deepened thermocline (nutricline) in the central part of the Indian Ocean (Vinayachandran et al., 2002; Wigger et al., 2009; Currie et al., 2013; Shi and Wang et al., 2021). During negative IOD events of years 1998 and 2016 i.e., when anomalous equatorial westerlies and northwesterlies prevailed, opposite PP and SST patterns were observed over these sites, as the east-west thermocline gradient reversed and drove a stronger coastal upwelling off southern India and a weaker one off (south-) western Sumatra and

Java (Figs. 6.S4, 6.S5). Despite the intense 1997 positive IOD event characterized by anomalous low PP in eastern Africa/Oman, no clear pattern may be highlighted during years 1998, 2006, 2016, and 2019 in the western part of the Indian Ocean (within the Arabian sea), as complex features in surface wind anomalies appear to be associated with rather heterogeneous PP and SST signals (Figs. 6.S2, 6.S3).

Remarkably, positive (negative) IODs are usually related to a weaker cooling (warming) off western Sumatra compared to southwestern Sumatra, which results in negative (positive) SSTA differences between southwestern and western Sumatra, thanks to the dominant anomalous alongshore southwesterlies (northwesterlies) (Fig. 6.S3). However, an exception has been observed during the extreme 1997 positive IOD event, as a positive SSTA difference has been observed in the area because of the occurrence of severe anomalous equatorial easterlies that suppressed the influence of anomalous alongshore southeasterlies (Vinayachandran et al., 2002; Chen et al., 2016).

3. Material and methods

3.1 Sampling and age models

Cores MD77-191 and BAR94-24 were sampled at 1−2 cm intervals along the upper 7.1 m and 3.5 m sediment sections, respectively. Their age models were based on 13 and 9 accelerator mass spectrometry (AMS) ^{14}C ages obtained on planktonic foraminifera and pteropods (Bassinot et al., 2011; Ma et al., 2020; this study) and converted to calendar ages using the online software CALIB version 8.2, and the MARINE20 curve (global ocean age: 550 years) (Table 6.S1, Fig. 6.S6). Core MD77-191 spans the last 16 kyr with sedimentation rates ranging between 13 and 90 cm kyr^{-1} (average of 58 cm kyr^{-1}), while core BAR94-24 covers the last 24 kyr with sedimentation rates varying between ~8 and 23 cm kyr^{-1} (average of 16 cm kyr^{-1}). We studied a total of 406 samples with temporal resolutions between 20 and 85 years from core MD77-191, and a total of 175 with temporal resolutions between ~50 and 250 years from core BAR94-24. Age models of cores GeoB10029-4, GeoB10038-4 and SO189-39KL are from Mohtadi et al. (2010, 2014).

3.2 Coccolith analysis and PP reconstructions

Coccolithophores are marine-calcifying phytoplankton living in the euphotic zone, responsible for the export of organic and carbonate particles (i.e., the coccoliths they produce) to the sedimentary reservoir. In contrast with most coccolithophore species that are found in the upper euphotic zone (< 100 m water depth), *Florisphaera profunda* dwells in the lower euphotic zone, at a water depth of ~100–200 m (Okada and Honjo, 1973). When nutricline gets shallower (deeper), more (less) nutrients

are brought into the upper euphotic zone and primary production (PP) increases (decreases), while the relative abundance of *F. profunda* (Fp%) decreases (increases). Based on this relationship, the coccoliths preserved in sediment cores, and more particularly those of *F. profunda* became good study material for paleoenvironmental reconstructions. Indeed, Fp%-PP empirical equations have been developed, based on PP estimates from satellite observations and coccoliths abundances in surface sediments (Beaufort et al., 1997; Hernández-Almeida et al., 2019) and have been widely used to reconstruct PP patterns in the past (e.g. de Garidel-Thoron et al., 2001; Zhou et al., 2020).

In this study, the "settling" technique of Duchamp-Alphonse et al. (2018) modified after Beaufort et al. (2014) was used to prepare coccolith smear slides and calculate PP to document coastal upwelling dynamics off northwestern Sumatra and off southern India. As such, a total of 406 and 175 samples were analysed from cores BAR94-24 and MD77-191, respectively. For each slide, at least 500 coccolith specimens were counted by eyes, under at least 3 random fields of view. The relative abundance of *F. profunda* (Fp%) was calculated as: Fp% = 100 × (Fp number / total coccolith number). The 95% confidence interval for Fp% was calculated following the method of Patterson and Fishbein (1984) and corresponds to a reproducibility smaller than ±5 %. Reconstructed PP was obtained using the tropical Indian Ocean empirical equation of Hernández-Almeida et al. (2019), as: $PP = [10^{(3.27-0.01\times Fp\%)}] \times 365/1000$. The unit of estimated PP is grams of carbon per meter square per year (gC m^{-2} yr^{-1}). PPA has been calculated by subtracting each PP value by the average PP of the studied interval: $PPA = PP - \overline{PP}_{\text{whole interval}}$. They have been used to interpret PP and upwelling dynamics in terms of easterly and westerly wind patterns, positive (negative) PPA indicating stronger (weaker) coastal upwelling, and alongshore winds.

3.3 Difference of SST anomaly

SSTA off southwestern and western Sumatra were calculated over the last 24 kyr, based on the published SST records from *Globigerinoides ruber* Mg/Ca signals obtained on cores GeoB10029-4, GeoB10038-4 (Mohtadi et al., 2010), and SO189-39KL (Mohtadi et al., 2014), by subtracting the averaged value estimated over the last 24 kyr to each discrete SST value, as follows: $SSTA = SST - \overline{SST}_{\text{last 24 kyr}}$. All the records were linearly interpolated at a regular 0.5 kyr time-interval and used to calculate ΔSSTA between southwestern (GeoB10038-4) and western (SO189-39KL and GeoB10029-4) Sumatra sites as follow: $\Delta SSTA = SSTA_{SW} - SSTA_{W}$. Both SST records show the warmest time at the Late Holocene. Therefore, in analogy to modern interannual variations, positive (negative) ΔSSTA values have been used to indicate a stronger (weaker) cooling and thus, a stronger (weaker) and wider (narrower) upwelling system off western Sumatra than off southwestern Sumatra (and by extent, Java).

The stronger cooling off western Sumatra is the result of stronger upwelling at the equator caused by dominant anomalous equatorial easterlies.

3.4 Climate model and simulations

In this study, we used atmospheric outputs of the state-of-the-art earth system model AWI-ESM-1-1-LR (termed AWI-ESM in the following, Lohmann et al. 2020; Shi et al. 2020) focusing on the atmospheric variables i.e., SLP, surface wind speed, and vertical velocity. Simulations were run for the pre-industrial control (CTRL), the LGM (21 ka), and the MH (6 ka) in the framework of Paleoclimate Modelling Intercomparison Project phase 4 (PMIP4; Kageyama et al., 2018; Brierley et al., 2020; Kageyama et al., 2021). Boundary conditions including orbital parameters and greenhouse gas concentration of the LGM and MH experiments meet the PMIP4 protocols as described in Kageyama et al. (2017) and Otto-Bliesner et al. (2017), respectively. In addition, the topography applied in LGM simulations is based on the ICE-6G_C reconstruction (Peltier et al., 2015) that integrates a 120 m lower sea-level compared to CTRL and emerges continental shelves of the studied area (mainly those of Sunda and Sahul; Fig. 6.1a) while in MH experiments, the topography is the same as in CTRL since there are only minor sea level changes from 6 ka to pre-industrial.

For each experiment, we calculated the atmospheric climatological mean states based on the monthly outputs from the last 100 simulation years. The anomalies of mean states for the LGM and MH as compared to CTRL, were calculated to examine the responses of climate to LGM and MH boundary conditions. We studied the seasonal changes in SLP (hPa), surface wind speed (m s^{-1}), and annual mean differences in vertical velocity (Pa s^{-1}) at 500 hPa (mid-troposphere) and precipitation rate (mm day^{-1}). For the SLP difference between LGM and CTRL experiments, we subtracted the area average (30°S–50°N, 30°E–150°E) to remove the effect of LGM background cooling and to highlight the changes in pressure gradients. We constructed two SLP indices characterized by the east-west gradient over the Indian Ocean based on the identification of 3 specific areas (boxes): Box 1 (10°N −20°N, 85°E −95°E), and Box 2 (20°S −10°S, 90°E −110°E) for the eastern part of the basin, and Box 3 (10°S −10°N, 50°E −70°E), for its western part. The indices are quantified by the differences of SLP between the eastern boxes and the western box: $SLP_{index,\ Box1\text{-}Box3}$, and $SLP_{index,\ Box2\text{-}Box3}$. The differences of these indices in LGM and MH, relative to CTRL experiment ($\Delta SLP_{index,\ Box1\text{-}Box3}$ and $\Delta SLP_{index,\ Box2\text{-}Box3}$), were calculated to evaluate the changes in the zonal gradient under LGM and MH conditions.

4. Results

4.1 Reconstructed PP

At sites MD77-191 and BAR94-24, coccolith assemblages mainly consist of *Florisphaera profunda*, *Emiliania huxleyi* and *Gephyrocapsa* spp. (Fig. 6.S7). In core MD77-191, Fp% varies between 37% and 78% of the assemblage, which corresponds to reconstructed PP ranging from ~290 to 117 gC m^{-2} yr^{-1} (Fig. 6.2). Remarkably, PP data obtained during the Late Holocene (~200−290 gC m^{-2} yr^{-1}) are consistent with modern VGPM values (~273 gC m^{-2} yr^{-1}; Behrenfeld and Falkowski, 1997). Over the last 16 ka, PP is characterized by a long-term decreasing trend from 16 to 9.5 ka, followed by a long-term increasing trend from 9.5 to 1 ka, a minimum of ~117 gC m^{-2} yr^{-1} being reached at ~9.5 ka. In core BAR94-24, Fp% varies between 55% and 88%, which corresponds to reconstructed PP varying between ~190 and 90 gC m^{-2} yr^{-1} (Fig. 6.2). In the same way, as for core MD77-191, values obtained in the late Holocene (100−140 gC m^{-2} yr^{-1}) are similar to modern ones (~138 gC m^{-2} yr^{-1}). The last deglaciation witnesses a PP decrease of ~17%, between rather stable values during the LGM (23−19 ka, ~140 gC m^{-2} yr^{-1}) and rather stable values during the Middle-Late Holocene (8 ka−present, ~120 gC m^{-2} yr^{-1}).

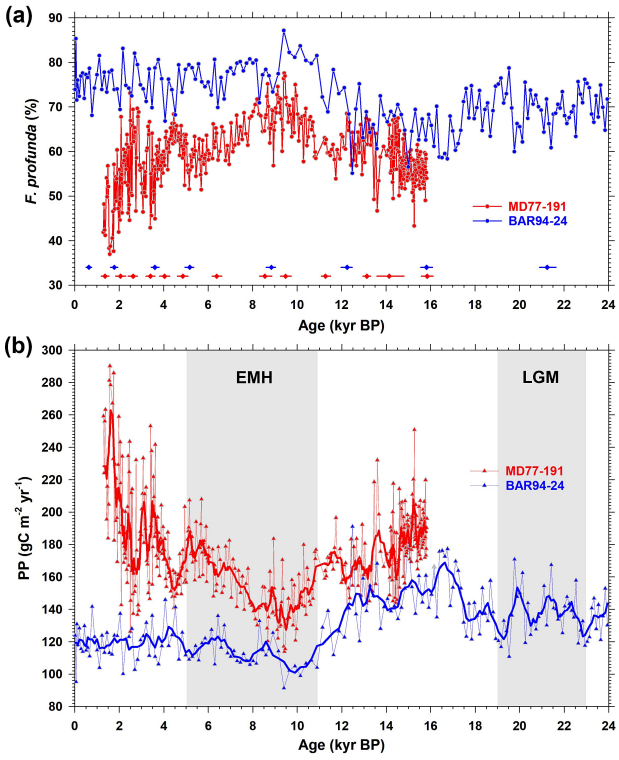

Fig. 6.2. (a) Variations of *Florisphaera profunda* relative abundances (%) in cores MD77-191 (red) and BAR94-24 (blue), located off southern India and northwestern Sumatra, respectively. The dots at the bottom represent radiocarbon dating points with 2σ error bars. (b) Reconstructed PP of cores MD77-191 (red) and BAR94-24 (blue). LGM= Last Glacial Maximum; EMH=Early-Mid Holocene.

4.2 Reconstructed SSTA

At sites SO189-39KL, GeoB10029-4 and GeoB10038-4, despite rather scattered trends, long-term increasing trends may be observed in SSTA values over the last 24 kyr, with minima during the LGM (−1.9, −1.7 and −0.9 ℃, respectively), and maxima during the late Holocene (1.6, 1.3 and 1.5 ℃, respectively) (Fig. 6.3). The magnitude of such SSTA rises between the LGM and the late Holocene is generally higher at sites SO189-39KL and GeoB10029-4 (3.5−3 °C) compared to site GeoB10038-4 (~2.3 °C) as they show slightly higher SSTA during the LGM (~1 °C) and slightly lower SSTA (−1.2 °C) during the Holocene (Fig. 6.3).

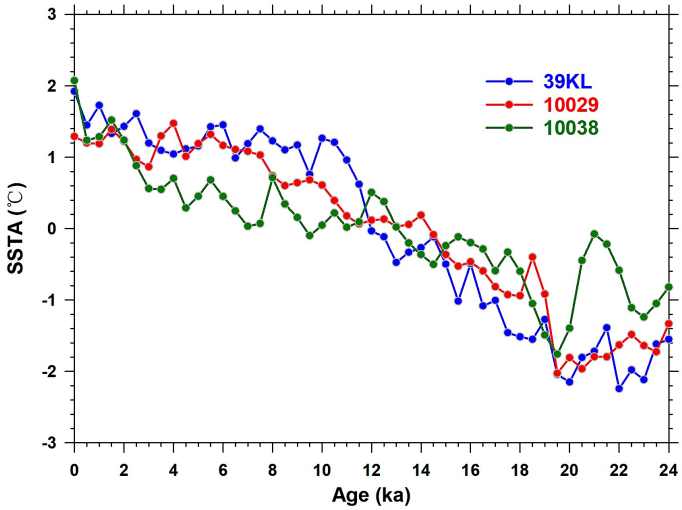

Fig. 6.3. 0.5 kyr interpolation of Sea Surface Temperature Anomalies (SSTA) in sediment cores GeoB10029-4 and SO189-39KL (off western Sumatra) and GeoB10038-4 (off southwestern Sumatra). SSTA were calculated by subtracting SST values to the SST mean of the last 24 kyrs. Original SST data and age models are from Mohtadi et al. (2010, 2014).

4.3 AWI-ESM simulations

Annual mean vertical velocity, surface wind, SLP, and precipitation rate are simulated in CTRL for the tropical Indian Ocean, and their anomalies in LGM and MH as compared to CTRL, are depicted in Fig. 6.4. The results of CTRL experiment are comparable to the atmospheric reanalysis of the 1979−2019 period (Figs. 6.1d, 6.4a), showing stronger convective circulation and higher SLP over the Indo-Pacific Warm Pool as well as divergent circulation and lower SLP over the western Indian Ocean that are accompanied by equatorial westerlies.

4.3.1 Last Glacial Maximum

Downdraught anomalies (up to 0.05 Pa s^{-1}) are simulated over the eastern Arabian Peninsula,

Indonesia, the northern Bay of Bengal, and the southeastern Indian Ocean, while updraught anomalies (up to −0.05 Pa s^{-1}) are obtained over the equatorial Indian Ocean (10°N−10°S) (Fig. 6.4b). Anomalous zonal SLP gradient can be found in the tropical Indian Ocean showing higher SLP over the northeastern and southeastern parts than over the western part. These patterns are associated with anomalous southeasterlies off southwestern Sumatra and anomalous equatorial easterlies off western Sumatra that extend to the central part of the basin and turn to southeasterlies crossing the southern tip of India (Fig. 6.4b). High SLP anomalies are simulated over the eastern Arabian Peninsula and account for the anomalous northeasterlies in (north-) western Indian Ocean, particularly along the coastal region of eastern Oman and Africa (Fig. 6.4b). Overall, precipitation rate anomalies correspond to these anomalous divergent and convergent circulations, which is reflected in drier than present conditions over the eastern part of the Indian Ocean (including the Maritime Continent and the northern Bay of Bengal), and wetter than present conditions over its central and western parts (including eastern Africa) (Figs. 6.4b, e).

4.3.2 Mid-Holocene

Vertical velocity anomalies are generally weak, ranging between −0.02 and 0.02 Pa s^{-1}. Downdraught anomalies are simulated over India, the northern Arabian Sea, and the southeastern Indian Ocean, while updraught anomalies are obtained over the equatorial Indian Ocean (10°N−10°S) (Fig. 6.4c). An anomalous zonal SLP gradient is simulated over the tropical Indian Ocean, with higher SLP over the northeastern and southeastern areas than over the western areas. These patterns result in the occurrence of anomalous southeasterlies alongshore Java and southwestern Sumatra that extend as equatorial easterlies in the central part of the basin and turn to northeasterlies across the southern tip of India (Fig. 6.4c). Anomalous northeasterlies in the (north-) western part of the basin, including eastern Oman and Africa can be found associated with higher SLP over India and the northern Arabian Sea (Fig. 6.4c). Corresponding to these anomalous divergent and convergent circulations, drier-than-present conditions are simulated over the southeastern Indian Ocean while wetter-than-present conditions are simulated over the equatorial Indian Ocean (Figs. 6.4c, f). Notably, the precipitation rate anomalies over the Maritime Continent are diverse showing drier conditions in Borneo and wetter ones in Sumatra.

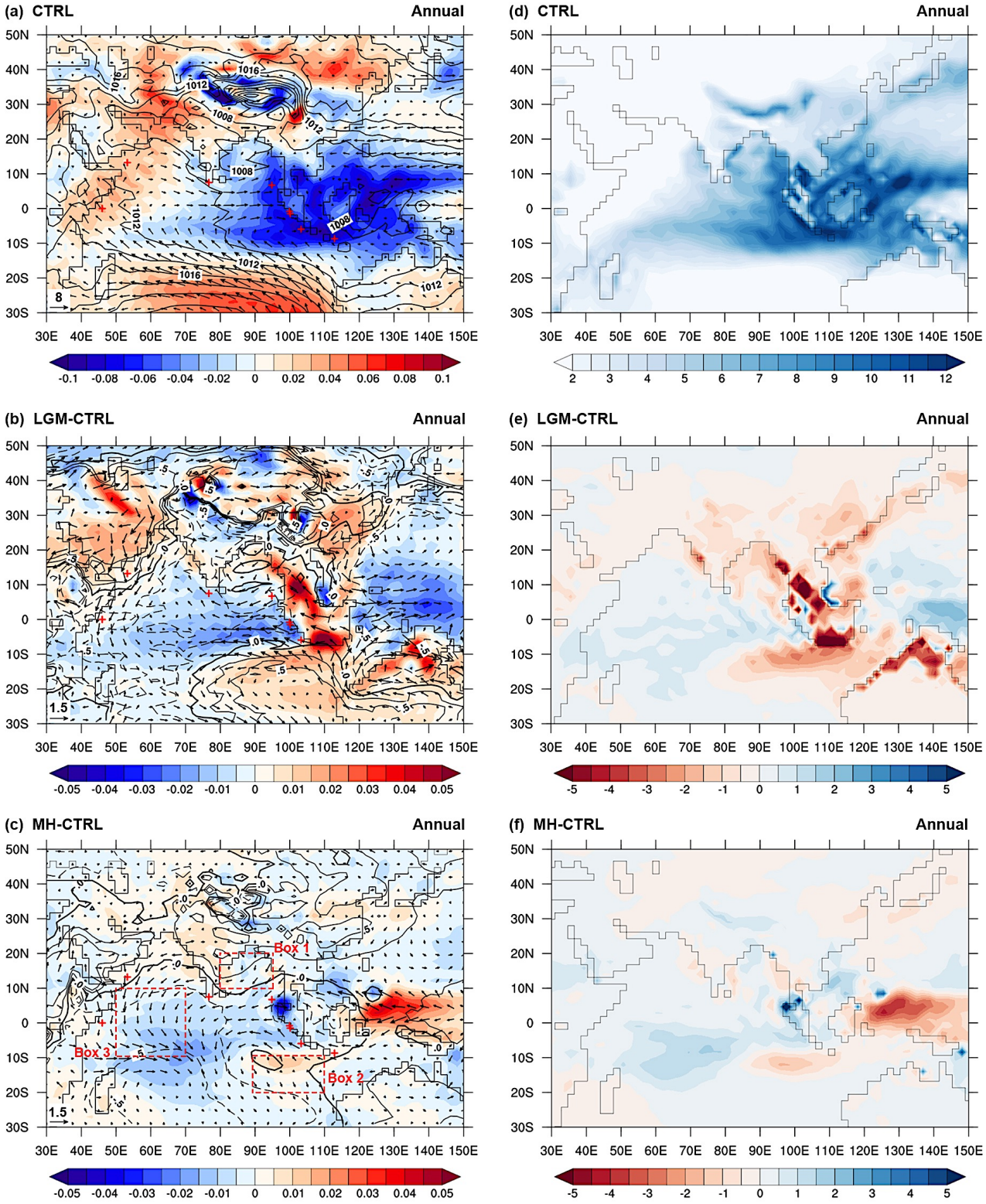

Fig. 6.4. (a) Simulated annual mean vertical velocity at 500 hPa level (color Pa s^{-1}), surface wind (vectors, m s^{-1}), and SLP (contours between 992 and 1032 hPa with 2 hPa spacing) by CTRL experiment. (b) Differences of the same parameters between LGM and CTRL experiments. (c) Differences of the same parameters between MH and CTRL experiments. Contours on (b) and (c) are between -0.5 and 0.5 hPa with 0.25 hPa spacing. (d) Simulated annual mean precipitation rate (mm day^{-1}) by CTRL experiment. (e) Differences in precipitation rate between MH and CTRL experiments. (f) Differences in precipitation rate between LGM and CTRL experiments. The crosses on (a)−(c) mark the sediment cores.

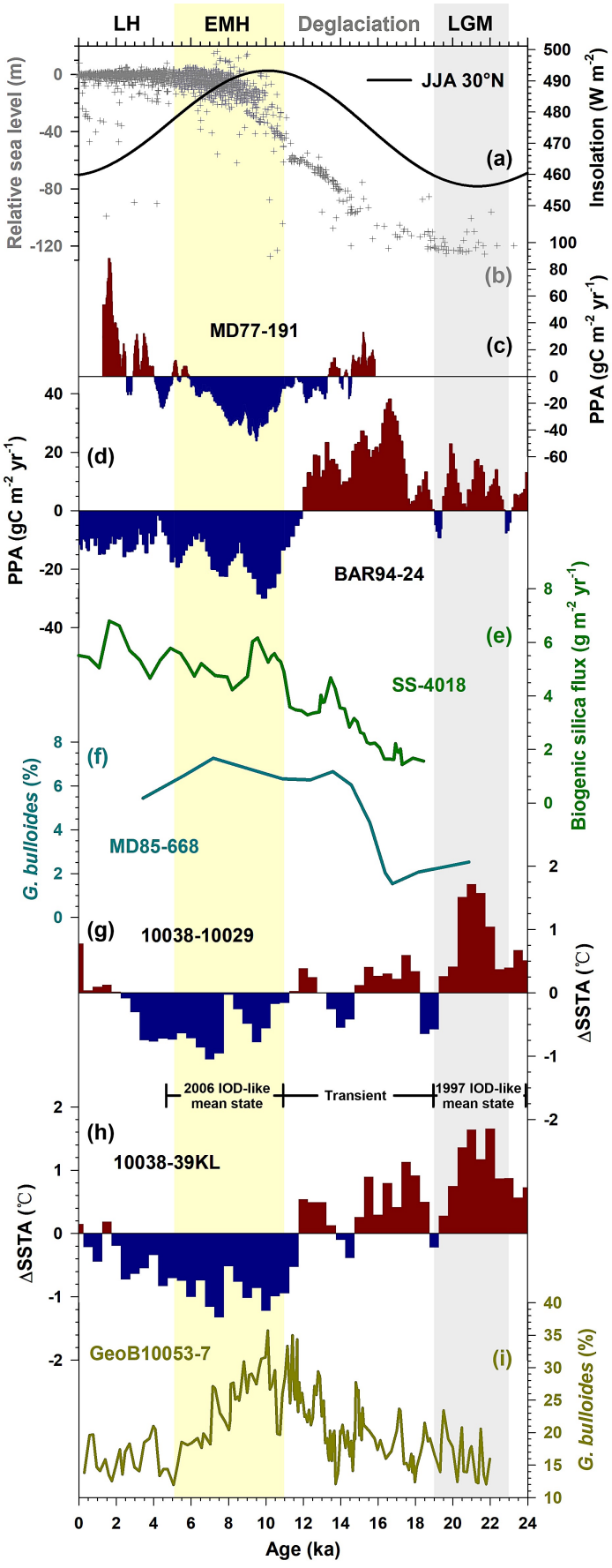

Fig. 6.5. (a) Summer (June-July-August) mean insolation at 30°N (Laskar et al., 2004). (b) Global relative sea level based on biological and geomorphological markers (Hibbert et al., 2018). (c) and (d) PPA of cores MD77-191 (7-point moving average) and BAR94-24 (5-point moving average). (e) Biogenic silica flux from core SS-4018 (Balaji et al., 2018) (f) *G. bulloides* percentages from core GeoB10053-7 (Vergnaud Grazzini et al., 1995). 0.5 kyr interpolated ΔSSTA between (g) cores GeoB10029-4 and GeoB10038-4, and between (h) cores SO188-39KL and GeoB10038-4 (original SST data is from Mohtadi et al., 2010, 2014). (i) *G. bulloides* percentage from core GeoB10053-7 (Mohtadi et al., 2011). EMH = Early-Mid Holocene; LGM = Last Glacial Maximum; LH = Late Holocene.

5. Discussion: The Indian Ocean Walker circulation evolution over the last 24 ka

5.1 During the Last Glacial Maximum

The high PPA obtained at site BAR94-24 (~10 gC m^{-2} kyr^{-1}), together with the positive ΔSSTA calculated between GeoB10038-4 and SO189-39KL/GeoB10029-4 (~1.6 °C), both highlight the development of a strong upwelling system off (north-) western Sumatra (Figs. 6.5, 6.S2, 6.S3) that might reflect the occurrence of stronger easterly winds in this eastern part of the tropical Indian Ocean (see section 2). Such an assumption is confirmed by the relatively low values in reconstructed PP obtained at sites GeoB10053-7 (Mohtadi et al., 2011), SS-4018 (Balaji et al., 2018), and MD85-668 (Vergnaud Grazzini et al., 1995) that highlight weaker coastal upwelling off Java, eastern Somalia and Africa (Figs. 6.5e, f, i), stronger equatorial easterlies along the entire basin, and call for a relatively weak Walker circulation in the tropical Indian Ocean. This scenario is also supported here, by the annual mean state simulated in the LGM experiment run with AWI-ESM, which depicts anomalous equatorial easterly winds over the basin (Fig. 6.4b). Furthermore, it agrees with previously reconstructed and/or simulated SSS and precipitation patterns that suggest, as for AWI-ESM simulations (Fig. 6.4e), relatively dry conditions over Southeast Asia (particularly in Sumatra and the Indonesian maritime continent) and the southeastern Indian Ocean, and relatively wet conditions over eastern Africa (e.g., Penny, 2001; Taylor et al., 2001; Wang et al., 2009; DiNezio and Tierney, 2013; DiNezio et al., 2018).

Remarkably, the occurrence of a strong and wide upwelling system off (north-) western Sumatra at the expense of the upwelling systems off southwestern Sumatra, suggests that the Walker circulation could probably be comparable to the 1997 positive IOD mode, when severe anomalous equatorial easterlies during winter suppressed the influence of anomalous alongshore southeasterlies during the next summer (section 2, Figs. 6.S3). This assumption is supported by seasonal AWI-ESM simulations and showed in SLP and surface wind fields anomalies (Fig. 6.6). Indeed, although inter-hemisphere SLP gradient and anomalous southeasterlies are found alongshore southwest Sumatra in summer (Fig. 6.6c), the anomalous equatorial easterlies in winter appear to be much stronger and thus, further expressed within the annual mean (Figs. 6.4b, 6.6d). Such a feature is also well represented by the ΔSLP indices (LGM−CTRL) between the eastern (north and south) and the western tropical Indian Ocean. The modelling results show positive values during almost the entire year (southeast Box 2–west Box 3) or during the winter season (northeast Box 1−west Box 3), with an overall peak in November (Fig. 6.7). In such a context, it is most probable that early winter anomalous zonal SLP gradients from both sides of the equator, caused anomalous equatorial easterlies and a weaker Walker

circulation to prevail during the LGM. As previously proposed by DiNezio et al. (2016, 2018), based on sea-level single forcing experiments (run with CESM1.2) that depict the weakened annual mean Walker circulation in response to the exposure of Sahul Shelf, those changes mainly arose from the autumn and winter responses. This is similar to the seasonal cycle of the $\Delta SLP_{Index,\ Box2-Box3}$ shown here, implying the same forcing factor behind the weakened Walker circulation. However, since the AWI-ESM experiments include all LGM forcing, we cannot exclude the impacts from other factors such as the ice sheets extensions and greenhouse gases concentrations in addition to the exposure of Sahul and Sunda shelf due to a maximum global ice sheet volume and a minimum global sea-level (~120 m lower than present, Fig. 6.5b).

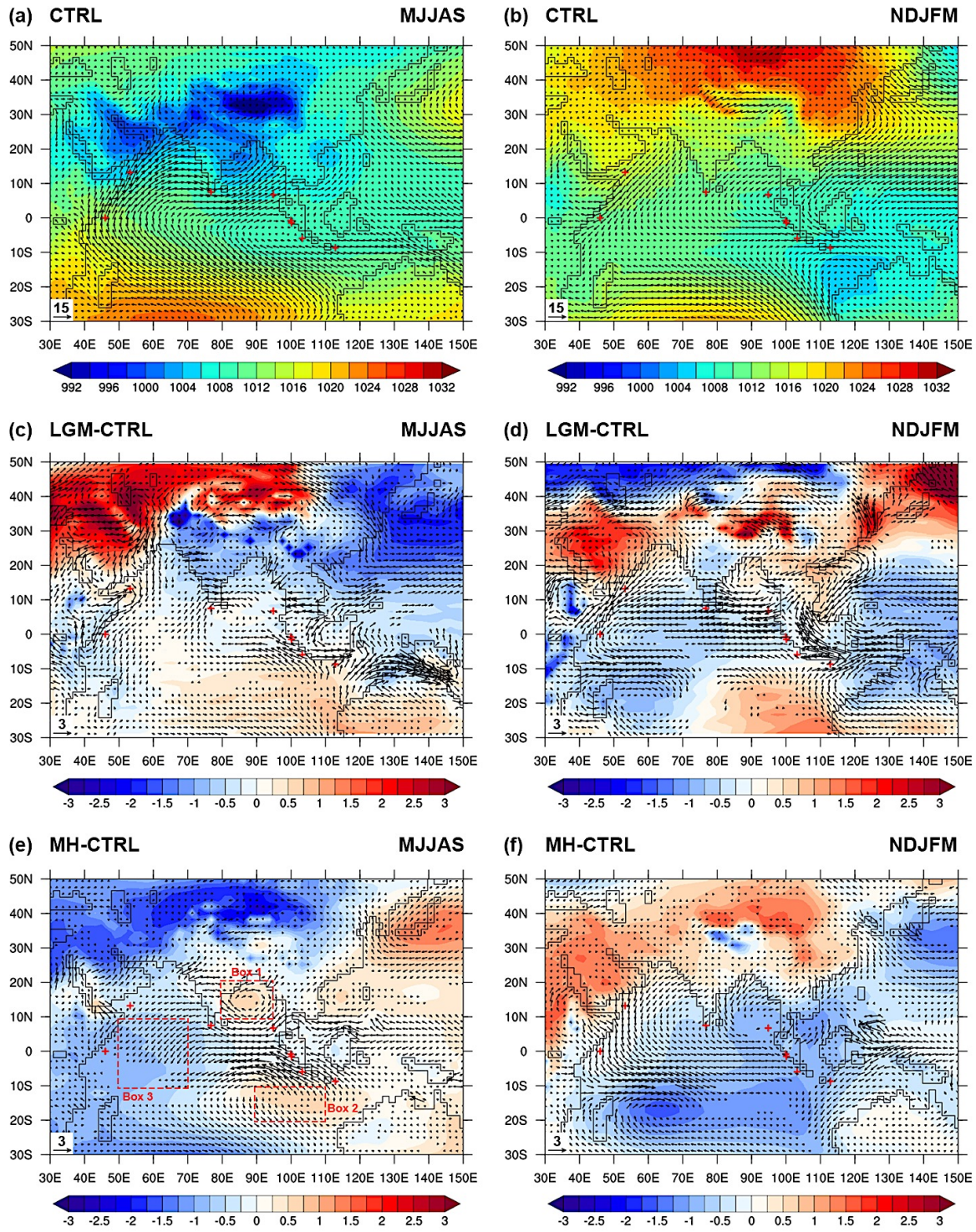

Fig. 6.6. Results of AWI-ESM experiment runs. Simulated SLP (color, hPa) and surface wind (vectors, m s^{-1}) obtained by CTRL experiment in (a) summer (May−June−July−August−September, MJJAS) and (b) winter (November−December−January−February−March, NDJFM). Differences of the same parameters between LGM and CTRL experiments in (c) summer and (d) winter. Differences of the same parameters between MH and CTRL experiments in (e) summer and (f) winter. Sea level pressure values shown in (e) and (f) have been calibrated by subtracting the area average values to remove the effect of LGM background cooling and to highlight the pressure gradient. Only differences of wind vector that are significant at the 95 % level are shown (student's t-test). The crosses mark the sediment cores.

5.2 Towards the Mid-Holocene

PPA from core BAR94-24 depicts a sharp decreasing trend during the deglaciation with maxima at ~17 ka, and minima at ~9 ka, while ΔSSTA show concomitant shifts from positive (~1.6°C) to negative (~ −1°C) values, thus indicating the deglacial weakening of the coastal upwelling system off (north-) western Sumatra and the concomitant strengthening of the upwelling system off southwestern Sumatra (Figs. 6.5, 6.S2, 6.S3). The most plausible explanation behind these PPA and ΔSSTA features is the strengthening of anomalous southeasterlies alongshore Java and southwestern Sumatra and the weakening of anomalous equatorial easterlies. While no clear PPA feature may be highlighted at site MD77-191 during the last deglaciation, such an assumption seems confirmed by the negative values of PPA at site MD77-191, and the maximum values of reconstructed upwelling at site GeoB10053-7 between 10 and 6 ka, that highlight reduced and enhanced upwelling systems off the southern tip of India and off Java during the EMH, respectively (Figs. 6.5c, i). PP-related records from sites SS-4018 and MD85-668 depict opposite trends compared to the site BAR94-24, with minima during the last deglaciation and maxima during the EMH (Figs. 6.5d, e, f) thus, suggesting a deglacial transition toward enhanced coastal upwelling systems off eastern Somalia and Africa. Such a finding could be puzzling under the predominance of equatorial easterly trade winds. However, as seen above (section 2, Figs. 6.S2, 6.S3), rather heterogeneous PP (and upwelling) patterns are observed in the western part of the Indian Ocean basin today, and no general trends may be highlighted. Thus, the most plausible explanation is the occurrence of both tropical easterlies and southeasterlies during the EMH, which likely resulted from an overall weaker Walker circulation in the tropical Indian Ocean during that period, a situation comparable to the one observed during the 2006 positive IOD mode which is characterized by the dominant anomalous southeasterlies off Sumatra and Java. This assumption is supported by the annual mean state simulated by the MH experiment run with AWI-ESM that documents strong alongshore southeasterlies off Java and southwestern Sumatra despite anomalous equatorial easterlies (Fig. 6.4c).

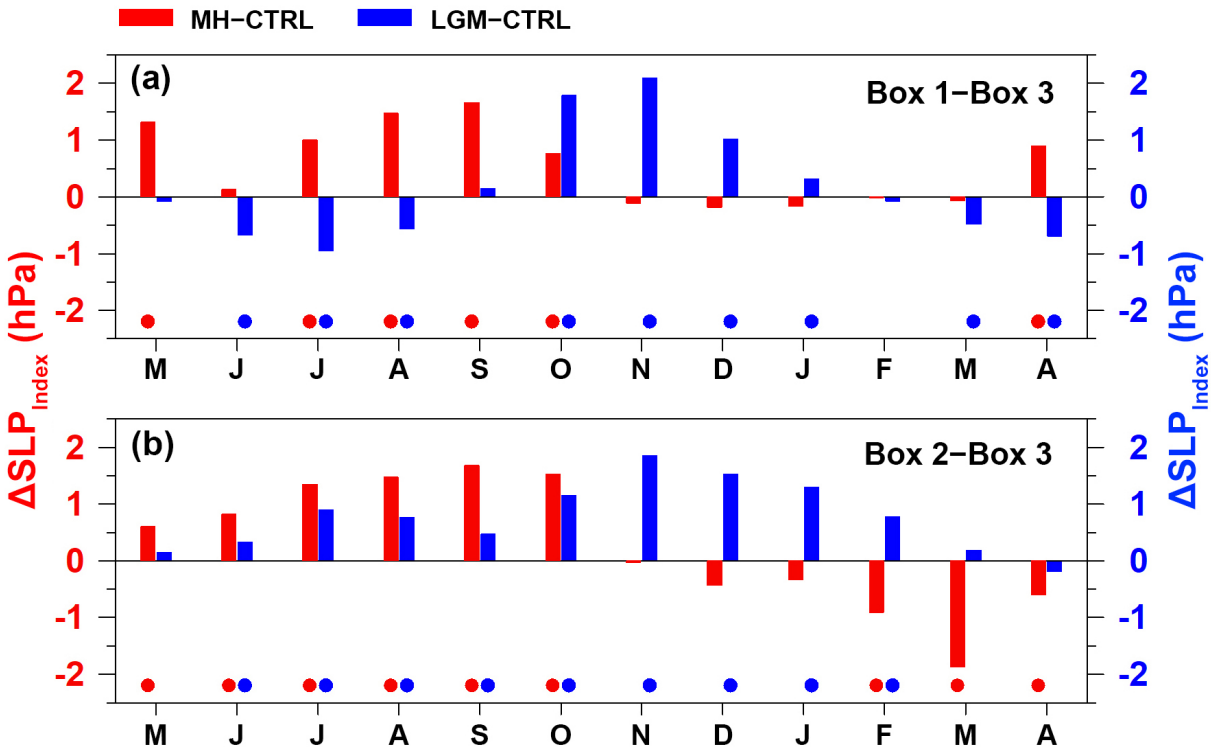

Fig. 6.7. ΔSLP indices selected in the northeastern (Box 1, 10°N−20°N, 85°E−95°E), southeastern (Box 2, 20°S −10°S, 90°E −110°E) and western (Box 3, 10°S−10°N, 50°E−70°E) parts of the tropical Indian Ocean (Figs. 5e, 6c) between LGM and CTRL (blue bars) and between MH and CTRL (red bars). The blue and red dots mark the differences with significance at the 95 % level (student's t-test).

It is also in good accordance with precipitation reconstructions that show relatively dry conditions over the Indonesian maritime continent and relatively wet ones in eastern Africa during the EMH (e.g., Tierney et al., 2011, 2012), which correspond to simulated descending and ascending air motions over Borneo and eastern Africa, respectively (Figs. 6.4c, f). Despite the occurrence of anomalous westerlies over the equatorial Indian Ocean during winter (Fig. 6.6f), the anomalous southeasterlies alongshore southwestern Sumatra appear to be much stronger, and thus dominate the annual mean patterns (Figs. 6.4c, 6.6e). Such result is corroborated by the ΔSLP indices (MH−CTRL) obtained between the eastern and the western tropical Indian Ocean, which show positive values during the summer season, with a paroxysm in September (Fig. 6.7). The anomalous SLP distribution in summer over the Indian Ocean found in MH as compared to CTRL (Fig. 6.6e), is a common feature observed in general coupled models (e.g., Liu et al., 2004; Zhao et al., 2005; Marzin and Braconnot, 2009; Bosmans et al., 2012; Zhao and Harrion, 2012; D'Agostino et al., 2019; Iwakiri and Watanabe, 2019). The higher SLP over the Bay of Bengal is connected to an enhanced high SLP system over the northwestern Pacific and together, they form a zonal band of high SLP anomaly driving an anomalous Walker-type (zonal)

circulation extending from the South China Sea to the western Indian Ocean (Fig. 6.6e; Zhao et al., 2005). The higher SLP over the northwestern Pacific in summer was proposed as a consequence of the enhanced land-sea contrast and the increased diabatic heating over the southern Tibet Plateau and Maritime Continent under smaller precession parameter (Mantsis et al., 2013; Wu et al., 2016), while the higher SLP over the southeastern Indian Ocean in summer was suggested as a result of the strengthened tropical seasonality (Iwakiri and Watanabe, 2019). Consequently, it is likely that late summer anomalous zonal SLP gradients caused anomalous equatorial easterlies together with southeasterlies alongshore Java and southwestern Sumatra and weakened Walker circulation during the EMH. Interestingly, the divergent circulation documented over southwestern Indonesia, appears to make part of an overall ascending air motion cell, that extends in the western part of the equatorial Pacific, up to Borneo (Fig. 6.4c). This pattern that is more related to a cross Pacific-Indian Ocean anomalous Walker-type circulation, is different from that of the LGM (Fig. 6.4b). However, further studies are needed to figure out the coupling and interaction between the Walker circulation cells of the Pacific and Indian Oceans.

5.3 During the Late Holocene

During the late Holocene i.e. from 4 ka to present, PPA obtained at site BAR94-24 depict slightly negative values (~ −18 gC m^{-2} kyr^{-1}), while PPA from site MDD77-191 sharply increased to reach maxima (~90 gC m^{-2} kyr^{-1}) at ~2 ka (Figs. 6.5c, d) which document a relatively weak coastal upwelling system off northwestern Sumatra and a rapid transition toward intense upwelling conditions off southern India. PP-related records at site SS-4018 also indicate a strong upwelling system off eastern Somalia, while those obtained off Java and southwestern Sumatra document reduced ones (Figs. 6.5e, i). Therefore, all the records are coherent in suggesting over the last 24 kyr the occurrence of anomalous westerlies along the equator and a relatively strong Walker circulation in the tropical Indian Ocean during the Late Holocene, as previously highlighted by paleoclimate reconstructions that revealed cold and dry conditions in east Africa and wet conditions in the eastern Indian Ocean (Gasse et al., 2000; Thompson et al., 2002; Niedermeyer et al., 2014).

6. Conclusions

Based on paleoclimate reconstructions and simulations, we infer the evolution of the zonal wind intensity (Walker circulation) over the equatorial Indian Ocean since the last 24 kyr. Both empirical data and simulations indicate that the Indian Ocean Walker circulation during the LGM and EMH was weaker than the present, but differences are found in their annual mean and seasonal states due to the

changes in zonal sea-level pressure gradients and atmospheric vertical motions. During the LGM, the weaker Walker circulation appears to be dominated by strong anomalous equatorial easterlies in early winter, in a similar way as the positive IOD mean state observed in 1997. During the EMH, anomalous equatorial easterlies and strong anomalous southeasterlies off Sumatra are detected in late summer, which appears to be similar to the positive IOD mean state of 2006. We suggest the deglaciation to be a transient period in-between these two intervals. It is only during the late Holocene that paleoceanographic records document anomalous equatorial westerly winds and provide evidence of stronger Walker circulation.

Our results help better understanding the impact of Walker circulation on the complex climate variability that exists over the Indian Ocean realm in the past. They should also help understanding future climate, as the LGM and the EMH allow us to test boundary conditions as crucial as ice sheet extent, sea-level and greenhouse gases are, for projections. However, further studies on paleoclimate reconstructions and the global warming scenario simulations are required to better understand the mechanisms associated with a changing Walker circulation. As a logical next step, we will analyse high time-resolution PPA and SSTA in the western Indian Ocean over the last 24 kyr, to provide a more complete overview of the tropical (equatorial) Indian Ocean. Single forcing experiments will also be needed to isolate the effects of greenhouse gas concentration and sea level changes.

Data availability

Coccolith data can be found in the supplementary materials. Modelling data can be downloaded in from the Earth System Grid Federation (ESGF; https://esgf.llnl.gov/nodes.html). The doi for the LGM simulation is: https://doi.org/10.22033/ESGF/CMIP6.9330. The doi for the MH simulation is: https://doi.org/10.22033/ESGF/CMIP6.9332 and the doi for the Pre-industrial control simulation is: https://doi.org/10.22033/ESGF/CMIP6.9335. The source code of the climate model is available from the AWI based svn repository (https://swrepo1.awi.de/projects/awi-cm/).

Declaration of competing interest

The authors declare that they have no known competing financial interests or personal relationships that could have appeared to influence the work reported in this paper.

Acknowledgements

The authors thank the University of Paris Saclay and the China Scholarship Council (CSC) for providing Xinquan Zhou scholarship, and the German Climate Computing Centre (DKRZ, Hamburg)

for providing computing resources. Xinquan Zhou would like to thank the Geosciences Paris-Saclay (UMR GEOPS) and the Laboratory of the Sciences du Climat et de l'Environnement (LSCE) for funding his study. This work is LSCE contribution n°XXXXX. The AWI-ESM simulation is a contribution to PalMod and PACMEDY projects funded by the BMBF. The authors also thank the people who conduct the CMIP6 and PMIP4 projects.

Appendix A. Supplementary materials

Supplementary figures, table, and data are available online.

References

Abram, N. J., Gagan, M. K., McCulloch, M. T., Chappell, J., Hantoro, W. S., 2003. Coral Reef death during the 1997 Indian Ocean Dipole linked to Indonesian wildfires. Science 301, 952−955.

Balaji, D., Bhushan, R., Chamyal, L. S., 2018. Variations of the Somali upwelling since 18.5 ka BP and its relationship with southwest monsoon rainfall. Climate of the Past 14, 1331−1343.

Bassinot, F. C., Marzin, C., Braconnot, P., Marti, O., Mathien-Blard, E., Lombard, F., Bopp, L., 2011. Holocene evolution of summer winds and marine productivity in the tropical Indian Ocean in response to insolation forcing: data-model comparison. Climate of the Past 7, 815−829.

Beaufort, L., Barbarin, N., Gally, Y., 2014. Optical measurements to determine the thickness of calcite crystals and the mass of thin carbon particles such as coccoliths. Nature Protocols 9, 633–642.

Beaufort, L., Lancelot, Y., Camberlin, P., Cayre, O., Vincent, E., Bassinot, F., Labeyrie, L., 1997. Insolation cycles as a major control of Equatorial Indian Ocean primary production. Science 278, 1451–1454.

Behera, S. K., Yamagata, T., 2003. Influence of the Indian Ocean Dipole on the Southern Oscillation. Journal of the Meteorological Society of Japan 81, 169−177.

Behrenfeld, M. J., Falkowski, P. G., 1997. Photosynthetic rates derived from satellite-based chlorophyll concentration. Limnology and Oceanography 42, 1–20.

Bjerknes, J., 1969. Atmospheric teleconnections from the equatorial Pacific. Monthly Weather Review 97, 163–172.

Bloszies, C., Forman, S. L., Wright, D. K., 2015. Water level history for Lake Turkanam Kenya in the past 15,000 years and a variable transition from the African Humid Period to Holocene aridity. Global and Planetary Change 132, 64−76.

Bosmans, J. H. C., Drijfhout, S. S., Tuenter, E., Lourens, L. J., Hilgen, F. J., Weber, S. L., 2012.

Monsoonal response to mid-holocene orbital forcing in a high resolution GCM. Climate of the Past 8, 723−740.

Brierley, C. M., Zhao, A., Harrison, S. P., Braconnot, P., Williams, C. J. R., Thornalley, D. J. R., Shi, X., Peterschmitt, J.-Y., Ohgaito, R., Kaufman, D. S., Kageyama, M., Hargreaves, J. C., Erb, M. P., Emile-Geay, J., D'Agostino, R., Chandan, D., Carré, M., Bartlein, P. J., Zheng, W., Zhang, Z., Zhang, Q., Yang, H., Volodin, E. M., Tomas, R. A., Routson, C., Peltier, W. R., Otto-Bliesner, B., Morozova, P. A., McKay, N. P., Lohmann, G., Legrande, A. N., Guo, C., Cao, J., Brady, E., Annan, J. D., Abe-Ouchi, A. Large-scale features and evaluation of the PMIP4-CMIP6 *midHolocene* simulations., 2020. Large-scale features and evaluation of the PMIP4-CMIP6 midHolocene simulations. Climate of the Past 16, 1847−1872.

Brown, J. N., McIntosh, P. C., Pook, M. J., Risbey, J. S., 2009. An investigation of the links between ENSO flavors and rainfall processes in southeastern Australia. Monthly Weather Review 137, 3786−3795.

Cai, W., Cowan, T., Sullivan, A., 2009. Recent unprecedented skewness towards positive Indian Ocean Dipole occurrences and its impact on Australian rainfall. Geophysical Research Letter 36, L11705. https://doi.org/10.1029/2009GL037604.

Chen, G., Han, W., Li, Y., Wang., D., 2016. Interannual variability of equatorial eastern Indian Ocean upwelling: Local versus Remote Forcing. Journal of Physical Oceanography 46, 798−807.

Chevalier, M., Brewer, S., Chase, B. M., 2017. Qualitative assessment of PMIP3 rainfall simulations across the eastern African monsoon domains during the mid-Holocene and the Last Glacial Maximum. Quaternary Science Reviews 156, 107−120.

Cullen, J. L., Prell, W. L., 1984. Planktonic foraminifera of the north- ern Indian Ocean: Distribution and preservation in surface sediments. Marine Micropaleontology 9, 1–52.

Currie, J. C., Lengaigne, M., Vialard, J., Kaplan, D. M., Aumont, O., Naqvi, S. W. A., Maury, O., 2013. Indian Ocean Dipole and El Niño/Southern Oscillation impacts on regional chlorophyll anomalies in the Indian Ocean. Biogeosciences 10, 6677−6698.

D'Agostino, R., Bader, J., Bordoni, S., Ferreira, D., Jungclaus, J., 2019. Northern Hemisphere monsoon response to mid-Holocene orbital forcing and greenhouse gas-induced global warming. Geophysical Research Letters 46, 1591–1601.

D'Arrigo, R., Wilson, R., 2008. El Niño and Indian Ocean influences on Indonesian drought: implications for forecasting rainfall and crop productivity. International Journal of Climatology 28, 611–616.

de Garidel-Thoronm T., Beaufort, L., Linsley, B. K., Dannemann, S., 2001. Millennial-scale dynamics

of the East Asian winter monsoon during the last 200,000 years. Paleoceanography 16, 491−502.

DiNezio, P. N., Tierney, J. E., 2013. The effect of sea level on glacial Indo-Pacific climate. Nature Geoscience 6, 485−491.

DiNezio, P. N., Timmermann, A., Tierney, J. E., Jin, F.-F., Otto-Bliesner, B., Rosenbloom, N., Mapes, B., Neale, R., Ivanovic, R. F., Montenegro, A., 2016. The climate response of the Indo-Pacific warm pool to glacial sea level. Paleoceanography 31, 866−894.

DiNezio, P. N., Tierney, J. E., Otto-Bliesner, B., Timmermann, A., Bhattacharya, T., Rosenbloom, N., Brady, E., 2018. Glacial changes in tropical climate amplified by the Indian Ocean. Science Advances 4, eaat9658. https://doi.org/10.1126/sciadv.aat9658.

Duchamp-Alphonse, S., Siani, G, Michel, E., Beaufort, L, Gally, Y., Jaccard, S. L., 2018. Enhanced ocean-atmosphere carbon partitioning via the carbonate counter pump during the last deglacial. Nature Communications 9, 2396. https://doi.org/ 10.1038/s41467-018-04625-7.

Gasse, F., 2000. Hydrological changes in the African tropics since the Last Glacial Maximum. Quaternary Science Reviews 19, 189−211.

Girishkumar, M. S., Ravichandran, M., Pant, V., 2012. Observed chlorophyll-a bloom in the southern Bay of Bengal during winter 2006−2007. International Journal of Remote Sensing 33, 1264−1275.

Hernández-Almeida, I., Ausín, B., Saavedra-Pellitero, M., Baumann, K.-H., Stoll, H. M., 2019. Quantitative reconstruction of primary productivity in low latitudes during the last glacial maximum and the mid-to-late Holocene from a global *Florisphaera profunda* calibration dataset, Quaternary Science Reviews 205, 166–181.

Hersbach, H., Bell, B., Berrisford, P. et al., 2020. The Era5 global reanalysis. Quarterly Journal of the Royal Meteorological Society 146, 1999–2049.

Hibbert, F., Williams, F., Fallon, S., Rohling, E. J., 2018. A database of biological and geomorphological sea-level markers from the Last Glacial Maximum to present. Scientific Data 5, 180088, https://doi.org/10.1038/sdata.2018.88.

Iskandar, I., Rao, S. A., Tozuka, T., 2009. Chlorophyll-a bloom along the southern coasts of Java and Sumatra during 2006. International Journal of Remote Sensing 30, 663–671.

Iwakiri, T., Watanabe, M., 2019. Strengthening of the Indian Ocean Dipole with increasing seasonal cycle in the mid-Holocene. Geophysical Research Letters 46, 8320–8328.

Kageyama, M., Albani, S., Braconnot, P., Harrison, S. P., Hopcroft, P. O., Ivanovic, R. F., Lambert, F., Marti, O., Peltier, W. R., Peterschmitt, J.-Y., Roche, D. M., Tarasov, L., Zhang, X., Brady, E. C., Haywood, A. M., LeGrande, A. N., Lunt, D. J., Mahowald, N. M., Mikolajewicz, U., Nisancioglu,

K. H., Otto-Bliesner, B. L., Renssen, H., Tomas, R. A., Zhang, Q., Abe-Ouchi, A., Bartlein, P. J., Cao, J., Li, Q., Lohmann, G., Ohgaito, R., Shi, X., Volodin, E., Yoshida, K., Zhang, X., Zheng, W., 2017. The PMIP4 contribution to CMIP6 – Part 4: Scientific objectives and experimental design of the PMIP4-CMIP6 Last Glacial Maximum experiments and PMIP4 sensitivity experiments. Geoscientific Model Development 10, 4035–4055.

Kageyama, M., Braconnot, P., Harrison, S. P., Haywood, A. M., Jungclaus, J. H., Otto-Bliesner, B. L., Peterschmitt, J.-Y., Abe-Ouchi, A., Albani, S., Bartlein, P. J., Brierley, C., Crucifix, M., Dolan, A., Fernandez-Donado, L., Fischer, H., Hopcroft, P. O., Ivanovic, R. F., Lambert, F., Lunt, D. J., Mahowald, N. M., Peltier, W. R., Phipps, S. J., Roche, D. M., Schmidt, G. A., Tarasov, L., Valdes, P. J., Zhang, Q., Zhou, T., 2018. The PMIP4 contribution to CMIP6 – Part 1: Overview and overarching analysis plan. Geoscientific Model Development 11, 1033–1057.

Kageyama, M., Harrison, S. P., Kapsch, M.-L., Lofverstrom, M., Lora, J. M., Mikolajewicz, U., Sherriff-Tadano, S., Vadsaria, T., Abe-Ouchi, A., Bouttes, N., Chandan, D., Gregoire, L. J., Ivanovic, R. F., Izumi, K., LeGrande, A. N., Lhardy, F., Lohmann, G., Morozova, P. A., Ohgaito, R., Paul, A., Peltier, W. R., Poulsen, C. J., Quiquet, A., Roche, D. M., Shi, X., Tierney, J. E., Valdes, P. J., Volodin, E., Zhu, J., 2021. The PMIP4 Last Glacial Maximum experiments: preliminary results and comparison with the PMIP3 simulations. Climate of the Past 17, 1065–1089.

Laskar, J., Robutel, P., Joutel, F., Gastineau, M., Correia, A. C. M., and Levrard, B., 2004. A long-term numerical solution for the insolation quantities of the Earth. Astronomy and Astrophysics 428, 261–285.

Lau, K.-M., Yang, S., 2015. TROPICA METEOROLOGY AND CLIMATE | Walker Circulation, in: North, G. R., Pyle, J., Zhang, F. (Eds.), Encyclopedia of Atmospheric Sciences (Second Edition). Academic Press, pp. 177−181.

L'Heureux, M. L., Lee, S., Lyon, B., 2013. Recent multidecadal strengthening of the Walker circulation across the tropical Pacific. Nature Climate Change 3, 571−576.

Lim, E.-P., Hendon, H. H., 2015. Understanding the contrast of Australian springtime rainfall of 1997 and 2002 in the frame work of two flavors of El Niño. Journal of Climate 28, 2804−2822.

Liu, Z., Harrison, S. P., Kutzbach, J., Otto-Bliesner, B., 2004. Global monsoon in the mid-Holocene and oceanic feedback. Climate Dynamics 22, 157−182.

Lohmann, G., Butzin, M., Eissner, N., Shi, X., Stepanek, C., 2020. Abrupt climate and weather changes across time scales. Paleoceanography and Paleoclimatology 35, e2019PA003782. https://doi.org/10.1029/2019PA003782.

Ma, R., Sépulcre, S., Bassinot, F., Haurine, F., Tisnérat-Laborde, N., Colin, C., 2020. North Indian Ocean Circulation since the Last Deglaciation as inferred from new elemental ratio records for benthic foraminifera Hoeglundina elegans. Paleoceanography and Paleoclimatology 35, e2019PA003801. https://doi.org/ 10.1029/2019PA003801.

Mantsis D. F., Clement A. C., Kirtman B., Broccoli A. J., Erb M. P., 2013. Precessional cycles and their influence on the North Pacific and North Atlantic summer anticyclones. Journal of Climate 26, 4596–4611.

Marzin, C., Braconnot, P., 2009. Variations of Indian and African monsoons induced by insolation changes at 6 and 9.5 kyr BP. Climate Dynamics 33, 215−231.

Mohtadi, M., Steinke, S., Lückge, A., Groeneveld, J., Hathorne, E. D., 2010. Glacial to Holocene surface hydrography of the tropical eastern Indian Ocean. Earth and Planetary Science Letters 292, 89−97.

Mohtadi, M., Oppo, D. W., Steinke, S., Stuut, J.-B. W., De Pol-Holz, R., Hebbeln, D., Lückge, A., 2011. Glacial to Holocene swings of the Asutralian-Indonesian monsoon. Nature Geoscience 4, 540−544.

Mohtadi, M., Prange, M., Oppo, D. W., De Pol-Holz, R., Merkel, U., Zhang, X., Steinke, S., Lückge, A., 2014. North Atlantic forcing of tropical Indian Ocean climate. Nature 509, 76−80.

Mohtadi, M., Prange, M., Schefuß, E., Jennerjahn, T. C., 2017. Late Holocene slowdown of the Indian Ocean Walker circulation. Nature Communications 8**,** 1015. https://doi.org/10.1038/s41467-017-00855-3.

Murtugudde, R., McCreary Jr., J. P., Busalacchi, A. J., 2000. Oceanic processes associated with anomalous events in the Indian Ocean with relevance to 1997−1998. Journal of Geophysical Research 105, 3295−3306.

Murtugudde, R. G., Signorini, S. R., Christian, J. R., Busalacchi, A. J., McClain, C. R., Picaut, J., 1999. Ocean color variability of the tropical Indo-Pacific basin observed by SeaWiFS during 1997−1998. Journal of Geophysical Research 104, 18351−18366.

Niedermeyer, E. M., Sessions, A. L., Feakins, S. L., Mohtadi, M., 2014. Hydroclimate of the western Indo-Pacific Warm Pool during the last 24,000 years. Proceedings of the National Academy of Sciences of the United States of America 111, 9402−9406.

Okada, H., Honjo, S., 1973. The distribution of oceanic coccolithophorids in the Pacific, Deep-Sea Research 20, 355–374.

Otto-Bliesner, B. L., Braconnot, P., Harrison, S. P., Lunt, D. J., Abe-Ouchi, A., Albani, S., Bartlein, P. J., Capron, E., Carlson, A. E., Dutton, A., Fischer, H., Goelzer, H., Govin, A., Hay- wood, A.,

Joos, F., LeGrande, A. N., Lipscomb, W. H., Lohmann, G., Mahowald, N., Nehrbass-Ahles, C., Pausata, F. S. R., Peterschmitt, J.-Y., Phipps, S. J., Renssen, H., and Zhang, Q., 2017. The PMIP4 contribution to CMIP6 – Part 2: Two interglacials, scientific objective and experimental design for Holocene and Last Interglacial simulations. Geoscientific Model Development 10, 3979–4003.

Patterson, R. T., Fishbein, E., 1984. Re-examination of the statistical methods used to determine the number of point counts needed for micropaleontological quantitative research. Journal of Paleontology 63, 245–248.

Peltier, W., Richard, D. F. Argus, R. Drummond., 2015. Space geodesy constrains ice age terminal deglaciation: The global ICE-6G_C (VM5a) model. Journal of Geophysical Research: Solid Earth 120, 450-487.

Penny, D., 2001. A 40,000 year palynological record from north-east Thailand; implications for biogeography and palaeo-environmental reconstruction. Palaeogeography, Palaeoclimatology, Palaeoecology 171, 97–128.

Rao, R. R., Kumar, M. S. G., Ravichandran, M., Samala, B. K., Sreedevi, N., 2006. Observed mini-cold pool off the southern tip of India and its intrusion into the south central Bay of Bengal during summer monsoon season. Geophysical Research Letters 33, L06607. https://doi.org/1029/2005GL025382

Saji, N. H., Goswami, B. N., Vinayachandran, P. N., Yamagata, T., 1999. A dipole mode in the tropical Indian Ocean. Nature 401, 360−363.

Shi, W., Wang, M., 2021. A biological Indian Ocean Dipole event in 2019. Scientific Reports 11, 2452. https://doi.org/10.1038/s41598-021-81410-5.

Sidorenko, D., Wang, Q., Danilov, S., Schröter, J., 2011. FESOM under coordinated ocean-ice reference experiment forcing. Ocean Dynamics 61, 881−890.

Shi X., Lohmann G, Sidorenko D, Yang H.,2020. Early-Holocene simulations using different forcings and resolutions in AWI-ESM. The Holocene 30, 996–1015.

Susanto. R. D., Gordon, A. L., Zheng, Q., 2001. Upwelling along the coasts of Java and Sumatra and its relation to ENSO. Geophysical Research Letters 28, 1599−1602.

Taylor, D., Yen, O., Sanderson, P., Dodson, J., 2001. Late Quaternary peat formation and vegetation dynamics in a lowland tropical swamp; Nee Soon, Singapore. Palaeogeography, Palaeoclimatology, Palaeoecology 171, 269–287

Thompson, L. G., Mosley-Thompson, M., Davis, M. E., Henderson, K. A., Brecher, H. H., Zagorodnov, V. S., Mashiotta, T. A., Lin, P.-N., Mikhalenko, V. N., Hardy, D. R., Beer, J., 2002. Kilimanjaro

ice core records: eviendence of Holocene climate change in tropical Africa. Science 298, 589–593.

Trewin, B., Ganter, C., 2019. Seasonal climate summary for the southern hemisphere (spring 2006): strong negative Indian Ocean Dipole ends, bring second wetter September to Australia. Journal of Southern Hemisphere Earth System Science 69, 273−289.

Thushara, V., Vinayachandran, P. N., 2020. Unprecedented surface chlorophyll blooms in the southeastern Arabian Sea during an extreme negative Indian Ocean Dipole. Geophysical Research Letters 47, e2019GL085026. https://doi.org/10.1029/2019GL085026.

Tierney, J. E., Lewis, S. C., Cook, B. I., LeGrande, A. N., Schmidt, G. A., 2011. Model, proxy and isotopic perspectives on the East Africa Humid Period. Earth and Planetary Science Letters 307, 103−112.

Tierney, J. E., Oppo, D. W., LeGrande, A. N., Huang, Y., Rosenthal, Y., Linsley, B. K., 2012. The influence of Indian Ocean atmospheric circulation on Warm Pool hydroclimate during the Holocene epoch. Journal of Geophysical Research 117, D19108. https://doi.org/ 10.1029/2012JD018060.

Ummenhofer, C. C., England, M. H., McIntosh, P. C., Meyers, G. A., Pook, M. J., Risbey, J. S., Gupta, A. S., Taschetto, A. S., 2009. What causes southeast Australia's worst droughts? Geophysical Research Letter 36, L04706. https://doi.org/ 10.1029/2008GL036801.

Vecchi, G. A., Soden, B. J., 2007. Global warming and the weakening of the tropical circulation. Journal of Climate 20, 4316−4340.

Vergnaud Grazzini, C. V., Vénec-Peyré, M. T., Caulet, J. P., Lerasle, N., 1995. Fertility tracers and monsoon forcing at an equatorial site of the Somali Basin (Northwest Indian Ocean). Marine Micropaleontology 26, 137−152.

Vinayachandran, P. N., Iizuka, S., Yamagata, T., 2002. Indian Ocean dipole mode events in an ocean general circulation model. Deep-Sea Research Ⅱ 49, 1573−1596.

Wang, X., Sun, X., Wang, P., Stattegger, K., 2009. Vegetation on the Sunda shelf, South China Sea, during the Last Glacial Maximum. Palaeogeography, Palaeoclimatology, Palaeoecology 278, 88–97.

Webster, P. J., Moore, A. M., Loschnigg, J. P, Leben, R. R., 1999. Coupled ocean-atmosphere dynamics in the Indian Ocean during 1997−98. Nature 401, 356−360.

Wiggert, J. D., Vialard, J. and Behrenfeld, M.J., 2009. Basin-Wide Modification of Dynamical and Biogeochemical Processes by the Positive Phase of the Indian Ocean Dipole During the SeaWiFS Era, in: Wggert, J. D., Hood, R. R., Naqvi, S. A., Brink, K. H., Smith, S. L. (Eds.),

Indian Ocean Biogeochemical Processes and Ecological Variability. American Geophysical Union, Geophysical Monograph Series, vol. 185, pp. 385−407.

Wu, C.-H., Chiang, J. C. H., Hsu, H.-H., Lee, S.-Y., 2016. Orbital control of the western North Pacific summer monsoon. Climate Dynamics 46, 897−911.

Zhao, Y., Braconnot, P., Marti, O., Harrison, S. P., Hewitt, C., Kitoh, A., Liu, Z., Mikolajewicz, U., Otto-Bliesner, B., Weber, S. L., 2005. A multi-model analysis of the role of the ocean on the African and Indian monsoon during the mid-Holocene. Climate Dynamics 25, 777−800.

Zhao, Y., Harrison, S. P., 2012. Mid-Holocene monsoons: a multi-model analysis of the inter-hemispheric differences in the responses to orbital forcing and ocean feedbacks. Climate Dynamics 39, 1457−1487.

Zhou, X., Duchamp-Alphonse, S., Kageyama, M., Bassinot, F., Beaufort, L., Colin, C., 2020. Dynamics of primary productivity in the northeastern Bay of Bengal over the last 26 000 years. Climate of the Past 16, 1969−1986.

Supplementary figures and table

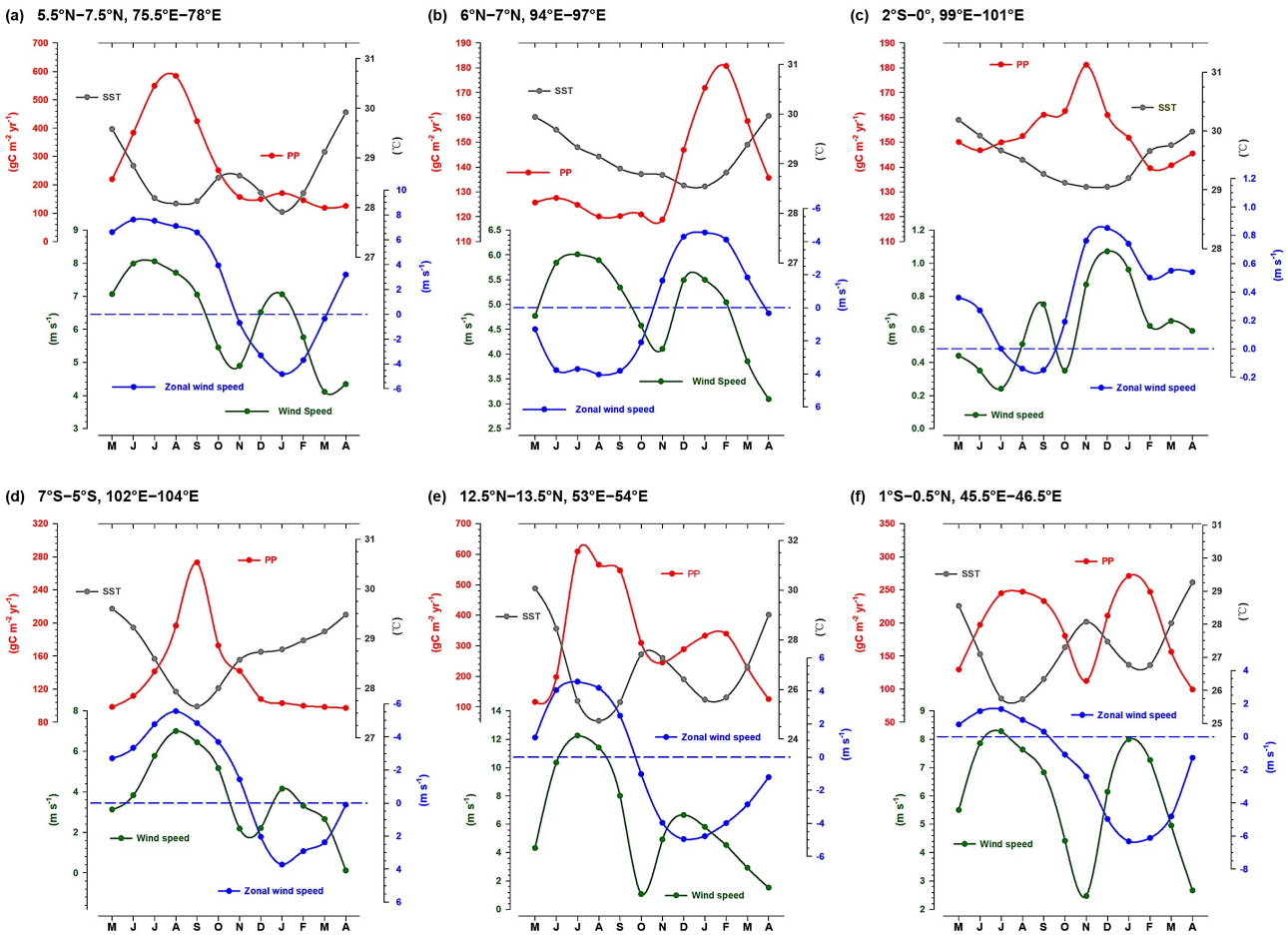

Fig. 6.S1. Seasonal variations (period 2003–2019) of primary productivity (PP), sea surface temperature (SST) and surface zonal wind speed off (a) the southern tip of India, (b) northwestern Sumatra, (c) western Sumatra, (d) southwestern Sumatra, (e) Somalia, and (f) equatorial east Africa. Wind speed data are from the reanalysis dataset ERA5 (https://www.ecmwf.int/en/forecasts/datasets/reanalysis-datasets/era5). SST data are from the NOAA OI SST V2 High Resolution Dataset (https://psl.noaa.gov/data/gridded/data.noaa.oisst.v2.highres.html; monthly 01/1992–12/2019). PP data are from the "Ocean Productivity" website (http://sites.science.oregonstate.edu/ocean.productivity).

1997 Positive IOD

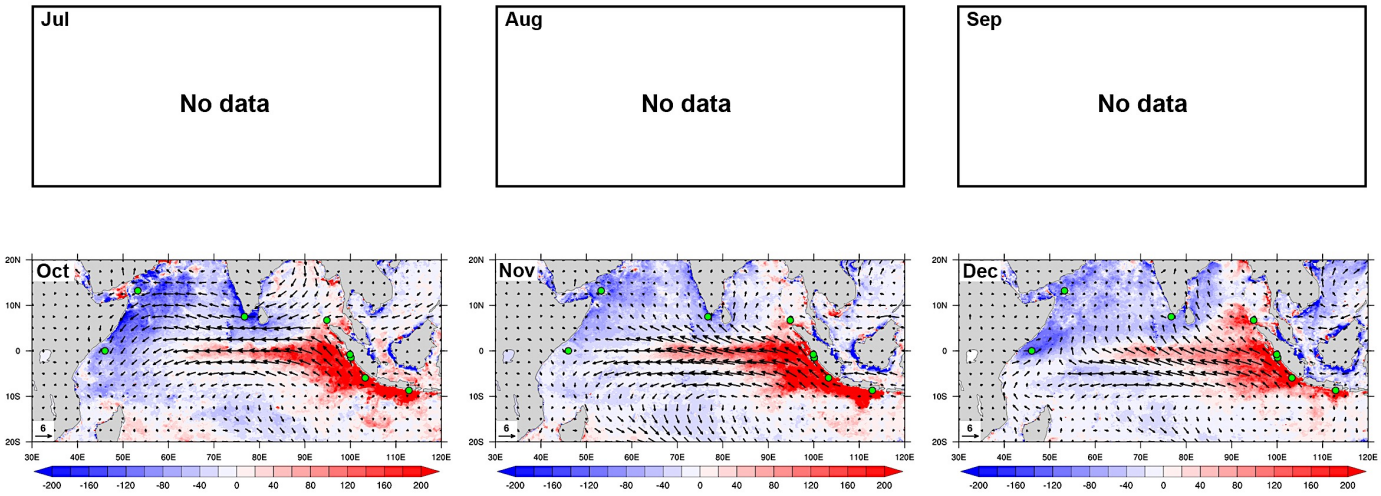

2006 Positive IOD

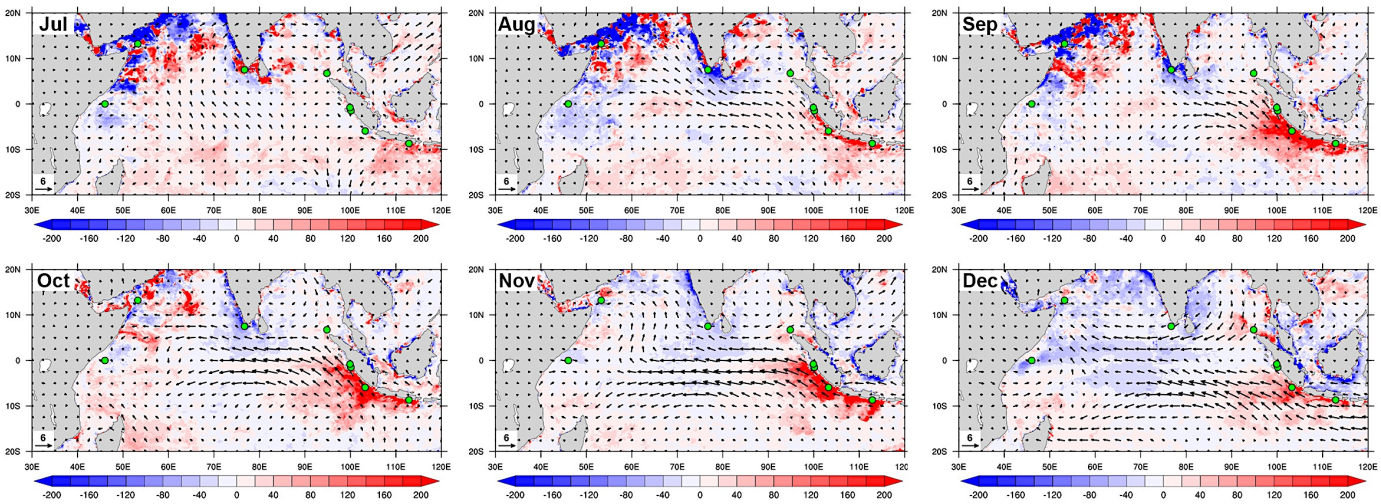

2019 Positive IOD

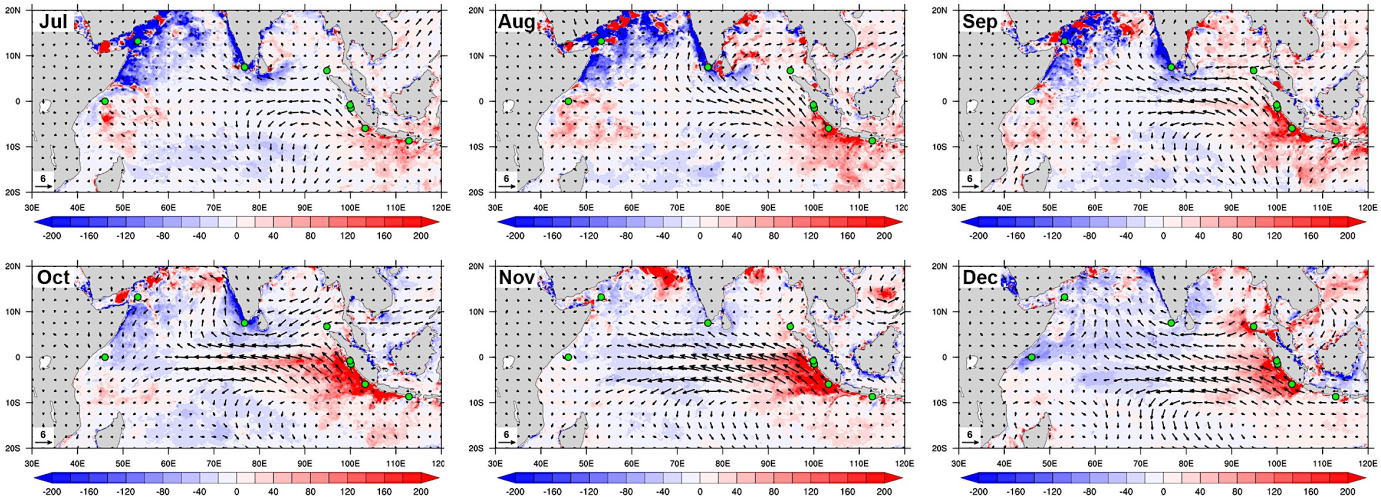

Fig. 6.S2. Monthly PP (color, gC m^{-2} yr^{-1}) and surface wind (vectors, m s^{-1}) anomalies from July to December of the positive 1997, 2006, and 2019 IOD modes. PP of 1997 is in the frame work of the SeaWiFS chlorophyll-a concentration dataset (monthly; 10/1997−12/2007), and PP of 2006, 2019 are in the frame work of the MODIS chlorophyll-a concentration dataset (monthly; 1/2003−12/2019). PP data are from the "Ocean Productivity" website (http://sites.science.oregonstate.edu/ocean.productivity), that were calculated by the Vertically Generalized Production Model (VGPM; Behrenfeld and Falkowski, 1997). Wind speed data are from the ERA5 reanalysis (https://www.ecmwf.int/en/forecasts/datasets/reanalysis-datasets/era5). Green circles mark the locations of sediment cores (see Fig. 1a).

1997 Positive IOD

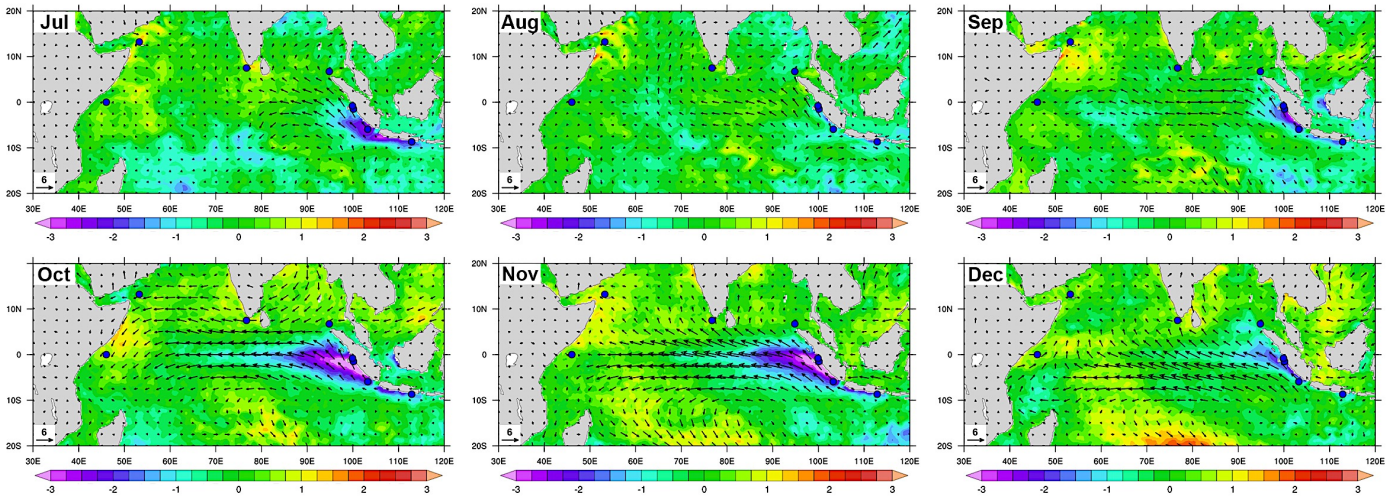

2006 Positive IOD

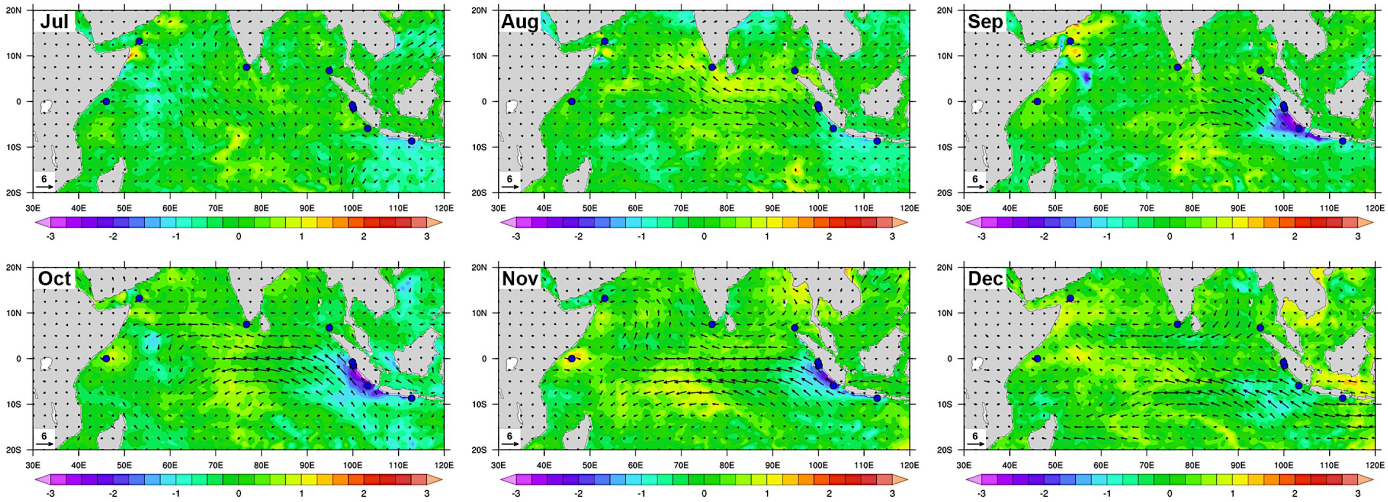

2019 Positive IOD

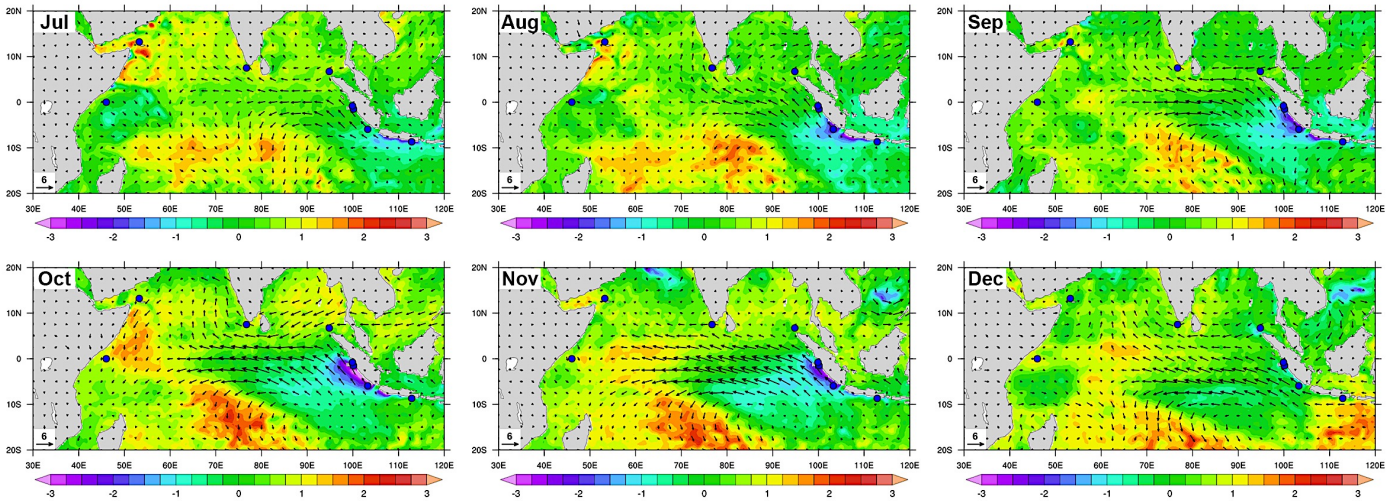

Fig. 6.S3. Monthly SST anomalies (color, ℃) and surface wind (vectors, m s^{-1}) anomalies from July to December of 1997, 2006, and 2019 positive IOD modes. SST data are from the NOAA OI SST V2 High-Resolution Dataset (https://psl.noaa.gov/data/gridded/data.noaa.oisst.v2.highres.html; monthly 01/1992−12/2019). Wind speed data are from the ERA5 reanalysis dataset (https://www.ecmwf.int/en/forecasts/datasets/reanalysis-datasets/era5; monthly 01/1992−12/2019). Blue circles mark the locations of sediment cores (see Fig. 6.1a).

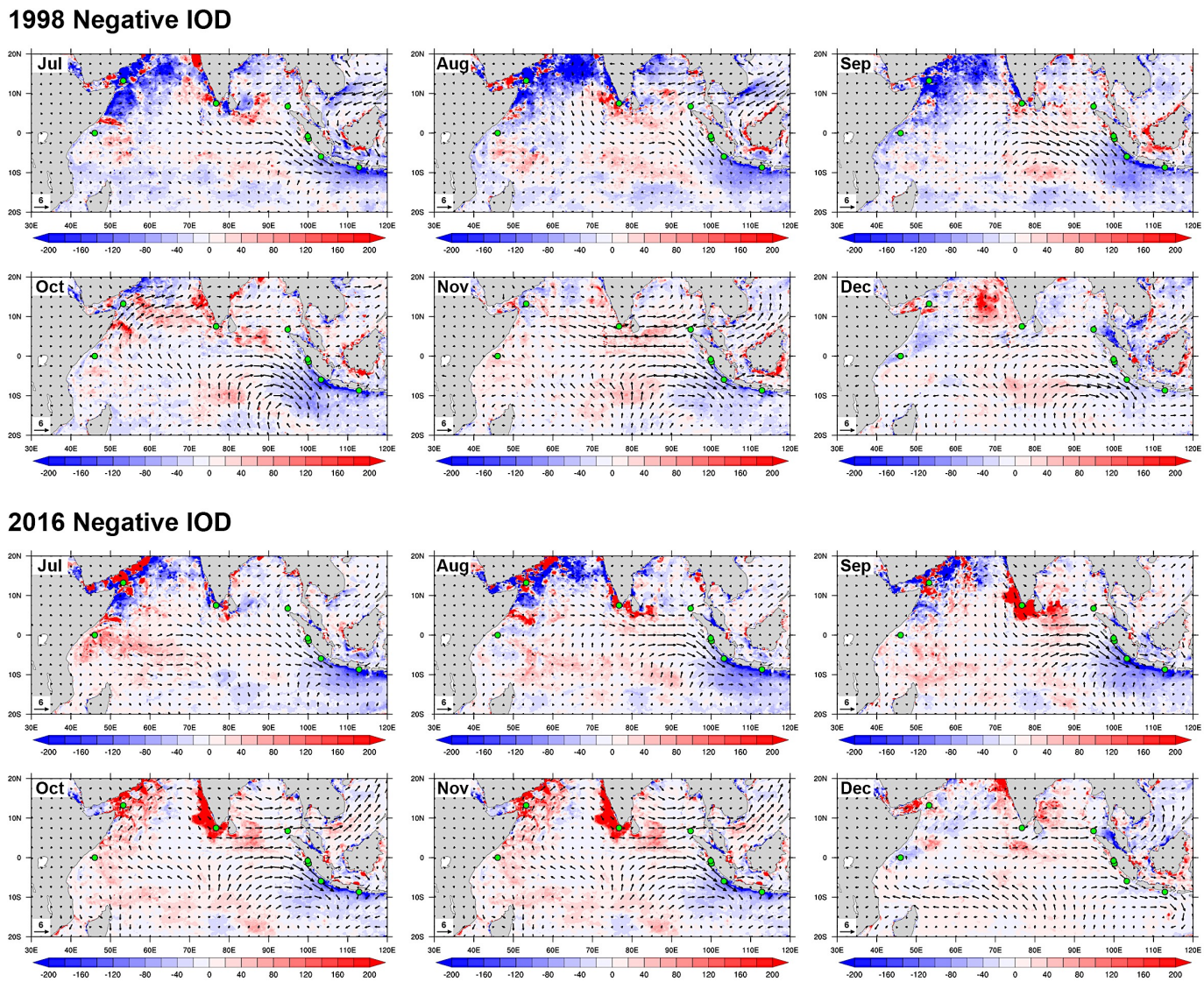

Fig. 6.S4. Monthly PP (color, gC m^{-2} yr^{-1}) and surface wind (vectors, m s^{-1}) anomalies from July to December of the negative 1998 and 2016 IOD modes. PP of 1998 is in the frame work of the SeaWiFS chlorophyll-a concentration dataset (monthly; 10/1997−12/2007), and PP of 2016 is in the frame work of the MODIS chlorophyll-a concentration dataset (monthly; 1/2003−12/2019). PP data are from the "Ocean Productivity" website (http://sites.science.oregonstate.edu/ocean.productivity), that were calculated by the Vertically Generalized Production Model (VGPM; Behrenfeld and Falkowski, 1997). Wind speed data are from the ERA5 reanalysis (https://www.ecmwf.int/en/forecasts/datasets/reanalysis-datasets/era5). Green circles mark the locations of sediment cores (see Fig. 6.1a).

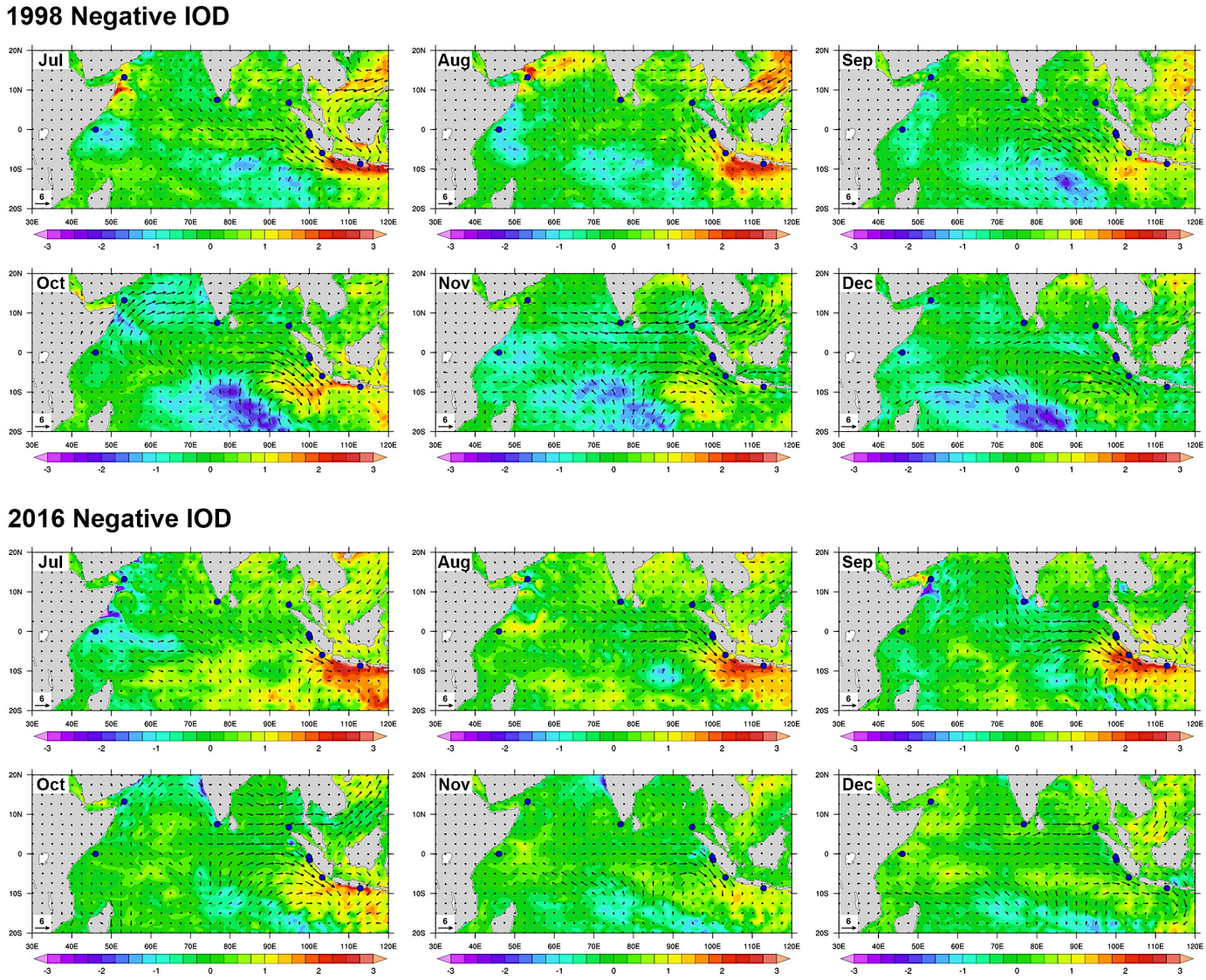

Fig. 6.S5. Monthly SST anomalies (color, ℃) and surface wind (vectors, m s^{-1}) anomalies from July to December of the 1998 and 2016 negative IOD modes. SST data are from the NOAA OI SST V2 High-Resolution Dataset (https://psl.noaa.gov/data/gridded/data.noaa.oisst.v2.highres.html; monthly 01/1992−12/2019). Wind speed data are from the ERA5 reanalysis dataset (https://www.ecmwf.int/en/forecasts/datasets/reanalysis-datasets/era5; monthly 01/1992−12/2019). Blue circles mark the locations of sediment cores (see Fig. 6.1a).

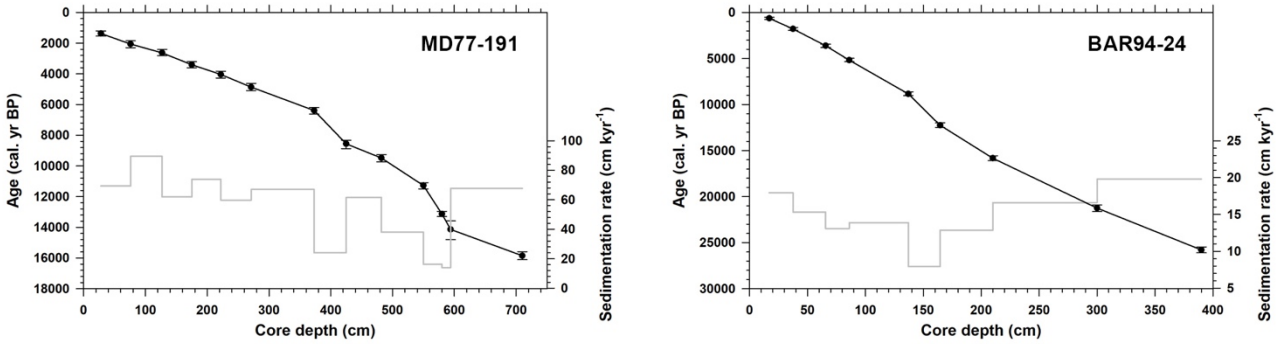

Fig. 6.S6. Age models and linear sedimentation rates of cores MD77-191 and BAR94-24. Dots are the calendar age medians. Error bars mark the calendar age 2σ.

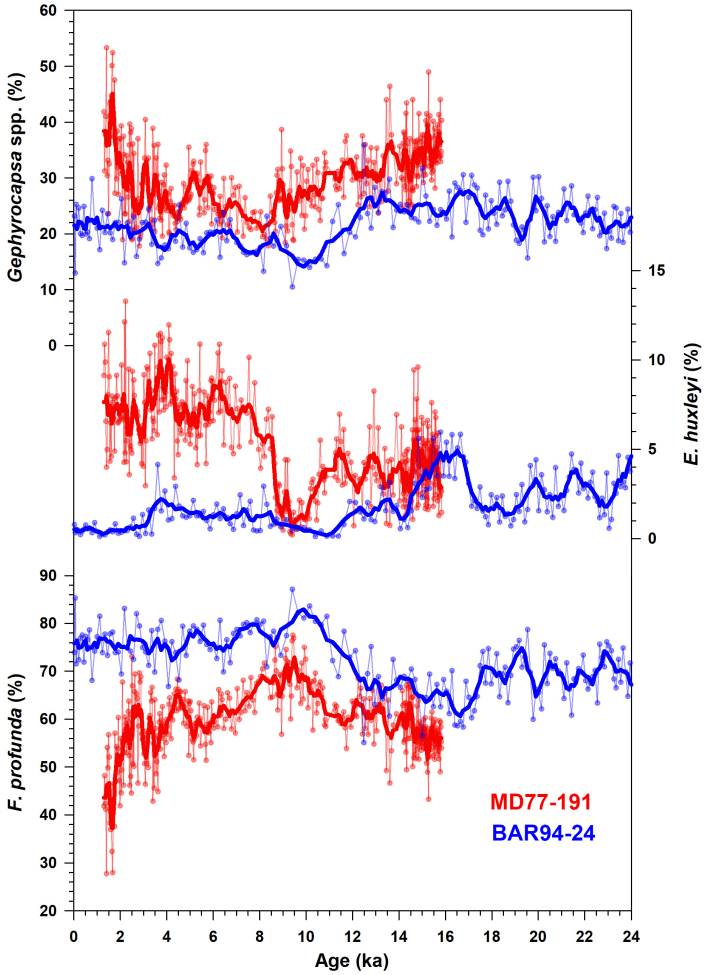

Fig. 6.S7. Relative abundances (%) of the main coccolith species in cores MD77-191 (red) and BAR94-24 (blue). The thick curves are smoothed results (7-point moving average for MD77-191 and 5-point moving average for BAR94-24).

Table 6.S1. Radiocarbon and calibrated ages of cores MD77-191 (Bassinot et al., 2011; Ma et al., 2020) and BAR94-24, determined on planktonic foraminifera and pteropods. Calendar years are the years before 1950 AD. *G. bulloides* = *Globigerina bulloides*; *G. ruber* = *Globigerinoides ruber*; *G. sacculifer* = *Globigerinoides sacculifer.*

Core MD77-191

Depth (cm)	Materials (species)	^{14}C ages (yr)	^{14}C ages error (yr)	Calendar ages median (yr)	Calendar ages lower 2σ (yr)	Calendar ages upper 2σ (yr)
28	*G. bulloides*	1970	60	1368	1197	1540
76	*G. bulloides*	2560	70	2060	1844	2294
127	*G. bulloides*	3020	60	2630	2406	2814
175	*G. bulloides*	*3660*	60	*3405*	*3206*	*3606*
222	*G. bulloides*	4160	60	4041	3825	4267
271	*G. bulloides*	4790	60	4862	4620	5092
373	*G. bulloides*	6150	80	6385	6181	6616
425	*G. bulloides*	8230	90	8554	8319	8863
482	*G. bulloides*	8970	80	9481	9254	9732
550	*G. ruber*	10300	50	11274	11092	11502
580	*G. ruber*	11810	50	13133	12962	13301
594	Pteropods sp.	12630	190	14136	13587	14805
710	*G. ruber*	13820	60	15851	15588	16115

Core BAR94-24

Depth (cm)	Materials (species)	^{14}C ages (yr)	^{14}C ages error (yr)	Calendar ages median (yr)	Calendar ages lower 2 σ (yr)	Calendar ages upper 2 σ (yr)
17	*G. ruber*	1240	35	637	517	758
37.5	*G. ruber*	2335	30	1779	1620	1932
65.5	*G. ruber*	3830	35	3607	3445	3791
86	*G. ruber*	5040	40	5174	4961	5350
137	*G. ruber*	8450	50	8843	8612	9022
164	*G. ruber*	10930	50	12246	11981	12473
210	*G. ruber*	13800	60	15825	15562	16089
300	*G. ruber*	18340	90	21245	20902	21635
390	*G. ruber* + *G. sacculifer*	22420	130	25789	25474	26105

General conclusions and perspectives

- **Conclusions**

Based on coccolith-related PP estimates from four sediment cores, and the use of outputs from 3 Earth climate models, I've reconstructed the paleoceanographic and paleoclimatic evolution over the tropical Indian Ocean and its surrounded continents since the Last Glacial Maximum (LGM). The time resolutions of the records allowed me to evaluate orbital to centennial scale variability, with a special focus on the millennial changes during the last deglaciation and particularly during the Heinrich Stadial 1 (HS1; 17−14.8 ka), the Bølling–Allerød (B-A; 14.8−13 ka), and the Younger Dryas (YD; 12.9−11.5 ka).

PP variations recorded in the northeastern Bay of Bengal indicate changes of upper seawater stratification controlled by sea surface salinity and represent the summer monsoon evolution. Those obtained in the northwestern Arabian Sea reflect both changes in temperature-driven mixing related to the winter monsoon dynamics and aeolian inputs. The two PP records that are located in the coastal upwelling cells closed to the equator document dynamics of equatorial zonal winds are related to the Walker circulation. All the major paleoclimate implications of the PP records are confirmed by modelling data.

During the LGM (23−19 ka), when ice sheets had larger extensions and greenhouse gas concentrations were lower than the present, a general cooling over Eurasia created a higher pressure cell over Siberia, that resulted in a higher land-sea thermal/pressure contrast during winter and a lower one during summer. The Indian winter monsoon was thus stronger, while the summer Indian monsoon was weaker. Under such conditions, winter winds that blew from the lands to the tropical Indian Ocean strengthened. They led to a stronger surface cooling over the northern Arabian Sea and thus, to a weaker upper seawater stratification, higher nutrient content in the euphotic zone, and thus, higher PP. The glacial conditions were also favorable for increased nutrient-rich dust supplies to the Arabian Sea. Weaker summer monsoon conditions resulted in weaker rainfall over South Asia. Indeed, due to the cooling over Eurasia, the ITCZ shifted southward, and the moisture flux over the Arabian Sea was weaker, as reflected by relatively high sea surface salinity conditions in the northernmost Bay of Bengal. PP records at the junction between the Bay of Bengal and the Andaman Sea are not particularly high. This is probably due to a relative freshness in the Andaman Sea during the LGM. The extension of ice sheets led to a 120 m decrease in the global sea level that generated the exposure of the Maritime Continent shelves. This configuration drove an anomalous divergence zone over the Indo-Pacific Warm Pool (including the southeastern Indian Ocean), and a weaker Indian Ocean Walker circulation,

as reflected by an enhanced coastal upwelling system (and higher PP) off the northwestern Sumatra, and reduced ones (and lower PP) off southern India and in the equatorial western Indian Ocean. Remarkably, the weaker Walker circulation is found to be contributed by the anomalous equatorial easterly winds during early winter.

During the last deglaciation (19−11 ka), glacial features gradually faded while the North Hemisphere summer insolation gradually reinforced. Under such conditions, the Indian winter and summer monsoons gradually weakened and strengthened, respectively. However, they were also both paced by millennial scale oscillations of the Atlantic Meridional Overturning Circulation (AMOC), related to the cold HS1 and YD periods, and the warm B-A period. During HS1 and YD, when the AMOC was weakened, the northward heat transport over the Atlantic was restricted which led to a general cooling over Eurasia throughout the year. Under this scenario, the land-sea thermal/pressure gradient was larger during winter and smaller during summer and thus, the winter and summer monsoons were stronger and weaker respectively, as documented by weaker SSS- and SST- related stratifications (and thus relatively high PP) in the northeastern Bay of Bengal and the northwestern Arabian Sea, respectively. During the B-A, when the AMOC recovered, the northward heat transport was stronger than during the HS1 and YD. As a result, the winter monsoon weakened and the summer monsoon strengthened, as revealed by stronger SSS- and SST- related stratifications (and thus lower high PP) in the two regions mentioned above, respectively. In the equatorial Indian Ocean, the anomalous easterly winds during early winter were getting weaker from the LGM, but the Indian Ocean Walker circulation did not shift to be stronger than present during the deglaciation.

During the Holocene (11–0 ka), the precession is the main forcing factor, the summer monsoon maximum being found during the Early-Mid Holocene when the precession parameter was smaller than today. The stronger Norther Hemisphere summer insolation induced by a smaller precession parameter during this period resulted in a larger land-sea thermal/pressure gradient during summer, and thus a stronger summer monsoon. The PP record from the northeastern Bay of Bengal shows a minimum corresponding to SSS minimum and salinity stratification maximum. During the Early-Mid Holocene, the Norther Hemisphere winter insolation was lower, and it can also make a larger land-sea thermal/pressure gradient during this season. As a result, the winter monsoon was stronger. This reflects in the stronger surface cooling in the northern Arabian Sea. However, the PP record of MD00-2354 shows a slight minimum during the Early-Mid Holocene as the nutrient input by aeolian dust was minimum and the subsurface cooling was probably strong that can result in a stronger stratification. Additionally, orbital parameters during the Early-Mid Holocene resulted in a stronger tropical seasonality. This change drove a weaker than present Indian Ocean Walker circulation. It is indicated

by the lower PP off the southern tip of Indian implying weaker equatorial westerly winds during summer.

- **Perspectives and future work**

a. Subsurface cooling in the Arabian Sea

In this PhD thesis, I have an unsolved question. The lower PP during the Early-Holocene with respect to the Late Holocene found in core MD00-2354 does not correspond to a weaker winter monsoon and a weaker surface cooling. The modelling results show a stronger subsurface cooling leading to a stronger stratification. This interpretation needs empirical data to support it. I propose to first reconstruct the variations of subsurface temperature in core MD00-2354 over the Holocene and to see if there is a cooling signal that is stronger than the surface during the early Holocene. If yes, it will be worth studying the mechanism of this subsurface cooling by modelling data to exploit if a precession-forced anomalous shallow overturning circulation in the western Indian Ocean drives this.

b. More Fp%-PP records to reconstruct millennial scale and long-term orbital scale variability

More paleo-PP records are needed, especially from some crucial regions of the tropical Indian Ocean, for the reconstructions of Indian monsoon and Indian Ocean Walker circulation on millennial and orbital scales. It is interesting to have longer records covering the last glacial period when the Dansgaard-Oeschger oscillations and Heinrich events occurred, and much longer records covering several glacial-interglacial cycles to see the phase with orbital parameters.

Recently, some researchers used the mass accumulation rates (MAR) of biogenic materials in the northern Bay of Bengal to indicate paleo-PP and interpreted their higher 'PP' as stronger Indian summer monsoon (e.g. Li et al., 2019; Liu et al., 2021; Lee et al., 2020). I compared the Fp%-PP record of MD77-176 with these MARs and found that the accumulation-free PP estimations are anti-correlated to the MARs (Fig. 1). This implies that the MAR-related proxies might not indicate PP in the Bay of Bengal where the terrestrial inputs by rivers are very strong. We can see that the higher PP intervals calculated from Fp% correspond to lower MARs. Therefore, the higher MAR is not associated to higher PP, but stronger terrestrial sediments and freshwater input. Fp% is an efficient and accurate proxy of PP and the upper seawater stratification, and it has high potentials in Indian summer monsoon reconstructions, which has been proved by chapter 3. However, as mentioned in chapters 3 and 5, the regions closed to the Andaman Sea (such as MD77-176) might be easily influenced by the local freshness during glacial periods. This can offset the signals of glacial-interglacial cycles that exist in the Indian summer monsoon. The northern Bay of Bengal is a more suitable region for summer

monsoon reconstructions, as it is closed to the Ganges–Brahmaputra–Meghna river system and under the direct influence of the runoff and rainfall (Clemens et al., 2016a).

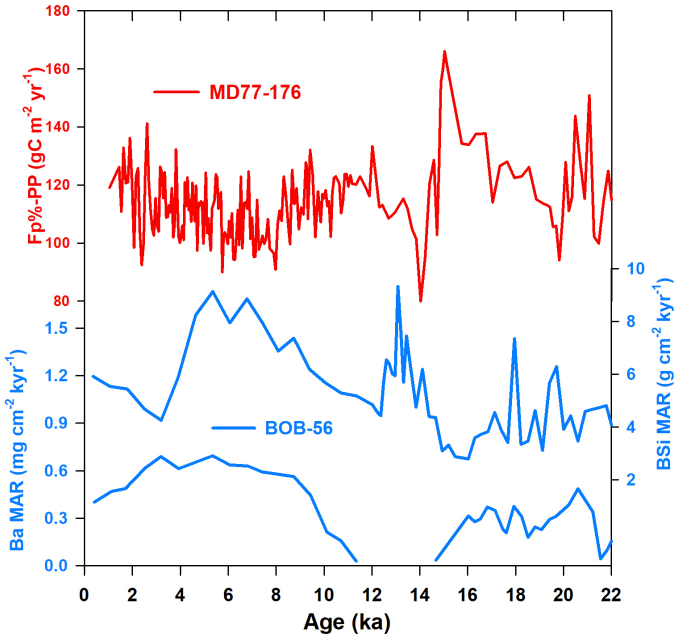

Fig. 1. Fp%-PP records of core MD77-176 (chapter 3). Mass accumulation rates of biogenic silica and barium in core BOB-56 (Li et al., 2019; Liu et al., 2021; see Fig. 2).

Here, I proposed several marine sediment cores for the summer monsoon reconstruction by the Fp%-PP method. Cores MD77-180 and MD12-3412 reach at least MIS6 with high-resolution *G. ruber* $\delta^{18}O$ data (Fig. 2; Joussain et al., 2016). The two cores provide the opportunity to study PP variability on millennial scale (Dansgaard-Oeschger oscillations and Heinrich events) during the last deglaciation and the last glacial period. However, these two cores lack the completed Holocene intervals, and we must pay attention to the turbidite depositions. Long-term records are necessary to study the orbital scale variability and its phase with the orbital parameters. The IODP sites U1445 and U1446 are located on the northwestern Bay of Bengal (Fig. 2), a region suggested as the best location for paleo-salinity and summer monsoon reconstructions (Clemens et al., 2016a). The recovery of the Pleistocene cores of these two sites is nearly 100 % with abundant calcareous particles including foraminifera and coccoliths (calcareous nannofossil). Calcareous nannofossil datum T (=top) *Pseudoemiliania lacunosa* (0.44 Ma) was found at 74.34 CSF-A (m) for U1445 and at 81.39 CSF-A (m) for U1446 (Clemens et al., 2016d; Clemens et al., 2016c). Therefore, it is possible to construct orbital scale age models covering the last 400 kyr by using foraminifera $\delta^{18}O$ for these two sites. The orbital scale Fp%-PP is expected to indicate the freshwater input and SSS-related stratification, and thus, the evolution of Indian summer monsoon. The Fp%-PP data will be compared to those published records interpreted

as Indian summer monsoon variability on orbital scale (Clemens et al., 2003; Caley et al., 2011; Bolton et al., 2013; Gebregiorgis et al., 2018). The glacial-interglacial cycles, and the phase in precession band will be the concentrations.

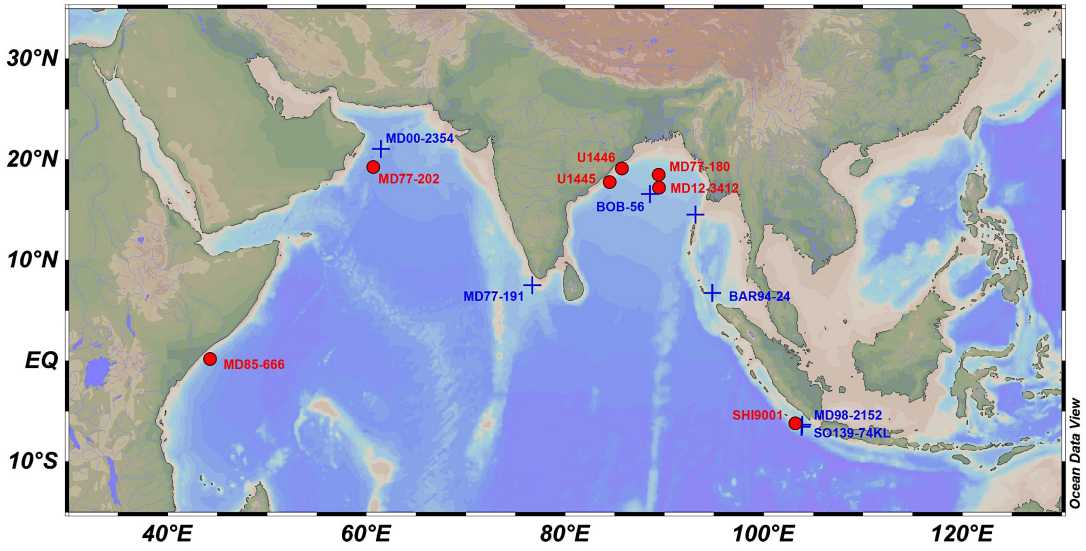

Fig. 2. Core locations. The red dots mark the proposed cores for future studies. The blue crosses mark the cores with published data.

Core MD77-202 from the western Arabian Sea is another candidate for paleo-PP study. High-resolution *G. ruber* $\delta^{18}O$ data of this core reaches MIS7. The Fp%-PP data will be compared to the widely cited TOC% and Ba/Al records from the northeastern and western Arabian Sea (Schulz et al., 1998; Ivanochko et al., 2005), which were interpreted as Indian summer monsoon evolution. However, I expect the Fp%-PP record, similar to the one of MD00-2354, to show a winter monsoon pattern.

Moreover, I suggest getting new Fp%-PP records from the tropical southeastern Indian Ocean and the equatorial western Indian Ocean, which are linked to the upper seawater stratification and are important to evaluate the Walker circulation variability. Some existed cores make this study possible. Core SHI9001 located off southwestern Sumatra and core MD85-666 located off equatorial East Africa coast both reach MIS7. Low-resolution Fp% data of SHI9001 shows significant glacial-interglacial cycles (Fig. 3). This pattern is in agreement with the evolutions of subsurface temperature and Sumatra vegetation reconstructed from the nearby core MD98-2152 (Fig. 3). The latter two are tied to the variations of Indian Ocean Walker circulation (Windler et al., 2019). However, this '100-kyr period' pattern is less obvious in the Fp% record of nearby core SO139-74KL (Fig. 3; Andruleit et al., 2008). The biases between the two Fp% records are probably due to different methods of slide preparation and coccolith counting. Next, I will improve the resolution of Fp% data of SHI9001. The record from the eastern Indian Ocean is necessary to be compared to the western core MD85-666 to have a

complete understanding of PP and seawater structure variations in the equatorial Indian Ocean. In chapter 4, I found that the Indian Ocean Walker circulation is sensitive to the orbital forcing over the Holocene. Therefore, the high-resolution Fp% records are important to evaluate if the '23-kyr period' signals exist in the long-term evolution of Indian Ocean Walker circulation.

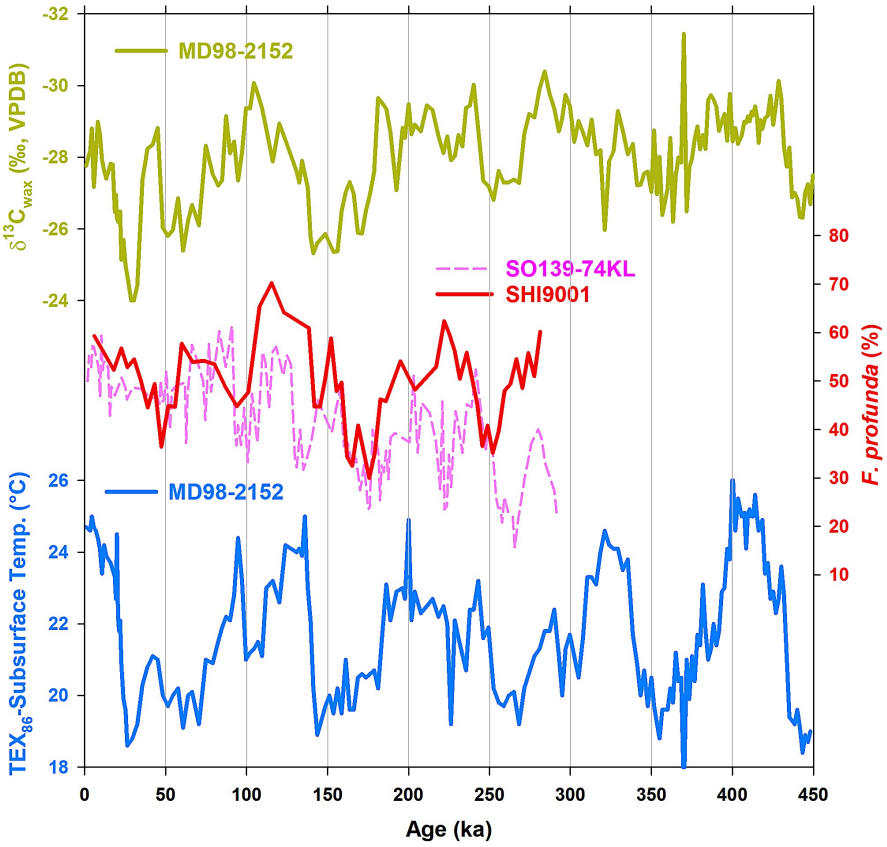

Fig. 3. Fp% records of cores SHI9001 (Zhou X., unpublished) and SO139-74KL (Andruleit et al., 2008). Subsurface temperature estimations by using the TEX86 method, and $\delta^{13}C$ measurements on sedimentary plant wax in core MD98-2152 (Windler et al., 2019).

c. Further studies on coccoliths in cores MD77-176 and MD00-2354

Geochemical and biogeochemical measurements on coccoliths are worth trying in the future. For example, the coccolith strontium/calcium ratio is a proxy of the coccolithophore growth rate (Stoll and Schrag et al., 2000; Saavedra-Pellitero et al., 2017), and the "vital effect" of coccolith carbon isotope (isotopic disequilibrium with dissolved inorganic carbon) is linked to both the growth (photosynthesis) rate and the aqueous CO_2 concentration ($[CO_2(aq)]$) (Hermoso et al., 2016; McClelland et al., 2017; Jin et al., 2018). The paleoenvironmental application of this "vital effect" is poorly studied, although researchers have proposed intracellular isotopic fraction models (e.g. McClelland et al., 2017). The tropical Indian Ocean is an ideal experimental field for exploring the indications of this "vital effect",

as the hydroclimatic and ecologic changes in this region are very dynamic since the LGM as revealed by previous studies and chapters of this thesis. If we can find the reconstruction methods of the [CO_2(aq)] and growth (photosynthesis) rate by using the carbon isotope "vital effect", it will be meaningful for the global carbon cycle study for geological periods. In the future, I plan to get the carbon isotopic "vital effect" signals of *Gephyrocapsa* over the last 25 kyr in cores MD00-2354 and MD77-176 and pay attention to the response to the nutrient availability controlled by monsoon dynamics, and the CO_2 raising. A procedure is the refinement of *Gephyrocapsa*. It needs to be pointed out that the coccolith isotopic compositions are tied to coccolith morphometric, which is likely modulated by the cellular growth rate. The *Gephyrocapsa* size in the two cores shows largely different evolutions, especially during the LGM (Fig. 4). This is an interesting finding with paleoclimate implications. More accurate measurements on coccoliths sizes will be done for the next steps. As we know that the aeolian flux over the Arabian Sea is much higher than the Bay of Bengal, and the LGM is a period favourable for dust supply. The large difference found in *Gephyrocapsa* sizes during this period might reflect an iron richness that can highly increase the coccolithophore growth rates and cell volumes.

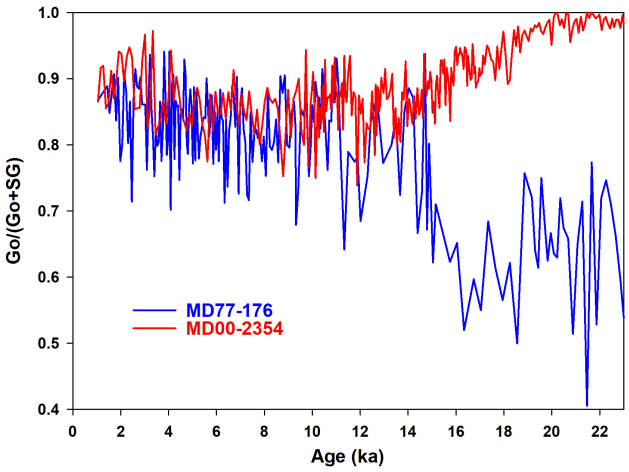

Fig. 4. Ratios between *Gephyrocapsa oceanic* (> 3 µm; Go) and small *Gephyrocapsa* (< 3 µm; SG) in cores MD77-176 and MD00-2354 over the last 23 kyr.

d. Perfectives on the AWI-ESM model for moisture budget analysis

As pointed out by previous studies, general coupled models have biases in simulating rainfall over the lands surrounding the tropical Indian Ocean. This is highlighted by the changes of Indian Ocean Walker circulation under LGM conditions (DiNezio and Tierney, 2013; Mohtadi et al., 2017; DiNezio et al., 2018). As mentioned in chapter 6, the AWI-ESM can simulate a weaker Walker circulation under LGM and Mid-Holocene conditions that are in agreement with the two Fp%-PP records linked to

equatorial atmospheric circulations. Here, I compare rainfall changes under LGM conditions simulated by AWI-ESM and MPI-ESM models in the framework of PMIP4. The two coupled models have the same atmospheric and land components, but their oceanic models are different. We can see that the zonal anomalies of rainfall over the Indian Ocean are more significant in AWI-ESM than in MPI-ESM (Fig. 5). In the southeastern Indian Ocean, AWI-ESM simulates decreased rainfall associated with strong surface cooling and anomalous southeasterly winds which are not obvious in MPI-ESM. These results of AWI-ESM are similar to the CESM model (DiNezio et al., 2016; DiNezio et al., 2018). The seasonality of the rainfall anomalies also indicates that the AWI-ESM can simulate a strengthened positive Bjerknes feedback in the southeastern Indian Ocean under LGM conditions (DiNezio et al., 2016). As the main difference between AWI-ESM and MPI-ESM is their oceanic models, it is reasonable to emphasize the advantage of FESOM model using unstructured mesh in simulating the equatorial processes that are important for the ocean-atmosphere feedbacks.

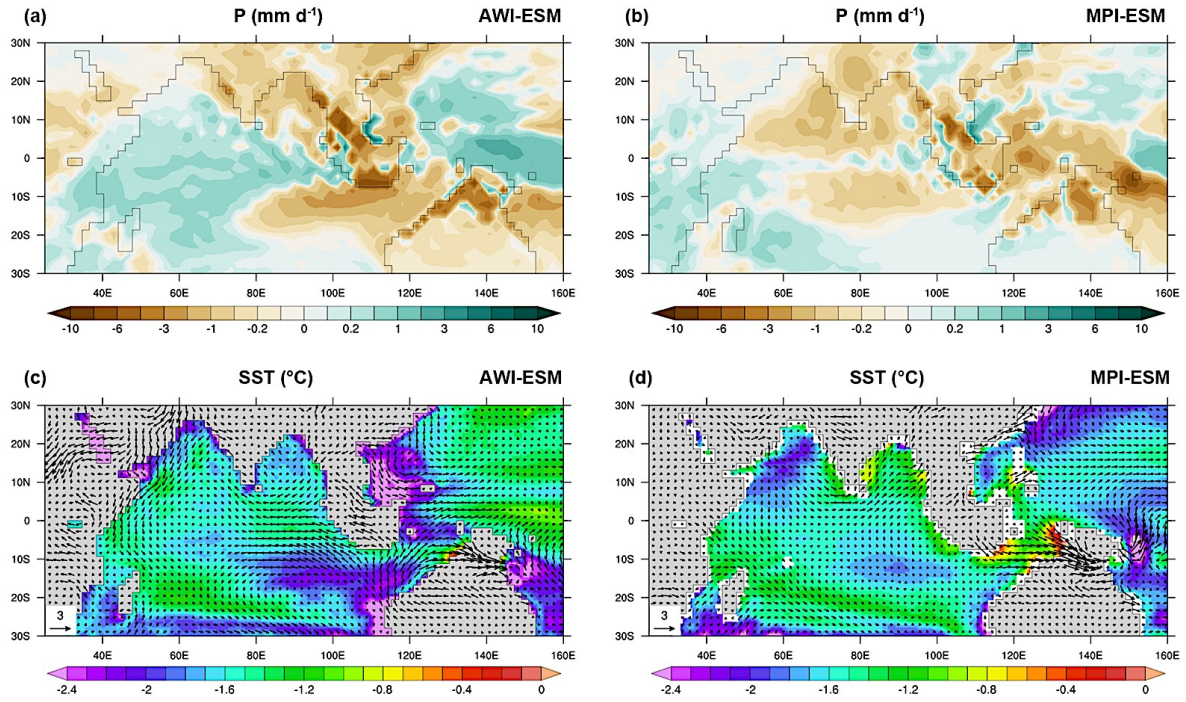

Fig. 5. Differences of annual mean precipitation rate (P, mm day^{-1}) between LGM and CTRL experiments of (a) AWI-ESM and (b) MPI-ESM. Differences of annual mean sea surface temperature (SST, colour, °C) and surface wind (vectors, m s^{-1}) between LGM and CTRL experiments of (e) AWI-ESM and (f) MPI-ESM. The data are from Earth System Grid Federation (https://esgf.llnl.gov/nodes.html).

By analysing the moisture budget, we can find that the zonal anomalies of rainfall over the Indian Ocean in AWI-ESM are mainly driven by an anomalous zonal atmospheric circulation accounting for dynamic moisture transport, rather than thermodynamic component linked to humidity (Fig. 6). The decomposition of moisture budget in thermodynamic and dynamic contributions flows this equation

(D'Agostino et al., 2019; D'Agostino and Lionello, 2020):

$$\delta(P-E) = -\frac{1}{\rho_w g}\int_0^{P_s} \nabla\cdot\left(\delta q \vec{\mathrm{V}}_{\mathrm{PI}}\right)\mathrm{dp} - \frac{1}{\rho_w g}\int_0^{P_s} \nabla\cdot\left(q_{\mathrm{PI}}\delta\vec{\mathrm{V}}\right)\mathrm{dp} + \delta R\,.$$

and

$$\delta TH = -\frac{1}{\rho_w g}\int_0^{P_s} \nabla\cdot\left(\delta q \vec{\mathrm{V}}_{\mathrm{PI}}\right)\mathrm{dp} = -\frac{1}{\rho_w g}\int_0^{P_s} \left(\vec{\mathrm{V}}_{\mathrm{PI}}\cdot\nabla\delta q + \delta q\cdot\nabla\vec{\mathrm{V}}_{\mathrm{PI}}\right)\mathrm{dp}\,.$$

$$\delta DY = -\frac{1}{\rho_w g}\int_0^{P_s} \nabla\cdot\left(q_{\mathrm{PI}}\delta\vec{\mathrm{V}}\right)\mathrm{dp} = -\frac{1}{\rho_w g}\int_0^{P_s} \left(\delta\vec{\mathrm{V}}\cdot\nabla q_{\mathrm{PI}} + q_{\mathrm{PI}}\cdot\nabla\delta\vec{\mathrm{V}}\right)\mathrm{dp}\,.$$

where P is precipitation rate, E is evaporation rate, q is specific humidity, $\vec{\mathrm{V}}$ is the horizontal vector wind, ρ_w is the water density. δ represents the difference between the LGM and pre-industrial controlling (PI) experiments. $\delta(P-E)$ is the changes in net precipitation rate (mm day^{-1}), i.e. the moisture conserved on the surface. δTH represents changes in moisture flux convergence arising from changes in moisture, and δDY involves changes in winds with unchanged moisture and is related to changes in the mean atmospheric flow. δR is the residual change that accounts for contributions by transient eddies and surface quantities. The changes in zonal difference (between southeastern and western Indian Ocean) of these moisture components are shown in Fig. 6 and are compared to the results of other models in the framework of PMIP2 and PMIP3.

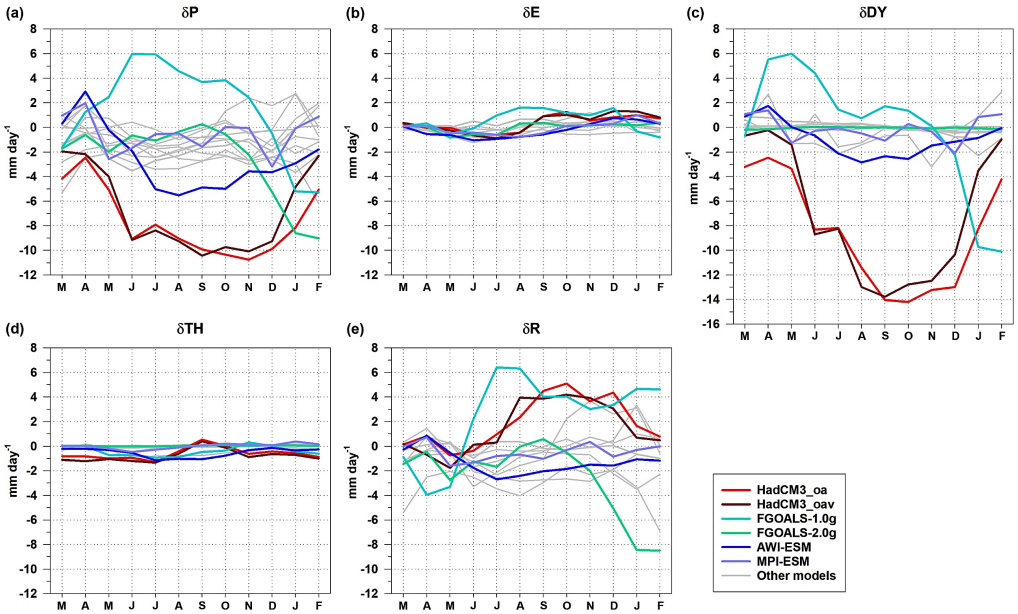

Fig. 6. Results of AWI-ESM and MPI-ESM models compared to the models in the framework of PMIP2 (Braconnot et al., 2007a) and PMIP3 (Braconnot et al., 2012) in simulating the zonal anomalies (differences between southeastern and western Indian Ocean) of moisture budget components under LGM conditions (LGM minus pre-industrial).

The Walker circulation is a process that cannot be ignored in controlling hydroclimate over the lands surrounding the tropical Indian Ocean, including South and Southeast Asia, Maritime Continent, North Australia, and East Africa. A model that can well simulate this process is necessary for the studies on the mechanisms of hydroclimatic changes including the rainfall amount and the seasonal cycles, and by the proxy-model comparison.

Appendix

Table A1. List of the terrestrial moisture proxy records indicating South Asian rainfall. See Fig. 1.13. in Chapter 1.

#	Core/Site	Lon.	Lat.	Proxy	Reference
1	Bittoo Cave	77.78	30.79	Speleothem $\delta^{18}O$	Kathayat et al. (2016)
2	Sahiya Cave	77.87	30.6	Speleothem $\delta^{18}O$	Kathayat et al. (2017)
3	Mawmluh Cave	91.88	25.26	Speleothem $\delta^{18}O$	Berkelhammer et al. (2012); Dutt et al. (2015)
4	Sanai Lake	80	27	Pollen	Sharma et al. (2004)
5	Tso Moriri	78.32	32.9	Pollen	Leipe et al. (2014)
6	Tengchongqinghai Lake	98.57	23.13	Pollen	Zhang et al. (2020)
7	Nong Pa Kho	102.9	17.1	Pollen	Penny, 2001
8	MD77-194	75.23	10.5	Pollen	van Campo, 1986
9	MD76-131	72.5	15.5	Pollen	van Campo, 1986
10	Nam Co	90.78	30.73	Pollen; TOC%	Kasper et al. (2015); Zhu et al. (2015)
11	Lonar Lake	76.51	19.98	Pollen; Mineralogy; $\delta^{13}C_{org}$	Prasad S. et al. (2014); Menzel et al. (2014); Sarkar et al. (2015)
12	Wadhwana Lake	73.48	22.18	Pollen; Algae	Prasad V. et al. (2014)
13	Sambhar playa	75.09	26.95	Major elements; $\delta^{18}O_{carb}$; $\delta^{13}C_{org}$	Sinha et al. (2006)
14	Kotla Dahar	76.95	28	Gastropod aragonite $\delta^{18}O$	Dixit et al. (2014a)
15	Nilgiri Hills	76.75	11.25	Peat $\delta^{13}C$	Sukumar et al. (1993); Rajagopalan et al. (1997)
16	Nonia Tal	79.4	22.9	Bulk $\delta^{13}C$; Magnetic parameters	Kumar et al. (2019)
17	Shantisagara Lake	75.88	14.14	Magnetic parameters	Sandeep et al. (2017)
18	Tangra Yumco	86.75	31.25	Major elements; TOC%	Ahlborn et al. (2016)
19	SO188-342KL	90.03	19.97	δD_{wax}	Contreras-Rosales et al. (2014)

Table A2. List of the summer upwelling record indicating the summer wind intensity. See Fig. 1.13. in Chapter 1.

#	Core	Lon.	Lat.	Proxy	Reference
1	ODP723A	57.61	18.05	*G. bulloides* %	Naidu and Malmgren (1996); Bassinot et al. (2011)
2	SO42-74KL	57.35	14.32	*G. bulloides* %	Schulz et al. (2002)
3	905	51.56	10.46	*G. bulloides* %	Jung et al. (2002)
4	SK237	75	10.98	*G. bulloides* %	Naik et al. (2017)
5	MD77-191	76.72	7.5	*G. bulloides* %	Bassinot et al. (2011)

Table A3. List of the ocean SSS record indicating South Asian rainfall. See Fig. 1.13. in Chapter 1.

#	Core	Lon.	Lat.	Proxy	Reference
1	SO90-126KL	90.03	19.97	$\delta^{18}O_{seawater}$	Kudrass et al. (2001); Sijinkumar et al. (2016)
2	MD77-180	89.42	18.47	$\delta^{18}O_{seawater}$	Colin et al. (1998); Sijinkumar et al. (2016)
3	MD77-176	93.12	14.5	$\delta^{18}O_{seawater}$	Marzin et al. (2013); Sijinkumar et al. (2016)
4	RC12-344	96.04	12.46	$\delta^{18}O_{seawater}$	Rashid et al. (2007); Sijinkumar et al. (2016)
5	SK168	94.3	11.42	$\delta^{18}O_{seawater}$	Sijinkumar et al. (2010, 2016)
6	AAS 11	94.28	9	$\delta^{18}O_{seawater}$	Ahmad et al. (2000); Sijinkumar et al. (2016)
7	RVS 2	93.58	7.43	$\delta^{18}O_{seawater}$	Sijinkumar et al. (2016)
8	SK157-16	90.83	7.8	$\delta^{18}O_{seawater}$	Raza et al. (2014); Sijinkumar et al. (2016)
9	SK157-15	90.3	8.77	$\delta^{18}O_{seawater}$	Raza et al. (2014); Sijinkumar et al. (2016)
	SK157-14	90.08	5.18	$\delta^{18}O_{seawater}$	Ahmad et al. (2008); Sijinkumar et al. (2016)
10	ODP758	90.39	5.38	$\delta^{18}O_{seawater}$	Bolton et al. (2013); Sijinkumar et al. (2016)
11	SK218-1	82	14.03	$\delta^{18}O_{seawater}$	Govil and Naidu (2011)
12	SK168/GC-1	94.49	11.71	Ba/Ca_{foram}	Gebregiorgis et al. (2016)
13	SK117/GC08	71.02	15.49	$\delta^{18}O_{seawater}$	Mahesh and Banakar (2014)
14	SK129/CR04	75.98	6.49	$\delta^{18}O_{seawater}$	Mahesh and Banakar (2014)
15	SK17	72.97	15.25	$\delta^{18}O_{seawater}$	Anand et al. (2008)
16	MD900963	73.88	5.06	$\delta^{18}O_{seawater}$	Rostek et al. (1993)
17	905	51.56	10.46	$\delta^{18}O_{seawater}$	Anand et al. (2008)

Table A4. List of the paleoclimate records with winter monsoon interpretations. See Fig. 1.14. in Chapter 1.

#	Core/Site	Lon.	Lat.	Proxy	Reference
1	SK-20-185	71.83	10	$\delta^{18}O_{foram}$	Sarkar et al. (1990)
2	SK117/GC08	71.02	15.49	$\delta^{18}O_{seawater}$	Mahesh and Banakar (2014)
3	SK129/CR04	75.98	6.49	$\delta^{18}O_{seawater}$	Mahesh and Banakar (2014)
4	SO42-74KL	57.35	14.32	Foraminifera	Schulz et al. (2002)
5	GOA6	53.77	14.98	Foraminifera	Ishikawa and Oda (2007)
6	SS-4018G	53.26	13.36	Foraminifera	Singh et al. (2016)
7	93KL	64.22	23.58	$U_{37}^{K'}$-SST	Böll et al. (2015)
8	SK17	72.97	15.25	*F. profunda* %	Cabarcos et al. (2014)

Table A5. List of the hydroclimate records within 15°S−15°N related to Indian OceanWalker circulation changes See Fig. 1.16. in Chapter 1.

#	Core	Lon.	Lat.	Proxy	Reference
1	Lake Walawi	34.19	-10.01	δD_{wax}	Konecke et al. (2011)
2	Lake Tanganyika	29.83	-6.7	δD_{wax}	Tierney et al. (2008)
3	Lake Challa	37.7	-3.32	δD_{wax}	Tierney (2011)
4	SO189-144KL	98.07	1.16	δD_{wax}	Niedermeyer et al. (2014)
5	P178-15P	44.3	11.96	δD_{wax}	Tierney et al. (2013)
6	BJ8-03-70GGC	119.28	-3.57	δD_{wax}	Tierney et al. (2012)
7	Lake Towuti	121.5	-2.7	δD_{wax}, $\delta^{13}C_{wax}$	Russell et al. (2014); Konecky et al. (2016)
8	SO18515	119.36	-3.63	δD_{wax}, $\delta^{13}C_{wax}$	Wicaksono et al. (2017)
9	MD09-2152	103.88	-6.33	$\delta^{13}C_{wax}$	Windler et al. (2019)
10	Lake Sacred	37.53	0.05	$\delta^{13}C_{org}$	Olago et al. (1999)
11	Batu Cave	101.7	3.22	$\delta^{13}C_{org}$	Wurster et al. (2010)
12	Gangub Cave	117.55	8.52	$\delta^{13}C_{org}$	Wurster et al. (2010)
13	Makangit Cave	119.45	10.47	$\delta^{13}C_{org}$	Wurster et al. (2010)
14	GeoB10069-3	120.92	-9.59	$\delta^{13}C_{org}$	Dubois et al. (2014)

15	BJ8-03-91GGC	118.39	-2.87	$\delta^{13}C_{org}$	Dubois et al. (2014)
16	Gunang Buda	114	4	Speleothem $\delta^{18}O$	Partin et al. (2007)
17	Liang Luar Cave	120.43	-8.53	Speleothem $\delta^{18}O$	Ayliffe et al. (2013)
18	Tangga Cave	100.75	-0.35	Speleothem $\delta^{18}O$	Wurtzel et al. (2018)
19	Klang Cave	98.73	8.33	Speleothem $\delta^{18}O$	Chawchat et al. (2021)
20	Mount Kenya	37.35	-0.15	Diatom $\delta^{18}O$	Barker et al. (2001)
21	Lake Cheshi	29.75	-9.08	Diatom	Stager (1988)
22	Lake Abhe	41.6	11.1	Lake level	Gasse and Street (1978)
23	Lake Suguta	36.5	2	Lake level	Garcin et al. (2009)
24	Lake Turkana	35.5	2.6	Lake level	Garcin et al. (2012)
25	Lake Chew Bahir	36.78	4.84	K-XRF	Foerster et al. (2012)
26	Lake Tana	37.25	12	Ti-XRF	Marshall et al. (2011)
27	Lake Victoria	33	-1	Magnetic susceptibility	Johnson et al. (1996)
28	Lake Masoko	33.76	-9.33	Pollen, magnetic susceptibility	Garcin et al. (2006)
29	G6-4	118.07	-10.78	Pollen	Wang et al. (1999)
30	Eastern Arc Mountains	35.92	-7.82	Pollen	Mumbi et al. (2008)
31	Bandung Basin	107.8	-7.2	Pollen	van der Kaars and Dam (1995)
32	BAR94-42	107.8	-7.2	Pollen	van der Kaars et al. (2010)
33	SHI9014	126.97	-5.77	Pollen	van der Kaars et al. (2000)
34	Haeapugua Basin	143	-5.5	Pollen	Haberle (1998)
35	Burundi highlights	29.5	-3.5	Pollen	Bonnefille and Chalie (2000)
36	Danau di Atas	100.77	-1.07	Pollen	Stuijts et al. (1988)
37	Mahakam Delta	117.5	-0.75	Pollen	Caratini and Tissot (1988)
38	Lake Sentarum	112.1	0.85	Pollen	Anshari et al. (2001)
39	Pea Bullok	99.03	2.25	Pollen	Maloney and McCormac (1995)
40	SO17964	112.21	6.16	Pollen	Sun et al. (2000)
41	MD06-3075	125.83	6.48	Pollen	Bian et al. (2011)

References

Abe-Ouchi, A., Saito, F., Kageyama, M., Braconnot, P., Harrison, S. P., Lambeck, K., Otto-Bliesner, B. L., Peltier, W. R., Tarasov, L., Peterschmitt, J.-Y., Takahashi, K., 2015. Ice-sheet configuration in the CMIP5/PMIP3 Last Glacial Maximum experiments. Geoscientific Model Development 8, 3621–3637.

Abram, N. J., Gagan, M. K., McCulloch, M. T., Chappell, J., Hantoro, W. S., 2003. Coral Reef death during the 1997 Indian Ocean Dipole linked to Indonesian wildfires. Science 301, 952−955.

Ackerman, S. A., Cox, S. K., 1989. Surface weather observations of atmospheric dust over the southwest summer monsoon region. Meteorology and Atmospheric Physics 41, 19–34.

Ahlborn, M., Haberzettl, T., Wang, J., Fürstenberg, S., Mäusbacher, R., Mazzocco, J., Pierson, J., Zhu, L., Frenzel, P., 2016. Holocene lake level history of the Tangra Yumco lake system, southern-central Tibetan Plateau. The Holocene 26, 176−187.

Ahmad, S. M., Babu, G. A., Padmakumari, V. M., Raza, W., 2008. Surface and deep water changes in the northeast Indian Ocean during the last 60 ka inferred from carbon and oxygen isotopes of planktonic and benthic foraminifera. Palaeogeography, Palaeoclimatology, Palaeoecology 262, 182−188.

Ahmad, S. M., Patil, D. J., Rao, P. S., Nath, B. N., Rao, B. R., Rajagopalan, G., 2000. Glacial-interglacial changes in the surface water characteristics of the Andaman Sea: Evidence from stable isotopic ratios of planktonic foraminifera. Journal of Earth System Science 109, 153−156.

Ajayamohan, R. S., Rao, S. A., Yamagata, T., 2008. Influence of Indian Ocean dipole on poleward propagation of boreal summer intraseasonal oscillations. Journal of Climate 21, 5437−5454.

An, Z., Wu, G., Li, J., Sun, Y., Liu, Y., Zhou, W., Cai, Y., Duan, A., Li, L., Mao, J., Cheng, H., Shi, Z., Tan, L, Yan, H., Ao, H., Chang, H., Feng, J., 2015. Global monsoon dynamics and climate change. Annual Review of Earth and Planetary Sciences 43, 29–77.

Anand, P., Kroon, D., Singh, A. D., Ganeshram, R. S., Ganssen, G., Elderfield, H., 2008. Coupled sea surface temperature–seawater δ18O reconstructions in the Arabian Sea at the millennial scale for the last 35 ka. Paleoceanography 23, PA4207.

Andruleit, H., Lückge, A., Wiedicke, M., Stäger, S., 2008. Late Quaternary development of the Java upwelling system (eastern Indian Ocean) as revealed by coccolithophores. Marine Micropaleontology 69, 3–15.

Aneesh, S., Sijikumar, S., 2018. Changes in the La Niña teleconnection to the Indian summer monsoon during recent period. Journal of Atmospheric and Solar-Terrestrial Physics 167, 74–79.

Ashok, K., Guan, Z., Yamagata, T., 2001. Impacts of the Indian Ocean Dipole on the relationship between the Indian Monsoon rainfall and ENSO. Geophysical Research Letter 28, 4499−4502.

Ashok, K., Guan, Z., Saji, N. H., Yamagata T., 2004. Individual and combined influences of ENSO and the Indian Ocean Dipole on the Indian Summer Monsoon. Journal of Climate 17, 3141−3155.

Aumont, O., Bopp, L., 2006. Globalizing results from ocean in situ iron fertilization studies. Global Biogeochemical Cycles 20, GB2017.

Ayliffe, L. K., Gagan, M. K., Zhao, J. X., Drysdale, R. N., Hellstrom, J. C., Hantoro, W. S., Griffiths, M. L., Scott-Gagan, H., Pierre, E., Cowley, J. A., Suwargadi, B. W., 2013. Rapid interhemispheric climate links via the Australasian monsoon during the last deglaciation. Nature communications 4, 1−6.

Babu, C. P., Brumsack, H.-J., Schnetger, B., Böttcher, M. E., 2002. Barium as a productivity proxy in continental margin sediments: a study from the eastern Arabian Sea. Marine Geology 184, 189−206.

Balaji, D., Bhushan, R., Chamyal, L. S., 2018. Variations of the Somali upwelling since 18.5 ka BP and its relationship with southwest monsoon rainfall. Climate of the Past 14, 1331−1343.

Balch, W. M., 2004. Re-evaluation of the physiological ecology of coccolithophores, in: Thierstein, H. R., Young, J. R. (Eds.), Coccolithophores: From Molecular Processes to Global Impact. Springer-Verlag Berlin Heidelberg, pp. 99−126.

Banakar, V. K., Oba, T., Chodankar, A. R., Kuramoto, T., Yamamoto, M., Minagawa, M., 2005. Monsoon related changes in sea surface productivity and water column denitrification in the Eastern Arabian Sea during the last glacial cycle. Marine Geology 219, 99−108.

Barker, P. A., Street-Perrott, F. A., Leng, M. J., Greenwood, P. B., Swain, D. L., Perrott, R. A., Telford, R. J., Ficken, K. J., 2001. A 14,000-year oxygen isotope record from diatom silica in two alpine lakes on Mt. Kenya. Science 292, 2307–2310.

Bassinot, F. C., Marzin, C., Braconnot, P., Marti, O., Mathien-Blard, E., Lombard, F., Bopp, L., 2011. Holocene evolution of summer winds and marine productivity in the tropical Indian Ocean in response to insolation forcing: data-model comparison. Climate of the Past 7, 815−829.

Baumann, K-H., Böckel, B, U., Frenz, M., 2004. Coccolith contribution to South Atlantic carbonate sedimentation, in: Thierstein, H. R., Young, J. R. (Eds.), Coccolithophores: From Molecular Processes to Global Impact. Springer-Verlag Berlin Heidelberg, pp. 367−402.

Baumann, K. H., Freitag, T., 2004. Pleistocene fluctuations in the northern Benguela Current system as revealed by coccolith assemblages. Marine Micropaleontology 52, 195−215.

Bayr, T., Dommenget, D., Martin, T., Power, S. B., 2014. The eastward shift of the Walker Circulation in response to global warming and its relationship to ENSO variability. Climate Dynamics 43, 2747−2763.

Beaufort, L., Lancelot, Y., Camberlin, P., Cayre, O., Vincent, E., Bassinot, F., Labeyrie, L., 1997. Insolation cycles as a major control of Equatorial Indian Ocean primary production, Science, 278, 1451–1454.

Beaufort, L., de Garidel-Thoron, T., Linsley, B., Oppo, D., Buchet, N., 2003. Biomass burning and oceanic primary production estimates in the Sulu Sea area over the last 380 kyr and the East Asian monsoon dynamics. Marine Geology 201, 53–65.

Beaufort, L., van der Kaars, S., Bassinot, F. C., Moron, V., 2010. Past dynamics of the Australian monsoon: precession, phase and links to the global monsoon concept. Climate of the Past 6, 695–706.

Beaufort, L., Barbarin, N., Gally, Y., 2014. Optical measurements to determine the thickness of calcite crystals and the mass of thin carbon particles such as coccoliths. Nature Protocols 9, 633–642.

Behrenfeld, M. J., Falkowski, P. G., 1997. Photosynthetic rates derived from satellite-based chlorophyll concentration. Limnology and Oceanography 42, 1−20.

Berkelhammer, M., Sinha, A., Stott, L., Cheng, H., Pausata, F. S. R., Yoshimura, K., 2012. An Abrupt Shift in the Indian Monsoon 4000 Years Ago, in: Giosan, L., Fuller, D. Q., Nicoll, K., Flad, R. K., Clift, P. D. (Eds.), Geophysical Monograph Series. American Geophysical Union: Washington, DC, USA, pp. 75−88.

Bian, Y., Jian, Z., Weng, C., Kuhnt, W., Bolliet, T., & Holbourn, A., 2011. A palynological and palaeoclimatological record from the southern Philippines since the Last Glacial Maximum. Chinese Science Bulletin 56, 2359−2365.

Billard, C., Inouye, I., 2004. What is new in coccolithophore biology, in: Thierstein, H. R., Young, J. R. (Eds.), Coccolithophores: From Molecular Processes to Global Impact. Springer-Verlag Berlin Heidelberg, pp. 1−30.

Bjerknes, J., 1969. Atmospheric teleconnections from the equatorial Pacific. Monthly Weather Review 97, 163–172.

Boeckel, B., Baumann, K. H., Henrich, R., Kinkel, H., 2006. Coccolith distribution patterns in South Atlantic and Southern Ocean surface sediments in relation to environmental gradients. Deep Sea Research Part I 53, 1073−1099.

Böll, A., Lückge, A., Munz, P., Forke, S., Schulz, H., Ramaswamy, V., Rixen, T., Gaye, B., Emeis, K.-C., 2014. Late Holocene primary productivity and sea surface temperature variations in the northeastern Arabian Sea: Implications for winter monsoon variability. Paleoceanography 29, 778–794.

Böll, A., Schulz, H., Munz, P., Rixen, T., Gaye, B., Emeis, K.-C., 2015. Contrasting sea surface temperature of summer and winter monsoon variability in the northern Arabian Sea over the last 25 ka. Palaeogeography, Palaeoclimatology, Palaeoecology 426, 10−21.

Bolton, C. T., Chang, L., Clemens, S. C., Kodama, K., Ikehara, M., Medina-Elizalde, M., Paterson, G. A., Roberts, A. P., Rohling, E. J., Yamamoto, Y., Zhao, X., 2013. A 500,000 year record of Indian summer monsoon dynamics recorded by eastern equatorial Indian Ocean upper water-column structure. Quaternary Science Reviews 77, 167−180.

Bonnefille, R., Chalie, F., 2000. Pollen-inferred precipitation time-series from equatorial mountains, Africa, the last 40 kyr BP. Global and Planetary Change 26, 25−50.

Bonan, G. B., Oleson, K. W., Vertenstein, M., Levis, S., 2002. The land surface climatology of the Community Land

Model Coupled to the NCAR Community Climate Model. Journal of Climate 15, 3123−3149.

Boos, W. R., Korty, R. L., 2016. Regional energy budget control of the intertropical convergence zone and application to mid-Holocene rainfall. Nature Geoscience 9, 892−897.

Braconnot, P., Marti, O., Joussaume, S., Leclainche, Y., 2000. Ocean feedback in response to 6 kyr BO insolation. Journal of Climate 13, 1537–1553.

Braconnot, P., Harrison, S. P., Kageyama, M., Bartlein, P. J., Masson-Delmotte, V., Abe-Ouchi, A., Otto-Bliesner, B., and Zhao, Y., 2012. Evaluation of climate models using palaeoclimatic data, Nature Climate Change 2, 417–424.

Braconnot, P., Otto-Bliesner, B., Harrison, S., Joussaume, S., Peterchmitt, J.-Y., Abe-Ouchi, A., Crucifix, M., Driesschaert, E., Fichefet, Th., Hewitt, C. D., Kageyama, M., Kitoh, A., Laîné, A., Loutre, M.-F., Marti, O., Merkel, U., Ramstein, G., Valdes, P., Weber, S. L., Yu, Y., and Zhao, Y., 2007a. Results of PMIP2 coupled simulations of the Mid-Holocene and Last Glacial Maximum–Part 1: experiments and large-scale features. Climate of the Past 3, 261–277.

Braconnot, P., Otto-Bliesner, B., Harrison, S., Joussaume, S., Peterchmitt, J.-Y., Abe-Ouchi, A., Crucifix, M., Driesschaert, E., Fichefet, Th., Hewitt, C. D., Kageyama, M., Kitoh, A., Loutre, M.-F., Marti, O., Merkel, U., Ramstein, G., Valdes, P., Weber, L., Yu, Y., and Zhao, Y., 2007b Results of PMIP2 coupled simulations of the Mid-Holocene and Last Glacial Maximum–Part 2: feedbacks with emphasis on the location of the ITCZ and mid- and high latitudes heat budget. Climate of the Past 3, 279–296.

Bradtmiller, L. I., Anderson, R. F., Fleisher, M. Q., Burckle, L. H., 2009. Comparing glacial and Holocene opal fluxes in the Pacific sector of the Southern Ocean. Paleoceanography 24, PA2214.

Briegleb, B. P., Bitz, C. M., Hunke, E. C., Lipscomb, W. H., Holland, M., Schramm, J. L., Moritz, R. E., 2004. Scientific description of the sea ice component in the Community Climate System Model, Version 3, University Corporation for Atmospheric Research, Boulder, Colorado, USA.

Broecker, W., Clark, E., 2009. Ratio of coccolith $CaCO_3$ to foraminifera $CaCO_3$ in late Holocene deep sea sediments. Paleoceanography 24, PA3205.

Brown, J. N., McIntosh, P. C., Pook, M. J., Risbey, J. S., 2009. An investigation of the links between ENSO flavors and rainfall processes in southeastern Australia. Monthly Weather Review 137, 3786−3795.

Budziak, D., Schneider, R. R., Rostek, F., Müller, P. J., Bard, E., Wefer, G., 2000. Late Quaternary insolation forcing on total organic carbon and C_{37} alkenone variations in the Arabian Sea. Paleoceanography 15, 307–321.

Cai, W., Cowan, T., Sullivan, A., 2009. Recent unprecedented skewness towards positive Indian Ocean Dipole occurrences and its impact on Australian rainfall. Geophysical Research Letter 36, L11705.

Cai, W., Yang, K., Wu, L., Huang, G., Santoso, A., Ng, B., Wang, G., Yamagata, T., 2021. Opposite response of strong and moderate positive Indian Ocean Dipole to global warming. Nature Climate Change 11, 27–32.

Cabarcos, E., Flores, J. A., Singh, A. D., Sierro, F. J., 2014. Monsoonal dynamics and evolution of the primary productivity in the eastern Arabian Sea over the past 30 ka. Palaeogeography, Palaeoclimatology, Palaeoecology 411, 249–256.

Caley, T., Malaizé, B., Zaragosi, S., Rossignol, L., Bourget, J., Eynaud, F., Martinez, P., Giraudeau, J., Charlier, K., Ellouz-Zimmermann, N., 2011. New Arabian Sea help decipher orbital timing of Indo-Asian monsoon. Earth and Planetary Science Letters 308, 433–444.

Caratini, C., Tissot, C., 1988. Paleogeographical evolution of the Mahakam delta in Kalimantan, Indonesia during the Quaternary and late Pliocene. Review of Palaeobotany and Palynology 55, 217–228.

Cermeño, P., Dutkiewicz, S., Harris, R. P., Follow, M., Schofield, O., Falkowski, P. G., 2008. The role of nutricline depth in regulating the ocean carbon cycle. PNAS 105, 20344–20349.

Charles, C. D., Froelich, P. N., Zibello, M. A., Mortlock, R. A., Morley, J. J., 1991. Biogenic opal in Southern Ocean sediments over the last 450,000 years: Implications for surface water chemistry and circulation. Paleoceanography 6, 697–728.

Chawchai, S., Tan, L., Löwemark, L., Wang, H. C., Yu, T. L., Chung, Y. C., Mii, H. S., Liu, G., Blaauw, M., Gong, S. Y., Wohhlfarth, B., Shen, C. C., 2021. Hydroclimate variability of central Indo-Pacific region during the Holocene. Quaternary Science Reviews 253, 106779.

Chen, L., Li, T., Yu, Y., & Behera, S. K., 2017. A possible explanation for the divergent projection of ENSO amplitude change under global warming. Climate Dynamics 49, 3799–3811.

Clemens, S., Prell, W., Murray, D., Shimmield, G., Weedon, G., 1991. Forcing mechanisms of the Indian Ocean monsoon 1353, 720–725.

Clemens, S. C., Prell, W. L., 2003. A 350,000 year summer-monsoon multi-proxy stack from the Owen Ridge, Northern Arabian Sea. Marine Geology 201, 35–51.

Clemens, S. C., Kuhnt, W. and Expedition 349 Scientists, 2016a. Expedition 353 summary. In Clemens, S. C., Kuhnt, W., LeVay, L. J. and the Expedition Scientists. Proceeding of the International Ocean Discovery Program 353.

Clemens, S. C., Kuhnt, W. and Expedition 349 Scientists, 2016b. Site U1445. In Clemens, S. C., Kuhnt, W., LeVay, L. J. and the Expedition Scientists. Proceeding of the International Ocean Discovery Program 353.

Clemens, S. C., Kuhnt, W. and Expedition 349 Scientists, 2016c. Site U1446. In Clemens, S. C., Kuhnt, W., LeVay, L. J. and the Expedition Scientists. Proceeding of the International Ocean Discovery Program 353.

Clement, A. C., Peterson, L. C., 2008. Mechanisms of abrupt climate change of the last glacial period. Reviews of Geophysics. Reviews of Geophysics 46, RG4002.

Chevalier, M., Brewer, S., Chase, B. M., 2017. Qualitative assessment of PMIP3 rainfall simulations across the eastern African monsoon domains during the mid-Holocene and the Last Glacial Maximum. Quaternary Science Reviews 156, 107–120.

Colin, C., Kissel, C., Blamart, D., Turpin, L., 1998. Magnetic properties of sediments in the Bay of Bengal and the Andaman Sea: impact of rapid North Atlantic Ocean climatic events on the strength of the Indian monsoon. Earth and Planetary Science Letters 160, 623–635.

Collins, W. D., Bitz, C. M., Blackmon, M. L., Bonan, G. B., Bretheton, C. S., Carton, J. A., Chang, P., Doney, S. C., Hack, J. J., Henderson, T. B., Kiehl, J. T., Large, W. G., McKenna, D. S., Santer, B. D., Smith, R. D., 2006a. The Community Climate System Model Version 3 (CCSM3). Journal of Climate 19, 2122–2143.

Collins, W. D., Rasch, P. J., Boville, B. A., Hack, J. J., McCaa, J. R., Williamson, D. L., Briegleb, B. P., Bitz, C. M., Lin, S.-J., Zhang, M., 2006b. The formulation and atmospheric simulation of the Community Atmosphere Model Version 3 (CAM3). Journal of Climate 19, 2144–2161.

Conti, L., Scardi, M., 2010. Fisheries yield and primary productivity in large marine ecosystem. Marine Ecology Progress Series 410, 233−244.

Contreras-Rosales, L. A., Jennerjahn, T., Tharammal, T., Meyer, V., Lückge, A., Paul, A., Schefuß, E., 2014. Evolution of the Indian Summer Monsoon and terrestrial vegetation in the Bay of Bengal region during the past 18 ka. Quaternary Science Review 102, 133–148.

Cowie, G., 2005. The biogeochemisty of Arabian Sea surficial sediments: A review of recent studies. Progress in Oceanography 65, 260–289.

Cullen, J. L., Prell, W. L., 1984. Planktonic foraminifera of the northern Indian Ocean: Distribution and preservation in surface sediments. Marine Micropaleontology 9, 1–52.

Curray, J. R., Emmel, F. J., Moore, D. G., 2002. The Bengal Fan: morphology, geometry, stratigraphy, history and processes. Marine and Petroleum Geology, 19, 1191–1223.

Currie, J. C., Lengaigne, M., Vialard, J., Kaplan, D. M., Aumont, O., Naqvi, S. W. A., Maury, O., 2013. Indian Ocean Dipole and El Niño/Southern Oscillation impacts on regional chlorophyll anomalies in the Indian Ocean. Biogeosciences 10, 6677−6698.

Curry, W. B., Ostermann, D. R., Guptha, M. V. S., Ittekkot, V., 1992. Foraminiferal production and monsoonal upwelling in the Arabian Sea: evidence from sediment traps. Geological Society, London, Special Publications 64, 93–106.

D'Agostino, R., Bader, J., Bordoni, S., Ferreira, D., Jungclaus, J., 2019. Northern Hemisphere monsoon response to Mid-Holocene orbital forcing and greenhouse gas-induced global warming. Geophysical Research Letters 46, 1591−1601.

D'Agostino, R., Lionello, P., 2020. The atmospheric moisture budget in the Mediterranean: Mechanisms for seasonal changes in the Last Glacial Maximum and future warming scenario. Quaternary Science Reviews, 241, 106392.

Dahl, K., Oppo, D. W., 2006. Sea surface temperature pattern reconstructions in the Arabian Sea. Paleoceanography 21, PA1014.

Dayem, K. E., Noone, D. C., Molnar, P., 2007. Tropical western Pacific warm pool and maritime continent precipitation rates and their contrasting relationships with the Walker Circulation. Journal of Geophysical Research: Atmospheres 112, D06101.

Dehairs, F., Fagel, N., Antia, A.N., Peinert, R., Elskens, M., Goeyens, L., 2000. Export production in the Bay of Biscay as estimated from barium—barite in settling material: a comparison with new production. Deep-Sea Research I 47, 583–601.

Deplazes, G., Lückge, A., Stuut, J. B. W., Pätzold, J., Kuhlmann, H., Husson, D., Fant, M., Haug, G. H., 2014. Weakening and strengthening of the Indian monsoon during Heinrich events and Dansgaard-Oeschger oscillations. Paleoceanography 29, 99–114.

de Garidel-Thoron, T., Beaufort, L., Linsley, B. K., Dannenmann, S., 2001. Millennial-scale dynamics of the East Asian winter monsoon during the last 200,000 years. Paleoceanography 16, 491–502.

Dickinson, R. E., Oleson, K. W., Bonan, G., Hoffman, F., Thirnton, P., Vertenstein, M., Yang, Z.-L., Zeng, X., 2006. The Community Land Model and its climate statistics as a component of the Community Climate System Model. Journal of Climate 19, 2302–2324.

DiNezio, P. N., 2010. Reconciling differing views of tropical Pacific climate change. EOS 91, 141–152.

DiNezio, P. N., Tierney, J. E., 2013. The effect of sea level on glacial Indo-Pacific climate. Nature Geoscience 6, 485−491.

DiNezio, P. N., Timmermann, A., Tierney, J. E., Jin, F. F., Otto-Bliesner, B., Rosenbloom, N., Mapes, B., Neale, R., Ivanovic, R. F., Montenegro, A., 2016. The climate response of the Indo-Pacific warm pool to glacial sea level. Paleoceanography 31, 866-894.

DiNezio, P. N., Tierney, J. E., Otto-Bliesner, B., Timmermann, A., Bhattacharya, T., Rosenbloom, N., Brady, E., 2018. Glacial changes in tropical climate amplified by the Indian Ocean. Science Advances 4, eaat9658. https://doi.org/10.1126/sciadv.aat9658.

Dixit, Y., Hodell, D. A., Petrie, C. A., 2014a. Abrupt weakening of the summer monsoon in northwest India ~ 4100 yr ago. Geology 42, 339–342.

Dixit, Y., Hodell, D. A., Sinha, R., Petrie, C. A., 2014b. Abrupt weakening of the Indian summer monsoon at 8.2 kyr B.P. Earth and Planetary Science Letters 391 16–23.

Dixit, Y., Tandon, S. K., 2016. Hydroclimatic variability on the Indian subcontinent in the past millennium: review and assessment. Earth-Science Reviews 161, 1–15.

Dixit, Y., 2020. Regional character of the "Global Monsoon": paleoclimate insights from northwest Indian lacustrine sediments. Oceanography 33, 56–64.

Doney, S. C., 2006. Plankton in a warmer world. Nature 444, 695–696.

Dubois, N., Oppo, D. W., Galy, V. V., Mohtadi, M., Van Der Kaars, S., Tierney, J. E., Rosenthal, Y., Eglinton, T. I., Lückge, A., Linsley, B. K., 2014. Indonesian vegetation response to changes in rainfall seasonality over the past 25,000 years. Nature Geoscience 7, 513–517.

Duchamp-Alphonse, S., Siani, G, Michel, E., Beaufort, L, Gally, Y., Jaccard, S. L., 2018. Enhanced ocean-atmosphere carbon partitioning via the carbonate counter pump during the last deglacial. Nature Communications 9, 2396. https://doi.org/ 10.1038/s41467-018-04625-7.

Dufresne, J.-L., Foujols, M.-A., Denvil, S., Caubel, A., Marti, O., Aumont, O., Balkanski, Y., Bekki, S., Bellenger, H., Benshila, R., Bony, S., Bopp, L., Braconnot, P., Brockmann, P., Cadule, P., Cheruy, F., Codron, F., Cozic, A., Cugnet, D., de Noblet, N., Duvel, J.-P., Ethé, C., Fairhead, L., Fichefet, T., Flavoni, S., Friedlingstein, P., Grandpeix, J.-Y., Guez, L., Guilyardi, E., Hauglustaine, D. A., Hourdin, F., Idelkadi, A., Ghattas, J., Joussaume, S., Kageyama, M., Krinner, G., Labetoulle, S., Lahellec, A., Lefebvre, M.-P., Lefevre, F., Levy, C., Li, Z. X., Lloyd, J., Lott, F., Madec, G., Mancip, M., Marchand, M., Masson, S., Meurdesoif, Y., Mignot, J., Musat, I., Parouty, S., Polcher, J., Rio, C., Schulz, M., Swingedouw, D., Szopa, S., Talandier, C., Terray, P., Viovy, N., Vuichard, N., 2013. Climate change projections us- ing the IPSL-CM5 Earth System Model: from CMIP3 to CMIP5.Climate Dynamics 40, 2123–2165.

Duplessy, J. C., 1982. Glacial to interglacial contrasts in the northern Indian Ocean. Nature 295, 494–498.

Dutt, S., Gupta, A. K., Clemens, S. C., Cheng, H., Singh, R. K., Kathayat, G., Edwards, R. L., 2015. Abrupt changes in Indian summer monsoon strength during 33,800 to 5500 years B.P. Geophysical Research Letters 42, 5526–5532.

Dymond, J., Suess, E., Lyle, M., 1992. Barium in deep sea sediments. A geochemical proxy for paleoproductivity. Paleoceanography 7, 163–181.

Eyring, V., Bony, S., Meehl, G. A., Senior, C. A., Stevens, B., Stouffer, R. J., Taylor, K. E., 2016. Overview of the Coupled Model Intercomparison Project Phase 6 (CMIP6) experimental design and organization. Geoscientific Model Development 9, 1937–1958.

Fasullo, J., Webster, P. J., 1999. Warm pool SST variability in relation to the surface energy balance. Journal of Climate 12, 1292–1305.

Fichefet, T., Maqueda, M. A. M.,1997. Sensitivity of a global sea ice model to the treatment of ice thermodynamics and dynamics. Journal of Geophysical Research-Oceans 102, 12609–12646.

Flores, J. A., Gersonde, R., Sierro, F. J., 1999. Pleistocene fluctuations in the Agulhas Current Retroflection based on the calcareous plankton record. Marine Micropaleontology 37, 1–22.

Foerster, V., Junginger, A., Langkamp, O., Gebru, T., Asrat, A., Umer, M., Lamb, H. F., Wennrich, V., Rethemeyer, J., Nowaczyk, N., Trauth, M. H., Schaebitz, F., 2012. Climatic change recorded in the sediments of the Chew Bahir basin, southern Ethiopia, during the last 45,000 years. Quaternary International 274, 25–37.

Gadgil, S., 2003. The Indian monsoon and its variability. Annual Review of Earth and Planetary Sciences 31, 429–467.

Gadgil, S., Vinayachandran, P. N., Francis, P. A., Gadgil, S., 2004. Extremes of the Indian summer monsoon rainfall, ENSO and equatorial Indian Ocean oscillation. Geophysical Research Letters 31, L12213.

Ganachaud, A., Wunsch, C., 2000. Improved estimates of global ocean circulation, heat transport and mixing from hydrographic data. Nature 408, 453–457.

Garcin, Y., Junginger, A., Melnick, D., Olago, D. O., Strecker, M. R., Trauth, M. H., 2009. Late Pleistocene–Holocene rise and collapse of Lake Suguta, northern Kenya Rift. Quaternary Science Reviews 28, 911–925.

Garcin, Y., Melnick, D., Strecker, M. R., Olago, D., Tiercelin, J. J., 2012. East African mid-Holocene wet–dry transition recorded in palaeo-shorelines of Lake Turkana, northern Kenya Rift. Earth and Planetary Science Letters 331, 322–334.

Garcin, Y., Vincens, A., Williamson, D., Guiot, J., Buchet, G., 2006. Wet phases in tropical southern Africa during the last glacial period. Geophysical Research Letters 33, L077033.

Gasse, E., Street, F. A., 1978. Late Quaternary lake-level fluctuations and environments of the northern Rift Valley and Afar region (Ethiopia and Djibouti). Palaeogeography, Palaeoclimatology, Palaeoecology 24, 279–325.

Gebregiorgis, D., Hathorne, E. C., Sijinkumar, A. V., Nath, B. N., Nürnberg, D., Frank, M., 2016. South Asian summer monsoon variability during the last ~54 kyrs inferred from surface water salinity and river runoff proxies. Quaternary Science Reviews 138, 6–15.

Gebregiorgis, D., Hathorne, E. C., Giosan, L., Clemens, S., Nürnberg, D., Frank, M., 2018. Southern Hemisphere forcing of South Asian monsoon precipitation over the past ~1 million years. Nature Communications 9, 4702.

Gehlen, M., Bopp, L., Emprin, N., Aumont, O., Heinze, C., Ragueneau, O., 2006. Reconciling surface ocean productivity, export fluxes and sediment composition in a global biogeochemical ocean model. Biogeosciences 3, 521–537.

Govil, P., Naidu, P. D., 2011. Variations of Indian monsoon precipitation during the last 32 kyr reflected in the surface hydrography of the Western Bay of Bengal. Quaternary Science Reviews 30, 3871–3879.

Goswami, B. N., Madhusoodanan, M. S., Neema, C. P., Sengupta, D., 2006. A physical mechanism for North Atlantic SST influence on the Indian summer monsoon. Geophysical Research Letters, 33, L02706.

Gupta, A. K., Anderson, D. M., Overpeck, J. T., 2003. Abrupt changes in the Asian southwest monsoon during the Holocene and their links to the North Atlantic Ocean. Nature 421, 354−357.

Gupta, A. K., Mohan, K., Das, M., Singhm R. K., 2013. Solar forcing of the Indian summer monsoon variability during the Allerød period. Scientific Reports 3, 2753.

Gupta, A. K., Mohan, K., Sarkar, S., Clemens, S, C., Ravindra, R., Uttam, R. K., 2015. East–West similarities and differences in the surface and deep northern Arabian Sea records during the past 21 Kyr. Palaeogeography, Palaeoclimatology, Palaeoecology 301, 75−85.

Günther, F., Witt, R., Schouten, S., Mäusbacher, R., Daut, G., Zhu, L., Xu, B., Yao, T., Gleixner, G., 2015. Quaternary ecological responses and impacts of the Indian Ocean Summer Monsoon at Nam Co, Southern Tibetan Plateau. Quaternary Science Reviews 112, 66−77.

Haberle, S. G., 1998. Late Quaternary vegetation change in the Tari Basin, Papua New Guinea. Palaeogeography, Palaeoclimatology, Palaeoecology 137, 1−24.

He, C., Liu, Z., Otto-Bliesner, B. L., Brady, E. C., Zhu, C., Tomas, R., Clark, P. U., Zhu, J., Jahn, A., Gu, S., Zhang, J., Nusbaumer, J., Noone, D., Cheng, H., Wang, Y., Yan, M., Bao, Y., 2021. Hydroclimate footprint of pan-Asian monsoon water isotope during the last deglaciation. Science Advances 7, eabe2611.

He, F., 2011. Simulating transient climate evolution of the last deglaciation with CCSM3, PhD dissertation, University of Wisconsin-Madison, Madison, Wisconsin, USA.

Hermoso, M., 2016. Isotopic record of Pleistocene glacial/interglacial cycles in pelagic carbonates: Revisiting historical data from the Caribbean Sea. Quaternary Science Reviews 137, 69−78.

Hernández-Almeida, I., Ausín, B., Saavedra-Pellitero, M., Baumann, K.-H., Stoll, H. M., 2019. Quantitative reconstruction of primary productivity in low latitudes during the last glacial maximum and the mid-to-late Holocene from a global *Florisphaera profunda* calibration dataset, Quaternary Science Reviews, 205, 166–181.

Hrudya, P. H., Varikoden, H., Vishnu, R., 2021. A review on the Indian summer monsoon rainfall, variability and its association with ENSO and IOD. Meteorology and Atmospheric Physics 133, 1−14.

Hsu, P. C., Li, T., Wang, B., 2011. Trends in global monsoon area and precipitation over the past 30 years. Geophysical Research Letters, 38, L08701.

Hsu, P. C., Li, T., Luo, J. J., Murakami, H., Kitoh, A., Zhao, M., 2012. Increase of global monsoon area and precipitation under global warming: A robust signal? Geophysical Research Letters 39, L06701.

Hourdin, F., Foujols, M.-A., Codron, F., Guemas, V., Dufresne, J.- L., Bony, S., Denvil, S., Guez, L., Lott, F., Ghattas, J., Braconnot, P., Marti, O., Meurdesoif, Y., Bopp, L., 2013. Impact of the LMDZ atmospheric grid configuration on the climate and sensitivity of the IPSL-CM5A coupled model. Climate Dynamics 40, 2167–2192.

Huguet, C., Routh, J., Fietz, S., Lone, M.A., Kalpana, M.S., Ghosh, P., Mangini, A., Kumar, V., Rangarajan, R., 2018. Temperature and Monsoon Tango in a Tropical Stalagmite: Last Glacial-Interglacial Climate Dynamics. Scientific Reports 8, 5386.

Husar, R. B., Prospero, J. M., Stowe, L. L., 1997. Characterization of tropospheric aerosols over the oceans with the NOAA advanced very high resolution radiometer optical thickness operational product. Journal of Geophysical Research: Atmospheres 102, 16889–16909.

IPCC, In press. Global Warming of 1.5°C. An IPCC Special Report on the impacts of global warming of 1.5°C above pre-industrial levels and related global greenhouse gas emission pathways, in the context of strengthening the global response to the threat of climate change, sustainable development, and efforts to eradicate poverty.

Ivanochko, T. S., Ganeshram, R. S., Brummer, G.-J. A., Ganssen, G., Jung, S. J. A., Moreton, S. G., Kroon, D., 2005. Variations in tropical convection as an amplifier of global climate change at the millennial scale. Earth and Planetary Science Letter 235, 302−314.

Ishikawa, S., Oda, M., 2007. Reconstruction of Indian monsoon variability over the past 230,000 years: Planktic foraminiferal evidence from the NW Arabian Sea open-ocean upwelling area. Marine Micropaleontology 63, 143−154.

Iwakiri, T., Watanabe, M., 2019. Strengthening of the Indian Ocean Dipole with increasing seasonal cycle in the mid-Holocene. Geophysical Research Letters 46, 8320–8328.

Ishfaq, A. M., Pattan, J. N., Matta, V. M., Banakar, V. K., 2013. Variation of paleo-productivity and terrigenous input in the eastern Arabian Sea during the past 100 ka. Journal of the Geological Society of India 81, 647-654.

Iskandar, I., Rao, S. A., Tozuka, T., 2009. Chlorophyll-a bloom along the southern coasts of Java and Sumatra during 2006. International Journal of Remote Sensing 30, 663–671.

Jiang, D., Tian, Z., Lang, X., Kageyama, M., Ramstein, G., 2015. The concept of global monsoon applied to the last glacial maximum: A multi-model analysis. Quaternary Science Reviews 126, 126–139.

Jin, X., Liu, C., Zhang, H., Zhou, C., Jiang, X., Wu, Z., Xu, J., 2018. Evolutionary driven of Gephyrocapsa coccolith isotopic vital effects over the past 400 ka. Earth and Planetary Science Letters 503, 236−247.

Johnson, T. C., Scholz, C. A., Talbot, M. R., Kelts, K., Ricketts, R. D., Ngobi, G., Beuning, K., Ssemmanda, I., McGill, J. W., 1996. Late Pleistocene desiccation of Lake Victoria and rapid evolution of cichlid fishes. Science 273, 1091−1093.

Joos, F., Spahni, R., 2008. Rates of change in natural and anthropogenic radiative forcing over the past 20,000 years. PNAS 105, 1425−1430.

Joussain, R., Colin, C., Liu, Z., Meynadier, L., Fournier, L., Fauquembergue, K., Zaragosi, S., Schimidt, F., Rojas, V., Bassinot, F., 2016. Climatic control of sediment transport from the Himalayas to the proximal NE Bengal Fan during the last glacial-interglacial cycle. Quaternary Science Reviews 148, 1–16.

Joussaume, S., Taylor, K.E., Braconnot, P., Mitchell, J.F.B., Kutzbach, J.E., Harrison, S.P., Prentice, I.C., Broccoli, A.J., Abe-Ouchi, A., Bartlein, P.J., Bonfils, C., Dong, B., Guiot, J., Herterich, K., Hewitt, C.D., Jolly, D., Kim, J.W., Kislov, A., Kitoh, A., Loutre, M.-F., Masson, V., McAvaney, B., McFarlane, N., de Noblet, N., Peltier, W.R., Peterschmitt, J.-Y., Pollard, D., Rind, D., Royer, J.-F., Schlesinger, M.E., Syktus, J., Thompson, S., Valdes, P., Vettoretti, G., Webb, R.S., Wyputta, U., 1999. Monsoon changes for 6000 years ago: results of 18 simulations from the Paleoclimate Modeling Intercomparison Project (PMIP). Geophysical Research Letters 26, 859– 862.

Ju, J., Slingo, J., 1995. The Asian summer monsoon and ENSO. Quarterly Journal of the Royal Meteorological Society 121, 1133–1168.

Jung, S. J., Ivanova, E., Reichart, G. J., Davies, G. R., Ganssen, G., Kroon, D., Van Hinte, J. E., 2002. Centennial-millennial-scale monsoon variations off Somalia over the last 35 ka. Geological Society, London, Special Publications 195, 341–352.

Kageyama, M., Merkel, U., Otto-Bliesner, B., Prange, M., Abe-Ouchi, A., Lohmann, G., Ohgaito, R., Roche, D. M., Singarayer, J., Swingedouw, D., X Zhang, 2013. Climatic impacts of fresh water hosing under Last Glacial Maximum conditions: a multi-model study. Climate of the Past 9, 935–953.

Kageyama, M., Albani, S., Braconnot, P., Harrison, S. P., Hopcroft, P. O., Ivanovic, R. F., Lambert, F., Marti, O., Peltier, W. R., Peterschmitt, J.-Y., Roche, D. M., Tarasov, L., Zhang, X., Brady, E. C., Haywood, A. M., LeGrande, A. N., Lunt, D. J., Mahowald, N. M., Mikolajewicz, U., Nisancioglu, K. H., Otto-Bliesner, B. L., Renssen, H., Tomas, R. A., Zhang, Q., Abe-Ouchi, A., Bartlein, P. J., Cao, J., Li, Q., Lohmann, G., Ohgaito, R., Shi, X., Volodin, E., Yoshida, K., Zhang, X., Zheng, W., 2017. The PMIP4 contribution to CMIP6 – Part 4: Scientific objectives and experimental design of the PMIP4-CMIP6 Last Glacial Maximum experiments and PMIP4 sensitivity experiments. Geoscientific Model Development 10, 4035–4055.

Kageyama, M., Braconnot, P., Harrison, S. P., Haywood, A. M., Jungclaus, J. H., Otto-Bliesner, B. L., Peterschmitt, J.-Y., Abe-Ouchi, A., Albani, S., Bartlein, P. J., Brierley, C., Crucifix, M., Dolan, A., Fernandez-Donado, L., Fischer, H., Hopcroft, P. O., Ivanovic, R. F., Lambert, F., Lunt, D. J., Mahowald, N. M., Peltier, W. R., Phipps, S. J., Roche, D. M., Schmidt, G. A., Tarasov, L., Valdes, P. J., Zhang, Q., Zhou, T., 2018. The PMIP4 contribution to CMIP6 – Part 1: Overview and over-arching analysis plan. Geoscientific Model Development 11, 1033–1057.

Kasper, T., Haberzettl, T., Wang, J., Daut, G., Doberschütz, S., Zhu, L., Mäusbacher, R., 2015. Hydrological variations on the Central Tibetan Plateau since the Last Glacial Maximum and their teleconnection to inter-regional and hemispheric climate variations. Journal of Quaternary Science 30, 70−78.

Kathayat, G., Cheng, H., Sinha, A., Spötl, C., Edwards, R. L., Zhang, H., Li, X., Yi, L., Ning, Y., Cai, Y., Lui, W. L., Breitenbach, S. F. M., 2016. Indian monsoon variability on millennial-orbital timescales. Scientific Reports 6, 24374.

Kathayat, G., Cheng, H., Sinha, A., Yi, L., Li, X., Zhang, H., Li, H., Ning, Y., Edwards, R. L., 2017. The Indian monsoon variability and civilization changes in the Indian subcontinent. Science advances 3, e1701296.

Kaushal, N., Breitenbach, S. F. M., Lechleitner, F. A., Sinha, A., Tewari, V. C., Ahmad, S. M., Berkelhammer, M., Band, s., Yadava, M., Ramesh, R., Henderson, G. M., 2018. The Indian Summer Monsoon from a Speleothem

$\delta^{18}O$ Perspective—A Review. Quaternary 1, 29. https://doi.org/ 10.3390/quat1030029.

Kerr, R. A., 2000. A North Atlantic climate pacemaker for the centuries. Science 288, 1984–1985.

King, J. A., Washington, R., Engelstaedter, S., 2021. Representation of the Indian Ocean Walker circulation in climate models and links to Kenyan rainfall. International Journal of Climatology 41, E616−E643.

Kinkel, H., Baumann, K. H., Cepek, M., 2000. Coccolithophores in the equatorial Atlantic Ocean: response to seasonal and Late Quaternary surface water variability. Marine Micropaleontology 39, 87−112.

Konecky, B., Russell, J., Bijaksana, S., 2016. Glacial aridity in central Indonesia coeval with intensified monsoon circulation. Earth and Planetary Science Letters 437, 15−24.

Konecky, B. L., Russell, J. M., Johnson, T. C., Brown, E. T., Berke, M. A., Werne, J. P., Huang, Y., 2011. Atmospheric circulation patterns during late Pleistocene climate changes at Lake Malawi, Africa. Earth and Planetary Science Letters 312, 318−326.

Krinner, G., Viovy, N., de Noblet-Ducoudré, N., Ogée, J., Polcher, J., Friedlingstein, P., Ciais, P., Sitch, S., Prentice, I. C., 2005. A dynamic global vegetation model for studies of the coupled atmosphere-biosphere system. Global Biogeochemical Cycles 19, GB1015.

Krishnamurthy, V., Goswami, B. N., 2000. Indian monsoon–ENSO relationship on interdecadal timescale. Journal of climate 13, 579−595.

Krishnaswamy, J., Vaidyanathan, S., Rajagopalan, B., Bonell, M., Sankaran, M., Bhalla, R. S., Badiger, S., 2015. Non-stationary and non-linear influence of ENSO and Indian Ocean Dipole on the variability of Indian monsoon rainfall and extreme rain events. Climate Dynamics 45, 175−184.

Kudrass, H. R., Hofmann, A., Doose, H., Meis, K., Erlenkeuser, H., 2001. Modulation and amplification of climatic changes in the Northern Hemisphere by the Indian summer monsoon during the past 80 k.y. Geology 29, 63−66.

Kumar, K. K., Rajagopalan, B., Cane, M. A., 1999. On the weakening relationship between Indian Monsoon and ENSO. Science 284, 2156−2159.

Kumar, K., Agrawal, S., Sharma, A., Pandey, S., 2019. Indian summer monsoon variability and vegetation changes in the core monsoon zone, India, during the Holocene: A multiproxy study. The Holocene 29, 110−119.

Kutzbach, J. E., 1981. Monsoon climate of the Early Holocene: climate experiment with the Earth's orbital parameters for 9000 years ago. Science 214, 59−61.

Kutzbach, J. E., Street-Perrott, F. A., 1985. Milankovitch forcing of fluctuations in the level of tropical lakes from 18 to 0 kyr BP. Nature 317, 130−134.

Laskar, J., Robutel, P., Joutel, F., Gastineau, M., Correia, A. C. M., Levrard, B., 2004. A long-term numerical solution for the insolation quantities of the Earth. Astronomy & Astrophysics 428, 261−285.

Lau, N. C., Nath, M. J., 2000. Impact of ENSO on the variability of the Asian–Australian monsoons as simulated in GCM experiments. Journal of Climate 13, 4287–4309.

Lau, K.-M., Yang, S., 2015. TROPICA METEOROLOGY AND CLIMATE | Walker Circulation, in: North, G. R., Pyle, J., Zhang, F. (Eds.), Encyclopedia of Atmospheric Sciences (Second Edition). Academic Press, pp. 177−181.

Le Borgne, R., Allain, V., Griffiths, S. P., Matear, R. J., McKinnon, A. D., Richardson, A. J., & Young, J. W. (2011). Vulnerability of open ocean food webs in the tropical Pacific to climate change, in: Bell, J. D., Johnson, J. E., Hobday, A. J. (Eds.), Vulnerability of tropical Pacific fisheries and aquaculture to climate change, 189-250.

Lechleitner, F. A., Breitenbach, S. F. M., Cheng, H., Plessen, B., Rehfeld, K., Goswami, B., Marwan, N., Eroglu, D., Adkins, J., Haug, G., 2017. Climatic and in-cave influences on $\delta^{18}O$ and $\delta^{13}C$ in a stalagmite from northeastern India through the last deglaciation. Quaternary Research 88, 458–471.

Lee, C. M., Jones, B. H., Brink, K. H., Fischer, A. S., 2000. The upper-ocean response to monsoonal forcing in the Arabian Sea: seasonal and spatial variability. Deep-Sea Research Ⅱ 47, 1177−1226.

Lee, J., Kim, S., Khim, B. K., 2020. A paleoproductivity shift in the northwestern Bay of Bengal (IODP Site U1445) across the Mid-Pleistocene transition in response to weakening of the Indian summer monsoon. Palaeogeography, Palaeoclimatology, Palaeoecology, 560, 110018.

Leipe, C., Demske, D., Tarasov, P. E., Members, H. P., 2014. A Holocene pollen record from the northwestern Himalayan lake Tso Moriri: implications for palaeoclimatic and archaeological research. Quaternary

International 348, 93−112.

Le Mézo, P., Beaufort, L., Bopp, L., Braconnot, P., Kageyama, M., 2017. From monsoon to marine productivity in the Arabian Sea: insights from glacial and interglacial climates. Climate of the Past 13, 759−778.

Li, J., Liu, S., Shi, X., Zhang, H., Fang, X., Cao, P., Yang, G., Xue, X., Khokiattiwong, S., and Kornkanitnan, N., 2019. Sedimentary responses to the sea level and Indian summer monsoon changes in the central Bay of Bengal since 40 ka. Marine Geology 415, 105947.

Lim, E.-P., Hendon, H. H., 2015. Understanding the contrast of Australian springtime ranfall of 1997 and 2002 in the frame work of two flavors of El Niño. Journal of Climate 28, 2804−2822.

Limbu, P. T. S., Guirong, T., 2019. Relationship between the October-December rainfall in Tanzania and the Walker circulation cell over Indian Ocean. Meteorologische Zeitschrift 28, 453−469.

Liu, C., Wang, P., Tian, J., Cheng, X., 2008. Coccolith evidence for Quaternary nutricline variations in the southern South China Sea. Marine Micropaleontology 69, 42−51.

Liu, S., Ye, W., Chen, M.-T., Pan, H.-J, Cao, P., Zhang, H., Khokiattiwong, S., Kornkanitnan, N., Shi, X., 2021. Millennial-scale variability of Indian summer monsoon during the last 42 kyr: Evidence based on foraminiferal Mg/Ca and oxygen isotope records from the central Bay of Bengal. Palaeogeography, Palaeoclimatology, Palaeoecology 562, 110112.

Liu, S., Zhang, H., Cao, P., Liu, M., Ye, W., Chen, M. T., Li, J., Pan, H.-J., Khokiattiwong, S., Kornkanitan, N., Shi, X., 2021. Paleoproductivity evolution in the northeastern Indian Ocean since the last glacial maximum: Evidence from biogenic silica variations. Deep Sea Research Part I 175, 103591.

Liu, Z., Wen, X., Brady, E. C., Otto-Bliesner, B., Yu, G., Lu, H., Cheng, H., Wang, Y., Zheng, W., Ding, Y., Edwards, R. L., Cheng, J., Liu, W., Yang, H., 2014. Chinese cave records and the East Asia summer monsoon. Quaternary Science Reviews 83, 115−128.

Liu, Z., Otto-Bliesner, B. L., He, F., Brady, W. C., Tomas, R., Clark, P. U., Carlson, A. E., Lynch-Stieglitz, J., Curry, W., Brook, E., Er- ickson, D., Jacob, R., Kutzbach, J., and Cheng, J., 2009. Transient Simulation of Last Deglaciation with a new mechanism for Bølling- Allerød Warming. Science 325, 310–314.

Lohmann, G., Butzin, M., Eissner, N., Shi, X., Stepanek, C., 2020. Abrupt climate and weather changes across time scales. Paleoceanography and Paleoclimatology 35, e2019PA003782.

Lu, R., Dong, B., Ding, H., 2006. Impact of the Atlantic Multidecadal Oscillation on the Asian summer monsoon. Geophysical Research Letters, 33, L24701.

Luo, F., Li, S., Furevik, T., 2011. The connection between the Atlantic multidecadal oscillation and the Indian summer monsoon in Bergen climate model version 2.0. Journal of Geophysical Research 116, D19117.

Ma, R., Sépulcre, S., Bassinot, F., Haurine, F., TisnératLaborde, N., Colin, C., 2020. North Indian Ocean circulation since the last deglaciation as inferred from new elemental ratio records for benthic foraminifera *Hoeglundina elegans*. Paleoceanography and Paleoclimatology, 35, e2019PA003801.

Madec, G., 2008. NEMO ocean engine, Note du pôle de modélisation, Institut Pierre-Simon Laplace (IPSL), Paris, France, No. 27, ISSN 1288-1619.

Madhupratap, M., Kumar, S. P., Bhattathiri, P. M. A., Kumar, M. D., Raghukumar, S., Nair, K. K. C., Ramaiah, N., 1996. Mechanism of the biological response to winter cooling in the northeastern Arabian Sea. Nature, 384, 549–552.

Madhupratap, M., Ganus, M., Ramaiah, N., Kumar, S. P., Muraleedharan, P. M., de Sousa, S. N., Sardessai, S., Muraleedharan, U., 2003. Biogeochemistry of the Bay of Bengal: physical, chemical and primary productivity characteristics of the central and western Bay of Bengal during summer monsoon 2001. Deep-Sea Research Ⅱ 50, 881–896.

Mahesh, B. S., Banakar, V. L., 2014. Change in the intensity of low-salinity water inflow from the Bay of Bengal into the Eastern Arabian Sea from the Last Glacial Maximum to the Holocene: Implications for monsoon variations. Palaeogeography, Palaeoclimatology, Palaeoecology 397, 31–37.

Mall, R. K., Singh, R., Gupta, A., Srinivasan, G., Rathore, L. S., 2006. Impact of climate change on Indian agriculture: a review. Climatic Change 78, 445–478.

Maloney, B. K., McCormac, F. G. 1995. A 30,000-year pollen and radiocarbon record from Highland Sumatra as

evidence for climatic change. Radiocarbon 37, 181–190.

Mariotti, V., Bopp, L., Tagliabue, A., Kageyama, M., Swingedouw, D., 2012. Marine productivity response to Heinrich events: a model-data comparison. Climate of the Past 8, 1581–1598.

Marshall, M. H., Lamb, H. F., Huws, D., Davies, S. J., Bates, R., Bloemendal, J., Boyle, J., Leng, M. J., Umer, M., Bryant, C., 2011. Late Pleistocene and Holocene drought events at Lake Tana, the source of the Blue Nile. Global and Planetary Change 78, 147–161.

Marzin, C., Braconnot, P., 2009. The role of the ocean feedback on Asian and African monsoon variations at 6 kyr and 9.5 kyr BP. C. R. Geoscience 341, 643–655.

Marzin, C., Kallel, N., Kageyama, M., Duplessy, J.-C., and Braconnot, P., 2013. Glacial fluctuations of the Indian monsoon and their rela- tionship with North Atlantic climate: new data and modelling experiments. Climate of the Past 9, 2135–2151.

Mathien-Blard, E., 2008. Révision du paléothermomètre Mg/Ca et son application sur l'hydrologie de surface de l'Océan Indien Tropical au cours de l'Holocène. PhD dissertation, Université Paris-Sud 11, Orsay, France.

McClelland, H. L. O., Bruggeman, J., Hermoso, M., Rickaby, R. E. M., 2017. The origin of carbon isotope vital effects in coccolith calcite. Nature communications 8, 1–16.

McCreary, J. P., Kohler, K. E., Hood, R. R., Olson, D. B., 1996. A four-component ecosystem model of biological activity in the Arabian Sea. Progress in Oceanography 37, 193–240.

McCreary, J. P., Murtugudde, R., Vialard, J., Vinayachandran, P. N., Wiggert, J. D., Hood, R. R., Shankar, D., Shetye, S., 2009. Biophysical processes in the Indian Ocean, in: Wggert, J. D., Hood, R. R., Naqvi, S. A., Brink, K. H., Smith, S. L. (Eds.), Indian Ocean Biogeochemical Processes and Ecological Variability. American Geophysical Union, Geophysical Monograph Series, vol. 185, pp 9–32.

McManus, J. F., Francois, R., Gherardi, J.-M., Keigwin, L. D., and Brown-Leger, S., 2004. Collapse and rapid resumption of Atlantic meridional circulation linked to deglacial climate changes. Nature 428, 834–837.

Menzel, P., Gaye, B., Mishra, P. K., Anoop, A., Basavaiah, N., Marwn, N., Plessen, B., Prasad, S., Riedel, N., Stebich, M., Wiesner, M. G., 2014. Linking Holocene drying trends from Lonar Lake in monsoonal central India to North Atlantic cooling events. Palaeogeography, Palaeoclimatology, Palaeoecology 410, 164–178.

Mirza, M. M. Q., 2002. Global warming and changes in the probability of occurrence of floods in Bangladesh and implications. Global Environmental Change 12, 127–138.

Misra, P., Tandon, S. K., Sinha, R., 2019. Holocene climate records from lake sediments in India: Assessment of coherence across climate zones. Earth-Science Reviews 190, 370–397.

Mohtadi, M., Prange, M., Schefuß, E., Jennerjahn, T. C., 2017. Late Holocene slowdown of the Indian Ocean Walker circulation. Nature Communications 8**,** 1015. https://doi.org/10.1038/s41467-017-00855-3.

Molfino, B., McIntyre, A., 1990a. Precessional forcing of nutricline dynamics in the Equatorial Atlantic. Science 249, 766–769.

Molfino, B., McIntyre, A., 1990b. Nutricline variation in the equatorial Atlantic coincident with the Younger Dryas. Paleoceanography 5, 997–1008.

Mumbi, C. T., Marchant, R., Hooghiemstra, H., Wooller, M. J., 2008. Late Quaternary vegetation reconstruction from the eastern Arc mountains, Tanzania. Quaternary Research 69, 326−341.

Mujumdar, M., Preethi, B., Sabin, T. P., Ashok, K., Saeed, S., Pai, D. S., Krishnan, R., 2012. The Asian summer monsoon response to the La Niña event of 2010. Meteorological Applications 19, 216−225.

Murtugudde, R. G., Signorini, S. R., Christian, J. R., Busalacchi, A. J., McClain, C. R., Picaut, J., 1999. Ocean color variability of the tropical Indo-Pacific basin observed by SeaWiFS during 1997−1998. Journal of Geophysical Research 104, 18351−18366.

Murtugudde, R., McCreary Jr., J. P., Busalacchi, A. J., 2000. Oceanic processes associated with anomalous events in the Indian Ocean with relevance to 1997−1998. Journal of Geophysical Research 105, 3295−3306.

Naidu, P. D., Malmgren, B. A., 1996. A high-resolution of late Quaternary upwelling along the Oman Margin, Arabian Sea based on planktonic foraminifera. Paleoceanography 11, 129−140.

Naik, D. K., Saraswat, R., Lea, D. W., Kurtarkar, S. R., Mackensen, A., 2017. Last glacial-interglacial productivity and associated changes in the eastern Arabian Sea. Palaeogeography, Palaeoclimatology, Palaeoecology 483,

147−156.

Nair, T. M. B., Ittekkot, V., Shankar, R., Gupta, M. V. S., 2005. Settling barium fluxes in the Arabian Sea: Critical evaluation of relationship with export production. Deep-Sea Research Ⅱ 52, 1930−1946.

Neale, R., Slingo, J., 2003. The Maritime Continent and its role in the global climate: A GCM study. Journal of Climate 16, 834−848.

Niedermeyer, E. M., Sessions, A. L., Feakins, S. J., Mohtadi, M., 2014. Hydroclimate of the western Indo-Pacific Warm Pool during the past 24,000 years. PNAS 111, 9402−9406.

Nilsson-Kerr, K., Anand, P., Sexton, P. F., Leng, M. J., Misra, S., Clemens, S. C. Hammond, S., 2019. Role of Asian summer monsoon subsystems in the inter-hemispheric progression of deglaciation. Nature Geoscience 12, 290−295.

Nishimura, M., Matsunaka, T., Morita, Y., Watanabe, T., Nakamura, T., Zhu, L., Nara, F. W., Imai, A., Izutsu, Y., Hasuike, K., 2014. Paleoclimatic changes on the southern Tibetan Plateau over the past 19,000 years recorded in Lake Pumoyum Co, and their implications for the southwest monsoon evolution. Palaeogeography, Palaeoclimatology, Palaeoecology 396, 75−92.

Okada, H., Honjo, S., 1973. The distribution of oceanic coccolithophorids in the Pacific. Deep-Sea Research 20, 355−374.

Okada, H., McIntyre, A., 1979. Seasonal distribution of modern coccolithophores in the western North Atlantic Ocean. Marine Biology 54, 319−328.

Olago, D. O., Street-Perrott, F. A., Perrott, R. A., Ivanovich, M., Harkness, D. D., 1999. Late Quaternary glacial-interglacial cycle of climatic and environmental change on Mount Kenya, Kenya. Journal of African Earth Sciences 29, 593−618.

Otto-Bliesner, B. L., Russell, J. M., Clark, P. U., Liu, Z., Overpeck, J. T., Konecky, B., deMenocal, P., Nicholson, S. E., He, F., Lu, Z., 2014. Coherent changes of southeastern equatorial and northern African rainfall during the last deglaciation. Science 346, 1223–1227.

Otto-Bliesner, B. L., Braconnot, P., Harrison, S. P., Lunt, D. J., Abe-Ouchi, A., Albani, S., Bartlein, P. J., Capron, E., Carlson, A. E., Dutton, A., Fischer, H., Goelzer, H., Govin, A., Hay- wood, A., Joos, F., LeGrande, A. N., Lipscomb, W. H., Lohmann, G., Mahowald, N., Nehrbass-Ahles, C., Pausata, F. S. R., Peterschmitt, J.-Y., Phipps, S. J., Renssen, H., and Zhang, Q., 2017. The PMIP4 contribution to CMIP6 – Part 2: Two interglacials, scientific objective and experimental design for Holocene and Last Interglacial simulations, Geoscientific Model Development 10, 3979– 4003.

Phillips, S. C., Johnson, J. E., Giosan, L., and Rose, K., 2014. Monsson-influenced variation in productivity and lithogenic sediment flux since 110 ka in the offshore Mahanadi Basin, northern Bay of Bengal, Marine and Petroleum Geology 58, 502–525.

Paropkari, A. L., Babu, C. P., Mascarenhas, A., 1992. A critical evaluation of depositional parameters controlling the variability of organic in Arabian Sea sediments. Marine Geology 107, 213–226.

Partin, J. W., Cobb, K. M., Adkins, J. F., Clark, B., Fernandez, D. P., 2007. Millennial-scale trends in west Pacific warm pool hydrology since the Last Glacial Maximum. Nature 449, 452–455.

Pattan, J. N., Masuzawa, T., Naidu, P. D., Parthiban, G., Yamamoto, M., 2003. Productivity fluctuations in the southeastern Arabian Sea during the last 140 ka. Palaeogeography, Palaeoclimatology, Palaeoecology 193, 575–590.

Peltier, W. R., 2004. Global glacial isostasy and the surface of the ice-age earth: The ICE-5G (VM2) model and GRACE. Annual Review of Earth and Planetary Sciences 32, 111–149.

Peltier, W., Richard, D. F. Argus, R. Drummond., 2015. Space geodesy constrains ice age terminal deglaciation: The global ICE-6G_C (VM5a) model. Journal of Geophysical Research: Solid Earth 120, 450-487.

Peng, J., Yang, X., Toney, J. L., Ruan, J., Li, G., Zhou, Q., Gao, H., Xie, Y., Chen, Q., Zhang, T., 2019. Indian Summer Monsoon variations and competing influences between hemispheres since ~35 ka recorded in Tengchongqinghai Lake, southwestern China. Palaeogeography, Palaeoclimatology, Palaeoecology 516, 113–125.

Penny, D., 2001. A 40,000 year palynological record from north-east Thailand; implications for biogeography and

palaeo-environmental reconstruction. Palaeogeography, Palaeoclimatology, Palaeoecology 171, 97–128.

Philander, S. G. H., Gu, D., Lambert, G., Li, T., Halpern, D., Lau, N. C., Pacanowski, R. C., 1996. Why the ITCZ is mostly north of the equator. Journal of Climate 9, 2958–2972.

Pondaven, P., Ragueneau, O., Tréguer, P., Hauvespre, A., Dezileau, L., Reyss, J. L., 2000. Resolving the 'opal paradox'in the Southern Ocean. Nature 405, 168–172.

Poulton, A. J., Adey, T. R., Balch, W. M., Holligan, P. M., 2007. Relating coccolithophore calcification rates to phytoplankton community dynamics: Regional differences and implications for carbon export. Deep Sea Research Part II 54, 538–557.

Poulton, A. J., Painter, S. C., Young, J. R., Bates, N. R., Bowler, B., Drapeau, D., Lyczyskowki, E., Balch, W. M., 2013. The 2008 Emiliania huxleyi bloom along the Patagonian Shelf: Ecology, biogeochemistry, and cellular calcification. Global Biogeochemical Cycles 27, 1023–1033.

Prasad, S., Anoop, A., Riedel, N., Sarkar, S., Menzel, P., Basavaiah, N., Krishnan, R., Fuller, D., Plessen, B., Gaye, B., Röhl, U., Wilkes, H., Sachse, D., Swant, R., Wiesner, M. G., Stebich, M., 2014. Prolonged monsoon droughts and links to Indo-Pacific warm pool: A Holocene record from Lonar Lake, central India. Earth and Planetary Science Letters 391, 171–182.

Prasad, V., Farooqui, A., Sharma, A., Phartiyal, B., Chakraborty, S., Bhandari, S., Raj, R., Singh, A., 2014. Mid–late Holocene monsoonal variations from mainland Gujarat, India: A multi-proxy study for evaluating climate culture relationship. Palaeogeography, Palaeoclimatology, Palaeoecology 397, 38–51.

Prasanna Kumar, S., Madhupratap, M., Dileep Kumar, M., Muraleedharan, P. M., de Souza, S. N., Ganus, M., Sarma, V. V. S. S., 2001a. High biological productivity in the central Arabian Sea during the summer monsoon driven by Ekman pumping and lateral advection. Current Science 81, 1633−1638.

Prasanna Kumar, S., Ramaiah, N., Ganus, M., Sarma, V. V. S. S., Muraleedharan, P. M., Raghukumar, S., Dileep Kumar, M., Madhupratap, M., 2001b. Physical forcing of biological productivity in the Northern Arabian Sea during the Northeast Monsoon. Deep-Sea Research Ⅱ 48, 1115−1126.

Prasanna Kumar, S., Muraleedharan, P. M., Prasad, T. G., Ganus, M., Ramaiah, N., de Souza, S. N., Sardesai, S., Madhupratap, M., 2002. Why is the Bay of Bengal less productive during summer monsoon compared to the Arabian Sea? Geophysical Research Letter 29, 2235. https://doi.org/ 10.1029/2002GL016013.

Prasanna Kumar, S., Narvekar, J., 2005. Seasonal variability of the mixed layer in the central Arabian Sea and its implication on nutrients and primary productivity. Deep-Sea Research Ⅱ 52, 1848−1861.

Raddatz, T. J., Reick, C. H., Knorr, W., Kattge, J., Roeckner, E., Schnur, R., 2007. Will the tropical land biosphere dominate the climate-carbon cycle feedback during the twentyfirst century? Climate Dynamics 29, 565–574.

Rajagopalan, G., Sukumar, R., Ramesh, R., Pant, R. K., Rajagopalan, G., 1997. Late Quaternary vegetational and climatic changes from tropical peats in southern India–an extended record up to 40,000 years BP. Current Science 73, 60−63.

Rajmanickam, V., Achyuthan, H., Eastoe, C., Farooqui, A., 2016. Early-Holocene to present palaeoenvironmental shifts and short climate events from the tropical wetland and lake sediments, Kukkal Lake, Southern India: Geochemistry and palynology. The Holocene 27, 404−417.

Rao, R. R., Sivakumar, R., 2003. Seasonal variability of sea surface salinity and salt budget of the mixed layer of the north Indian Ocean. Journal of Geophysical Research: Oceans 108, 3009.

Rao, R. R., Girish Kumar, M. S., Ravichandran, M., Samala, B. K., Anitha, G., 2006. Observed intraseasonal variability of mini-cold pool off the southern tip of India and its intrusion into the south central Bay of Bengal during summer monsoon season. Geophysical Research Letters 33, L15606.

Ratna, S. B., Cherchi, A., Osborn, T. J., Joshi, M., Uppara, U., 2020. The extreme positive Indian Ocean Dipole of 2019 and associated Indian Summer monsoon rainfall response. Geophysical Research Letter 48, e2020GL091497. https://doi.org/10.1029/2020GL091497.

Rashid, H., Flower, B. P., Poore, R. Z., Quinn, T. M., 2007. A ~25 ka Indian Ocean monsoon variability record from the Andaman Sea. Quaternary Science Reviews 26, 2586−2597.

Rayner, N. A. A., Parker, D. E., Horton, E. B., Folland, C. K., Alexander, L. V., Rowell, D. P., Kent, E. C., Kaplan, A., 2003. Global analyses of sea surface temperature, sea ice, and night marine air temperature since the late

nineteenth century. Journal of Geophysical Research: Atmospheres 108, 4407.

Raza, T., Ahmad, S. M., Sahoo, M., Banerjee, B., Bal, I., Dash, S., Suseela, G., Mukherjee, I., 2014. Hydrographic changes in the southern Bay of Bengal during the last~ 65,000 y inferred from carbon and oxygen isotopes of foraminiferal fossil shells. Quaternary International 333, 77−85.

Reichart, G. J., den Dulk, M., Visser, H. J., van der Weijden, C. H., Zachariasse, W. J., 1997. A 225 kyr record of dust supply, paleoproductivity and the oxygen minimum zone from the Murray Ridge (northern Arabian Sea). Palaeogeography, Palaeoclimatology, Palaeoecology 134, 149−169.

Reid, F. M. H., 1980. Coccolithophorids of the North Pacific Central Gyre with notes on their vertical and seasonal distribution. Micropaleontology 26, 151−176.

Rogalla, U., Andruleit, H., 2005. Precessional forcing of coccolithophore assemblages in the northern Arabian Sea: Implications for monsoonal dynamics during the last 200,000 years. Marine Geology 217, 31−48.

Rost, B., Riebesell, U., 2004. Coccolithophore calcification and the biological pump: response to environmental changes, in: Thierstein, H. R., Young, J. R. (Eds.), Coccolithophores: From Molecular Processes to Global Impact. Springer-Verlag Berlin Heidelberg, pp. 99−126.

Rostek, F., Bard, E., Beaufort, L., Sonzogni, C., Ganssen, G., 1997. Sea surface temperature and productivity records for the past 240 kyr in the Arabian Sea. Deep-Sea Research Ⅱ 44, 1461−1480.

Roth, P. H., 1994. Distribution of coccoliths in oceanic sediments. In: Winter, A., Siesser, W.G. (Eds.), Coccolithophores. Cambridge University Press, London, pp 161−178.

Roxy, M. K., Modi, A., Murtugudde, R., Valsala, V., Panickal, S., Prasanna Kumar, S., Ravichdran, M., Vichi, M., Lévy, M. (2016). A reduction in marine primary productivity driven by rapid warming over the tropical Indian Ocean. Geophysical Research Letters 43, 826−833.

Russell, J. M., Vogel, H., Konecky, B. L., Bijaksana, S., Huang, Y., Melles, M., Wattrus, N., Costa, K., King, J. W., 2014. Glacial forcing of central Indonesian hydroclimate since 60,000 y BP. PNAS 111, 5100−5105.

Saavedra-Pellitero, M., Flores, J. A., Baumann, K. H., Sierro, F. J., 2010. Coccolith distribution patterns in surface sediments of Equatorial and Southeastern Pacific Ocean. Geobios 43, 131−149.

Saavedra-Pellitero, M., Flores, J. A., Lamy, F., Sierro, F. J., Cortina, A., 2011. Coccolithophore estimates of paleotemperature and paleoproductivity changes in the southeast Pacific over the past~ 27 kyr. Paleoceanography 26, PA1201.

Saavedra-Pellitero, M., Baumann, K. H., Ullermann, J., Lamy, F., 2017. Marine Isotope Stage 11 in the Pacific sector of the Southern Ocean; a coccolithophore perspective. Quaternary Science Reviews 158, 1−14.

Saji, N. H., Goswami, B. N., Vinayachandran, P. N., Yamagata, T., 1999. A dipole mode in the tropical Indian Ocean. Nature 401, 360−363.

Sandeep, K., Shankar, R., Warrier, A. K., Yadava, M. G., Ramesh, R., Jani, R. A., Weijian, Z., Xuefeng, L., 2017. A multi-proxy lake sediment record of Indian summer monsoon variability during the Holocene in southern India. Palaeogeography, Palaeoclimatology, Palaeoecology 476, 1−14.

Sanyal, P., Sinha, R., 2015. Evolution of the Indian summer monsoon: synthesis of continental records, in: Clift, P. D., Tada, R., Zheng, H. (Eds.), Monsoon Evolution and Tectonics–Climate Linkage in Asia. Geological Society, London, Special Publications 342, 153–183.

Sharma, S., Joachimski, M., Sharma, M., Tobschall, H. J., Singh, I. B., Sharma, C., Chauhan, M. S., Morgenroth, G., 2004. Lateglacial and Holocene environmental changes in Ganga plain, Northern India. Quaternary Science Reviews 23, 145–159.

Sarkar, A., Ramesh, R., Bhattacharya, S. K., Rajagopalan, G., 1990. Oxygen isotope evidence for a stronger winter monsoon current during the last glaciation. Nature 343, 549–551.

Sarkar, S., Prasad, S., Wilkes, H., Riedel, N., Martina, S., Basavaiah, N., Sachse, D., 2015. Monsoon source shifts during the drying mid-Holocene: Biomarker isotope based evidence from the core ‘monsoon zone’ (CMZ) of India. Quaternary Science Reviews 123, 144–157.

Schneider, T., Bischoff, T., Haug, G. H., 2014. Migrations and dynamics of the intertropical convergence zone. Nature 513, 45−53.

Schott, F. A., McCreary, J. P., 2001. The monsoon circulation of the Indian Ocean. Progress in Oceanography 52,

1−123.

Schulz, H., von Rad, U., Erlenkeuser, H., 1998. Correlation between Arabian Sea and Greenland climate oscillations of the past 110,000 years. Nature 393, 54−57.

Schulz, H., von Rad, U., Ittekkot, V., 2002. Planktic foraminifera, particle flux and oceanic productivity off Pakistan, NE Arabian Sea: modern analogues and application to the paleoclimatic record, in: Clift, P. D., Kroon, D., Gaedicke, D., Craig, J. (Eds.), The tectonic and climatic evolution of the Arabian Sea region. Geological Society, London, Special Publication, vol. 195, pp. 499−516.

Seager, R., Naik, N., Vecchi, G. A., 2010. Thermodynamic and dynamic mechanisms for large-scale changes in the hydrological cycle in response to global warming. Journal of Climate 23, 4651−4668.

Shankar, D., Vinayachandran, P. N., Unnikrishnan A. S., 2002. The monsoon currents in the north Indian Ocean. Progress in Oceanography 52, 63−120.

Sharma, S., Joachimski, M., Sharma, M., Tobschall, H. J., Singh, I. B., Sharma, C., Chauhan, M. S., Morgenroth, G., 2004. Lateglacial and Holocene environmental changes in Ganga plain, Northern India. Quaternary Science Reviews 23, 145−159.

Shenoi, S. S. C., Nasnodkar, N., Rajesh, G., Joseph, K. J., Suresh, I., Almeida, A. M., 2009. On the diurnal ranges of Sea Surface Temperature (SST) in the north Indian Ocean. Journal of Earth System Science 118, 483.

Shi, J., Yan, Q., 2019. Evolution of the Asian-African monsoonal precipitation over the last 21 kyr and the associated dynamics mechanisms. Climate Dynamics 32, 6551−6569.

Shi, W., Wang, M., 2021. A biological Indian Ocean Dipole event in 2019. Scientific Reports 11, 2452.

Shi, X., Lohmann, G., Sidorenko, D., Yang, H., 2020. Early-Holocene simulations using different forcings and resolutions in AWI-ESM. The Holocene 30, 996−1015.

Sidorenko, D., Rackow, T., Jung, T., Semmler, T., Barbi, D., Danilov, S., 2015. Towards multi-resolution global climate modeling with ECHAM6-FESOM—Part I: Model formulation and mean climate. Climate Dynamics 44, 757–780.

Sidorenko, D., Wang, Q., Danilov, S., Schröter, J., 2011. FESOM under coordinated ocean-ice reference experiment forcing. Ocean Dynamics, 61, 881–890.

Sijinkumar, A. V., Nath, B. N., Guptha, M. V. S., 2010. Late Quaternary record of pteropod preservation from the Andaman Sea. Marine Geology 275, 221−229.

Sijinkumar, A. V., Clemens, S., Nath, B. N., Prell, W., Benshila, R., Lengaigne, M., 2016. $\delta^{18}O$ and salinity variability from the Last Glacial Maximum to Recent in the Bay of Bengal and Andaman Sea. Quaternary Science Reviews 135, 79−91.

Singh, A. D., Kroon, D., Ganeshram, R. S., 2006. Millennial scale variations in productivity and OMZ intensity in the eastern Arabian Sea. Journal-Geological Society of India 68, 369.

Singh, A. K., Tiwari, M., Srivastava, A., Sinha, D. K., Ramesh, R., 2016. Wind strength variability in the western Arabian sea since the Last Glacial Maxium: southwest vs. northeast monsoon modes. Journal of Climate Change 2, 57−70.

Sinha, R., Smykatz-Kloss, W., Stüben, D., Harrison, S. P., Berner, Z., Kramar, U., 2006. Late Quaternary palaeoclimatic reconstruction from the lacustrine sediments of the Sambhar playa core, Thar Desert margin, India. Palaeogeography, Palaeoclimatology, Palaeoecology 233, 252−270.

Smith, R. D., Gent, P. R., 2002. Reference manual for the Parallel Ocean Program (POP), ocean component of the Community Climate System Model (CCSM2.0 and 3.0). Los Alamos National Laboratory, Los Alamos, New Mexico, USA, LAUR-02-2484.

Srinivasan, V., Ramamurthy, K., 1973. Northeast monsoon. Comprehensive articles on selected topics. Forecasting Manual Part IV, FMU Report No IV-18.4, India Meteorological Department, Poona, India.

Stager, J. C., 1988. Environmental changes at Lake Cheshi, Zambia since 40,000 years BP. Quaternary Research 29, 54–65.

Stevens, B., Giorgetta, M., Esch, M., Mauritsen, T., Crueger, T., Rast, S., 2013. Atmospheric component of the MPI Earth system model: ECHAM6. Journal of Advances in Modeling Earth Systems 5, 146–172.

Stoll, H. M., Schrag, D. P., 2000. Coccolith Sr/Ca as a new indicator of coccolithophorid calcification and growth

rate. Geochemistry, Geophysics, Geosystems, 1, 1006.

Stuijts, I., Newsome, J. C., & Flenley, J. R., 1988. Evidence for late Quaternary vegetational change in the Sumatran and Javan highlands. Review of Palaeobotany and Palynology 55, 207–216.

Subrahmanyam, B., Murty, V. S. N., Heffner, D. M., 2011. Sea surface salinity variability in the tropical Indian Ocean. Remote Sensing of Environment 115, 944–956.

Sukumar, R., Ramesh, R., Pant, R. K., Rajagopalan, G., 1993. A $\delta^{13}C$ record of late Quaternary climate change from tropical peats in southern India. Nature 364, 703–706.

Sun, W., Zhang, E., Shulmeister, J., Bird, M. I., Chang, J., Shen, J., 2019. Abrupt changes in Indian summer monsoon strength during the last deglaciation and early Holocene based on stable isotope evidence from Lake Chenghai, southwest China. Quaternary Science Reviews 218, 1−9.

Sun, X., Li, X., Luo, Y., Chen, X., 2000. The vegetation and climate at the last glaciation on the emerged continental shelf of the South China Sea. Palaeogeography, Palaeoclimatology, Palaeoecology 160, 301−316.

Talley, L. D., 2003. Shallow, intermediate, and deep overturning components of the global heat budget. Journal of Physical Oceanography 33, 530-560.

Tan, C. T., Ishizaka, J., Matsumura, S., Yusoff, F. M., Mohamed, M. I. H., 2006. Seasonal variability of SeaWiFS chlorophyll *a* in the Malacca Straits in relation to Asian monsoon. Continental Shelf Research 26, 168−178.

Tangunan, D., Baumann, K.-H., Pätzold, J., Henrich, R., Kucera, M., De Pol-Holz, R., Groeneveld, J., 2017. Insolation forcing of coccolithophore productivity in the western tropical Indian Ocean over the last two glacial-interglacial cycles. Paleoceanography 32, 692−709.

Taylor, K. E., Stouffer, R. J., and Meehl, G. A., 2012. An overview of CMIP5 and the experiment design, Bulletin of the American Meteorological Society 93, 485–498.

Tierney, J. E., Russell, J. M., Huang, Y., Damsté, J. S. S., Hopmans, E. C., Cohen, A. S., 2008. Northern hemisphere controls on tropical southeast African climate during the past 60,000 years. Science 322, 252−255.

Tierney, J. E., Russell, J. M., Damsté, J. S. S., Huang, Y., & Verschuren, D., 2011. Late Quaternary behavior of the East African monsoon and the importance of the Congo Air Boundary. Quaternary Science Reviews 30, 798−807.

Tierney, J. E., Zhu, J., King, J., Malevich, S. B., Hakim, G. J., Poulsen, C. J., 2020. Glacial cooling and climate sensitivity revisited. Nature 584, 569−573.

Thushara, V., Vinayachandran, P. N., 2016. Formation of summer phytoplankton bloom in the northwestern Bay of Bengal in a coupled physical-ecosystem model. Journal of Geophysical Research: Oceans 121, 8535−8550.

Thushara, V., Vinayachandran, P. N., 2020. Unprecedented surface chlorophyll blooms in the Southeastern Arabian Sea during an extreme negative Indian Ocean Dipole. Geophysical Research Letters 47, e2019GL085026.

Tozuka, T., Endo, S., Yamagata, T., 2016. Anomalous Walker circulations associated with two flavors of the Indian Ocean Dipole. Geophysical Research Letters 43, 5378−5384.

Trenberth, K. E., Solomon, A., 1994. The global heat balance: Heat transports in the atmosphere and ocean. Climate Dynamics 10, 107−134.

Trenberth, K. E., Hoar, T. J., 1997. El Niño and climate change. Geophysical Research Letter 24, 3057−3060.

Trenberth, K. E., Caron, J. M., 2001. Estimates of meridional atmosphere and ocean heat transports. Journal of Climate 14, 3433−3443.

Trenberth, K. E., Fasullo, J. T., 2008. An observational estimate of inferred ocean energy divergence. Journal of Physical Oceanography 38, 984−999.

Trenberth, K. E., Dai, A., Van Der Schrier, G., Jones, P. D., Barichivich, J., Briffa, K. R., Sheffield, J., 2014. Global warming and changes in drought. Nature Climate Change 4, 17−22.

Ummenhofer, C. C., England, M. H., McIntosh, P. C., Meyers, G. A., Pook, M. J., Risbey, J. S., Gupta, A. S., Taschetto, A. S., 2009. What causes southeast Australia's worst droughts? Geophysical Research Letter 36, L04706. https://doi.org/ 10.1029/2008GL036801.

van Campo, E., 1986. Monsoon fluctuations in two 20,000-yr BP oxygen-isotope/pollen records off southwest India 1. Quaternary Research 26, 376−388.

van der Kaars, W. A., Dam, M. A. C., 1995. A 135,000-year record of vegetational and climatic change from the

Bandung area, West-Java, Indonesia. Palaeogeography, Palaeoclimatology, Palaeoecology 117, 55−72.

van der Kaars, S., Bassinot, F., De Deckker, P., Guichard, F., 2010. Changes in monsoon and ocean circulation and the vegetation cover of southwest Sumatra through the last 83,000 years: The record from marine core BAR94-42. Palaeogeography, Palaeoclimatology, Palaeoecology 296, 52−78.

van Der Kaars, S., Wang, X., Kershaw, P., Guichard, F., Setiabudi, D. A., 2000. A Late Quaternary palaeoecological record from the Banda Sea, Indonesia: patterns of vegetation, climate and biomass burning in Indonesia and northern Australia. Palaeogeography, Palaeoclimatology, Palaeoecology *155*, 135−153.

van der Weijden, C. H., Reichart, G. J., Visser, H. J., 1999. Enhanced preservation of organic matter in sediments deposited within the oxygen minimum zone in the northeastern Arabian Sea. Deep Sea Ⅱ 46, 807−830.

Venrick, E., 1982. Phytoplankton in an Oligotrophic Ocean: Observations and Questions: Ecological Archives M052-002. Ecological Monographs 52, 129−154.

Vinayachandran, P. N., Murty, V. S. N., and Ramesh Bahu, V., 2002a. Observations of barrier layer formation in the Bay of Bengal during summer monsoon, Journal of Geophysical Research 107, 8018, https://doi.org/10.1029/2001JC000831.

Vinayachandran, P. N., Iizuka, S., Yamagata, T., 2002b. Indian Ocean dipole mode events in an ocean general circulation model. Deep-Sea Research Ⅱ 49, 1573−1596.

Vinayachandran, P. N., Chauhan, P., Mohan, M., Nayak, S., 2004. Biological response of the sea around Sri Lanka to summer monsoon. Geophysical Research Letter 31, L01302. https://doi.org/ 10.1029/2003GL018533.

Vinayachandran, P. N., McCreary, J. P., Hood, R. R., Kohler, K. E., 2005. A numerical investigation of the phytoplankton bloom in the Bay of Bengal during Northeast Monsoon. Journal of Geophysical Research 110, C12001. https://doi.org/ 10.1029/2005JC002966.

Waliser, D. E., Gautier, C.,1993. A satellite-derived climatology of the ITCZ. Journal of Climate 6, 2162-2174.

Wallace, J. E., Hobbs, P. V., 2003. Atmospheric Science: An Introductory Survey. Academic Press, Elservier, USA.

Wang, B., Clemens, S. C., Liu, P., 2003. Contrasting the Indian and East Asian monsoons: implications on geologic timescales. Marine Geology 201, 5−21.

Wang, B., Ding, Q., 2008. Global monsoon: Dominant mode of annual variation in the tropics. Dynamics of Atmospheres and Oceans 44, 165−183.

Wang, P. X., Wag, B., Cheng, H., Fasullo, J., Guo Z., Kiefer, T., Liu, Z., 2017. The global monsoon across time scales: Mechanisms and outstanding issues. Earth-Science Review 174, 84−121.

Wang, Q., Danilov, S., Sidorenko, D., Timmermann, R., Wekerle, C., Wang, X., Jung, T., Schröter, J., 2014. The Finite Element Sea ice-Ocean Model (FESOM): formulation of an unstructured-mesh ocean general circulation model. Geoscientific Model Development 6, 3893−3976.

Wang, X., van der Kaars, S., Kershaw, P., Bird, M., Jansen, F., 1999. A record of fire, vegetation and climate through the last three glacial cycles from Lombok Ridge core G6-4, eastern Indian Ocean, Indonesia. Palaeogeography, Palaeoclimatology, Palaeoecology 147, 241−256.

Wang, Y., Li, S., Luo, D., 2009. Seasonal response of Asian monsoonal climate to the Atlantic Multidecadal Oscillation. Journal of Geophysical Research 114, D02112

Wasson, R. J., Smith, G. I., Agrawl, D. P., 1984. Late Quaternary sediments, minerals, and inferred geochemical history of Didwana lake, Thar Desert, India. Palaeogeography, Palaeoclimatology, Palaeoecology 46, 345−372.

Webster, P. J., Fasullo, J., 2015. TROPICA METEOROLOGY AND CLIMATE | Monsoon: dynamical theory, in: North, G. R., Pyle, J., Zhang, F. (Eds.), Encyclopedia of Atmospheric Sciences (Second Edition). Academic Press, pp. 151−164.

Wen, X., Liu, Z., Wang, S., Cheng, J., Zhu, J., 2016. Correlation and anti-correlation of the East Asian summer and winter monsoons during the last 21,000 years. Nature Communications 7, 1−7.

Wicaksono, S. A., Russell, J. M., Holbourn, A., Kuhnt, W., 2017. Hydrological and vegetation shifts in the Wallacean region of central Indonesia since the Last Glacial Maximum. Quaternary Science Reviews 157, 152−163.

Wiggert, J.D., Vialard, J. and Behrenfeld, M.J., 2009. Basin-Wide Modification of Dynamical and Biogeochemical Processes by the Positive Phase of the Indian Ocean Dipole During the SeaWiFS Era, in: Wggert, J. D., Hood, R. R., Naqvi, S. A., Brink, K. H., Smith, S. L. (Eds.), Indian Ocean Biogeochemical Processes and Ecological

Variability. American Geophysical Union, Geophysical Monograph Series, vol. 185, pp. 385−407.

Windler, G., Tierney, J. E., DiNezio, P. N., Gibson, K., Thunell, R., 2019. Shelf exposure influence on Indo-Pacific Warm Pool climate for the last 450,000 years. Earth and Planetary Science Letters 516,66–76.

Winter, A., Jordan, R.W., Roth, P.H., 1994. Biogeography of living coccolithophores in ocean waters. In: Winter, A., Siesser, W.G. (Eds.), Coccolithophores. Cambridge University Press, London, pp 161−178.

Wyrtki, K., 1973. An equatorial jet in the Indian Ocean. Science 181, 262−264.

Wu, R., Kirtman, B. P., 2004. Understanding the impacts of the Indian Ocean on ENSO variability in a coupled GCM. Journal of Climate 17, 4019−4031.

Wurster, C. M., Bird, M. I., Bull, I. D., Creed, F., Bryant, C., Dungait, J. A., Paz, V., 2010. Forest contraction in north equatorial Southeast Asia during the Last Glacial Period. PNAS 107, 15508−15511.

Wurtzel, J. B., Abram, N. J., Lewis, S. C., Bajo, P., Hellstrom, J. C., Troitzsch, U., Heslop, D., 2018. Tropical Indo-Pacific hydroclimate response to North Atlantic forcing during the last deglaciation as recorded by a speleothem from Sumatra, Indonesia. Earth and Planetary Science Letters 492, 264−278.

Yan, M., Wang, B., Liu, J., 2016. Global monsoon change during the Last Glacial Maximum: a multi-model study. Climate Dynamics 47, 359−374.

Yan, Q., Owen, L. A., Zhang, Z., Jiang, N., Zhang, R., 2020. Deciphering the evolution and forcing mechanisms of glaciation over the Himalayan-Tibetan orogen during the past 20,000 years. Earth and Planetary Science Letters 541, 116295.

Young, J., 1994. Functions of coccoliths. In: Winter, A., Siesser, W.G. (Eds.), Coccolithophores. Cambridge University Press, London, pp 63−82.

Young, J., 1998. Neogene. In: Bown, P. (Ed.), Calcareous Nannofossil Biostratigraphy. Kluwer Academic Publishers.

Young, J. R., Ziveri, P., 2000. Calculation of coccolith volume and its use in calibration of carbonate flux estimates. Deep-Sea Research Part II 47, 1679–1700.

Zhang, H., Liu, C., Jin, X., Shi, J., Zhao, S., Jian, Z., 2016. Dynamics of primary productivity in the northern South China Sea over the past 24,000 years. Geochemistry, Geophysics, Geosystems 17, 4878−4891.

Zhang, R., Delworth, T. L., 2006. Impact of Atlantic multidecadal oscillations on India/Sahel rainfall and Atlantic hurricanes. Geophysical Research Letters 33, L17712.

Zhang, R., Sutton, R., Danabasoglu, G., Kwon, Y. O., Marsh, R., Yeager, S. G., Amrhein, D. E., Little, C. M., 2019. A review of the role of the Atlantic meridional overturning circulation in Atlantic multidecadal variability and associated climate impacts. Reviews of Geophysics 57, 316−375.

Zhang, X., Zheng, Z., Huang, K., Yang, X., Tian, L., 2020. Sensitivity of altitudinal vegetation in southwest China to changes in the Indian summer monsoon during the past 68000 years. Quaternary Science Reviews 239, 106359.

Zhao, Y., Braconnot, P., Marti, O., Harrison, S. P., Hewitt, C., Kitoh, A., Liu, Z., Mikolajewicz, U., Otto-Bliesner, B., Weber, S. L., 2005. A muti-model analysis of the role of the ocean on the African and Indian monsoon during the Holocene. Climate Dynamics 25, 777−800.

Zhao, Y., Harrison, S. P., 2012. Mid-Holocene monsoons: a milti-model analysis of the interhemispheric differences in the responses to orbital forcing and ocean feedbacks. Climate Dynamics 39, 1457−1487.

Zhu, L., Lü, X., Wang, J., Peng, P., Kasper, T., Daut, G., Haberzettl, T., Frenzel, P., Li, Q., Yang, R., Schwalb, A., Mäusvacher, R., 2015. Climate change on the Tibetan Plateau in response to shifting atmospheric circulation since the LGM. Scientific Reports 5, 13318.

Ziveri, P., Baumann, K.-H., Böckel, B, U., Bollmann, J., Young, J. R., 2004. Biogeography of selected Holocene coccoliths in the Atlantic OCean, in: Thierstein, H. R., Young, J. R. (Eds.), Coccolithophores: From Molecular Processes to Global Impact. Springer-Verlag Berlin Heidelberg, pp. 367−402.

Ziveri, P., de Bernardi, B., Baumann, K.-H., Stoll, H. M., Mortyn, P. G., 2007. Sinking of coccolith carbonate and potential contribution to organic carbon ballasting in the deep ocean. Deep-Sea Research Part II 54, 659– 675.

université PARIS-SACLAY

ÉCOLE DOCTORALE
Sciences mécaniques et énergétiques, matériaux et géosciences (SMEMAG)

Titre : Variabilité climatique de l'Océan Indien Tropical depuis le Dernier Maximum Glaciaire et son impact sur la productivité primaire : apport des comparaisons modèles-données

Mots clés : paléoclimats, mousson indienne, circulation de Walker, productivité primaire, coccolithes, simulations paléoclimatiques

Résumé : L'objectif de cette étude est de reconstruire la dynamique orbitale à millénaire de la productivité primaire (PP) de l'océan Indien tropical au cours des 25 000 dernières années et de comprendre leurs relations avec les changements climatiques de cette période, et plus particulièrement ceux de la circulation atmosphérique. Sur la base d'une comparaison modèle-données, nous montrons que les changements de PP de l'Océan Indien septentrional sont liés aux changements de la mousson indienne d'hiver et d'été, tandis que ceux de l'océan Indien équatorial sont plutôt associés aux changements de la circulation de Walker. Ces reconstitutions ont permis de mieux comprendre les schémas spatio-temporels de la mousson indienne, et leurs liens avec la circulation de Walker.

Title : Climate variability over the tropical Indian Ocean since the Last Glacial Maximum and its impact on primary productivity: insights from model-data comparisons

Keywords : paleoclimates, Indian monsoon, Walker circulation, primary productivity, coccoliths, paleoclimate simulations

Abstract : The aim of this study is to reconstruct orbital to millennial scales primary productivity (PP) patterns of the tropical Indian Ocean over the last 25 000 years and understand their relationships with climate features and more particularly atmospheric circulation. Based on a model-data comparison, we demonstrate that PP patterns from northern Indian Ocean are related to the changes in Indian winter vs summer monsoon while those from the equatorial Indian Ocean are rather sensitive to changes of the Walker circulation. This work helped better understanding the patterns and timing of the Indian monsoon and their links to the Walker circulation.